LABORATOIRE LAGRANGE CNRS UMR 2793
Univerisité de Nice Sophia-Antipolis
Observatoire de la Côte d'Azur

Studies of the physical nature of asteroids: current trends and perspectives

Marco Delbo

Thése d'Habilitation à Diriger des Recherches
Ecole Doctorale Sciences Fondamentales et Appliquées
(ED-SFA)

Rapporteurs: **Bernard Marty**, **Jean-Marc Petit**, **Sean Raymond**
Membres du jury: **Bernard Marty**, **Sean Raymond**, **Emmanuel Lellouch**, **Olivier Groussin**, **Patrick Michel**, **Tristan Guillot**

OBSERVATOIRE DE LA COTE D'AZUR
Date de soutenace 2 juillet 2015

Contents

Preface

In this manuscript (*mémoire*) I summarise the work I have carried out in the last ∼10 years devoted to the physical characterisation of asteroids. As it is common practice, some relevant papers are attached to the manuscript.

Some of my works, of rather technical nature, were devoted to improve the methods of the physical characterisation of asteroids. Other works were dedicated to the preparation of instruments and space missions to observe asteroids remotely, such as ESA's Gaia, or to visit asteroids, such as NASA's OSIRS-REx. Clearly, one of the most challenging, interesting, and rewording aspects of my work is to understand the nature of asteroids and discover new processes that have shaped these bodies and their surfaces throughout the last 4.5 Ga of the evolution of our Solar System.

Possibly, these projects must be carried out taking into account the rapidly changing panorama and state of the art of the physical study of asteroids and other minor bodies, and how these studies fit in the global scenarios of the formation of our and other planetary systems. Furthermore, it is important to understand what are the open issues in this and other related fields of research.

The first chapter of this manuscript deals with these aspects: i.e. the state of the art of the research and its implication for the global picture of understanding the formation of our solar system. Next, I present some open questions. The second chapter focuses on the great improvements in the physical characterisation of asteroids of the last 10 years and how my works fit into these research. The third chapter presents some of the perspectives for this research.

This *mémoire* is structured as a broad review chapter. It is not exhaustive, but it can be used as student's introduction to the context and the problems of the physical characterisation of asteroids.

Nice, 14 May 2015. Marco Delbo

1

Introduction

REVOLVING around the Sun between the orbits of Mars and Jupiter, asteroids are small airless bodies considered to be leftovers from the processes of planetary formation. Understanding the chronological origin, diverse physical nature, varied compositions, and orbital distribution of asteroids is essential to constrain models of Solar System formation and evolution.

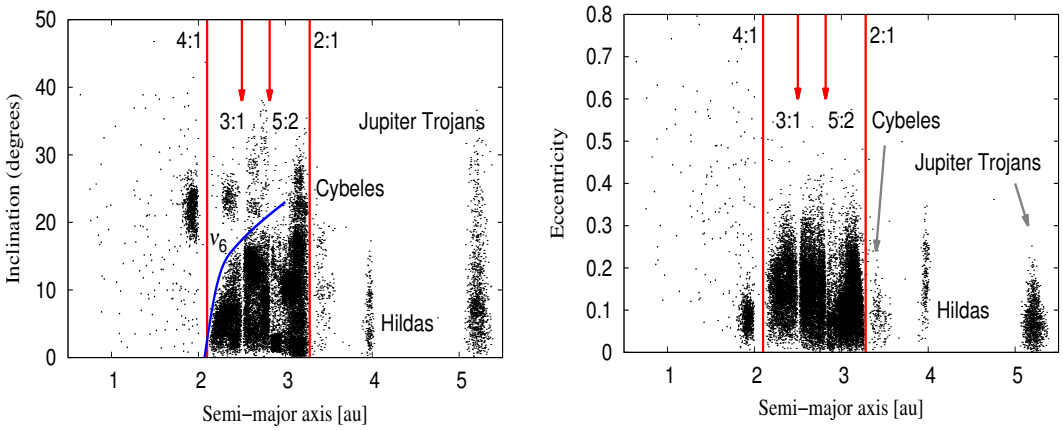

Figure 1.1: Orbital element distribution of asteroids in the inner Solar System (a<5 au). Left panel: inclination (degrees) versus semi-major axis (au). Right panel: eccentricity versus semi-major axis. Prominent Kirkwood gaps, created my mean motion resonance, are marked in red. The ν_6 secular resonance is indicated in blue. Names are given to some major asteroid groups.

1.1 Physics of asteroids: context and state-of-the-art

Asteroid physical studies

The purpose of asteroid physical studies is to construct a detailed compositional map of the asteroid population (and sub populations thereof) and to determine the formation location of these bodies. As we shall see, an important aspect of these studies is to establish a chronology for the formation and destruction of asteroids throughout the whole history of the Solar System, whose origin is fixed at 4.567 billions of years ago [4].

Furthermore, it is fundamental to understand how these bodies have been subject to different degree of modifications since their formation due to processes such as (i) disruptive collisions amongst them, (ii) impact cratering, (iii) early thermal heating due to radioactive nuclides, and (iv) surface space weathering [27]. The latter is the surface alteration due to a number of phenomena such as the constant exposure to solar and galactic cosmic rays, micrometeorite bombardment, and radiative heating from the sun[1]. The importance of the latter has been recognised only recently [112, 46].

Implications for models of Solar System formation

The story of asteroids begins in a very active Solar System: violent dynamical scenarios for its earlier stages [130] are invoked by modern theories of planetary formations such as the Grand Tack Hypothesis [181] and the Nice Model [171, 128, 62]. These theories, which describe the early ($\sim$ 4.56 Ga) and the final ($\sim$ 4.1 Ga) phases of the giant planets migration in our Solar System, respectively, have to reproduce the distribution of the orbital and physical properties of the different classes of minor bodies, such as asteroids [127, 51], comets, Jupiter Trojans [128, 138], and Transneptunian objects [62].

The Grand Tack

In essence, according to the Grand Tack hypothesis, Jupiter formed in the first few millions of years, likely beyond the *snow-line* in the protoplanetary disk (at e.g. 3.5 au) and migrated inward down to until 1.5 au, when it was stopped by the inward migration of the forming Saturn. The giant planets perturbed the orbits of those planetesimals that have orbits interior to that of Jupiter. Several of these small bodies, which formed between 1.5 and 3.5 au were pushed inward,

[1] Analyses of soil samples from both the Moon and the asteroid Itokawa showed that nanophase metallic particles accumulate on the rims of regolith grains with time. This causes changes in the reflectance spectrum that can be observed from telescopic observations. In the case of the asteroid (4) Vesta spectroscopic measurements from the NASA's DAWN mission indicate that space weathering is due to locally homogenized upper regolith that is generated with time through small-scale mixing of diverse surface components [144].

or scattered into orbits at higher heliocentric distances. Next, the migration of the two giant planets reversed, until they stopped in a compact configuration with Jupiter at about 5.2 au and Saturn at about 7 au. On their way out, the planets scattered planetesimals inward, repopulating that zone of the Solar System that today corresponds to the Main Belt (2 – 3.5 au).

The Nice Model

The Nice model makes the hypothesis that, after the dissipation of the gas and dust of the primordial Solar System disk, the four giant planets were placed on small-eccentricity orbits between 5.2 and 17 au, in a more compact orbital configuration than they are today. A disk of planetesimals of ∼35 Earth masses, extended from the orbit of the outermost giant planet to about 35 au. This disk of debris perturbs the orbit of the planets with the three outermost of them slowly migrating outward because of planets-planetismals scattering. After several hundreds of millions of years of slow and smooth migration, Jupiter and Saturn cross their mutual 1:2 mean-motion resonance. This resonance increases their orbital eccentricities, destabilising the entire planetary system. The arrangement of the giant planets alters quickly and dramatically. Jupiter shifts Saturn out towards its present position, and this relocation causes mutual gravitational encounters between Saturn and the two ice giants, which propel Neptune and Uranus onto much more eccentric orbits. These ice giants then plough into the planetesimal disk, scattering tens of thousands of planetesimals from their formerly stable orbits in the outer Solar System. This disruption almost entirely scatters the primordial disk, removing 99% of its mass, a scenario which explains the modern-day absence of a dense trans-Neptunian population.

Late Heavy Bombardment

Some of the planetesimals are thrown into the inner Solar System, producing a sudden influx of impacts on the terrestrial planets: the Late Heavy Bombardment (LHB).

Jupiter Trojans

The puzzling properties of Jupiter Trojans, such as their wide range of orbital inclinations and their singular spectral characteristics, could be explained if they actually originated in the trans-Neptunian belt but were scattered and later captured in the giant planet's Lagrangian points [128, 138].

Acquiring a profound knowledge of all these processes by studying asteroid physical properties and dynamics is therefore another prerequisite for unraveling the clues about our Solar System's distant past recorded within these bodies. For instance, the current orbital configuration of the Main Belt cannot be explained without an early (Izidoro, A., et al. In preparation[2]) and a later

[2]Izidoro et al. find that disks with shallow density gradients allow the dynamical excitation

planetary migration [124, 127].

Further implications

All these studies have far-reaching implications. They provide key constraints to our understanding of how planets like our own form, how volatiles, such as water and organics, have originated and have been distributed to their present locations in our Solar System and, ultimately, how these processes are linked to the emergence of life on Earth.

The Main Belt as a living Relic (W. Bottke)

But there is more: in fact, "the Main Belt is a living relic. On-going collisional and dynamical evolution processes, however, are slowly obscuring the traces left behind" [17]. Another goal of asteroid studies is to find the observational constraints to model the collisional evolution of the Main Belt, from the epoch of the LHB up to now. Three types of information are particularly needed in this respect: the first is the knowledge of basic asteroid physical properties such as sizes, albedos and mineralogical composition. The second is a comprehension of the geological features of the surfaces of asteroids at different heliocentric distances, of different mineralogy, sizes and ages. The third is the understanding of the processes that create, modify and erase these features, as well as a chronology for the formation and destruction of asteroids.

Asteroid families

Beside the orbital structure of asteroids, sculpted by the presence of the orbital resonances with the planets, there is another major dynamical feature in the asteroid belt manifesting itself at a smaller scale in orbital element space: the asteroid families. These can be identified as groupings of asteroids in orbital elements space, and are typically called dynamical families [123]. Some of these families are believed to play a fundamental role in the delivery of asteroids and meteoroids from the Main Belt to near-Earth space [180, 21, 147]

Disruption and collisions of asteroids

The formation of a family is due to impacts between asteroids. We call this a collisional family. These impacts can dig giant craters such as *Venenia* and *Reasilvia* on (4) Vesta or catastrophically disrupt asteroids. The debris created

of the asteroid belt by a self-stirring process, but lead inevitably to the formation of a Mars analog which is significantly more massive than the real planet. Instead, a disk with a surface density gradient proportional to $1/r^5$ beyond 1 AU allows us to reproduce the Earth/Mars mass ratio, but leaves the asteroid belt on a dynamical state way too cold compared to the real belt. Therefore, we conclude that no disk profile can explain at the same time the structure of the terrestrial planet system and of the asteroid belt. Thus, the asteroid belt has to have been depleted and dynamically excited by an external agent as, for instance, in the Grand Tack scenario.

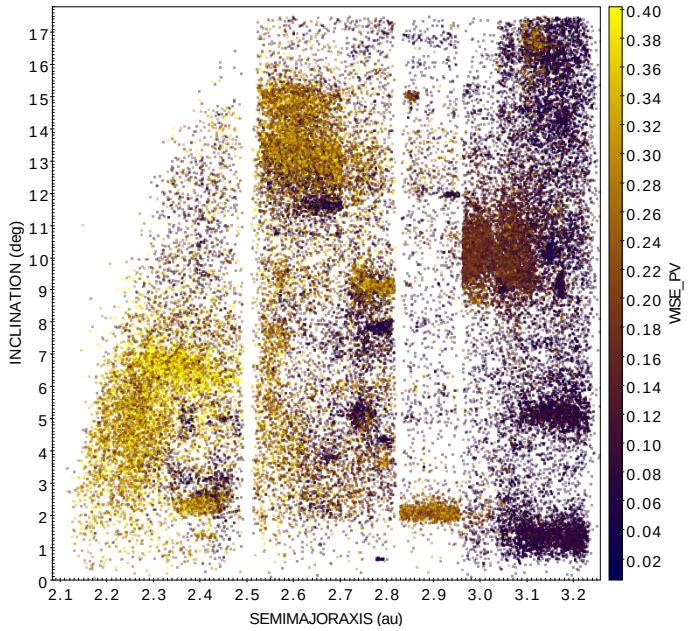

Figure 1.2: Main Asteroid Belt. Asteroids are colour coded according to their albedos [115]. Most of the groupings in the orbital element space are asteroid families.

by these impacts can re-accumulate and form new asteroids [122]: these are rubble-pile asteroids and constitute members of the families (e.g. the Vesta's families, due to cratering events; the Themis' family due to a catastrophic destruction of the parent asteroid). It is thought that collisions that happen today are generally disruptive, given the high velocity of asteroid-asteroid encounters (average is $\sim$ 5km/s), but some low-speed collisions can still implant exogenous material into asteroids [60].

Observations of disruption and collisions of asteroids in real time

However, disruption of asteroids by high-velocity collisions or rotational spin-up, believed to be the primary mechanism for destruction and the production of new asteroids, have been theoretically studied but never shown in action until only a few years ago: extraordinary HST observations [86] showed the recent disruption of the main-belt asteroid P/2010 A2. It was later determined [160] that the peculiar tailed shape of the object P/2010 A2 arose from a single event, likely due to an impact, rather than a period of cometary activity, in agreement with other independent results.

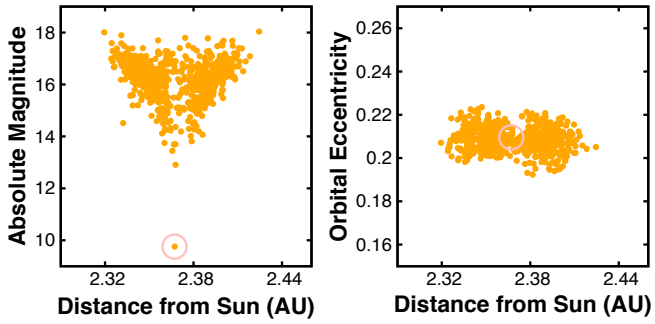

Figure 1.3: The Erigone family, showing (left) family member sizes as a function of their semimajor axis, and (right) their eccentricity as a function of their semimajor axis. The size-dependent Yarkovsky drift creates the "V" shape on the left (where larger Absolute Mag. is smaller size). The pink circle shows the location of the parent body, (163) Erigone.

Moreover, the big ($\sim$ 115 km in diameter) asteroid (596) Scheila in December 2010, showed a cometary-like tail that was interpreted as due to the release of dust due to impact excavation [14, 87]. Since there was no detection [14] of any of the gases that are typically associated with either hypervolatile activity thought to be responsible for cometary outbursts ($CO+$, CO_2+), or of any volatiles excavated with the dust (OH, NH, CN, C_2, C_3), it was suggested that the dust does not contain any ice. Based on these observations, it was concluded that Scheila was most likely impacted by another Main Belt asteroid less than 100 m in diameter.

The mysterious (3200) Phaethon

But asteroids show activity not only because of impacts. For instance, (3200) Phaethon, established to be the parent body of the massive (10^{12}-10^{13} kg) [85] Geminids meteor stream, once thought to be an extinct comet because of its association with said meteors, is instead an asteroid. Spectroscopically, Phaethon is very different from cometary nuclei, with Phaethon having a blue reflectance in the visible and near-infrared [104] and comets extremely red ones [32]. Phaethon spectrum is also very similar to that of (2) Pallas and Pallas's family members [39]. A dynamical link with this Main Belt asteroid and its family was also found [39]. As it is not a comet-like activity that produces the Geminids, neither was a collision [65], the mechanism is still not clear, even though a small activity was observed on Phaethon after one of its very close perihelion passages [85].

Main Belt Comets or Activated Asteroids

Regarding asteroidal activity, a breakthrough in the field was the discovery of the so-called main belt comets (MBCs) [81]. These objects, located in the Main Belt, display sporadic activity. Dynamically, MBCs are not comets, therefore some researchers prefer to call them activated asteroids. A possible explanation for their activity is related to the sublimation of volatile species, including water ice, likely exposed by small impacts. This had a big implication at the time of their discovery, as water ice had never been observed in or on asteroids. Water ice is also not stable over billions of years on the their surfaces, although and MBC can harbour water ice since the beginning of the Solar System under a regolith layer [157]. Most of these objects turned out to belong to the collisional family of the asteroid (24) Themis.

Water ice on (24) Themis

The discovery of the MBCs triggered attention to (24) Themis and its family, in particular detailed spectroscopic investigations were attempted using SPEX at the NASA IRTF. The most intriguing result was the detection of a spectroscopic band at 3 microns that was interpreted as water frost and the presence of organics [31, 149]. As water ice is not stable over the age of the Solar System at this heliocentric distance, a mechanism capable of replenish water at the surface e.g. impact excavation of subsurface ice, is required to explain these observations. Water ice was also detected on other outer belt asteroids such as (65) Cybele [103]. It must be said that the presence of the mineral goethite can be an alternative explanation for the origin of the 3.1 micron band on dark asteroids [10].

Water vapour from (1) Ceres

Models of Solar System origin suggest that some of the icy bodies, formed beyond the snow-line, may have migrated into the asteroid belt [181]. So, the observations of (24) Themis, and (65) Cybele and of the MBCs support these kind of models. Moreover, hydrated minerals have been found on the surfaces of many asteroids including the dwarf planet (1) Ceres [99, 94]. This is an indication that water was present on Ceres at least during the initial phases of Solar System evolution. However, a lot of attempts to find traces of water on this body failed[3], until the recent detection of water vapour using the Herschel space telescope [95].

Origin and delivery of water and organics to Earth

These discoveries shed new light on the important problem of how much material and from which zone of the solar nebula was delivered to the different terrestrial planets at the time of their formation. This is a crucial question to

[3]besides the presence of water vapour suggested by a marginal detection of the photodissociation product of water, hydroxyl

improve our understanding of the connection between planetary evolution and life. At the same time, it has been shown that water delivery to the early dry terrestrial planets it is typically done by plantesimals formed beyond 3.5 au, during the latests stages of planetary accretion [145, 146]. Once it was thought that comets could be the primary source of Earth's water. But it is known that water from Oort cloud comets is too enriched in Deuterium to match Earth water. On the other hand, the water included in the CI and CM carbonaceous chondrites has just the right D/H ratio. As the best analogs for the CI and CM meteorites are primitive, low-albedo, C-complex asteroids, such as Ceres and Themis, this also indicated that asteroids formed in the outer belt are the more likely source of Earth's water. To complicate this nice story, note in Fig. 1.4 the two JFCs with D/H similar to that of the Earth [74]. This led to think that Oort cloud comets and JFCs formed from different reservoirs in the proto-planetary nebula, in contrast with Solar System formation hypothesis such as the Nice Model. But, the recent measurement of a D/H ratio of the JFC 67P Churimov/Gerasimenko almost 4 times higher than that of the Earth, by ESA's ROSETTA shows that these type of comets can be Deuterium rich [3], as Oort comets are.

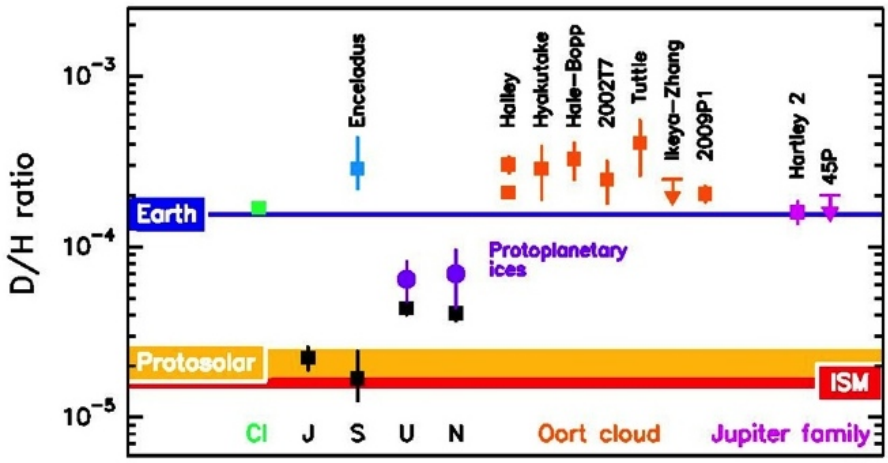

Figure 1.4: Deuterium/Hydrogen ratio measured for different celestial bodies compared to the Earth value. Adapted from [74]

Indeed, recent results, including the analysis from the samples of the space mission Stardust, are strengthening the idea that there is a sort of continuum

between dark asteroids found in the outer Main Belt and comets. As a matter of fact, the chemical composition, the mineralogy and the oxygen isotopic composition of the dust from comet Wild 2 are very similar to those of a class of meteorites, carbonaceous chondrites, allegedly coming from dark asteroids [63].

1.2 Open questions

The sources of meteorites

In the light of the recent discoveries described in the previous section, some questions[4] emerge: carbonaceous chondrites (CCs) of the CI and CM groups contain water with approximately the same D/H ratio of Earth's water; these meteorites are broadly associated, on the basis of low-albedo and reflectance spectra, with asteroids of the C-Complex, such as Themis and Ceres; however, it is not clear whether the CIs and CMs that fall on Earth are coming from those asteroids for which water as detected. Thus, we do not know what is the D/H ratio of the water of asteroids such as Ceres and Themis !

The missing Ceres' family

In addition, very likely, we do not get meteorites from Ceres, as this body has no known family [148, 123], and the presence of a family is necessary to produce meteorites. However, it is common for other large asteroids to have collisional families: these asteroids are likely as old as the Solar System [126, 156], and the probability that they had a sizeable collision to produce a family is exceeding one. One possible explanation for the missing Ceres' family is that the latter existed in the past, but its asteroid members evaporated on timescales shorter than the age of the asteroid belt. This idea is favoured by models of Ceres' thermal history, which predict a differentiated object with an icy sub-surface covered by a $\sim$ 0.1-1 km of regolith. Impacts could produce a collisional family of predominately icy bodies, which could evaporate in timescales of several hundred My [148].

The missing D-type families

The same explanation might also be valid for D-type asteroids, which all lack families: D-types could be water ice-rich bodies, implanted in the asteroid belt during the LHB [102]. On the other hand, (24) Themis, which has water [31, 149], has a huge and very old family (>2.5 Ga, maybe even >3.5 G) [26, 163].

Missing carbonaceous meteorites ?

[4]This is a personal view of the problems and the important questions that are still unresolved. Certainly, this view also emerges from discussions with important close collegues: V.E. Ali-Lagoa, R. Binzel, B. Bottke, H. Campins, A. Crida, S. Jacobson, J. Hanus, G. Libourel, P. Michel, F. Mignard, A. Morbidelli, P. Tanga, K. Walsh, and others.

Next, we have to consider that the record of CCs that we receive on Earth is extremely biased. Consider for instance that km- and sub-km-sized NEAs with C-complex taxonomy and low albedos, the immediate precursors of CCs, comprise about a fourth to a third of all NEAs [166, 110], whereas CC meteorites only provide <3% of all meteorite falls [28]. The reason for this mismatch is not completely understood: one obvious explanation (i) is that many fragile CC, such as the CI and the CM meteorites fail to survive passage through Earth's atmosphere. Other less obvious possibilities are that (ii) small, m-sized NEAs, are efficiently destroyed or eroded by thermal processes [33, 46], transforming these bodies to dust before they can hit the Earth, or that (iii) the these m-sized NEAs are not delivered to the near Earth space, as the Main Belt is severely depleted of these small asteroids.

These questions are just parts of a more general problem: i.e. establishing connections between meteorites, NEAs, and their parent main belt asteroids is an important goal of planetary science [28]. This is also important to maximize the science return from sample return missions such are NASA's OSIRIS-REx and JAXA's Hayabusa II [30, 29, 180, 22][5].

Recent progress in this field include the confirmation of the hypotheses formulated in the '70s that (i) HEDs came from Vesta [156, 40], and that (ii) Ordinary Chondrites (OCs) are originating from S-type asteroids [13, 114, 75, 136][6].

[5] I participated to several studies devoted to this topics: (i) a search for the source regions of 2008 TC_3 [60], which fell in the Namibian desert and produced the Almahata Sitta meteorites [84]; (ii) the physical studies and identification the source of (162173) 1999 JU_3 [30, 29] a potentially hazardous NEA and target of JAXA's Hayabusa II sample return mission; (iii) the investigation of the dynamics of (101955) Bennu [22], which is also a potentially hazardous NEA and target of NASA's OSIRIS-REx sample return mission, in order to find the source region of this body; (iv) these studied led to a better understanding of the inner Main Belt, including our discovery of two asteroid families important for the delivery to near-Earth space of C-type NEAs and CCs [180].

[6] Regarding the link between S-types and OCs, the long standing question was that S-types have reflectance spectra typically redder and with shallower absorption bands than those of OCs. The S-type are the most abundant type of asteroids with mafic silicate spectra, and OCs are the most abundant meteorites. This problem was understood in term of the *space weathering*, [27]. The latter is the reddening and the shallowing of the mafic silicate absorption bands of the S-type surface due to the bombardment of ions from the Sun [173] and micrometeorites Thus, a fresh surface with a reflectance of an OC slowly assumes that of an S-type in some My [173]. The inverse process is also possible: it is believed that weathered S-types can be refreshed by close approaches to Earth [12] Confirmation that OCs are originating from S-type was beautifully demonstrated by in-situ spectroscopy [75] and

However, the association between S-types and OCs is not exempt of problems. For instance, observations show that the fraction of NEAs with fresh surfaces, whose reflectance spectra resemble those of OCs, is increasing with decreasing perihelion distance [113]. This is contrary to the intuitive idea that asteroids that go closer to the Sun would be more weathered, because more strongly exposed to the solar radiation than asteroids that stay further away from our star. While a not full convincing solution for this problem was advanced [12], the discovery the importance of asteroid surface thermal cracking [46] offers a natural explanation for this effect (also presented in section 2.5).

The source origins of the different groups of OCs are also not completely understood: we recall here that, according to their iron content, OCs are divided into H (high total Fe), L (low total Fe) and LL (low total Fe, low metallic Fe) groups, with 42.8%, 47.4% and 9.8% of OC falls belonging to each group, respectively. These meteorite groups are closely related because the chondrules in H, L and LL chondrites are similar. However, quite surprisingly, the large majority of the S-type NEAs, the immediate precursors of OCs, have spectra similar to LLs and not to L or the H OCs [174]. Moreover, S-type NEAs share composition similarity with the asteroids from the family of (8) Flora [174]. Flora's asteroid family is massive and lies close to the brink of the ν_6 resonance, which is very effective in delivering material, including meteorites, to NEA space. So, why are not the LLs the most abundant class of OCs that we can find on Earth if they originate from the Flora family ?

Why aren't LL the most abundant OCs?

Furthermore, dynamical studies [139] identified the source of OCs of the L group in the asteroid family of (1272) Gefion, which is mainly[7] located between ∼2.7 and ∼2.8 au. A potential problem with this result is the low relative efficiency of meteorite delivery from the Gefion family location. Dynamical models indicate that meteoroids from Gefion have ∼10 lower probability of

Ls from Gefion, which is far away from Earth

later by the laboratory analysis of samples returned from the surface of the S-type asteroid (25143) Itokawa [136]. In addition, it was found that younger S-type asteroid have spectra more resembling those of OCs than older asteroids, indicating that the spectral differences between OCs and S-types is due to an ageing of the surface [13].

[7]In order to explain the falls of L-chondrites, it is hypothesised [139] that the Gefion family extends to smaller heliocentric distances, down to 2.5 au, in order to feed the 3:1 MMR with Jupiter with meteoritic material. This "extension" of Gefion, is supposed to be beyond the current detection limit of asteroid discovery surveys. However, (Morbidelli, private communication) the SFD of the Flora family, beats the SFD of Gefion at all sizes. To explain the mismatch between the L and LL recovery statistic, it is necessary to invoke a change in the slope of the SFD of Gefion at metric sizes.

striking the Earth than those coming out of Flora family. All things being equal, this would suggest that meteoroids from the Flora family should dominate meteorite fall statistics. But as we said above, this is not the case. One possible solution is that the Gefion breakup produced a much larger number of sub-km fragments than the Flora breakup; and/or the sub-km precursor objects to Flora meteoroids have been efficiently depleted over the Flora family age, by e.g. the Yarkovsky effect.

Hs from Hebe, but where is Hebe's family ?

Moreover, the asteroid (6) Hebe was spectroscopically identified [58] as the parent of the H group of the OC. But, the asteroid Hebe appears to have no family. Consequently, it is not clear how small fragments of this asteroid reaches the resonances and are being delivered to near-Earth space.

Fireballs observations

Can the observation of fireballs[8] help in linking meteorites to specific asteroids ? Unfortunately, the orbit measured for any particular meteorite producing fireball is heavily evolved from the original orbit of the parent asteroid. As a result, linking individual fireballs with specific asteroids is generally not possible. Rather, classes of meteorites and source regions in the main asteroid belt can be statistically associated using the orbit distribution of many meteorites and models of Main Belt – near Earth asteroid delivery [19].

Almahata Sitta: different mineralogical types of meteorites from the same asteroid

A discovery that challenges the theories of asteroid formation and evolution was the finding of the Almahata Sitta meteorites coming from the fireball due to the atmospheric impact of the asteroid 2008 TC_3 [84]. TC3 was a fragile body that disrupted relatively high in the atmosphere. A large number ($\sim$ 600) of small (0.2 – 379 g) meteorites were recovered, but no big meteorite was found. The big surprise was that the meteorites were of various mineralogical types: mineralogical analysis of 110 meteorites revealed 75 ureilites, 28 enstatite chondrites (both EH and EL), 5 ordinary chondrites (H, L, LL), one carbonaceous chondrite (CB) and one a previously unknown type of chondrite related to R-chondrites [76]. This fact completely changed our paradigm that one meteorite fall produces meteorites of one type and that (undifferentiated) asteroids have a certain mineralogical composition, although polymict meteorite breccias were known before. None of the foreign lithologies was found to be directly embedded within the ureilitic meteorites[9]. It therefore seems that the chondritic material

[8] A fireball is a brighter-than-usual meteor. The International Astronomical Union defines a fireball as "a meteor brighter than any of the planets" (magnitude -4 or greater).

[9] For this reason, the Gayon-Markt et al's model seems not correct. This model is based on implanting EC and OC on the urelite parent body.

was only loosely bound within the asteroid.

The second confirmed case of heterogeneous meteorite is Benesov [164]. Surprisingly, one meteorite was H chondrite, one was LL chondrite and one was LL chondrite with embedded achondritic clast. The size and location of all four meteorites exactly in the predicted area for corresponding masses, the same degree of weathering and composition consistent with the bolide spectrum along with the extremely low probability of two coincidental falls in the given area, means that almost certainly all meteorites came from the Benesov bolide. The heterogeneous nature of the Beneov meteoroid is supported by its early separation into smaller bodies during the atmospheric flight [15].

Benesov

These findings shed new light on some old meteorite finds, such as the Galim meteorite fall (LL + EH), Hajmah (ureilite+L), Gao-Guenie (H+CR), and Markovka (H+L) [16]. Asteroids with mixed mineralogies might be more abundant than what we thought. However, the mechanism(s) of formation of these bodies remain mysterious [76]. Low velocity (e.g. < 0.5 km/s) impacts between asteroids are invoked to explain this mixing, but in the Main Belt the occurrence of such impacts is too low to explain substantial asteroid mixing [60]. One possible solution is that the heterogeneous composition of some asteroids was inherited from a time when the asteroid belt was in a different dynamical state, most likely in the very early Solar system.

However, new laboratory experiments [7, 6] show that projectile material can survive impacts at speed much higher than 0.5 km/s, implying that asteroid mineralogical mixing is probably more efficient than previously thought and that earlier studies [60] should be revised.

Projectile survival after hypervelocity impacts: implications for asteroid mixing

Furthermore, analysis of the the meteorites samples suggest that there were at least 100 planetesimal that encountered a total or partial melting and differentiation (formation of an iron core, mantle and crust) during the early phases of Solar System formation. Some of these differentiated (big) asteroids are predicted to be in the Main Belt today, e.g. Vesta [156], Ceres, Pallas, etc. Other large asteroids, that likely underwent partial or total differentiation have been catastrophically disrupted by impacts. The debris of these impacts are the family members. The formation of an asteroid family from a differentiated asteroid should produce asteroid members corresponding to the curst, the mantle and the core. However, spectroscopic observations show that the mineralogical compositions of asteroid families are homogenous [143].

No clear indication of asteroid differentiation in families

Moreover, it was predicted [156] that Vesta underwent differentiation: i.e.

formation of an iron core, pyroxene and olivine-rich mantle, and HED crust [89]. Vesta's density as reported by the Dawn spacecraft team is consistent with the presence of an iron core [156]. The chemical trends of the HED meteorites, including the depletion of sodium, the FeO abundance, and the trace element enrichments are also consistent with the differentiation. However, very surprisingly, there is a total absence of exposed mantle material on Vesta's surface [5], among Vestoid asteroids, or in our collection of basaltic meteorites. One possible explanation is a non chondritic initial composition of the planetesimal that made Vesta [38]. This is striking, because the Earth, and Mars have a chondritic composition as well as the largest fraction of the meteorites that fall on Earth. More likely the problems should be searched in the models [37] used to predict the thickness of the crust, and of the olivine mantle (A. Morbidelli, private communication).

Missing traces of expected differentiation in Vesta

Metallic asteroids

However, radar and thermal infrared observations show there are asteroids with regolith with high iron content [159, 158], such as (216) Kleopatra [142] and (16) Psyche [117]. These objects are thought to be the exposed iron cores of fully differentiated asteroids. Interestingly, none of these two asteroids have known asteroid families. This might contrasts with the evidence that they are the exposed metallic core of differentiated parent bodies that were catastrophically disrupted. The catastrophic disruption of these metallic asteroids, provided it happened in the Main Belt, should have each produced a large number of fragments resulting in the formation of asteroid families. Another possibility is that these asteroids are not indigenous to the Main Belt: they formed in the terrestrial planet region. The protoplanets emerging from the population of planeterismal induced collisional evolution among the remaining planetesimals and scattered some of the survivors into the Main Belt, where they stayed for billions of years before escaping via a combination of collisions, Yarkovsky thermal forces, and resonances to produce iron meteorites [20].

Missing families, in particular the oldest ones

Is the lack of known family members for asteroids Psyche and Kleopatra due to a physical process or due to a systematic bias in the methods used to form asteroid families that eschews older families ? Further evidences suggest that the census family of asteroids is incomplete. For instance, note that recent models of formation and evolution of our Solar System such as the Nice Model [62] predicts the existence of a dozen families formed after the destruction of asteroids D$>$ 200 km, but also a hundred families older than $\sim$ 2 Ga formed after the destruction of asteroids of D$>$ 100 km [25].

However, observations indicate that either these models have discrepancies

or that we are not able to properly identify families from parent bodies with D> 100 km as old as 2-3 Ga. Indeed, the number of observed large families (D> 200 km) is approximately equal to the expected number observed, but there is a very significant lack of small families (D> 100 km) compared to model predictions [26].

2

Asteroid physical studies: from Astrophysics to Geophysics

For decades, physical characterisation of asteroids involved essentially techniques of Astrophysics. This consisted in measuring magnitudes and reflectance spectra in the visible and near-infrared, allowing asteroids to be classified in broad mineralogical classes. Furthermore, in order to derive sizes and albedos, thermal infrared measurements of these bodes were obtained using the largest telescopes on the ground such as the Keck [45]. Typically, near-Earth asteroids were targeted from the ground, as for main belt asteroids we relied on measurements obtained from space by IRAS (the Minor Planet Survey, IMPS, and the Supplementary IRAS Minor Plant Survey, SIMPS, containing size and albedo for 2228 asteroids [169]).

The WISE revolution

But, in the last years asteroid physical characterisation has changed pace: the number of asteroids with known sizes and albedos improved tremendously with the release of NASA's Wide-field Infrared Survey Explorer (WISE) enormous thermal infrared catalogue. This survey provided photometric observations of more than 150,000 asteroids [115, 109, 116, 110], two orders of magnitude more than IRAS. Other infrared missions such as NASA's Spitzer [170, 73, 133], JAXA's AKARI [172] and ESA's Herschel have collected detailed thermal infrared data of minor bodies, including spectra in almost all domains of the thermal infrared [111]. High quality spectroscopic measurements in the near-infrared have been obtained essentially with the NASA IRTF ground based telescope. Very efficient discovery surveys have reached a great power over the

The IRTF/SPEx revolution

Importance of discovery surveys

last few years. Indeed, quoting *Jedicke et al.* [83], "Without asteroid surveys there would be no asteroid science".The cumulative efforts of over 200 years of asteroid surveying has resulted in the discovery of over half a million asteroids.

Images from spacecraft

However, the big revolution came from space missions such as NASA's *NEAR-Schoemaker* and *Dawn*, JAXA's *Hayabusa*, ESA's *Rosetta*, that have carried out detailed *in-situ* investigation of serval asteroids and comets. Space missions have imaged the surface of these tiny worlds and revealed to us a wide range of geological features such as craters, boulders, hills, cracks, ridges, regoliths of different grain size, albedo and spectral variegation on the surface. Asteroids are no longer just dots in the Solar System, but bodies with complex shapes and surface Geophysics [135](see e.g. Fig. 3.1).

Asteroid geology from remote sensing data

In addition, geological information about the surface of asteroids can be also obtained form remote sensing thermal infrared data, which allow one to derive the thermal inertia. As we shall see, this physical parameter is a sensitive indicator of the "rockiness" of the surface.

Geology and dynamics of asteroids

Moreover, we realised recently that asteroid geology has an effect also on the dynamics of these bodies: the Yarkovsky effect is a secular variation of the semimajor axis of the orbits of asteroids on a time scale of the order of 10^{-4} au/Myr for a main-belt asteroid at 2.5 au from the Sun with a diameter of 1 km and a bulk density of 2500 kg/m^3 [23]. This phenomenon is due to the non-zero thermal inertia of asteroid surfaces. In the case, because the temperature distribution is no longer symmetric with respect to the direction to the Sun [49] (Fig 2), the momentum carried off by the photons emitted in the thermal infrared has a component along the orbital velocity vector of the body, causing a decrease or increase of the asteroid orbital energy depending on whether the rotation sense of the body is prograde or retrograde. The intensity of the Yarkovsky effect depends on physical parameters such as the asteroid size, density, rotation period and thermal inertia. The gross shape and the

Importance of the Yarkovsky effect

macroscopic roughness of the asteroid also plays a role [151, 152, 153] The Yarkovsky effect is responsible for the slow but continuous transport of small asteroids and meteoroids from the zone of their formation into chaotic resonance regions that can deliver them to near-Earth space [129]). The Yarkovsky effect also offers an explanation for the spreading of asteroid dynamical families [137, 23].

YORP

Moreover, the emission of thermal photons also produces a net torque that alters the spin vector of small bodies in two ways: it accelerates or decelerates the spin rate and also changes the direction of the spin axis. This mechanism

was named by [155] as the Yarkovsky-O'Keefe-Radzievskii-Paddack effect, or YORP for short. The YORP effect is extremely sensitive to the shape of the asteroid [165, 24], the detail of the heat transfer in at the surface of the body [61], and the mass and density distribution [106].

Recent reviews have been written on these topics [179, 49].

2.1 Shapes, sizes and albedos

Knowledge of physical properties is crucial to understand asteroids: for instance, size information is fundamental to constrain the asteroid size frequency distribution that informs us about the collisional evolution of these bodies [18, 17], is paramount for the study of asteroid families, for the Earth-impact risk assessment of near-Earth asteroids (NEAs) [69], and for planning asteroid space missions. Accurate sizes are also a prerequisite to calculate the volumes of those asteroids with known mass, allowing us to derive the bulk density, which inform us about the internal structure of these bodies [35].

Sized and albedos of NEOs from ground-based telescopes

In the pre-WISE era, the largest telescopes on the ground have been used to obtain thermal infrared observations, which were used for the determination of NEA sizes and albedos [44, 45, 41]. This was essential toward determining the compositional [13] and size distribution [166] of objects that have the potential for colliding with the Earth (see Fig. 2.1).

Sizes and albedos of NEOs from space-borne telescopes

This work is still being continued in the framework of different international projects such as *ExploreNEOs*, that has already characterised 558 NEAs using the *Warm Spitzer Telescope*, which also allowed the characterisation of potential spacecraft targets [133] and the discovery of cometary activity around the NEA (3552) Don Quixote [125], previously expected to be an extinct comet[1]. Other on going works[2] include understanding the details of the NEA size distribution in the 1 km to 100 m range, which has important implications for both the evolution of near-Earth space and assessment of the impact hazard posed by bodies with sizes similar to that of the parent of the Chelyabinsk meteorite.

[1] I was awarded grants from my institute (BQR) and from ESA (Space Situation Awareness, or SSA) that allowed myself and my first "Poincaré" post-doc (**Michael "Migo" Mueller**) to carry out NEA physical characterisation.

[2] The European Union, in the framework of the Horizons 2020 "Science and Technology for Near-Earth Objet Prevention" has selected projects such as NEOShield 2 to characterise small NEAs in the size range of 50-300 m. I am Co-I of NEOShield 2, and I was awarded a grant to support post-doc (**Victor Emmanuel Ali-Lagoa**)

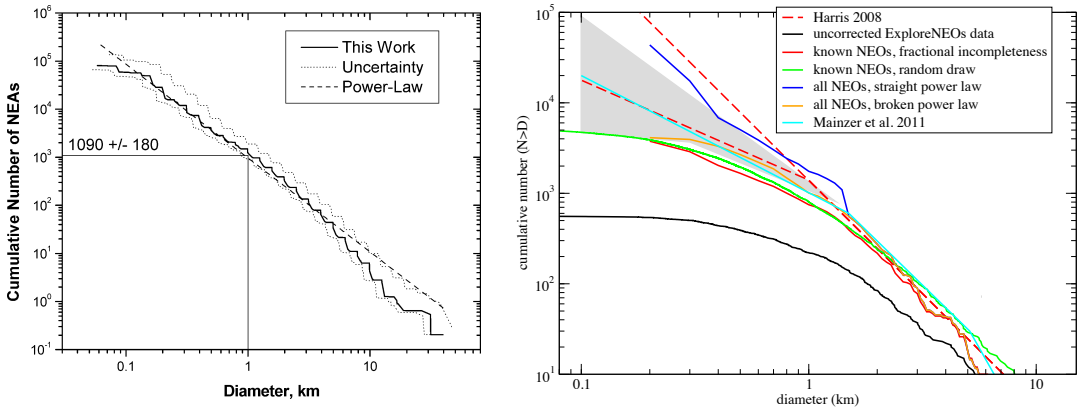

Figure 2.1: Cumulative size distribution for the various NEA populations as described in the text. LEFT: The solid line shows the cumulative number of NEAs larger than a given diameter. The absolute magnitude distribution is converted to a diameter distribution using the albedos from [45] and fractional abundances for the taxonomic complexes from [13]. The dotted lines represent an approximate error envelope. The plot is from [166]. RIGHT: the grey area shows the approximate region of the NEA size distribution derived by the *ExploreNEOs* program (Trilling et al. submitted to AJ). The lower bound (orange line) must be a fairly extreme solution since it predicts that the number of unknown small NEAs (orange line minus red or green line) is small, which is unlikely (though the underlying Harris' broken power law does predict an upturn in the number of NEAs smaller than 100 m, a regime that is beyond the constraints of our data). The agreement between our solution (grey region) and the independently derived NEOWISE result (cyan line) is compelling.

Thermal modelling

The most utilised method to derive asteroid sizes is by measuring their thermal infrared emission and comparing it with prediction from an asteroid thermal model, which is used to find the values of the size and albedo that give the best fit to the observations [44, 45, 49, 70, 72].

However, the this is not a direct method as it requires assumptions of surface temperature and thermal emission. Therefore, it is always important to confront infrared diameters with those measured by direct methods. Direct methods of size determination are disk resolved imaging by *in-situ* spacecrafts, or by adaptive-optics systems at the largest telescopes, or by stellar occultations. The first require a visit by a spacecraft, the second is limited to very large asteroids (e.g. $>$ 100 km), the latter require accurate occultation predictions and ultimate precision in asteroid orbits and stellar catalogs (see § 3.1 for the perspective of asteroid occultations in the post-Gaia era).

Interferometric studies of asteroids

To overcome these limitations, ground-based, long-baseline interferometry was used [47] to obtain precise determination of the size of an asteroid and of its shape for the first time[3]; spatial resolutions between 20 and 200 milli-

[3]The instrument MIDI of the ESO VLTI was used for this study. Data reduction and

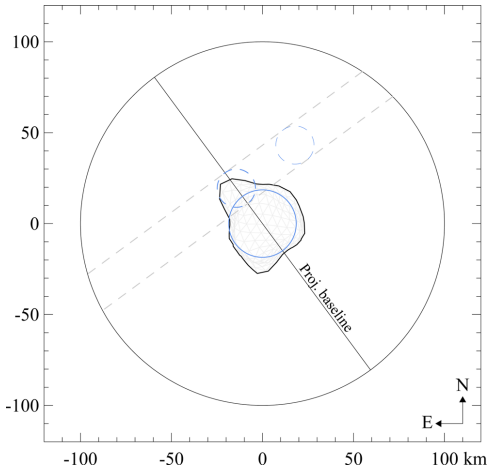

Figure 2.2: Comparison of the bilobed or binary model of Barbara derived from VLTI measurements [47] (blue lines) with the KOALA shape model (black contour) at the time of VLTI observations. The irregular shape of Barbara mislead the interpretation, by mimicking the signal of a binary system projected on the VLTI baseline. As spatial resolution is missing in the direction perpendicular to the baseline, the dashed lines enclose possible locations for a satellite compatible with the VLTI signal.

arcseconds can be obtained from the ground (*see the attached paper [47] by Delbo et al., 2009*). A bilobate shape for the asteroid (234) asteroid was derived [47][4]. These findings inspired follow up observations, including stellar occultations, which enable building an accurate shape model in very good agreement with the interferometric data [168]. See also Fig 2.2.

Furthermore, the simple geometric model of ref.[47] was adapted [36] to the study of binary systems to analyse the interferometric data in combination with the results of the lightcurve modelling. They applied interferometry to study small binary asteroids ($\sim$ 10 km) in the main belt for the first time. The study of binary asteroids is extremely useful because by measuring the period and the semimajor axis of their mutual orbital, one can measure the mass of the system, which can be used to infer the body's bulk density provided volume (size and shape) is known. When the asteroid density is compared with that of the meteorite analog one can estimate the body's bulk porosity, which gives information about the asteroid internal structure. The latter can inform us

analysis were carried out in collaboration with **Alexis Matter**, in the framework of his PhD thesis at OCA. VLTI study of asteroids represent 1/3 of Matter's PhD thesis.

[4] a binary system was another possible solution compatible with the data.

about the origin of the body (e.g. monolith or rubble-pile), and it also can give fundamental clues about the potential differentiation of the asteroid.

Interferometry: basic concepts

Mid-infrared interferometric instruments measure the total flux and the visibility of a source, the latter being related to the intensity of the Fourier Transform (FT) of the spatial flux distribution along the interferometer's baseline projected on the plane of sky. Thus, the data analysis procedure consisted in generating images of the thermal infrared emission of the asteroids at different wavelengths as viewed by the interferometer and then in obtaining the model visibility and flux for each image. The former is related to the FT of the image, the latter is simply the sum of the pixels. The free parameters of the thermal model (e.g. size, albedo, and surface temperature) are adjusted in order to minimize the distance between the disk integrated flux and visibility of the model, and the corresponding observed quantities [47, 118, 117, 36, 54].

Provided the asteroid shape is known, interferometry can be used measure other surface thermal properties [118, 117], such as the thermal inertia, the latter informing us about the nature of the surface material (see § 2.3).

2.2 Spectroscopy and Mineralogy

Introduction

Reflectance spectroscopy is used to investigate the mineralogical nature of asteroids, by attempting the identification of bands and other features due to mineral assemblies or by spectral matching with known meteorite spectra. This procedure is far from reproducing unique solutions and in some case can lead to discordant results e.g. the mysterious nature of (21) Lutetia[5]. Particular attention in the last years has been devoted to the main-belt origin of low albedo NEOs that spectroscopically match to carbonaceous chondrites. A driver for this interest has been (i) the development of JAXA's Hayabusa 2 and NASA's OSIRIS-REx, two sample return missions to primitive and organic-rich aster-

[5]This asteroid has a M-type taxonomy, that was interpreted with a metallic composition in the early classification schemes. The flat and featureless visible and near-infrared spectra obtained by VIRTIS during the fly-by of ROSETTA do not allow discrimination between a carbonaceous and/or enstatite nature. Mid-infrared observations by the Spitzer space telescope obtained a few years before are more in favour of a carbonaceous chondrite like composition [9]. However, later works [176] showed that the spectral (from 0.3 to 25 micron) and physical (albedo, density) properties of Lutetia are quantitatively similar to the class of meteorites known as enstatite chondrites. HST/STIS observations in the Near Ultraviolet, are favouring the enstatite chondrites association: http://adsabs.harvard.edu/abs/2014DPS....4650604S

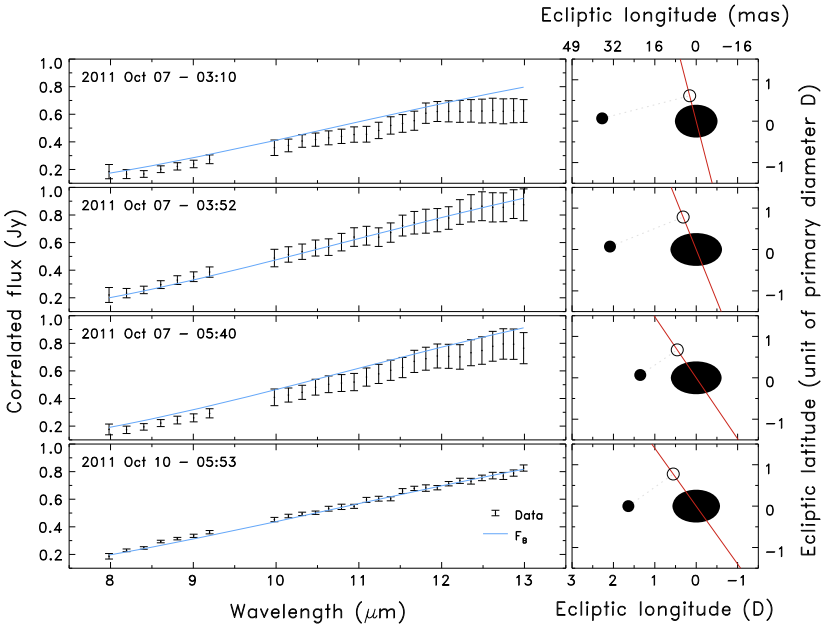

Figure 2.3: Left: Correlated flux of Isberga observed with MIDI over four epochs. The best-fit solution of binary model (FB) is also plotted as a solid blue line. Right: Corresponding geometry of the system on the plane of the sky. The red line represents the projected VLTI baseline, the black ellipse Isberga, the black disk its satellite, and the black circle the projection of the satellite on the baseline. Adapted from [36]

oids, and (ii) because it is thought that carbonaceous rich asteroids have brought water and organics and other seeds of life to the early dry Earth. The landscape of the inner Main Belt is dominated by a handful of asteroid families and a diffuse population of "background" objects [180]. The identification source asteroid families offer the possibility to link NEOs to a unique body in the asteroid, i.e. the parent of the family.

Asteroid families

Inspired by these motivations Gayon-Markt[6], et al. i.e. ref.[60] performed a detailed spectroscopical and dynamical investigation of the most likely source region of OSIRS-REx and Hayabusa 2 targets: the inner main belt at low inclination ($2.1< a < 2.5$ au and $i < 8°$) . One of Gayon et al. results was that background asteroids with colours consistent with primitive spectra (B-type) in the region showed an orbital and size distribution typical of asteroid families.

Discovery of asteroid families

[6]**Julie Gayon-Markt** was my two-years CNES post doc. She worked on the development and tests of the algorithms and software for the unsupervised classification of asteroids from Gaia low-resolution spectroscopic observations.

The paper by Gayon-Markt et. 2012, ref. [60], is here attached.

New Polana and Eulalia asteroid families

Further studies of primitive Inner Belt asteroid families, were carried out [180]. These works focused on the primitive, low-albedo, component of the Nysa-Polana complex and found that the most of the low-albedo background asteroids belongs to a family that formed over 2000 Myr ago, parented by asteroid (142) Polana. *Walsh, Delbo, et al.* named this family *New Polana*. They also find that the asteroids thought to belong to the once-called Polana family, are included in a family that formed 900–1500 Myr ago parented by asteroid (495) Eulalia. Further studies [56] discovered additional structures associated with the Eulalia family (maybe a sub impact family).

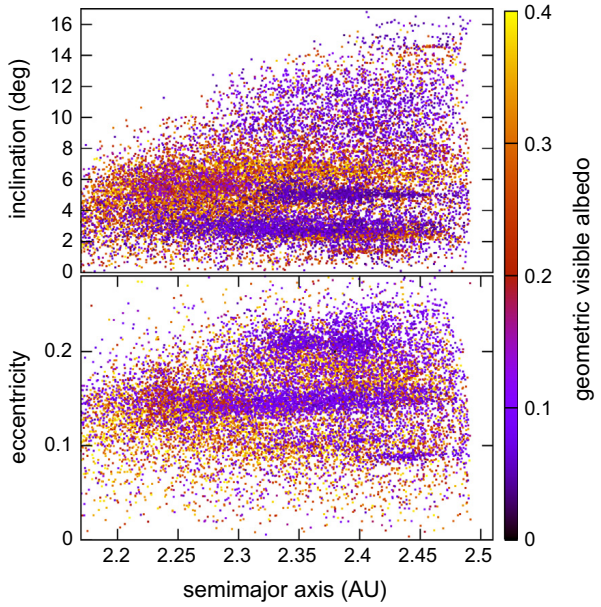

Figure 2.4: The entire inner Main Belt, including all asteroids that were observed by WISE and whose D and pV were published in the Preliminary release of Albedos and Diameters [115, 116] plotted using computed synthetic proper elements [123]. The plots show the orbital inclination and the eccentricity as a function of their semimajor axis (AU). The color of each point represents their WISE-determined albedo with values shown in the colorbar on the right. The low-albedo component of the Nysa-Polana complex is visible as the large low-albedo complex at e∼0.15 and i∼3° extending across almost the entire IMB.

A mechanism for the origin of the multi-lithology Earth-impactor NEO 2008 TC3

Gayon et al.'s studied also a mechanism to explain to origin of the remarkable asteroid 2008 TC3. This was a near-Earth asteroid that impacted the Earth on 2008 October 7. Meteorites were produced by the break-up of 2008 TC3 in

the high atmosphere and at present, about 600 meteorites – called *Almahata Sitta* coming from 2008 TC3 were recovered [84]. A mineralogical study of Almahata Sitta fragments showed that the asteroid 2008 TC3 was made of meteorites of different types (ureilites, H, L and E chondrites). Understanding the origin of this body and how it was put together remain a challenge. [60] showed that asteroids with spectroscopic classes that can be associated with the different meteorite types of Almahata Sitta are present in the region of the main belt that includes the once-called *Nysa-Polana* family and objects of the background at low inclination. Gayon et al., also showed that there is little chance that 2008 TC3 was formed by low-velocity collisions between asteroids of different mineralogies, in the current asteroid belt. It seems more likely that the heterogeneous composition of 2008 TC3 was inherited from a time when the asteroid belt was in a different dynamical state, most likely in the very early Solar system. Because ureilites are fragments of a large, thermally metamorphosed asteroid, this suggests that the phases of collisional erosion (the break-up of the ureilite parent body) and collisional accretion (the formation of the parent body of 2008TC3) overlapped for some time in the primordial asteroid belt. This have important implication for our understanding of the dynamics and physics of the early phases of our solar system [88].

Toward a better understanding of primitive asteroids : the B-types

A class of primitive asteroids of particular interest is that of the B-type, which show an unique blue reflectance spectrum. Recent work on B-type asteroids has shown that the near-infrared spectral slopes (de Leon et al. 2012) and the WISE 3-micron reflectances (Ali-Lagoa et al. 2013) of these objects form a continuum that ranges from slightly negative (blue) to moderately positive (red) values. A tantalising interpretation is that this diversity might be related to a gradient in the composition as a function of size on the original parent bodies of these objects. This would be consistent with the fact that (2) Pallas and its collisional family, which is thought to be the result of a cratering event, only show extreme values in the range of physical properties found (significantly higher visible albedos and significantly lower 3-micron reflectances [1]) and therefore sample the surface of the B-type parent bodies, of which Pallas is the only survivor.

2.3 Thermal inertia of asteroids

Remote telescopic observations, from the ground and/or from space-based observatories, give access to a limited set of asteroid properties such as magnitudes, sizes and albedos, and spectral properties, but cannot provide any detailed information of the surface geological features such as the rock, regolith, and crater abundance as well as the mechanical and thermal properties of the constituents.

Advantage of space missions

Only in-situ observations with space missions can access this information. Unfortunately, the number of space missions devoted to asteroids is very limited. In fact, only three space missions have been fully devoted to these objects so far. Yet, each rendezvous with an asteroid has turned our geological understanding on its head, with relevance in the closer-to-home fields of granular mechanics, landslides, earthquakes, faulting, and impact cratering. For instance, while both the 17 km-sized asteroid (433) Eros (NEAR mission) and the 0.32 km-sized (25143) Itokawa (Haybusa mission) have the same spectral type and nearly the same albedo, images of their surfaces show two totally different worlds. Eros is covered with a deep layer of fine regolith, while Itokawa is covered with a shallow layer of coarser, rubble-like regolith and many large rocks.

Thermal inertia: the ultimate physical parameter

This difference can actually be captured by the value of the thermal inertia, without going there. Thermal inertia, the resistance of a material to temperature change, is a sensitive indicator for the properties of the grainy soil [49] on asteroids. Thermal inertia is defined by Eq. 2.1

$$\Gamma = \sqrt{\kappa \rho C} \tag{2.1}$$

where κ is the material's thermal conductivity, ρ its density, and C its heat capacity.

Thermophysical models (TPMs)

The determination of asteroids thermal inertia is obtained by means of thermophysical models (TPMs). These are computer numerical codes that allow one to calculate the temperature of asteroids' surface and immediate sub-surface. These temperatures depend on absorption of sunlight, multiple scattering of reflected and thermally emitted photons, and heat conduction. Physical parameters such as albedo (or reflectivity), thermal conductivity, heat capacity, emissivity, density and roughness, along with the shape (e.g., elevation model) of the body, its orientation in space, and its previous thermal history are taken into account. From the synthetic surface temperatures, thermally emitted fluxes (typically in the medium-infrared) can be calculated. Physical properties are

constrained by fitting model fluxes to observational data. Typically TPMs produce the value of the thermal inertia averaged over the whole surface of the body.

Ten years ago, thermal properties were known for only a few asteroids, i.e., (1) Ceres, (2) Pallas, (3) Juno, (4) Vesta, (532) Herculina [134], and (433) Eros [100]. Since then, the number of asteroids with known thermal properties has increased steadily. But still, our knowledge of asteroid thermal inertia is limited to only 16 and 27 near-Earth and Main Belt asteroids, respectively (Delbo et al. 2015, and references therein). This is due to the fact that these measurements are very difficult, as they require thermal data of very good quality, a shape and spin state model of the asteroid, an advanced thermophysical model (TPM). Above all, the know-how to use these instruments, understanding the sources of measurement errors and judging the reliability of the results is essential. For example, an enormous catalog of thermal data became available only recently thanks to the observations from NASA Wide-field Infrared Survey Explorer (WISE), but its exploitation with TPMs requires an accurate understanding of the measurement errors and good asteroid shape models. As a consequence, a massive use of TPMs on WISE data has not yet been attempted.

Early works [42, 50] attempted to put the thermal inertia of asteroids in a global context. (*The paper by Delbo et al. (2007) is attached*).

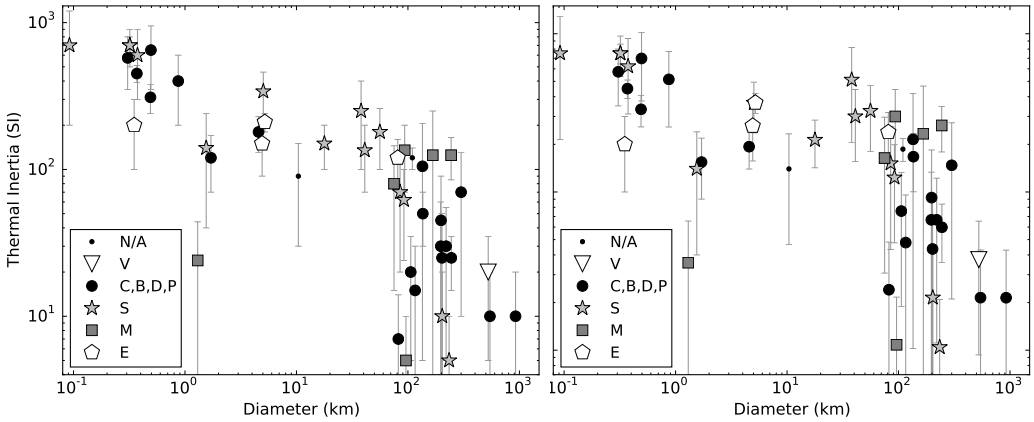

Figure 2.5: Thermal inertia values vs. asteroid sizes, from [49] and references therein for different taxonomic types (see key). Left plot: original measurements, right plot: Γ corrected to 1 au heliocentric distance for temperature dependent thermal inertia [49].

An inverse correlation between Γ and D was noticed [42], and later confirmed

Inverse correlation between thermal inertia and size

and updated [50, 34]. This supported the intuitive view that large asteroids have, over many hundreds of millions of years, developed substantial insulating regolith layers, responsible for the low values of their surface thermal inertia. On the other hand, much smaller bodies, with shorter collisional lifetimes [18, 114], have less regolith, and or larger regolith grains (less mature regolith), and therefore display a larger thermal inertia.

In the light of the recently published values of Γ [49] (see also Fig. 2.5), said inversion correlation between Γ and D is less clear, in particular, when the values of the thermal inertia are temperature corrected (Fig. 2.5). However, the Γ vs D distribution of $D > 100$ km (large) asteroids is different than that of $D < 100$ km (small) asteroids. Small asteroids typically have higher Γ-values than large asteroids, which present a large scatter of Γ-values, ranging from a few to a few hundreds J $m^{-2}s^{-1/2}K^{-1}$. This is a clear indication of a diverse regolith nature amongst these large bodies. A shortage of low Γ values for small asteroids is also clear, with the notable exception of 1950 DA, which has an anomalously low Γ-value compared to other NEAs of similar size [154].

Fig. 2.5 also shows previously unnoticed high-thermal-inertia C types, maybe related to CR carbonaceous chondrites, which contain abundant metal phases. We also note that all E types in our sample appear to have a size-independent thermal inertia.

2.4 Geological interpretation of thermal inertia

Typically, the measurement of the thermal inertia of an asteroid can be compared with a reference value for a solid rocky surface. It is known that the lower the thermal inertia compared to these reference values, the smaller is the average grain size of the regolith: this is because the value of the thermal inertia decreases with increasing porosity of the soil or rock [184, 64]. Interpretation of thermal inertia data for asteroids has traditionally lagged behind that for the Moon and Mars, which are extraordinarily developed. This was due to lack of (i) good quality astronomical data, of (ii) laboratory measurements on asteroid analogs and of (iii) detailed models of asteroids soils.

The situation has only started to change in the last years: concerning astronomical data (a), space telescopes (Spitzer, WISE) have collected an extraordinary amount of new thermal data. However, only few laboratory data on meteorite thermal properties (b) are starting to appear [140, 141], and theoret-

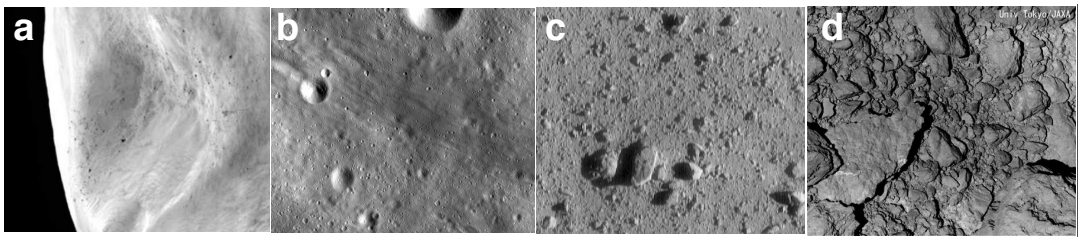

Figure 2.6: Higher Γ-values correspond to coarser regoliths. (a) image of the soil of (21) Lutetia from OSIRIS on board of the ESA Rosetta showing abundant, thick (600 m) and very fine regolith. A value of $\Gamma < 10$ J m^{-2}s$^{-1/2}$K^{-1} was derived for this body. (b) image of the soil of (4) Vesta from the Dawn mission also showing fine regolith. The average thermal inertia Vesta is $\Gamma \sim 30$ J m^{-2}s$^{-1/2}$K^{-1}. (c) close-up image of (433) Eros from the NASA *Schoemaker NEAR* mission reveals coarse regolith with grain size in the mm-range and the presence of surface rocks and some boulders. The value of Γ is ∼150 J m^{-2}s$^{-1/2}$K^{-1} for Eros. (d) image from the JAXA *Hayabusa* mission of the surface of (25143) Itokawa displaying its blocky nature with very little amount of fine regolith. The value of Γ is ∼750 J m^{-2}s$^{-1/2}$K^{-1} for Itokawa.

ical models (c) that allow interpreting thermal inertia measurements in terms of regolith properties, only capture average properties of the soil, such as the average regolith grain size [64].

Several space missions flew-by, orbited, and landed on asteroids with regoliths of different nature and known Γ-values. These images (see Fig. 2.6) provide *ground-truth* for estimating regolith properties, in particular its grain size, from thermal inertia data, demonstrating that asteroids with larger Γ-values have coarser regoliths.

Extremely low values of the thermal inertia

We also note that the some of the C-complex outer main-belt asteroids and Jupiter Trojans have very low thermal inertia in the range between a few and a few tens of J m^{-2}s$^{-1/2}$K^{-1}. In order to reduce the thermal inertia of a material by at least one order of magnitude (from the lowest measured thermal inertia of a meteorite, ∼650 J m^{-2}s$^{-1/2}$K^{-1} at 200 K [140], to the typical values for these large asteroids (Fig. 2.5), a very large porosity (>90%) of the first few mm of the regolith is required [175]. This is consistent with the discovery that emission features in the mid-infrared domain ($7 - 25$ μm) are rather universal among large asteroids and Jupiter Trojans [175], and that said features can be reproduced in the laboratory by suspending meteorite and/or mineral powder (with grain sizes < 30 μm) in IR-transparent KBr (potassium bromide) powder [175]. As KBr is not supposed to be present on the surfaces of these minor bodies, regolith grains must be "suspended" in void space likely due to cohesive forces and/or dust levitation. On the other hand, radar data indicate a significant porosity (40-50 %) of the first ∼1 m of regolith [108, 175], indicating decreasing

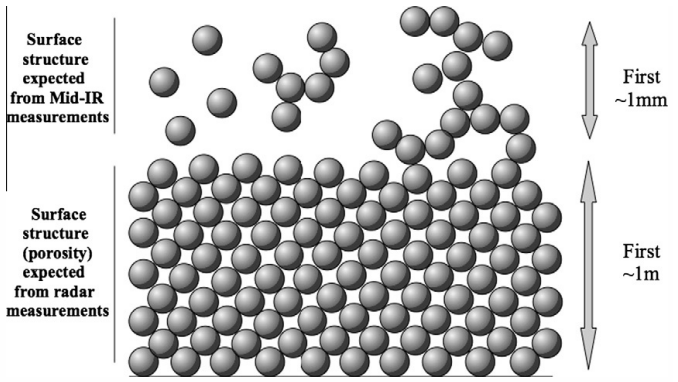

Figure 2.7: Schematic model of the asteroid surface structure as deduced from both the good correspondence between the KBr-diluted meteorite spectra and the asteroid spectra (for the first millimeter) and the low surface density inferred from radar measurements (for the first meter). The high porosity within the first millimeter may be due to cohesive forces (see grains on the upper right-hand side) and/or dust levitation (see grains on the upper left-hand side) [175].

porosity with increasing depth [175].

2.5 Surface processes

Where are bare rock-surface asteroids ?

Note that before the first thermal inertia measurements of small asteroids [131, 41] and before spacecraft encounters with asteroids, many scientists assumed that the smallest asteroids were all monolithic rocks with a bare surface, although, there had been a few articles suggesting possible alternative surface properties and internal structures [80, 120, 71]. Given the low gravitational acceleration on the surface of an asteroid, it was thought that regolith formation would not be possible; even if small fragments of rock were created during the impact process nothing would be retained on the surface [79, 78]. However, the NASA Galileo and NEAR-Shoemaker space missions revealed a substantial regolith covering (951) Gaspra, (243) Ida and (433) Eros [167, 150, 177], and the JAXA Hayabusa mission revealed (25143) Itokawa to be a rubble pile asteroid essentially made of regolith throughout [57, 183]. In addition to finding each of these bodies to be regolith-covered, there is strong evidence that this regolith has very complex and active dynamics.

Regolith is everywhere

Classic scenario of regolith formation

Regolith generation has traditionally been attributed to the fall back of impact ejecta and by the comminution of boulders by micrometeoroid impact [80, 77]. However, laboratory experiments [79] and impact models [80] show that

crater ejecta velocities are typically larger than several tens of cm/s, which corresponds to the gravitational escape velocity of km-sized asteroids. Therefore, impact debris cannot be the main source of regolith on small asteroids [80]. It has been shown [46] that thermal fatigue [119, 107, 178], a mechanism of rock weathering and fragmentation with no subsequent ejection, is the dominant process governing regolith generation on small asteroids (*The paper by Delbo et al., 2014 is here attached*).

Classic scenario of regolith formation has problems of explaining regolith on very small asteroids

It is found that rocks larger than a few centimeters break up faster by thermal fragmentation, induced by the diurnal temperature variations, than by micrometeoroid impacts. Since thermal fragmentation is independent of the asteroid size, this process can also contribute to regolith production on larger asteroids. Production of fresh regolith originating from thermal fatigue fragmentation may be an important process for the rejuvenation of near-Earth asteroids' surfaces, as well as for explaining the observed shortage of low-perihelion carbonaceous near-Earth asteroids [110].

A new scenario for regolith formation: thermal cracking

Implications of this discovery

The work of [46] provides also the rates of asteroidal rock break up by meteorite impacts in the asteroid main belt and near-Earth space for the first time.

However, it is not only the temperature excursions that cause surface process on asteroids, but also the temperatures themselves ! An important result in the last years, was the realisation that a large number of asteroids and meteorites, having close approaches with the Sun, reach temperatures high enough to modify the mineralogy of their surfaces [112].

All these studies contributed to build the evidence that the heating driven by the sun is an important process of *space weathering* of asteroid surface. Previous known space weathering process where the micrometeorite bombardment – that can mechanical break and locally heat it the surface material – and the implantation of ions from the solar wind.

The surface alteration by space weathering phenomena is an important issues related to sample return missions to primitive asteroids, such as JAXA's Hayabusa 2 and NASA's OSIRS-REx. In particular it is worth to assess whether the surface (and the subsurface) of the object has been preserved from weathering processes active in space. It is well known, for instance, that the implantation of ions by the solar wind and the bombardment of micrometeorites can alter the spectroscopic properties of asteroids [75] (Hapke 2001; Sasaki et al. 2001). However, these processes affect only the first few microns of the surface, while current sampling devices aim at collecting material at depth larger than a

Surface weathering: importance for sample return missions

few millimeters. On the other hand, NEOs can easily reach temperatures >400 K [121, 48], and the heat penetration depth is of the order of some centimeters for a body with a rotation period of some hours [162].

2.6 Asteroid Thermal Models

Most of the studies presented above have one method in common: the use of an asteroid thermal model. Asteroid thermal modelling is about calculating the temperature of asteroids' surface and immediate subsurface, which depend on absorption of sunlight, multiple scattering of reflected and thermally emitted photons, and heat conduction. Physical parameters such as albedo (or reflectivity), thermal conductivity, heat capacity, emissivity, density and roughness, along with the shape (e.g., elevation model) of the body, its orientation in space, and its previous thermal history are taken into account. From the synthetic surface temperatures, thermally emitted fluxes (typically in the infrared) can be calculated. Physical properties are constrained by fitting model fluxes to observational data. One differentiates between sophisticated *thermophysical models or TPMs* [101, 161, 162, 97, 96, 98, 41, 132, 151] and *simple thermal models*, which typically assume spherical shape, neglect heat conduction (or simplify its treatment), and do not treat surface roughness [72, 44]. In the past, usage of TPMs was reserved to the few exceptional asteroids for which detailed shape models and high quality thermal infrared data existed [72]. In the last ten years, however, TPMs became significantly more applicable, thanks both to new space-born infrared telescopes such as *Spitzer*, *WISE* and *AKARI* [111] and to the availability of an ever-growing number of asteroid shape models [54]. The TPM developed by [41] is one of the most used for asteroids [49, 54]. *The review paper, Asteroids IV book chapter by Delbo et al. 2015, ref. [49] is here attached.*

The Astrophysical Journal, 694:1228–1236, 2009 April 1 doi:10.1088/0004-637X/694/2/1228

FIRST VLTI-MIDI DIRECT DETERMINATIONS OF ASTEROID SIZES*

M. Delbo[1,2], S. Ligori[3], A. Matter[4], A. Cellino[5], and J. Berthier[6]
[1] UNS, CNRS, Observatoire de la Côte d'Azur, BP 4229 06304 Nice cedex 04, France
[2] INAF-Osservatorio Astronomico di Torino Strada Osservatorio 20, 10025 Pino Torinese, Torino, Italy; delbo@oca.eu
[3] INAF-Osservatorio Astronomico di Torino Strada Osservatorio 20, 10025 Pino Torinese, Torino, Italy
[4] UNS, Observatoire de la Côte d'Azur, BP 4229 06304 Nice cedex 04, France
[5] INAF-Osservatorio Astronomico di Torino Strada Osservatorio 20, 10025 Pino Torinese, Torino, Italy
[6] Institut de Mecanique Celeste (IMCCE) 77 av. Denfert Rochereau, 75014 Paris, France
Received 2008 August 26; accepted 2008 December 16; published 2009 March 24

ABSTRACT

We have obtained the first successful interferometric measurements of asteroid sizes and shapes by means of the Very Large Telescope Interferometer-Mid-Infrared Interferometric Instrument (VLTI-MIDI). The VLTI can spatially resolve asteroids in a range of sizes and heliocentric distances that are not accessible to other techniques such as adaptive optics and radar. We have observed, as a typical bench mark, the asteroid (951) Gaspra, visited in the past by the Galileo space probe, and we derive a size in good agreement with the ground truth coming from the in situ measurements by the Galileo mission. Moreover, we have also observed the asteroid (234) Barbara, known to exhibit unusual polarimetric properties, and we found evidence of a potential binary nature. In particular, our data are best fit by a system of two bodies of 37 and 21 km in diameter, separated by a center-to-center distance of ∼24 km (projected along the direction of the baseline at the epoch of our observations).

Key words: infrared: solar system – minor planets, asteroids – techniques: interferometric

1. INTRODUCTION

The study of the physics of asteroids is crucial to constrain models of formation, growth and physical properties of the planetesimals that accreted into the inner solar system planets.

Most asteroids are too small to allow a direct determination of their fundamental physical properties, including sizes,[1] shapes, and masses.[2] According to current expectations, in the next decade, the Gaia mission of the European Space Agency will provide accurate mass determinations for about 100 of the largest main belt asteroids (MBAs) and will be able to directly measure the sizes of all MBAs larger than 30 km (∼1000 objects) (Mouret et al. 2007; Mignard et al. 2007). At present, however, the most important source of progress in this field is related to the increasing rate of discovery of binary systems. These discoveries have been made possible by adaptive optics imaging at several large telescopes, radar—particularly suited for the study of near-Earth objects (NEAs)—and optical lightcurve observations. Binary asteroids are extremely important to derive the mass of the system; the sizes and shapes of the components are then needed to estimate average densities, which in turn provide crucial information about the internal structure of the bodies.

Unfortunately, asteroid sizes are generally not measurable by means of direct imaging. Improvements in the performances of modern adaptive optics systems are currently making significant progress, but this is forcedly limited to size measurements of the largest MBAa, and very close approaching NEAs (Conrad et al. 2007). Radar has been proven to be a powerful tool to infer shapes and sizes for a sample of kilometer- and subkilometer-sized objects. This technique, however, is mostly limited to the population of NEAs, which can experience close encounters with our planet. This is due to the fact that the intensity of the radar echo decreases with the fourth power of the distance.

To summarize, the vast majority of asteroid sizes, due to their small apparent angular extension and orbital location in the Main Belt, remain beyond the range of measurability using current techniques. As a consequence, nearly all of the available information we have today about asteroid sizes comes from the results of indirect methods of size determination.

The most widely adopted technique to determine asteroid sizes is thermal infrared radiometry (see Harris & Lagerros 2002, and references therein). This method is based on the fact that the infrared flux $I(\lambda)$ carries information about the size of the source. In particular, $I(\lambda)$ is proportional to the area of the asteroid visible to the observer. However, $I(\lambda)$ depends also upon the temperature distribution on the asteroid surface. Different models of asteroid thermal infrared emission (the so-called asteroid thermal models; see Section 2, Harris & Lagerros 2002; Delbo & Harris 2002, and references therein) are used to estimate the surface temperature distribution allowing one to derive D from measurements of $I(\lambda)$. The asteroid's geometric visible albedo, p_V, can then be obtained from Equation (1) which represents the fundamental relation linking the effective diameter, D (in km), the albedo, and the absolute magnitude H (the magnitude in the V band that would be measured by observing the object at 1 AU distance from both the Sun and the observer, and at zero phase angle):

$$\log p_V = 6.247 - 2\log D - 0.4H. \quad (1)$$

We note that the value of p_V is per se a very important physical parameter, because it is a function of the composition, texture, and roughness of an asteroid's surface. Polarimetric observations can also be used to estimate the value of p_V (Muinonen et al. 2002; Cellino et al. 2005) from empirical

* Based on data obtained at the Very Large Telescope Interferometer (VLTI) of the European Southern Observatory (ESO): program ID 076.C-0798.
[1] Only for the largest hundred main belt asteroids their sizes can be directly measured with present-day adaptive optics systems at 10 m class telescopes (Conrad et al. 2007).
[2] At the time of writing, only 15 multiple main belt asteroids had their components resolved, allowing determination of their orbits and thus of the masses of the systems (Marchis et al. 2008).

relations between the albedo and the degree of polarization of the reflected light from the asteroid surface. The asteroid effective diameter D can then be determined from p_V using Equation (1).

We note that the value of the absolute magnitude H is derived from photometric observations of the asteroid under different illumination conditions (Muinonen et al. 2002). However, in practice, the H value is usually not determined at the same time of radiometric or polarimetric observations. Its value is in most circumstances simply taken from public catalogs, such as the Minor Planet Center's orbital database, which are known to be affected by significant systematic errors of 0.3 mag or more, mainly for asteroids smaller than ∼40–50 km (Cellino et al. 2009; Parker et al. 2008).

As a conclusion, it can be said that there are currently significant uncertainties on the size (and albedo) values for MBAs of moderate sizes ($D < 50$ km): all but about a thousand of the over one million asteroids in the main belt are smaller than 50 km.

There is thus a strong need to extend direct size measurements to smaller asteroids. However, this is a very challenging task. The only technique that has been so far nominally available, namely the measurement of stellar occultations, is hardly applicable in practice due to the very narrow strips of observability of occultation events and to the actual limits in current accuracies of stellar astrometric catalogues and of asteroid orbital elements (see Tanga & Delbo 2007).

As we show in this paper, a new very powerful facility for the direct measurement of asteroid sizes is now available, namely the Very Large Telescope Interferometer (VLTI) of the European Southern Observatory (ESO). In particular, the VLTI can be successfully applied to objects that (1) are not too big (apparent angular diameters $\lesssim$100–200 mas), but, on the other hand, (2) are sufficiently bright (brighter than visible magnitude ∼13–14). Although these constraints certainly limit the number of objects for which the VLTI can provide direct size and shape determinations, a large number of asteroids still exist that fall within the above magnitude and size ranges (see Figure 1 and Delbo et al. 2006; Loreggia et al. 2008). The results presented in this paper, based on our pilot program, are a nice confirmation of the above statement.

Generally speaking, the VLTI has the capability of measuring sizes (and shapes) of asteroids from measurements of the visibility (contrast) of interferometric fringes. Visibility is a function of the apparent angular extension of the body along the projected interferometer baseline. At present, visibilities can be measured at the VLTI in the near infrared (1–2.5 μm) using the Astronomical Multi-BEam combineR (AMBER; Petrov & The AMBER Consortium 2003) and in medium infrared (N band) by means of the Mid-Infrared Interferometric Instrument (MIDI; Leinert et al. 2003; Przygodda et al. 2003). Because VLTI baseline lengths vary between 16 and 120 m, spatial resolutions of λ/B between about 2 and 12 mas and 20 and 200 mas can be, in principle, obtained with the AMBER and MIDI, respectively. For a general technical overview of the VLTI, see, for instance, Glindemann et al. (2003). Details of the VLTI instruments can also be found on the ESO web pages: http://www.eso.org/projects/vlti/.

One particularly interesting feature of the MIDI instrument is that it also measures the total (noncoherent) spectral energy distribution, $I(\lambda)$, of the source in the 8–13 μm spectral interval. These thermal infrared data can then be used to derive asteroid sizes through the application of asteroid thermal models (see, e.g., Harris & Lagerros 2002; Delbo & Harris 2002, and references therein).

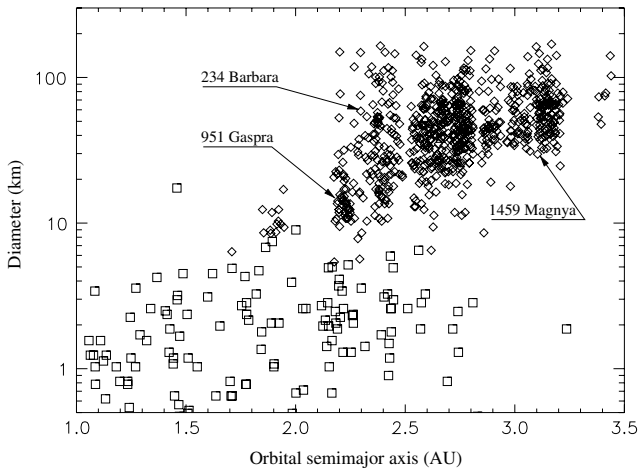

Figure 1. Asteroids for which MIDI can provide direct size determination, according to the present instrument requirements: i.e, (1) a correlated thermal infrared flux (flux × visibility) at 11.8 μm greater or equal to 1 Jy and (2) a visibility greater or equal to 0.1. Diamonds: MBAs. Squares: NEAs. Orbital element are from the minor planet center (MPC). Diameters have been calculated from the MPC H values assuming an average albedo of 0.2. Ephemerides have been calculated every 5 days for NEAs and every 15 days for MBAs for a time span of 15 years starting from 2005 June 1 to check for those bodies meeting conditions (1) and (2).

In this paper, we report the results of the first successful observations of asteroids with the VLTI-MIDI. In particular, the selected targets were (951) Gaspra and (234) Barbara.

For (951) Gaspra we have a priori detailed information of the size and shape: this object was flown by by the space mission Galileo on its way to Jupiter (Thomas et al. 1994). This target was selected with the purpose of performing a test of the real performances of the MIDI-VLTI system by comparing the results of our size determination, with the ground truth coming from the in situ measurements by the Galileo space probe.

As for (234) Barbara, this asteroid belongs to a rare taxonomic class (Ld) and has been discovered by one of us to exhibit a very anomalous behavior in terms of polarimetric properties (Cellino et al. 2006) (in more technical terms, this object displays a phase–polarization curve that reaches strongly negative values at unusually large phase angles, larger than 20°). These properties have been until recently unique, whereas a handful of other relatively small objects belonging to the same or other unusual taxonomic classes have been recently found to share the same polarimetric behavior (Gil-Hutton et al. 2008). Interestingly, (234) Barbara has a long rotation period (26.5 hr, Schober 1981; Harris & Young 1983) which might be suggestive of a possible binary system. The effective diameter derived from IRAS radiometric is of 44 ± 1 km (Tedesco et al. 2002) which implies a geometric albedo (p_V) of 0.22 ± 0.01 when an absolute magnitude $H = 9.02$ is assumed. Taken at face value, the polarimetric parameters of this object would give an albedo (p_V) of ∼0.325 (Cellino et al. 2006), quite larger than the IRAS value. However, Cellino et al. (2006) claim that the unique polarimetric behavior of this object should prevent anyone from using usual polarization–albedo relations to infer reliable albedo estimates for this asteroid.

This paper is organized as follows. In Section 2, we describe the theoretical models used for the interpretation of MIDI data; we present details of MIDI observations of (951) Gaspra and

(234) Barbara in Section 3 along with the adopted data reduction procedure; results are presented in Section 4, followed by a discussion (Section 5) and a concluding (Section 6) section.

2. ANALYSIS OF MIDI OBSERVATIONS

The main purpose of the MIDI is to combine coherently the infrared light collected by two of the four 8 m UT telescopes (or by two of the four AT telescopes) of the ESO VLT: both telescopes observe the same target and when the optical path distances of the two beams are equal, interferometric fringes form on the detector. Fringe contrast (the ratio between the maximum and the minimum intensity) carries information on the angular extension of the source. More precisely, the MIDI measures the source's spatial coherence function or interferometric visibility. Given the brightness distribution $O(x, y, \lambda)$ of a source on the projected sky plane, (x, y), and the corresponding total flux intensity $I(\lambda) = \int\int O(x, y, \lambda)dxdy$, the visibility is given by $V(u, v) = \hat{O}(u, v)/I(\lambda)$, where $\hat{O}(u, v) = \int\int O(x, y, \lambda)e^{-2\pi i(xu+yv)}dxdy$ is the Fourier transform of $O(x, y, \lambda)$, $u = B_x/\lambda$ and $v = B_y/\lambda$ are the spatial frequencies in rad^{-1} along the x- and y-coordinates, respectively, B_x and B_y are the components along the two orthogonal directions of the interferometer's baseline projected on the plane of the sky, and λ is the wavelength of the light.

For maximum sensitivity, MIDI observations are usually carried in a dispersed mode: a prism, with a spectral resolution $R \simeq 30$, and a long slit inserted along the optical path allows visibility measurements to be obtained simultaneously at different wavelengths in the spectral range between 8 and 13 μm. Because $V \equiv V(u = B_x/\lambda, v = B_y/\lambda)$, obtaining V at different λ is also equivalent to a variation of the baseline length at constant λ.

In principle, by measuring $V(u, v)$ for a set of different values of u and v, possibly filling the uv-plane, one could directly derive the spatial flux distribution of the source $O(x, y, \lambda)$ by taking the inverse Fourier transform of $V(u, v)$ (aperture synthesis). However, because at present the MIDI acquisition of one calibrated visibility observation requires about 1 hr of time when observations are executed in the service mode, images of asteroids from interferometric measurements are difficult to obtain from aperture synthesis methods. An additional complication comes also from the fact that asteroids rotate considerably during such an interval of time.

When visibility measurements are available at only one or few baselines, which is the most common observing circumstance, simple parametric model-fitting techniques must be used. In the following, we describe two geometric models used to derive the sizes of our targets from MIDI visibility measurements, namely a disk of uniform intensity and a binary system made of two uniform disks.

We also used simple models of asteroid thermal emission (see Harris & Lagerros 2002) in order to derive the sizes of our targets from the MIDI spectrophotometry only (Figures 2(b) and 3(b)). Theoretical visibilities calculated from these models with asteroid sizes fixed to the values derived from spectrophotometry were afterwards compared to the measured visibilities.

2.1. Uniform Disk Model

If the image of the asteroid on the plane of the sky is approximated by a uniform circular disk of angular diameter θ, the amplitude of the visibility as a function of $u = B/\lambda$ is given by

$$|V_\theta(u)| = |2J_1(\pi\theta u)/(\pi\theta u)|\,, \quad (2)$$

where J_1 is the first-order Bessel function of first kind and B is the length of the baseline projected on the plane of the sky. The angular diameter of the disk can be derived from a single visibility measurement. The equivalent uniform disk diameter $\tilde{D}$ of the asteroid is then trivially derived from θ, and the known geocentric distance Δ of the body. Note that for a highly irregularly-shaped body (such as (951) Gaspra), θ and $\tilde{D}$ correspond to the angular and the physical extension of the body along the projected baseline (see Figure 4).

2.2. Binary System Model

Since the rate of discovery of binary systems has been steadily increasing in recent years, and the detection/characterization of binary systems is a primary application of high-resolution techniques such as the VLTI, it is worth developing a model of a binary source to be applied to the analysis of VLTI data. Here, we assume that the image on the plane of the sky, projected along the baseline B of a binary asteroid system, is given by two uniform disks of diameters θ_1 and θ_2 separated by an angular distance ρ (with the corresponding physical diameters $\tilde{D}_1$, $\tilde{D}_2$, and physical separation a): $O_b(x, \lambda) = O_{\theta_1}(x, \lambda) + \delta(x - \rho) \otimes O_{\theta_2}(x, \lambda)$, where $\otimes$ is the convolution operator and the x-coordinate is taken along the baseline, in this case.

As mentioned above, the visibility function is the Fourier Transform of $O_b(x, \lambda)$ divided by the total flux intensity I: namely, $V_b = [\hat{O}_{\theta_1} + \hat{O}_{\theta_2} \exp(-i2\pi u\rho)]/I$. Because $\hat{O}_\theta = V_\theta I_\theta$, $I = I_{\theta_1} + I_{\theta_2}$, and $\theta_1^2/\theta_2^2 = I_{\theta_1}/I_{\theta_2}$, we can derive an analytical expression for the visibility amplitude of the binary asteroid by inserting these equations in the modulus of V_b: after a little algebra, we obtain

$$|V_b(u)| = \frac{\sqrt{V_{\theta_1}^2 I_{\theta_1}^2 + V_{\theta_2}^2 I_{\theta_2}^2 + 2V_{\theta_1} I_{\theta_1} V_{\theta_2} I_{\theta_2} \cos(2\pi u\rho)}}{I}. \quad (3)$$

Note that Equation (3) is a function of the three parameters θ_1, θ_2, and ρ. These parameters are adjusted (e.g., by means of the Monte Carlo procedure) until the χ^2 between the model ($V_b(u)$) and the observed ($V(u_i)$) visibilities is minimized, where $\chi^2 = \sum_{i=0}^{N}((V_b(u_i) - V(u_i))^2/\sigma_{V(u_i)}^2)$.

2.3. Asteroid Thermal Models

In order to interpret thermal infrared observations of asteroids, models of the temperature distribution and corresponding infrared emission at the surface of these objects have been developed. Sophisticated thermo-physical asteroid models are nowadays used when information about the body's shape and spin vector is known. Infrared fluxes are then computed as a function of the asteroid's albedo, thermal inertia and macroscopic roughness, and these parameters are then adjusted until a best fit to the data is obtained (see Mueller 2007; Delbo et al. 2007; Delbo & Tanga 2009, for details).

In the most common situation of bodies for which spin vector and shape information is not available, simplified thermal models based on an assumed spherical shape must be adopted. In the case of our MIDI data, the refined standard thermal model (STM; Lebofsky et al. 1986), the near-Earth asteroid thermal model (NEATM; Harris 1998), and the fast rotating thermal model (FRM; see Harris & Lagerros 2002; Delbo & Harris 2002, and references therein) were used to fit the measured

Table 1
Observational Circumstances and Relevant Data

Asteroid	Date	UT	r (AU)	Δ (AU)	α (deg)
Barbara	2005-11-15	07:21:05	2.1297371	1.2051145	12.6
Gaspra	2005-11-14	03:21:43	1.8566048	0.8685061	02.2
Gaspra	2005-11-14	04:29:28	1.8566492	0.8685798	02.3
Gaspra	2005-11-14	05:04:27	1.8566857	0.8686429	02.3

Notes. Asteroid ephemerides were generated using the JPL Horizons System: http://ssd.jpl.nasa.gov/?horizons. r and Δ are the heliocentric and geocentric distances of the targets; α is the solar phase angle (the Sun–target–observer angle).

Table 2
VLTI Configuration and Other Relevant Interferometric Parameters of the Performed Observations

Asteroid	Telescopes	B (m)	θ_B (deg)	R.A.	Decl.
(234) Barbara	UT2-UT3	46.285	36.41	03:57:51.40	−08:03:33.2
(951) Gaspra (1)	UT2-UT3	34.730	59.85	03:03:22.65	+20:47:46.0
(951) Gaspra (2)	UT2-UT3	40.495	58.75	03:03:19.79	+20:47:24.2
(951) Gaspra (3)	UT2-UT3	42.785	56.35	03:03:17.45	+20:47:06.1

Notes. B is the length in m of the baseline projected on the plane of sky; θ_B is its position angle from north to east. R.A. and decl. are the J2000 right ascension and the declination of the targets at the time of the observations.

photometric infrared fluxes in order to derive the diameters and the albedos of (951) Gaspra and (234) Barbara.

In a second step, interferometric visibilities were also computed by taking the Fourier transform along the projected baseline spatial infrared emission of the STM, FRM, and NEATM using the sizes derived from MIDI spectrophotometry only. Models visibilities were then compared to the measured ones (see Figures 1(a) and 2(a)).

Without entering into details at this stage, we remind the reader that the STM has been found to be most appropriate for the large MBAs. In the case of small fast-rotators, like some near-Earth objects, the surface temperature distribution is not well reproduced by the STM. The FRM, or even better the NEATM, are better suited. The NEATM is mostly an improved version of the STM, in which the value of the so-called "beaming parameter," one of the parameters of the model, is not arbitrarily fixed like in the case of STM, but it is actually derived from the data taken in different thermal IR bands. This leads usually to a much better fit of the measured thermal IR data. The corresponding relative errors are generally less than 15% in diameter and 30% in albedo. For a more detailed description of the uncertainties on diameters and albedos when derived from the NEATM, STM and FRM see (Delbo et al. 2003; Delbo 2004; Harris 2006).

3. MIDI OBSERVATIONS AND DATA REDUCTION

The observations of (234) Barbara and (951) Gaspra were carried out in the service mode, on November 15, 2005 between 07 and 08 UT, and on November 14, 2005 between 05 and 06 UT, respectively. A typical observing sequence with MIDI is described extensively by Przygodda et al. (2003). Three consecutive visibility measurements were obtained for (951) Gaspra, whereas in the case of (234) Barbara only one visibility observation was acquired. Table 1 reports the observational circumstances for the two targets including their phase angle, and their heliocentric and geocentric distances, for each visibility measurement.[3] Interferometric fringes were detected in all cases, demonstrating the feasibility of ground-based interferometric observations of solar system minor bodies for the first time.

In the case of (234) Barbara and (951) Gaspra the 47 m long interferometric baseline was used by coherently combining the light from the UT2 (KUEYEN) and UT3 (MELIPAL) telescopes (UT2–UT3 baseline). Table 2 gives the value of the projected baseline and other relevant parameters during the observations of our targets. The telescopes and the delay lines of the interferometer were tracked at the rates predicted from the ephemerides of each target. Our observations included medium-infrared photometric standard stars and visibility calibrators chosen from the ESO database, namely HD 31421 for (951) Gaspra and HD 2324 for (234) Barbara. Absolutely calibrated infrared spectra for the calibration stars were taken from the database of Cohen et al. (1999). Absolutely calibrated fluxes for the target asteroids were obtained by multiplying the ratio target/calibration star raw counts at each wavelength by the absolute fluxes of the calibration stars. Instrumental target visibilities were obtained by the ratio of the source raw correlated flux and the source raw photometric flux. Calibrated visibilities were calculated by dividing the instrumental visibility of the target asteroid and the one of the corresponding calibrator star. Calibrators are stars have small and known angular diameter, so that their visibility is close to unity at all wavelengths. Figures 2 and 3 show the resulting calibrated interferometric visibilities, as well as the measured thermal IR fluxes of (951) Gaspra and (234) Barbara, respectively. The predicted interferometric visibilities corresponding to different size solutions resulting from the different models of Section 2 are also shown in the figures. Different thermal models give correspondingly different predictions of the interferometric visibilities.

Visibility measurements can be extracted from MIDI observations by using two different data reduction software packages, namely the MIDI Interactive Analysis (MIA) or the Expert WorkStation (EWS). MIA does a power spectrum analysis (or incoherent analysis) of the MIDI dispersed fringes in order to obtain one visibility "spectrum" for each exposure. In contrast, EWS performs a coherent analysis of the dispersed fringes and enables one to obtain, in addition to the visibility, the phase of fringes as a function of λ. The data of both asteroids were reduced by using in parallel MIA and EWS. The use of both packages gives indications of the visibility uncertainties. At the beginning of the data reduction, the two-dimensional frames in the raw data files are converted to one-dimensional spectra. As a first step, both MIA and EWS use masks to select those regions of the detector where fringes (coherent flux) and photometric images (photometric incoherent fluxes) of the source form. By default, EWS uses a pre-defined mask which always selects the region of the detector where the signals of the fringes and photometric channels are expected to be present. The MIA mask is defined by searching the spectrum on the detector and performing a Gaussian fit over the signal in order to parameterize its position and width. When faint sources are observed, the MIA mask might have trouble finding the position of the signals on the detector. This was the case for (951) Gaspra and consequently the pre-defined EWS mask was used. Because (234)

[3] Note that we observed during an exceptionally close opposition of (951) Gaspra, and that these are not very frequent. Last such favorable opposition, with (951) Gaspra at a geocentric distance, $\Delta < 1$ AU took place in 2008 September. Next ones will take place in 2015 December, 2018 October, 2028 November, 2031 September, 2038 December, 2041 October, and 2051 November.

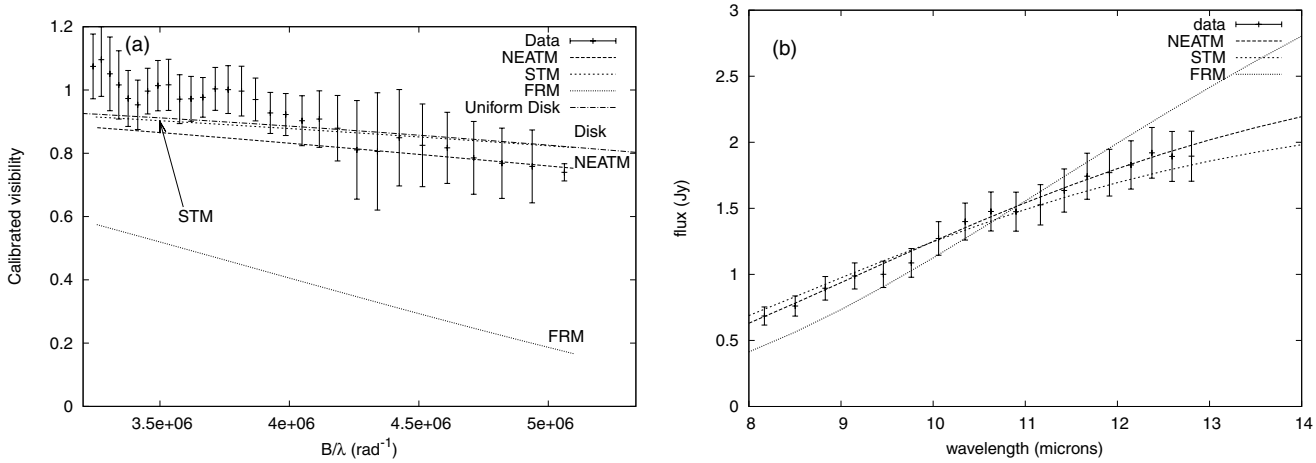

Figure 2. (*a*) Observed interferometric visibility data for (951) Gaspra, and the corresponding best fit by means of a uniform disk model. The NEATM, STM, and FRM curves are the predicted interferometric visibility derived from the three thermal model solutions obtained from the measured infrared fluxes in the range between 8 and 13 μm (measured visibilities were not used in the thermal models fits). (*b*) The measured thermal infrared fluxes at different wavelengths, and the corresponding best-fit solutions by means of the three thermal models described in the text.

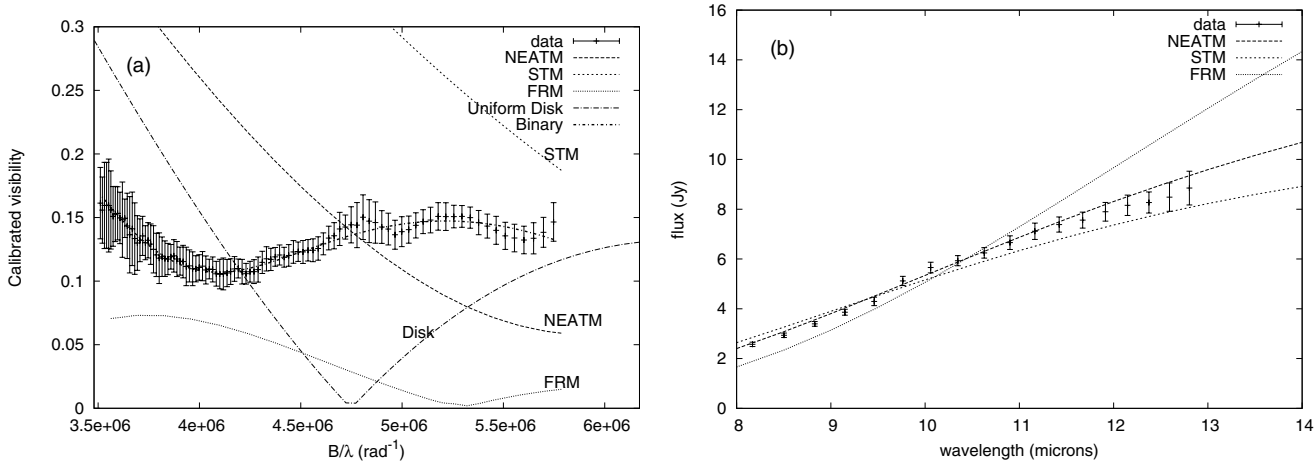

Figure 3. Same as Figure 2, but for (234) Barbara. In (*a*), in addition to the interferometric visibility predicted by a uniform disk model and to the thermal model solutions, the best-fit interferometric visibility of the binary model (see the text) is also plotted. Note how the latter model produces a clearly much better fit to the observations than the others.

Barbara was brighter, the MIA mask was used without problems to extract the fringes and the photometric images.

Suppression of the sky background, which is the predominant flux contribution in the *N* band, is an issue. Sky background generates a DC offset of the whole spectrum. This DC component creates a fringe artifact at zero OPD (optical path difference between the two beams) when EWS calculates the Fourier transform of the measured signal dispersed along wavelengths on the detector, in order to estimate the fringe position. If the source is weak and so is the signal within the fringe, the artifact at zero OPD may be considered as the real fringe by EWS. As our sources are weak and the fringe tracking was not performed around the zero OPD, we used an option of EWS (dAve) to remove the DC background component of the signal by subtracting the mean of all pixels in the spectrum from each individual pixel.

Moreover, at the end of the data reduction process of MIA, the calculated visibilities turned out to be quite noisy. Since we do not request high spectral resolution we modified the λ binning (the default value is 3 pixels for each spectral channel) to 8 pixels for the calculation of the visibilities.

In the next section, we describe how asteroid physical parameters were derived from MIDI measurements.

4. RESULTS

Asteroid sizes were derived from the application of the models described in Section 2 to MIDI measurements. First of all, the STM, the FRM, and the NEATM were fit to the measured infrared fluxes $I(\lambda)$ only, to obtain effective diameters. Flux data and thermal models' best-fit continua for (951) Gaspra and (234) Barbara are plotted in Figures 2 and 3, respectively. The geometric visible albedos were calculated from the derived sizes, utilizing H values from the Minor Planet Center, namely $H = 11.46$ for (951) Gaspra and $H = 9.02$ for (234) Barbara. Table 4 reports D and p_V obtained from the application of the thermal models and the corresponding angular extension of the body at the time of our VLTI observation. An uncertainty of 0.5 mag (see Cellino et al. 2009), affecting the uncertainty on the derived albedo, was assumed on the adopted value of the absolute magnitude H (from the MPC).

We then computed interferometric visibilities corresponding to the obtained NEATM, STM, and FRM solutions (by using

Table 3
Results From Geometric Models Fits to Measured Visibilities

Asteroid	D (km)	θ (mas)	Notes
Gaspra	11 ± 1	17 ± 2	EWS mask
Barbara	44.6 ± 0.3	51.0 ± 0.4	poor fit
Barbara(1)	37.1 ± 0.5	43.0 ± 0.5	primary
Barbara(2)	21.0 ± 0.2	24.2 ± 0.2	satellite
	a (km)	ρ (mas)	
(1)–(2)	24.2 ± 0.2	28.1 ± 0.2	separation

Note. Uncertainties are 1σ.

Table 4
Results from Thermal Model Fits

Asteroid	$\tilde{D}$ (km)	p_V	η	θ_D (mas)	Model
Gaspra	13.8 ± 1.0	0.24 ± 0.14	1.06 ± 0.17	22.0 ± 1.6	NEATM
Gaspra	11.6 ± 0.4	0.34 ± 0.13	(0.756)	18.4 ± 0.6	STM
Gaspra	24.0 ± 0.3	0.08 ± 0.04	···	38.1 ± 0.5	FRM
Barbara	51 ± 2	0.17 ± 0.09	1.17 ± 0.05	58 ± 2	NEATM
Barbara	40 ± 1	0.27 ± 0.09	(0.756)	46 ± 1	STM
Barbara	89 ± 1	0.06 ± 0.03	···	102 ± 1	FRM

Notes. Uncertainties are at 1σ level. D is the diameter of a sphere with the same projected area visible to the observer; p_V is the geometric albedo in visible light; η is the beaming parameter. An uncertainty of 0.5 mag was assumed on the adopted value of the absolute magnitude H (from the MPC). Values of η in brackets are default values. θ_D is the angular extension of D in mas at the distance of the asteroid.

the values of the diameters and the albedos obtained from models fits to the infrared fluxes). We calculated the Fourier transform of the model thermal infrared emission and evaluated this function at ($u = B\cos\theta_B, v = B\sin\theta_B$). The values of B and θ_B are reported in Table 2 for each VLTI observation. The predicted interferometric visibilities corresponding to the different thermal radiometry solutions are overplotted along with the measured values in Figures 2 and 3 as the three dotted lines labeled NEATM, STM, and FRM.

In a second step, we used the simple geometric models described in Section 2 to analyze measured visibilities.

4.1. (951) Gaspra

Fringes were detected for all interferometric observations reported in Tables 1 and 2. However, by careful analysis of the acquisition images, we discovered a failure in the acquisition of the source during the first MIDI measurement (the one taken at UT 03:21:43). So, we limited our analysis to the second and the third observations, only. In order to increase the signal to noise ratio of the visibility measurements, we computed the average visibility extracted using the EWS mask between the second and third measurement (i.e., those obtained at 04:29:28 and 05:04:27 UT). Figure 2 shows the obtained data points. The error bars correspond to half of the difference between the two measurements.

We note that for $B/\lambda \lesssim 3.8 \times 10^6$ rad^{-1}, corresponding to $\lambda \gtrsim 11\ \mu$m, Figure 2 shows that the visibility oscillates around 1, which we interpret as due to the lack of spatial resolution at these wavelengths.

We performed a least-squares fit of Equation (2) (uniform disk model) to the data points of Figure 2 using θ as the only free parameter and using $B = 41.64$ m. We obtain $\theta = 17 \pm 2$ mas, which corresponds to $\tilde{D} = 11 \pm 1$ km at the distance of the asteroid. (see Table 3 for a summary of our results). The comparison of our VLTI/MIDI size determination of (951) Gaspra with the asteroid's projected size known from Galileo spacecraft observations is discussed in Section 5.

4.2. (234) Barbara

The visibility of (234) Barbara extracted from MIDI observations are shown in Figure 3. Error bars, obtained using the EWS data reduction software, represent the standard deviation of the visibility. As for the case of (951) Gaspra, a least-squares fit of Equation (2) was performed to the data points with the angular diameter θ of the uniform disk as the only free parameter. We obtained $\theta = 51.0 \pm 0.4$ mas, which corresponds to $\tilde{D} = 44.6 \pm 0.3$ km at the distance of the asteroid. However, Figure 3 clearly shows that a uniform disk model provides a poor fit to the measurements. Model visibilities calculated by means of the NEATM, the STM, and the FRM thermal models also give a poor fit of the actual measurements. This is likely an indication that the spatial distribution of the source's infrared flux differs from that of a uniform single body.

An application of the binary disk model to the measured visibility, however, gives much better results. In this case, we found a remarkably good match between the model and the observations, as shown in Figure 3. Best-fit values of the model parameters θ_1, θ_2, and ρ are 43.0 ± 0.5, 24.2 ± 0.2, and 28.1 ± 0.2 mas, respectively. When we take into account the distance to the asteroid at the time of our observations we derive diameters of $\tilde{D}_1 = 37.1 \pm 0.5$ km and $\tilde{D}_2 = 21.0 \pm 0.2$ km for the primary and the secondary components of the binary system. The center-to-center distance projected on the interferometer baseline was of $a = 24.2 \pm 0.2$ km.

5. DISCUSSION

For (951) Gaspra we have a priori information on its size, shape, and spin vector state from spacecraft observations (Thomas et al. 1994). This is the main reason why we decided to observe this object, in order to obtain a reliable estimate of the resulting accuracy in the size determination from thermal models and by means of the uniform disk model fit to MIDI interferometric observations. We caution here that a single uniform disk model may provide a poor description of the spatial distribution of the infrared emission of asteroids in some cases, as clearly demonstrated by our observations of (234) Barbara.

In order to estimate the reliability of our size determinations of (951) Gaspra, we compared the sizes derived from our MIDI measurements with that published by Thomas et al. (1994). As a first step, we computed the orientation of the shape of the asteroid at the epoch of the VLTI observation using an asteroid physical ephemerides service of the Institut de Mécanique Celeste et de Calcul des Ephemerides (IMCCE) in Paris.[4] The shape model of the asteroid, derived from the Galileo spacecraft observations, is that of Thomas et al. (1994). Two spin vector models are available, namely a first one with $\alpha_p = 9.^\circ5$, $\delta_p = 26.^\circ7$ (Thomas et al. 1994) and a second one with $\lambda_p = 20^\circ$, $\beta_p = 19^\circ$ (Kaasalainen et al. 2001), where α_p and δ_p are J2000 equatorial coordinate of the asteroid's pole, whereas λ_p and β_p are its J2000 ecliptic longitude and latitude. Figure 4 shows the orientation of (951) Gaspra, assuming the spin model 1, at the time of the second and the third visibility measurement. Note that the asteroid was observed almost pole-on. Figure 5 shows a comparison of the object shape model adopted and one image taken by the Galileo mission.

[4] Internet service available at http://www.imcce.fr → Ephemerides → Ephemeris for physical observation of the solar bodies.

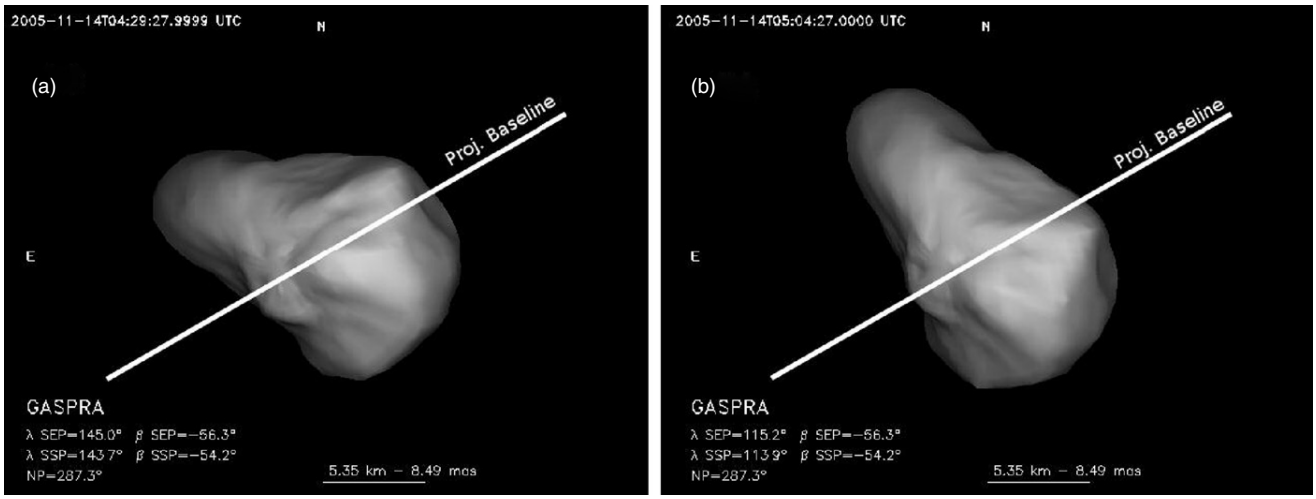

Figure 4. Shape model of (951) Gaspra projected on the plane of the sky at the time of the second (a) and third (b) VLTI visibility measurement, computed using the MOVIS software.

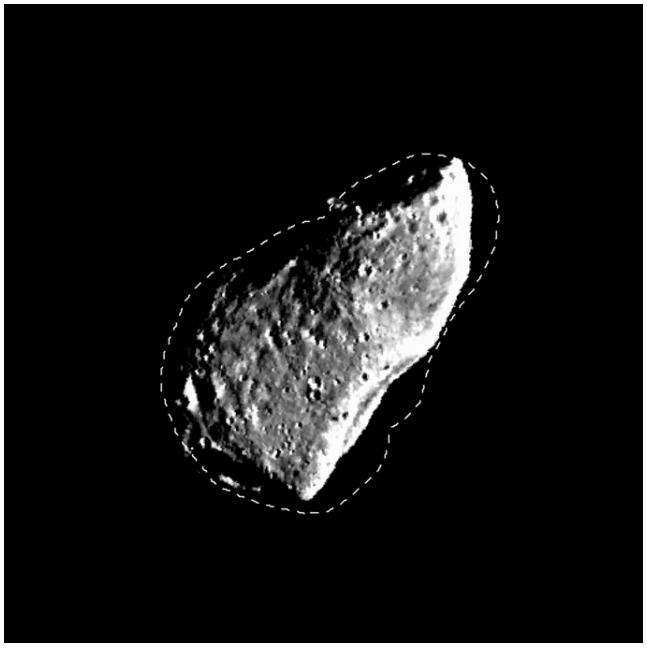

Figure 5. Comparison of an image of (951) Gaspra taken by the Galileo mission on 1991-10-29 at 22:26 UT from a distance of 5300 km and our shape model (dashed line) observed under the same circumstances. The scale of the image is 54 m pixel^{-1}.

From the shape model, we found that total projected area visible to the observer was 380 mas^2. Taking $2 \times \sqrt{380.0/\pi}$ we obtain a value of $\theta_D = 22$ mas corresponding to $D = 14.71$ km. Thomas et al. (1994) give detailed information about the accuracy of the shape model: from their Figure 5 one can estimate a conservative error of 1 km along the projected radius of the shape model of (951) Gaspra at the time of our observation. We can take 15 ± 2 km as the value for D from Thomas et al. (1994) shape model. When we compare this latter value with the size solutions derived from thermal models, we find very good agreement with the estimate of D from the NEATM. Even though the NEATM was developed for the observation of relatively small near-Earth asteroids, there is no reason to believe that it should not be suited to apply also to main belt asteroids of the same size, and this is confirmed by our MIDI data of (951) Gaspra.

As for the other thermal models, the STM predicts a fairly smaller diameter, whereas the size estimate of the FRM turns out to be very inaccurate. The latter result is not surprising: given the pole-on aspect of the asteroid with respect to the sun, the effect of rotation and thermal inertia in smoothing out the surface temperature is strongly reduced, and the ideal circumstances for the application of the FRM are certainly not met.

Figure 4 shows also the orientation of the projected baseline of the interferometer. The angular extension of (951) Gaspra was 19.5, and 16.9 mas, respectively. From Thomas et al. (1994), Figure 5 one can estimate an error of 2 km in the shape model along the direction of the VLTI projected baseline. This value correspond to 3 mas at the distance of the asteroid. We can thus take 19 ± 3 mas and 17 ± 3 mas as the extensions of the shape of (951) Gaspra at the time of the second and the third visibility measurement, respectively.

Assuming the pole solution of Kaasalainen et al. (2001) (model 2) the difference in total projected area of the asteroid visible to the observer with respect to the pole solution 1 turns out to be negligible. The size of (951) Gaspra along the projected baseline, however, turns out to be 17 ± 3 mas at the time of both the second and the third visibility measurement using the Kaasalainen et al. (2001) pole.

The result of this analysis indicates that the expected value of the projected size of (951) Gaspra along the VLTI baseline at the epochs of our observations is in excellent agreement with the angular extension of the body derived from fitting the uniform disk model to the MIDI measurements, i.e., 17 ± 2 mas.

Our MIDI observations of (234) Barbara strongly suggest that this asteroid is composed of two bodies with diameters of 37 and 21 km. We note that, taken at face value, the separation of ∼24 km between the centers of the two disks is smaller than the sum of the radii of the two bodies of ∼29 km. This might be an indication of a bi-lobated shape. On the other hand, because the separation of the two objects is measured along the projected baseline on the plane of the sky, the actual distance between the two components can be much larger, implying a binary system, as shown in Figure 6. At the moment, we are not

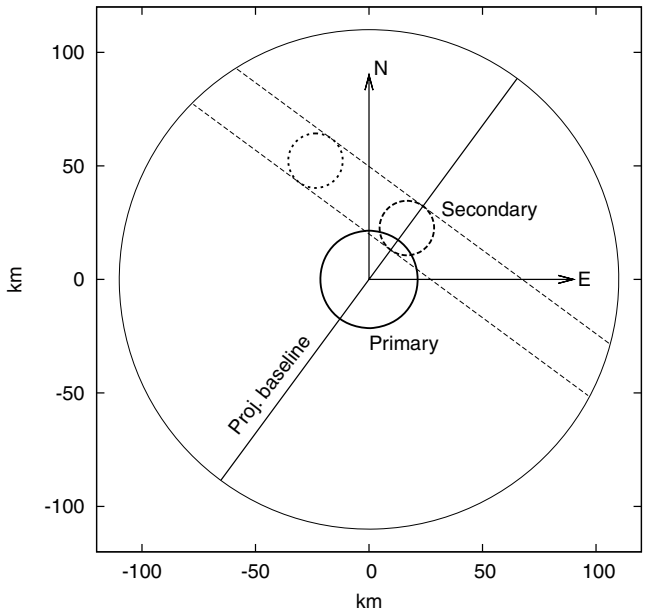

Figure 6. Sketch of the binary model for the asteroid (234) Barbara resulting from VLTI-MIDI observations. The most external circle represents the width of the 10 μm beam of the UT telescopes in which the source must be positioned in order to provide an interferometric signal measurable by MIDI. The secondary component of the system can be anywhere within the two dashed lines perpendicular to the interferometer projected baseline.

able to distinguish between the possibility that (234) Barbara is a single object having a bi-lobated shape, or it is actually a detached or contact binary system. Further interferometric observations using different projected baselines coupled with optical lightcurve measurements are required to test the different possible alternatives.

In order to compare the size of (234) Barbara derived from the geometric binary model and those obtained from thermal modeling, we compare the diameters of the spheres with equivalent area, D. The total surface of the binary model varies from 1420 ± 30 km^2, corresponding to the fully separated case, to 1370 ± 30 km^2 when the center-to-center distance of the two disks is 29 km. These values correspond to D of 43 ± 1 km and 42 ± 1 km, respectively, and they lie in between the NEATM and the STM size estimates.

6. CONCLUSIONS

We have obtained the first direct measurements of asteroid sizes from ground based interferometry in the thermal infrared using the MIDI of the ESO VLTI. Our observations of (951) Gaspra convincingly show that MIDI observations can spatially resolve asteroids as small as $\sim$12 km in the Main Belt with excellent accuracy. This is suggested by the comparison of our VLTI results with the shape model obtained by means of in situ imaging observations during the flyby of the Galileo mission. Our observations suggest that the second target, (234) Barbara, is a potential binary system. However, further investigation are required to fully prove this hypothesis and to derive the geometric parameters of the system (in particular, the separation of the two components, which might also be in contact). We note that a binary nature of (234) Barbara is not surprising given the slow rotation period of this object obtained in the past from lightcurve observations. A binary nature, however, can not explain per se the unusual polarimetric properties of this object (Cellino et al. 2006). The above properties are most likely due to an unusual surface composition of this object, as also suggested by its unusual taxonomic classification. We have here a very interesting example of an object which seems to exhibit clear evidence of a complex history, and this makes it a high-priority target for further observations and theoretical investigations.

We thank the staff and the Science Archive Operation of the European Southern Observatory (ESO), and in particular Markus Wittkowski. The comments and suggestions from an anonymous referee are gratefully acknowledged. The work of M.D.B. has been supported by the European Space Agency (ESA). This research was partially carried out while M.D.B. was a Henri Poincaré Fellow at the Observatoire de la Côte d'Azur. The Henri Poincaré Fellowship is funded by the CNRS-INSU, the Conseil Général des Alpes-Maritimes, and the Rotary International—District 1730. This work has been partially funded through the project PRIN INAF 2007 no. 6. M.D.B. thanks O. Chesneau, D. Loreggia, L. Saba, and M. Zio for valuable comments and discussions, and D. Licchelli for having made at disposal the set of lightcurves of (951) Gaspra obtained quasi-simultaneously to the MIDI observations.

REFERENCES

Cellino, A., Belskaya, I. N., Bendjoya, P., di Martino, M., Gil-Hutton, R., Muinonen, K., & Tedesco, E. F. 2006, Icarus, 180, 565
Cellino, A., Dell'Oro, A., & Tedesco, E. F. 2009, P&SS, 57, 173
Cellino, A., Gil-Hutton, R., Di Martino, M., Bendjoya, Ph., Belskaya, I. N., & Tedesco, E. F. 2005, Icarus, 179, 304
Conrad, A. R., et al. 2007, Icarus, 191, 616
Cohen, M., Walker, R. G., Carter, B., Hammersley, P., Kidger, M., & Noguchi, K. 1999, AJ, 117, 1864
Delbo, M. 2004, Freie Universitaet Berlin, Digitale Dissertation. online at http://www.diss.fu-berlin.de/2004/289/indexe.html
Delbo, M., Dell'Oro, A., Harris, A. W., Mottola, S., & Mueller, M. 2007, Icarus, 190, 236
Delbó, M., & Harris, A. W. 2002, Meteorit. Planet. Sci., 37, 1929
Delbo, M., Harris, A. W., Binzel, R. P., Pravec, P., & Davies, J. K. 2003, Icarus, 166, 116
Delbo, M., & Tanga, P. 2009, Planet. Space Sci., 57, 259
Delbo, M., et al. 2006, Icarus, 181, 618
Gil-Hutton, R., Mesa, V., Cellino, A., Bendjoya, P., Peñaloza, L., & Lovos, F. 2008, A&A, 482, 309
Glindemann, A., et al. 2003, Ap&SS, 286, 35
Harris, A. W. 1998, Icarus, 131, 291
Harris, A. W. 2006, in Proc. IAU Symp. 229, Asteroids, Comets, Meteors, ed. L. Daniela, M. Sylvio Ferraz, & F. J. Angel (Cambridge: Cambridge Univ. Press), 449
Harris, A. W., & Lagerros, J. S. V. 2002, in Asteroids III, ed. W. F. Bottke, A. Cellino, R. P. Paolicchi, & P. Binzel (Tucson, AZ: Univ. of Arizona Press), 205
Harris, A. W., & Young, J. W. 1983, Icarus, 54, 59
Kaasalainen, M., Torppa, J., & Muinonen, K. 2001, Icarus, 153, 37
Lebofsky, L. A., et al. 1986, Icarus, 68, 239
Leinert, C., et al. 2003, Ap&SS, 286, 73
Loreggia, D., Delbo, M., Gai, M., Lattanzi, M. G., Ligori, S., Saba, L., Wittkowski, M., & Cellino, A. 2008, in Eso Astrophysics Symp., The Power of Optical/IR Interferometry: Recent Scientific Results and 2nd Generation, (Berlin: Springer), 565
Marchis, F., Descamps, P., Baek, M., Harris, A. W., Kaasalainen, M., Berthier, J., Hestroffer, D., & Vachier, F. 2008, Icarus, 196, 97
Mignard, F., et al. 2007, Earth Moon Planets, 101, 97
Mouret, S., Hestroffer, D., & Mignard, F. 2007, A&A, 472, 1017
Muinonen, K., Piironen, J., Shkuratov, Y. G., Ovcharenko, A., & Clark, B. E. 2002, in Asteroids III, ed. W. F. Bottke, A. Cellino, R. P. Paolicchi, & P. Binzel (Tucson, AZ: Univ. of Arizona Press), 123
Mueller, M. 2007, Freie Universitaet Berlin, Digitale Dissertation, online at http://www.diss.fu-berlin.de/2007/471/indexe.html

Parker, A., Ivezić, Ž., Jurić, M., Lupton, R., Sekora, M. D., & Kowalski, A. 2008, Icarus, 198, 138
Petrov, R. G., et al. 2003, Ap&SS, 286, 57
Przygodda, F., Chesneau, O., Graser, U., Leinert, C., & Morel, S. 2003, Ap&SS, 286, 85
Schober, H. J. 1981, A&A, 96, 302
Tanga, P., & Delbo, M. 2007, A&A, 474, 1015
Thomas, P. C., Veverka, J., Simonelli, D., Helfenstein, P., Carcich, B., Belton, M. J. S., Davies, M. E., & Chapman, C. 1994, Icarus, 107, 23
Tedesco, E. F., Noah, P. V., Noah, M., & Price, S. D. 2002, AJ, 123, 1056

Monthly Notices
of the
ROYAL ASTRONOMICAL SOCIETY

Mon. Not. R. Astron. Soc. (2012) doi:10.1111/j.1365-2966.2012.21220.x

On the origin of the Almahata Sitta meteorite and 2008 TC_3 asteroid

Julie Gayon-Markt,[1⋆] Marco Delbo,[1] Alessandro Morbidelli[1] and Simone Marchi[1,2]

[1]*Laboratoire Lagrange UMR 7293, Université Nice Sophia-Antipolis, CNRS, Observatoire de la Côte d'Azur, B.P. 4229, 06304 Nice Cedex 4, France*
[2]*NASA Lunar Science Institute, Center for Lunar Origin and Evolution, Southwest Research Institute, 1050 Walnut St, Suite 300, Boulder, CO 80302, USA*

Accepted 2012 May 1. Received 2012 April 30; in original form 2012 April 10

ABSTRACT

Asteroid 2008 TC_3 was a near-Earth asteroid that impacted the Earth on 2008 October 7. Meteorites were produced by the break-up of 2008 TC_3 in the high atmosphere and at present, about 600 meteorites – called Almahata Sitta – coming from 2008 TC_3 have been recovered. A mineralogical study of Almahata Sitta fragments shows that the asteroid 2008 TC_3 was made of meteorites of different types (ureilites, H, L and E chondrites). Understanding the origin of this body and how it was put together remain a challenge. Here we perform a detailed spectroscopical and dynamical investigation to show that the most likely source region of 2008 TC_3 is in the inner main belt at low inclination ($i < 8^\circ$). We show that asteroids with spectroscopic classes that can be associated with the different meteorite types of Almahata Sitta are present in the region of the main belt that includes the Nysa-Polana family and objects of the background at low inclination. Searching for a possible scenario of formation for 2008 TC_3, we show that there is little chance that 2008 TC_3 was formed by low-velocity collisions between asteroids of different mineralogies, in the current asteroid belt. It seems more likely that the heterogeneous composition of 2008 TC_3 was inherited from a time when the asteroid belt was in a different dynamical state, most likely in the very early Solar system. Because ureilites are fragments of a large, thermally metamorphosed asteroid, this suggests that the phases of collisional erosion (the break-up of the ureilite parent body) and collisional accretion (the formation of the parent body of 2008 TC_3) overlapped for some time in the primordial asteroid belt.

Key words: techniques: spectroscopic – catalogues – meteorites, meteors, meteoroids – minor planets, asteroids: individual: 2008 TC_3.

1 INTRODUCTION

Meteorites are a partial sample of asteroids that survive the passage through the Earth's atmosphere. The identification of the source regions of the different type of meteorites is essential to be able to link the mineralogical properties of meteorites to the parent asteroids and, consequently, to address the mineralogical evolution in the asteroid belt. However, this is not an easy task and only some of these links could be established: for instance, the group of howardites, eucrites and diogenites (HEDs) meteorites are thought to come from the Vesta family of asteroids (e.g. Binzel & Xu 1993); more speculatively, L ordinary chondrites could come from the Gefion family (Nesvorný et al. 2009), while asteroids of the Flora family bear spectral similarities with the LL chondrites (Vernazza et al. 2008). However, the parent bodies of most meteorite types, if still intact, are unknown.

The discovery and spectroscopic observation of the near-Earth asteroid (NEA) 2008 TC_3 (henceforth TC_3) 20 h before it impacted the Earth's high atmosphere, and the subsequent recovery of meteorites (called Almahata Sitta) – clearly coming from this body – was a major result in this respect (Jenniskens et al. 2009; Shaddad et al. 2010). It allowed a direct link between an asteroid and meteorites to be established for the first time: the asteroid was classified as belonging to the spectroscopic F-class (in the Tholen classification; Tholen 1984) or B-class (in the Bus classification; Bus & Binzel 2002) on the basis of the flat shape of its reflectance spectrum in the region between 500 and 1000 nm. Moreover, among the 47 meteorites initially recovered, it was observed that the visible spectrum of the fragment #7 matches the telescopic spectrum of TC_3 obtained before the impact with the Earth's atmosphere (Jenniskens et al. 2009). Fragment #7 is an achondrite polymict ureilite (Jenniskens et al. 2009). Ureilites are in a group of achondritic meteorites that exhibit both primitive and evolved characteristics (Cloutis et al. 2010): in particular, they are characterized by olivine and pyroxene-rich clasts among carboneous material (mainly graphite); fine-grained graphite is also present, which lower the albedo of the meteorites (about

⋆E-mail: julie.gayon@oca.eu

10–12 per cent; Hiroi et al. 2010). Ureilites were initially thought to derive from S-class asteroids (see for instance Gaffey et al. 1993). However, because of its spectral properties, Jenniskens et al. (2009) propose a link with B-class asteroids according to the Bus classification or F-class in the Tholen classification. This is more plausible than a link with S-class asteroids, given the low albedos of ureilite meteorites, consistent with B- or F-class asteroids but not with the S-class.

It is worth to note that the F-class can be distinguished from the B-class from a much weaker ultraviolet (UV) drop-off in the spectra of the former compared to the latter and also because B-class asteroids show a moderately higher average albedo than F-class bodies. However, in the Bus classification these two classes are merged in a unique class (the B-class). This is because the Bus & Binzel (2002) spectral classification is based on spectra acquired with CCD spectrographs, which – in general – do not observe far enough in the UV to observe the above-mentioned drop-off feature. We will refer in this work to B-class asteroids including both Tholen B and F classes, and Bus B-class.

Interestingly, mineralogical studies of Almahata Sitta show that, among the ∼600 fragments recovered (Shaddad et al. 2010), about 70–80 per cent are ureilites, while the remaining 20–30 per cent are enstatite chondrites, H and L ordinary chondrites. More specifically, Bischoff et al. (2010) show that, among a subsample of 40 deeply studied meteorites from Almahata Sitta, 23 fragments are achondritic ureilites and 17 have chondritic litologies with 14 of them corresponding to enstatite chondrites, two to H ordinary chondrites and one to a new type of chondrite (see Horstmann et al. 2010 for more details). Although small clasts of different types are quite common in brecciated meteorites (see Meibom & Clark 1999, for a review) and carboneous material is found in some HED meteorites, it is the first time that meteorites of very different mineralogies (i.e. primitive fragments with achondrite polymict ureilites and evolved ones such as ordinary chondrites or enstatite chondrites) are associated with the same fall. This led to make the hypothesis that TC_3 was an asteroid made of blocks of different mineralogies, held together very loosely (given the explosion of the body at the anomalously high altitude; Jenniskens et al. 2009; Bischoff et al. 2010; Shaddad et al. 2010).

Tracing back TC_3 to its source region in the asteroid main belt would allow us to understand the origin of the Almahata Sitta meteorites and how TC_3 was put together by loosely assembling meteorites of different mineralogies. Establishing this link would also be fundamental to shed light on the source region of ureilites, that albeit rare, is the fourth major class of primitive meteorites recovered on Earth after the CV, CI and CO carbonaceous chondrites.

In their attempt to find the source region of TC_3 and Almahata Sitta, Jenniskens et al. (2010) selected all B-class asteroids, according to the Bus classification, and objects of the Tholen F and B classes and searched for spectra similarities with TC_3 and Almahata Sitta. As a result of their study, they showed spectral similarities between TC_3 and ungrouped asteroids as well as several dynamical asteroid groups (or families) as possible origins for the TC_3 asteroid, namely Polana (2.4 au, 3°), Hoffmeister (2.8 au, 4.°5), Pallas (2.8 au, 33°), Themis (3.15 au, 1.°5) and Theobalda (3.2 au, 14°). Later, from dynamical grounds, Jenniskens et al. (2010) concluded that asteroids from the inner asteroid belt (i.e. with orbital semimajor axis $a < 2.5$ au) are the likely parent bodies of TC_3. This reduces the choice to dispersed B-class asteroids in the inner main belt and the Polana asteroid group. In Section 2, we revisit this issue studying the possible dynamical source regions for TC_3.

We recall here that the Polana group is part of a cluster of asteroids known as the Nysa-Polana family (Nesvorný 2010), which is located in the inner main belt, between the ν_6 secular resonance (at heliocentric distance ≈2.1 au) and the 3:1 mean motion resonance with Jupiter (at heliocentric distance of 2.5 au). This family has a complex – twofold – structure in orbital proper element space (Nesvorný 2010), suggesting that it is the outcome of at least two independent break-up events in the same orbital region. From the few spectral data available at the time, Cellino et al. (2001) argued that the Nysa-Polana family contains asteroids of three spectral classes. The first class is that of B-class objects, like asteroid (142) Polana itself – note that Cellino et al. (2001) uses the F-class classification from the Tholen (1984) taxonomy; the second class is the S-class, with the largest member being identified as the asteroid (878) Mildred; the third class is that of X-class objects, such as the asteroid (44) Nysa. In this paper, we revisit this result using a much wider data set of spectrophotometric data provided by the Moving Objects Catalog (MOC) of the Sloan Digital Survey (SDSS; Ivezic et al. 2002), which is analysed here using a new classification algorithm (Michel, Bendjoya & Rojo Guerra 2005, described in Section 3) developed for the *Gaia* space mission of the European Space Agency (ESA).

A detailed study of the mineralogy of the Nysa-Polana family is of great importance also for better understanding the origin of other NEOs. In particular, Campins et al. (2010) claimed that the asteroid (101955) 1999 RQ_{36}, target of the sample return mission *OSIRIS-REx* (approved in the program New Frontiers of NASA), was delivered to near-Earth space via the ν_6 secular resonance from the Polana group. Moreover, the binary asteroid (175706) 1996 FG_3, primary target of the sample return mission *Marco Polo-R*, under study at the ESA, might have formed within the Polana group and delivered to the near-Earth space via the overlapping Jupiter 7:2 and Mars 5:9 mean motion resonances rather than the ν_6 (see Walsh et al. 2012).

As a consequence, in Sections 4 and 5, we perform a spectroscopic analysis using the SDSS data of the asteroids of the Nysa-Polana family as well as dispersed asteroids of the inner main belt (called objects of the background) in order to find spectral matches with TC_3 and Almahata Sitta.

Finally, in Section 6, we investigate a possible formation scenario for the TC_3 asteroid as a rubble pile of rocks of different mineralogical types, which is based on the peculiar low inclination of the Nysa-Polana family and dispersed asteroids.

2 DYNAMICAL HISTORY AND MAIN-BELT ORIGIN OF TC_3

The large majority of NEAs are fragments generated by the collisional disruption of larger asteroids of the main belt; said fragments drift in orbital semimajor axis by the so-called Yarkovsky effect until they reach regions of orbital instabilities (mean motion resonances with Jupiter and secular resonances) which, by enhancing their orbital eccentricities, deliver them to the near-Earth space (see Morbidelli et al. 2002, for a review).

According to model by Bottke et al. (2002), there are five main intermediate sources of NEAs:

(1) the ν_6 secular resonance, which marks the inner edge of the asteroid belt and occurs when the precession frequency of the longitude of perihelion of an asteroid is equal to that of Saturn;

(2) the 3:1 mean motion resonance located at $a \sim 2.5$ au, where the orbital period of an asteroid is 1/3 of that of Jupiter;

(3) Mars-crossing asteroids, defined as objects which are not NEAs (i.e. their perihelion distance q is larger than 1.3 au), but whose semimajor axis evolves in a random-walk fashion as a result of close and distant encounters with Mars;

(4) the outer belt population, whose eccentricities can increase up to planet-crossing values due to a network of high-order orbital resonances with Jupiter and three-body resonance of type asteroid Jupiter–Saturn (Morbidelli & Nesvorny 1999);

(5) dormant Jupiter family comets.

The orbital elements of TC$_3$ before impact are not known very precisely. Here are different estimates: $a = 1.29$ au, $e = 0.299$ and $i = 2\overset{\circ}{.}441$ (NEODyS website http://Newton.dm.unipi.it/neodys); $a = 1.308$ au, $e = 0.312$ and $i = 2\overset{\circ}{.}542$ (Jenniskens et al. 2010). For each of these orbits we computed, using the original orbital evolution files of Bottke et al. (2002), which are the most likely intermediate sources among those enumerated above. We found that TC$_3$ has a probability of 63–66 per cent to come from the ν_6 source and 34–37 per cent to come from the Mars crosser population. Apparently, none of the simulations for the 3/1 resonance in Bottke et al. (2002) produces objects within ± 0.05 au in a, ± 0.05 in e and $\pm 2\overset{\circ}{.}5$ in i of TC$_3$. This contrasts with the claim reported in Jenniskens et al. (2010), that TC$_3$ has a 20 per cent probability to come from the 3/1 resonance in the Bottke et al. (2002) model. We suspect that there has been an error in the manipulation of the Bottke et al. (2002) model in that work.

Of the Mars crossers that can produce the TC$_3$ orbit in Bottke et al. (2002) simulations, none has semimajor axis larger than 2.5 au. From this, and remembering that the ν_6 resonance lays at the inner edge of the belt, we conclude – in agreement with Jenniskens et al. (2010) – that TC$_3$ most likely comes from the inner asteroid belt, inside of 2.5 au.

As noted in Jenniskens et al. (2010), there are two populations of asteroids in the inner belt with spectra broadly consistent with that of TC$_3$: the Polana members, with an orbital inclination of 2°–3°, and a population of dispersed B-class asteroids, with inclinations ranging up to 15°. These objects are too dispersed to belong to a relatively young collisional family, but their broad cluster in orbital space suggests that they might belong to an old collisional family, dynamically dispersed probably during the phase when the orbits of the giant planets changed substantially, about 4 Gyr ago.

To determine whether it is more likely that TC$_3$ comes from the Nysa-Polana family or from the population of dispersed B-class asteroids, we turn, once again, to the original simulations in Bottke et al. (2002). In that work, the initial distribution of asteroids in the ν_6 was uniform in inclination. In particular, 50 per cent of the initial conditions had initial inclination larger than 8°. However, 93 per cent of the particles which reproduced the orbit of TC$_3$ at some time during their evolution have initial inclination $i < 8^\circ$. For the Mars crossers, all those reproducing the orbit of TC$_3$ have initial $i < 8^\circ$. This suggests that the most likely source of TC$_3$ is at low inclination, consistent with the Nysa-Polana family and with the dispersed B-class asteroids with $i < 8^\circ$. This is not surprising, given that the inclination of TC$_3$ is $2\overset{\circ}{.}3$–$2\overset{\circ}{.}5$. However, the dynamics rules out a TC$_3$ origin from the dispersed B-class asteroids at higher inclination (i.e. $i > 8^\circ$).

Finally, Campins et al. (2010) have shown that the Polana group can easily deliver small enough fragments in the ν_6 resonance. In fact, the extrapolated Yarkovsky-induced semimajor axis distribution of Polana group members predicts that asteroids fainter than $H \sim 18.5$ can reach the border of the ν_6 resonance, which is at 2.15 au for a Polana-like inclination. Assuming a Polana-like geometric visible albedo of 0.05, $H = 18.5$ translates into a diameter $D \sim 2$ km, which is much larger than the size of TC$_3$.

For all these reasons we conclude that, from the dynamical viewpoint, the Nysa-Polana family and dispersed B-class asteroids with $i < 8^\circ$ are the most likely sources of TC$_3$. Thus, we will focus on the Nysa-Polana family and the background at low inclination in the next sections.

3 SPECTROSCOPIC ANALYSIS METHOD

3.1 Asteroid spectral classification algorithm

In order to search for spectral groups in the Nysa-Polana asteroid family or in the inner main belt background at low inclination, we used the unsupervised classification algorithm that will be adopted for the classification of asteroid spectra from the multiband photometers (Jordi et al. 2010) on board the *Gaia* space mission of the ESA.

While *Gaia* is mainly devoted to the observations of 10^9 stars, it is expected that this mission will also observe more than 250 000 asteroids multiple times over 5 yr (mission lifetime; Mignard et al. 2007). Spectral classification of asteroids will be performed by an unsupervised classification algorithm based on the works of Michel et al. (2005) and Galluccio et al. (2008). An unsupervised approach has the advantage that no a priori information is taken into account to build the spectral groups.

The algorithm is based on a method for partitioning a set V of N data points ($V \in \mathbb{R}^L$), where L in our case is the number of spectral bands into K non-overlapping clusters (or groups of data points) such that (a) the intercluster variance is maximized and (b) the intracluster variance is minimized. Each spectrum is considered as a vertex of tree. A tree is a graph that is connected (i.e. every vertex is connected to at least another vertex) and acyclic (i.e. the graph has no loops). The minimum spanning tree (MST; i.e. the tree passing through each vertex of the set) with the minimal length is calculated using the so-called Prim's algorithm (see Galluccio et al. 2009, and references therein). The length of each edge of the tree (i.e. the distance between two spectra) is determined using the Kullback–Leibler metric: let $v_i = \{v_{i1}, \ldots, v_{iL}\}$ the feature vector corresponding to a reflectance spectrum (L being the number of wavelengths); at a given wavelength λ_j, each spectrum is associated with a (positive) normalized quantity: $\tilde{v_{ij}} = v_{ij} / \sum_{j=1}^{L} v_{ij}$, which can be interpreted as the probability distribution that a certain amount of information has been measured around the wavelength λ. To measure the similarity between two probability density functions, we compute the symmetrized Kullback–Leibler divergence:

$$d_{\mathrm{KL}}(v_i \,||\, v_k) = \sum_{j=1}^{L} (\tilde{v_{ij}} - \tilde{v}_{kj}) \log \frac{\tilde{v_{ij}}}{\tilde{v_{kj}}}.$$

The identification of the cluster is performed by first computing, at each step of the MST construction, the length of the newly connected edge and then by identifying valleys in the curve obtained by plotting the MST edge length as a function of the iteration of the construction (see Fig. 1). The valleys in this curve identify the number and the position of high-density region of points, i.e. the clusters (see Galluccio et al. 2009, for a more thorough description of the algorithm).

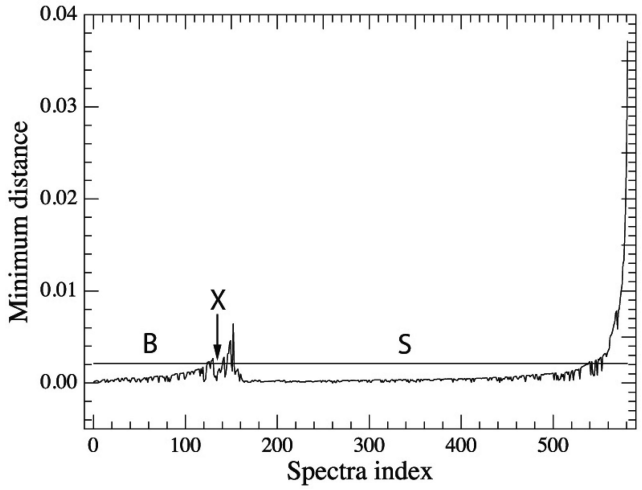

Figure 1. Minimum distance between spectra computed by the MST method as a function of the spectra index. The cut-off used to obtain the B, X and S groups was determined such as already classified asteroids belong to their appropriate group.

3.2 Spectral data

In order to increase the sample statistics compared to the relatively small number of asteroids observed by Cellino et al. (2001) and identify meaningful spectral groups within the Nysa-Polana family, we used our spectral classification algorithm on the observations contained in the SDSS MOC4 (http://www.sdss.org; Ivezic et al. 2002). The MOC4 contains magnitudes of 104 449 main belt asteroids. Each asteroid was observed, in general, at multiple epochs over five spectral bands in the visible light, namely u', g', r', i', z' at the following central wavelengths (λ) of 354, 477, 623, 763, 913 nm, respectively.

To obtain the surface reflectance of the asteroids, we needed to remove the solar contribution ($u_\odot$, $g_\odot$, $r_\odot$, $i_\odot$, $z_\odot$) to the observed magnitudes. The solar contribution is calculated from transformation equations between the SDSS $u'g'r'i'z'$ magnitudes and the usual $UBVR_cI_c$ system. We find $u_\odot = 6.55$, $g_\odot = 5.12$, $r_\odot = 4.68$, $i_\odot = 4.57$, $z_\odot = 4.54$ (see the SDSS website for more details: http://www.sdss.org). In order to compare asteroid spectral reflectances and be able to classify them, we chose to normalize each spectrum relatively to the r' band ($\lambda_{r'} = 623$ nm). Finally, we obtained the following asteroid reflectance for the $\lambda_{u'}$ wavelength:

$$F_{u'} = 10^{-0.4(C_{u'} - C_{r'})},$$

with

$$C_{u'} = u' - u_\odot \text{ and } C_{r'} = r' - r_\odot,$$

the reflectance colours at $\lambda_{u'}$ and $\lambda_{r'}$, respectively. The same computations were performed for the $\lambda_{g'}$, $\lambda_{i'}$ and $\lambda_{z'}$ wavelengths.

We searched in the MOC4 data base for all asteroids belonging to the Nysa-Polana family and for dispersed objects. Concerning the family members identification, we used the definition of dynamical families of Nesvorný (2010). Among the Nysa-Polana family, 4134 objects have been observed at least once by SDSS [as a comparison, the number of spectra obtained in the visible light or near-infrared, for the Nysa-Polana family, in the Main-belt Asteroid Spectroscopic Survey (SMASS), Eight-Color Asteroid Survey (ECAS) and 52-Color catalogues are 15, 13 and 2, respectively]. For those asteroids with more than one observation, we calculated the weighted mean reflectance by averaging the reflectancies derived at each epoch weighing each point with its respective signal-to-noise ratio.

However, likely due to non-photometric conditions some of the observed objects have high uncertainties in the measured magnitudes. In the visible light, the separation of asteroid spectroscopic group is based on the overall slope of their reflectance and in the presence (or absence) and strength of the 1 μm absorption feature. In order to avoid the superposition of spectral groups we selected asteroid with the less noisy observations. Namely, we rejected observations with a relative uncertainty >10 per cent on the in-band photometric flux derived from the MOC4 magnitudes. In the end, the taxonomic classification of the Nysa-Polana dynamical family was performed over 579 objects and over 2828 objects for the background at low inclination.

4 SPECTRAL ANALYSIS OF THE NYSA-POLANA FAMILY

4.1 Application of the spectral classification method

Fig. 1 shows the MST length as a function of the number of iterations (i.e. addition of spectra) in the case of the SDSS MOC4 spectrophotometric data of the 579 asteroids of the Nysa-Polana family. The figure clearly shows three main valleys corresponding to three groups composed of 118, 13 and 378 asteroids, respectively. The remaining objects (70) are considered as unclassified asteroids. This is due to their large value of the MST length which means no spectral similarity among the family is found for these 70 objects.

Fig. 2 shows asteroid spectra of each group and their average spectrum. Error bars are the 1σ standard deviation. We also compared the spectra of each spectral group of asteroids with the mean spectrum of different taxonomic classes from the Bus classification (http://smass.mit.edu/busdemeoclass.html). In each panel, we only plot the Bus mean spectra which present the closer similarity with the mean spectra of each group.

(i) For the first group (top panel of Fig. 2, 378 objects), we find that all spectra resemble the S-class mean spectra of Bus.

(ii) In the middle panel of Fig. 2, the 118 spectra of the second group fits with B-class asteroids (such as 142 Polana, for instance).

(iii) The bottom panel shows the third more populous group containing 13 asteroids. Comparing the spectra of this group and the mean spectrum of the X-class, X_c-class, X_k-class and X_e-class, we find that the third group of 13 objects corresponds to asteroids of the X-complex and its subclasses.

We note that groups (1) and (2) are consistent with the two main spectral classes found by Cellino et al. (2001). Moreover, the same authors had already identified the presence of asteroids with X-class spectral reflectances. They also noted that two of the largest asteroids, (44) Nysa and (135) Herta have spectra consistent with an X-class. As a consequence, we confirm their results using the SDSS MOC4 large sample of spectra.

In Fig. 3 we plot the asteroids of the three spectroscopic groups of the Nysa-Polana family as a function of a^* and $i' - z'$ (with $a^* = 0.89(g' - r') + 0.45(r' - i') - 0.57$). We show that the S-class group is well defined with $a^* \in [0; 0.25]$ and $i' - z' \in [-0.15; 0.08]$. The B-class region stretches from ~ -0.2 to ~ -0.06 for a^* and from -0.1 to 0.14 for $i' - z'$ and we find for the X-class

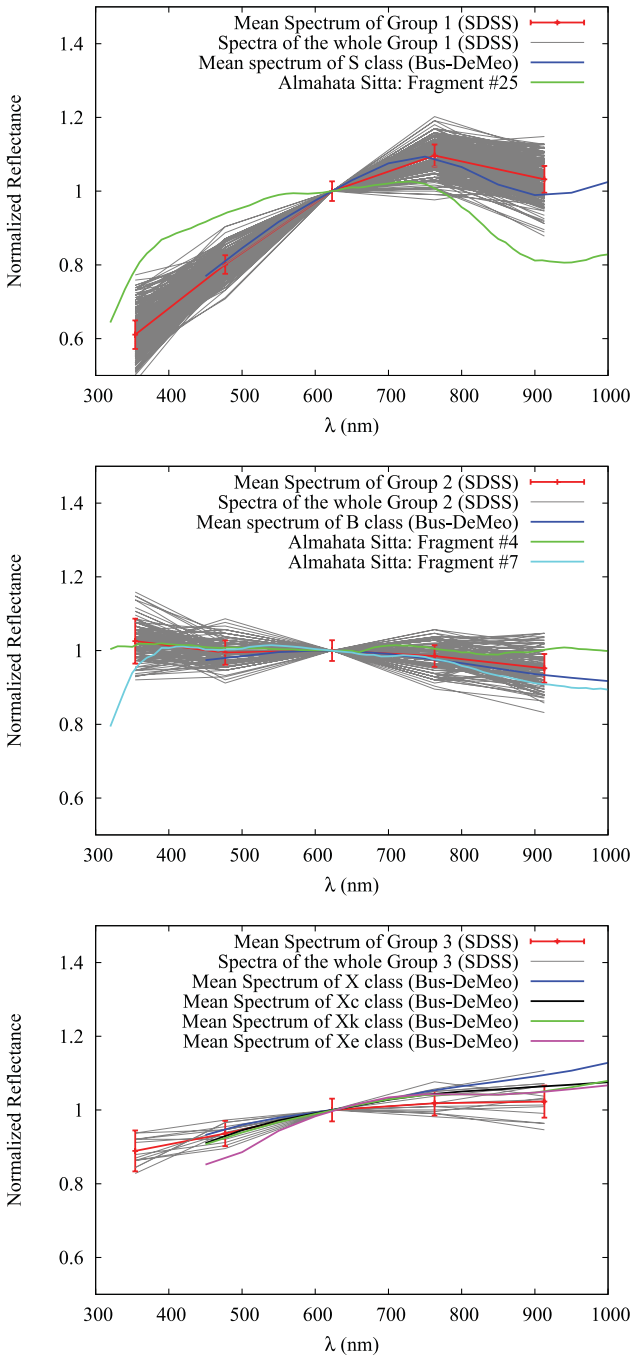

Figure 2. Panel (a), (b) and (c) represent the spectra for each group with their mean spectrum. A comparison with several spectra classes coming from the Bus taxonomy is also performed: Group 1 with S-class spectrum, Group 2 with B-class spectrum and Group 3 with X subclasses. We also find a good agreement with several Almahata Sitta fragments. Spectral differences with fragment #25 (H-chondrite) appearing in panel (a) are likely due to space weathering. Fragments #4 and #7 in panel (b) are ureilites.

region, $a^* \in [-0.1; -0.02]$ and $i' - z' \in [-0.02; 0.08]$. The colour palette used in Fig. 3 is that of Parker et al. (2008). Blue dots correspond to asteroids with neutral or slightly blue spectra (B-class), asteroids with neutral to slightly red spectra (X-class) are displayed in the plot with purple colours, while S-class asteroids are red to yellow.

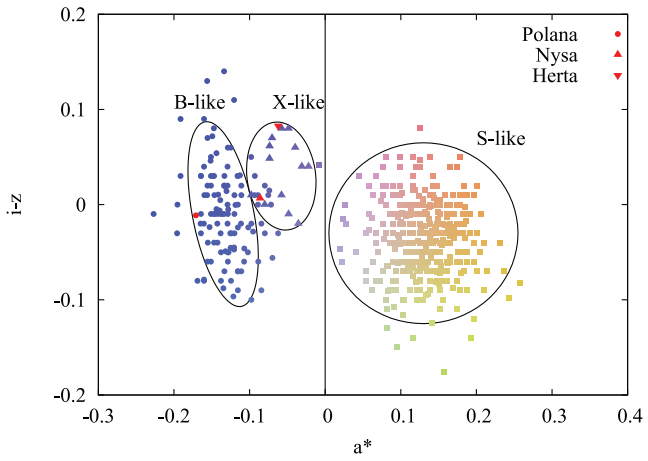

Figure 3. Distribution of S-class (■), B-class (●) and X-class (▲) objects of the Nysa-Polana family as a function of a^* and $i' - z'$ (calculated from SDSS magnitudes). Ellipses represent the location of S, B and X regions. The colour palette is the same of Parker et al. (2008). Although Polana (B), Nysa (X) and Herta (X) have not been observed by SDSS, we have calculated their a^* and $i' - z'$ values from the ECAS catalogue and located them in this plot.

4.2 Comparison with Almahata Sitta meteorites

It is very interesting to note that the three asteroid spectroscopic groups that we found in the Nysa-Polana family are likely to be the analogues of the different meteorite mineralogies found in Almahata Sitta. To strengthen this argument, we also compare – in Fig. 2 – the mean spectrum of each asteroid spectroscopic class of the Nysa-Polana family (S, B, X; red curves) with published spectra (from Hiroi et al. 2010) of some fragments of Almahata Sitta. We note that at the time of writing, spectra of E-chondrites from Almahata Sitta are not yet publicly available. So, comparisons between the classes of asteroids in the Nysa-Polana family and fragments of Almahata Sitta were performed for the S and B classes only. However, comparison of spectra of other E-chondrites (from the RELAB data base from Gaffey 1976) with the average spectrum of the Nysa-Polana X-class shows a good agreement.

Concerning the B class, we find that the mean spectrum of the Nysa-Polana B-class asteroids matches the spectra of the fragments #4 and #7 (ureilites) of Almahata Sitta. It is important to note that this spectral match was obtained only considering the visible wavelengths between about 350 and 900 nm. We remind that, from spectroscopic and albedo similarities, Jenniskens et al. (2009, 2010) have proposed a link between the B-class (or the F-class) and ureilite meteorites. An important caveat is that the link between B-class asteroids and the Almahata Sitta ureilites proposed by Jenniskens et al. (2009, 2010) is based on the noisy spectrum of TC$_3$. Moreover, B-class asteroids are more commonly associated with carbonaceous chondrites by several studies (see Clark et al. 2010, for a review about B-class objects, their meteorite analogues and their composition). However, a recent spectroscopic survey of B-class asteroids by De Leon et al. (2012) shows that the ensemble of the reflectance spectra of the 45 B-class asteroids analysed in their work have a continuous shape variation in the range between 500 and 2500 nm, from a monotonic negative (blue) slope to a positive (red) slope. De Leon et al. (2012) apply a clustering technique to reduce the ensemble of the spectra to six optimized averaged spectra or 'groups'. Interestingly the RELAB spectrum of the fragment #4 of Almahata Sitta shows a good match with the group #3

of De Leon et al. (2012) in the region between 500 and 2500 nm (De Leon, private communication).

Concerning the S-class, we show, in Fig. 2, that fragment #25 (an ordinary chondrite) is rather close to the S-class mean spectrum, as expected, but not in very good agreement (see e.g. the review of Chapman 2004, for spectroscopical links between ordinary chondrites and S-class asteroids). One possible explanation for this spectral mismatch is the space weathering of S-class asteroids. We discuss this possibility in the following subsection.

4.3 Space weathering of S-class members of the Nysa-Polana family

Space weathering is a physical process caused by cosmic rays, collisions, ion bombardment, that alters physical and spectral properties of the surface of atmosphereless planetary bodies. More particularly, due to space weathering, S-class asteroids become darker (their albedo is reduced), redder (the reflectance increases with increasing wavelength) and the depth of absorption bands are reduced. As a consequence, the spectral slope changes due to this process (Clark et al. 2002; Chapman 2004).

In Marchi et al. (2006), a strong relation was found between the spectral slope of S-class asteroids and their 'exposure' to space weathering. The exposure of an asteroid to space weathering corresponds to time integral the flux of solar ions that the body receives along its orbit. The exposure to space weathering depends on the age of the asteroid and its average distance from the Sun. Therefore, in order to know if space weathering affected S-class asteroids of the Nysa-Polana family, we calculate the exposure to space weathering of these bodies as shown in Marchi et al. (2006) and Paolicchi et al. (2007).

We compute the slope α of a SDSS spectrophotometric data by fitting a linear equation normalized to 1 at λ_r (623 nm) to the data points. To calculate the exposure, we need to estimate the average collisional age of main belt asteroids ($T_{\rm MBA}$), which can be constrained by the age of the belt ($t_{\rm LHB} \sim 4$ Gyr) and by collisional times ($\tau_{\rm coll}$):

$$T_{\rm MBA} \simeq \tau_{\rm coll}\left[1-\left(1+\frac{t_{\rm LHB}}{\tau_{\rm coll}}\right)\mathrm{e}^{-\frac{t_{\rm LHB}}{\tau_{\rm coll}}}\right]+t_{\rm LHB}\,\mathrm{e}^{-\frac{t_{\rm LHB}}{\tau_{\rm coll}}}.$$

According to Bottke et al. (2005), the collisional lifetime can be estimated as a function of asteroid diameter (using SDSS H absolute magnitudes and assuming an albedo of $\rho_V = 0.2$ for all S-class objects). In the end, we have

$$\text{exposure} \propto \frac{T_{\rm MBA}}{a^2\sqrt{1-e^2}},$$

with a and e the asteroid proper semimajor axis and eccentricity, respectively.

In Fig. 4, we plot both the spectral slope of Nysa-Polana S-class objects as a function of the exposure to space weathering and the best linear fit to this distribution. The two-tailed probability for the linear correlation is lower than 0.001 per cent which means the linear correlation is significant.[1] This shows that the spectral slope increases with the exposure.

Semimajor axes and eccentricities do not vary much within the Nysa-Polana family. As a consequence, the exposure variation mainly comes from asteroid diameter, through the computation of

[1] A linear fit is considered significant whenever the two-tail probability is lower then 5 per cent.

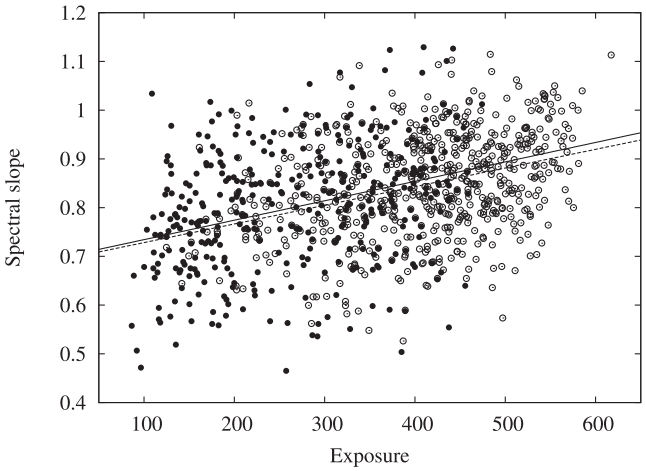

Figure 4. Spectral slope as a function of the exposure to space weathering of S-class objects of the Nysa-Polana family (black dots and black line) and S-class objects of the background at low inclination (circles and dashed line). As a comparison, the spectral slope of H-chondrites which are thought to come from S-class asteroids is of about 0.1–0.2.

$T_{\rm MBA}$. Hence, plotting the spectral slope as a function of the exposure, or $T_{\rm MBA}$, or asteroid diameters (d) provides quite similar figures (not shown here) – where the exposure increases with time or diameter – but with the following abscissa ranges: $0.5 < T_{\rm MBA} < 2.5$ Gyr or $1 < d < 6$ km.

The spectral slope increase with exposure or asteroid age is then the proof that space weathering occurs for S-class asteroids of the Nysa-Polana family. We also note that the spectral slope of the fragment #25 of Almahata Sitta has the value of 0.03.

As a consequence, the spectral mismatch between asteroids of the S-component of the Nysa-Polana family and the ordinary chondrites of Almahata Sitta – as observed in Fig. 2 – can be explained by space weathering.

5 ANALYSIS OF ASTEROIDS OF THE BACKGROUND AT LOW INCLINATION

As mentioned in Sections 1 and 2, the other possible origin source for TC_3, from a dynamical point of view, is the population of dispersed asteroids at low inclination. In the present section, we perform the same spectroscopic study as for the Nysa-Polana family (Section 4) but using objects of the background located in the inner main belt ($2.1 < a < 2.5$ au) with a proper inclination lower than 8°. Selecting the best observations of the SDSS MOC4 catalogue (i.e. observations with a relative uncertainty >10 per cent on the in-band photometric flux, corresponding to 2828 objects), we find four large groups of asteroids corresponding to the following spectral classes: B, C, X, S, as well as small clusters of Q, V and A-class asteroids. In addition, for the B, X and S groups of the background, we obtain mean spectra very similar to those of the Nysa-Polana family (not shown here). We also note that space weathering is also found for S-class asteroids of the background (see Fig. 4). As a consequence, the three ingredients required to form TC_3 (S-class asteroid/H-chondrite; B-class asteroid/ureilite; X-class asteroid/enstatite chondrite) are found in both the Nysa-Polana family and in the background at low inclination.

In our attempt to definitively conclude on the origin region of TC_3, we have compared the distribution of B-class asteroids for the two

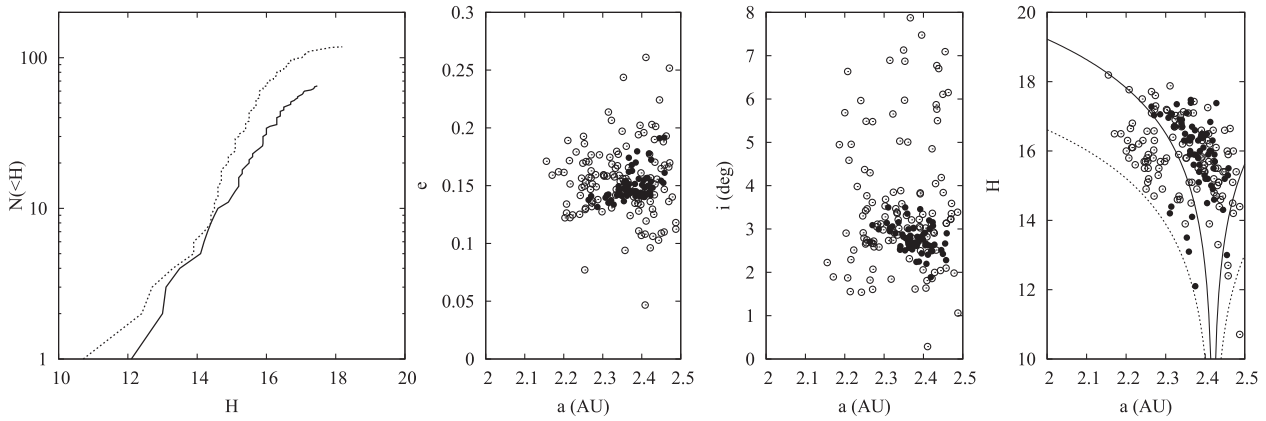

Figure 5. Plot 1: cumulative number of asteroid $N(<H)$ as a function of the H absolute magnitude for B-class asteroids of the Nysa-Polana family (black curve) and the background at low inclination ($i < 8^\circ$; dashed curve). Plots 2–4: distribution in eccentricity (plot 2), inclination (plot 3) and H absolute magnitude (plot 4) as a function of semimajor axis. Black points correspond to Polana B-class asteroids and black circles to B-class dispersed objects from the background at low inclination. Plot 4 shows the H-dependent semimajor axis distribution induced by the Yarkovsky effect that best fits the boundaries of the observed distribution for the Polana group (black curves) and for the background at low inclination (dashed curve).

source regions. In order to get a homogeneous selection of B-class asteroids both from the Nysa-Polana family and the background at low inclination, we have selected objects such as their spectra are similar to the B-class mean spectrum of the Nysa-Polana family, within the 1σ error bar. Although this selection reduces the size of the original B-class groups, we limit the overlap of classes (B and X classes can overlap; see Fig. 2).

From this selection, we plot in Fig. 5, the cumulative number of asteroids as a function of H absolute magnitude as well as the distribution in eccentricity, inclination and H magnitude as a function of semimajor axis. We find more B-class asteroids from the background at low inclination (dashed curve in the first plot of Fig. 5) than from the Polana group (black curve). As a consequence, the background at low inclination seems to dominate the Polana group, even if, around magnitude 17, the slope of the Polana group curve looks a little steeper than the curve for the background. In the other plots in orbital elements, we can see that the two regions overlap in some points and that B-class objects of the background are much more dispersed compared to Polana asteroids.

As in Campins et al. (2010), we also represent the absolute magnitude (H) a function of semimajor axis, both for the Polana group and the background (the plot of Campins et al. 2010 was done for the whole Nysa-Polana family). The plot appears to be V shaped which is a feature known to be associated both with the size-dependent ejection velocity field and with the drift in the proper semimajor axis induced by the Yarkovsky effect (e.g. Vokrouhlický et al. 2006). In the plot, the black curve shows the H-dependent semimajor axis distribution induced by the Yarkovsky effect that best fits the boundaries of the observed distribution for the Polana B-class asteroids. Objects below this curve are expected to be interlopers and may belong to the background. The extrapolated Yarkovsky-induced distribution predicts that the Polana group should reach the outer edge of the ν_6 resonance for objects with $H \sim 18$, which for a Polana-like albedo of $p_v = 5$ per cent translates into a diameter $D \sim 2$ km. This means that objects smaller than 2 km, such as TC$_3$, can easily escape the Polana group and the inner main belt.

Concerning the background at low inclination, different size limits can be computed due to a large variation of proper orbital inclinations. For an inclination of $\sim 0^\circ$, the ν_6 resonance boundary is found at $a \sim 2.1$ au, which gives us an H magnitude of ~ 16 and an asteroid diameter limit of $d \sim 4$ km. For the highest inclination ($i \sim 8^\circ$), we obtain $H \sim 14.5$ at $a \sim 2.2$ au, which is equivalent to a B-class asteroid ($p_v = 5$ per cent) of 8 km. As a result, the background at low inclination could have also delivered TC$_3$ through the ν_6 resonance.

Because the background at low inclination is not a dynamical family, its V-shaped structure in $H(a)$ was not especially expected. We then think that the background at low inclination could correspond to an old break-up of the Nysa-Polana family. As a consequence, we can conclude that TC$_3$ comes from the inner main belt, more particularly from the background at low inclination or the Nysa-Polana family, and that these two sources could be genetically linked.

6 POSSIBLE FORMATION SCENARIO OF 2008 TC$_3$

Meteorite strewn fields with fragments of different mineralogical types are very rare. Almahata Sitta and Kaidun (Ivanov et al. 1984) are probably the only known specimen. In the scenario that mixing occurs by a collisional process, the paucity of mineralogically mixed meteorites suggests that the process that formed Almahata Sitta, i.e. mixing the material between projectile and target is very rare; in most cases the projectile is pulverized and leaves negligible traces in the target (Melosh 1989).

It is unclear which conditions allow for mixing between projectile and target. Impact velocity is probably a key parameter. The average impact velocity between asteroids in the main belt is 4.4–5.3 km s^{-1} (Bottke et al. 1994). If projectile/target mixing were possible at these impact speeds, meteorites like Almahata Sitta would probably be frequent, which is not the case. Thus, we think that unusually low impact velocities are needed for mixing. This could prevent the target from pulverizing and could lead to macroscopic projectile fragments being implanted in the regolith of the impacted body or gravitationally bound to fragments of the target, if the latter is catastrophically disrupted by the impact. The fact that we give evidence that TC$_3$ comes from the Nysa-Polana family (see Section 4) or the background at low inclination (see Section 5), which are characterized by a mixing a taxonomic classes, also suggests that a specificity of the members of these families/regions may be unusually low collision velocities with projectiles that are also on low-inclination orbits.

For all these reasons we did a systematic search for projectiles that could hit Nysa-Polana family members or dispersed asteroids of the background at very low speeds. We did this search using the algorithm for the calculation of the intrinsic collision probability P_i between pairs of asteroids, described in Wetherill (1967). This algorithm, given the semimajor axis a, eccentricity e and inclination i of the two orbits (we use proper values for each pair of selected asteroids) assumes that the angles M, ω and Ω (mean anomaly, argument of perihelion and longitude of the ascending node) of the two objects have a uniform probability distribution over the range 0–2π; then it computes which fraction of these angles corresponds to the two objects being closer to each other than 1 km; finally, this fraction is translated into an intrinsic collision probability per year (P_i), using the orbital periods of the two objects and assuming that they are not in resonance with each other. For our goals, we modified this algorithm in order to take into account only orbital intersections corresponding to relative speeds smaller than 0.5 km s^{-1}. Admittedly, this velocity threshold is arbitrary. Given the exceptional character of Almahata Sitta, we need a threshold much smaller than the typical impact velocity among random asteroids, that is to say a subsonic impact velocity, in order to preserve the target.

Because most of Almahata Sitta fragments recovered are mainly made of ureilites, which we consider as analogues of B-class asteroids (as previously mentioned in Section 1 and according to Jenniskens et al. 2010), we assume that the favourite scenario for the formation of TC_3 involves a low-velocity collision of asteroids of X and S classes (projectiles) with a B-class member (target) of the Nysa-Polana family.

As for projectiles we considered all asteroids known in the Asteroid Orbital Elements Database (ASTORB) file (ftp://ftp.lowell.edu/pub/elgb/astorb.html) of the whole main belt and we computed the probability of collision of each asteroid with a B-class object near the centre of the B-class group of the Nysa-Polana family. Fig. 6 shows the region of orbital element space where impacts can occur (impact probability >0). This figure shows that asteroids included in the region of low-velocity impacts have different SDSS colours and thus different taxonomies. As a consequence, collisions involving B-, S- and X-class asteroids are likely to be possible.

In the end, depending on the location of the target within the Polana group, we find that projectiles come from one of the following families: (i) Nysa-Polana, (ii) Flora or (iii) Massalia, located in the inner main belt, or (iv) Hestia which is in the central main belt, very close to the 3:1 mean motion resonance with Jupiter. More particularly, for targets with a semimajor axis (a) smaller or equal than 2.3 au, the Flora family and objects of the background, very close to the Flora and Nysa-Polana family are the main source of projectiles; for targets with $2.3 < a < 2.4$ au and eccentricities larger than ∼0.15, projectiles in general are likely to come from the Nysa-Polana family; for targets with $2.3 < a < 2.4$ au and eccentricities smaller than ∼0.15, projectiles are likely to come from the Massalia family; for targets with $a \geq 2.4$ au projectiles come from the Hestia family. Similar results are found when studying collisions involving B-class asteroids of the background at low inclination.

Once identified the region of potential impactors, we proceeded to estimate the likelihood and the frequency of impacts, which depend on the sizes, number density of asteroids and average impact probability in the region. The average impact probability in the region was derived by averaging the intrinsic impact probabilities (one of the output of our algorithm) of the asteroids in the region; we found $P_i = 3 \times 10^{-19}$ impacts km^{-2} yr^{-1}.

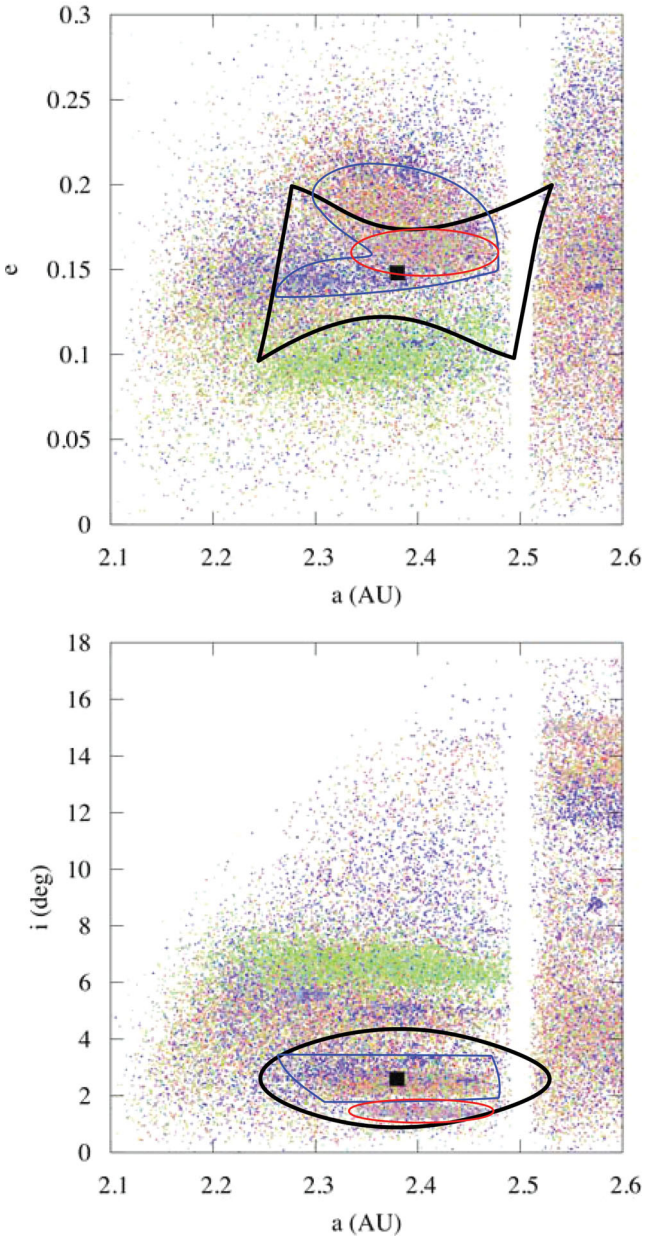

Figure 6. Distribution of proper orbital element for asteroids of the inner main belt: semimajor axes and eccentricities (top panel) or inclinations (bottom panel). For an asteroid target (black square), the region of orbital element space where impactors can come from is plotted in black. The location of the Nysa-Polana and Massalia families are, respectively, represented in blue and red. The colour palette corresponds to the Parker's colour distribution as mentioned in Parker et al. (2008) and depends on the value of a^* and $i' - z'$, with $a^* = 0.89(g' - r') + 0.45(r' - i') - 0.57$, g', r', i', z' corresponding to SDSS magnitudes at the following central wavelengths: 477, 623, 763 and 913 nm, respectively. Bluer dots ($a^* \in [-0.25; 0]$ and $i' - z' \in [-0.2; 0.2]$) are related to dark objects while yellow to red colours ($a^* \in [0; 0.25]$ and $i' - z' \in [-0.2; 0.2]$) gather brighter objects (see Fig. 3 for more details). Data come from the SDSS MOC4.

First of all, we estimated the number of impacts and the size of the impactors hitting TC_3 during its collisional lifetime assuming a diameter of 4 m (given by its H value of 30.9, Jenniskens et al. 2009, and assuming a geometric visible albedo of 0.05). The impact probability per projectile for TC_3 is given by $P_p = R^2 \tau_{coll} P_i$, with R the radius of TC_3 and τ_{coll} its collisional lifetime estimated from

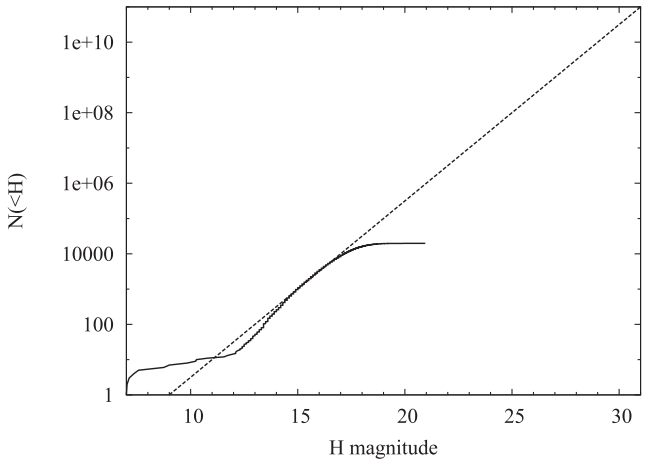

Figure 7. SFD of the asteroid population in the impact region. The SFD is plotted in terms of the cumulative number of asteroid as function of their absolute magnitude (H).

Marchi et al. (2006) ($\tau_{\rm coll} = 16.2$ Myr). As a consequence, we find that TC$_3$ has an impact probability per projectile of the order of 2×10^{-17} during its collisional lifetime.

To obtain the number of impacts on TC$_3$ during its collisional lifetime, we estimated the number of projectiles by calculating the size frequency distribution (SFD) of the population of the asteroids in the impact region and extrapolating the corresponding function to asteroid sizes below the detection limit of current discovery surveys. Fig. 7 shows the SFD in terms of the cumulative number of asteroid as function of their absolute magnitude (H). We used H values from the ASTORB file. In order to extrapolate the SFD asteroid sizes below the current detection limits, we calculated the equation of the straight line that best fits the base-10 logarithm of the known SFD and that is compatible with the SFD of the whole main belt (see Bottke et al. 2002) (see Fig. 7). The line has equation $y = \alpha H + \beta$, where y is the $\log_{10}(N(>H))$ 10-base logarithm of the cumulative number of asteroids with H smaller or equal than a threshold value. The best-fitting values for α and β are 0.5 and -4.5, respectively, implying about 10^4 asteroids with $H < 17$, 10^6 objects with $H < 21$, 10^9 with $H < 27$ and 10^{11} with $H < 31$, if the linear extrapolation is assumed to be valid. We can deduce that for $H < 31$, we obtain only $\sim 10^{-6}$ impacts with TC$_3$. In the end, one impact at $v \leq 0.5\,{\rm km\,s^{-1}}$ during TC$_3$ collisional lifetime would require $1/P_{\rm p}$ objects (i.e. 5×10^{16} objects). Using the SFD equation, this means we need a collision with an object of magnitude $H \sim 42$. This corresponds to the size of a pebble of 2.4 cm of diameter. Clearly the contamination brought by low-speed impacts is very small (the volume ratio between TC$_3$ and the pebble is 1.1×10^{-7}) and certainly not at the level of 20–30 per cent as implied by the number of chondrites found amongst the ureilites of the Almahata Sitta meteorites.

Much more likely, TC$_3$ was a fragment of a larger asteroid that was liberated by an impact near the ν_6 resonance few millions years ago. In fact, we note that (1) the dynamical time to deliver asteroids from the ν_6 resonance to orbits similar to that of TC$_3$ is of the order of 19 Myr (see Campins et al. 2010, for 1999 RQ$_{36}$ coming from the Polana region); (2) the cosmic ray exposure age of Almahata Sitta meteorites is of 19.5 ± 2.5 Myr (Welten et al. 2010); as a consequence, TC$_3$ spent most of its life as a single asteroid travelling from the ν_6 resonance to the orbit that brought it to impact the Earth.

It makes sense to investigate what was the contamination brought by low-velocity impacts on the parent body of TC$_3$. The average impact probability implies that we have $\sim 1.4 \times 10^{-9}$ impacts km^{-2} over the age of the Solar system, which correspond to one impact of an asteroid of $H \sim 27$ taking into account the SFD of the objects in the region. The diameter of an asteroid with $H = 27$ is between 10 and 25 m depending on the albedo. Again the level of contamination is very little, of the order of 1×10^{-5}.

When we take into account the necessity of mixing meteorites of at least three different mineralogies, we conclude that the formation of TC$_3$ by means of low-velocity collisions is not a realistic scenario.

7 CONCLUSION

From our study, it seems that the Nysa-Polana family and the background at low inclination are good candidates for the origin of 2008 TC$_3$ and Almahata Sitta. First of all, as mentioned in Section 2, the Nysa-Polana family is located close to the ν_6 secular resonance which is the favourite route leading to primitive NEOs and more particularly to asteroid 2008 TC$_3$. Moreover, the proper inclination of the Nysa-Polana family is very similar to that of TC$_3$, which should have been maintained during the transfer of TC$_3$ to the NEOs region through the ν_6 secular resonance. We also know, from our algorithm of spectral classification (Section 3), that the Nysa-Polana family gathers the three spectral classes (S, B and X), which are proposed analogues to Almahata Sitta fragments (Section 4) under the hypothesis that ureilites are linked to B-class asteroids. More specifically, (1) the mean spectrum of B-class asteroids of the Nysa-Polana family is spectrally matched – at least in the visible – with available spectra of ureilitic fragments of Almahata Sitta, (2) considering space-weathering effects, the mean spectrum of S-class asteroids of the Nysa-Polana family is compatible with the spectrum of the H-chondrite fragment #25, (3) a good agreement is found between X-class asteroids and enstatite chondrites from other meteorite falls (we remind that enstatite chondrites are part of Almahata Sitta). Of course, a comparison with enstatite chondrites from Almahata Sitta fragments would be very useful to get a definitive match between the Nysa-Polana family and Almahata Sitta. In Section 5, the same kind of work was performed for objects of the inner main belt coming from the background at low inclination ($i < 8^\circ$). We concluded that these dispersed asteroids could also be at the origin of TC$_3$.

In Section 6, we tried to explain the formation of TC$_3$ by low-velocity impacts (below $0.5\,{\rm km\,s^{-1}}$) between different mineralogies in the neighbourhood of and within the Nysa-Polana family. Selecting TC$_3$ as the target asteroid ($d = 4$ m), we find a probability per projectile about 10^{-17} impacts during its collisional lifetime (i.e. in 16.2 Myr). As a consequence, impacts at low velocity are extremely rare and there is little chance that TC3 was formed by low-velocity impacts in the current asteroid belt. This implies that the heterogeneous composition of the parent body of TC$_3$ has to be inherited from a time when the asteroid belt was in a different dynamical state, most likely in the very early Solar system. One could think that an asteroid of ureilite composition was contaminated by impactors of different nature when the asteroid belt was still massive and dynamically cold, so that mutual collisions were frequent and at low velocity. However, this view is probably simplistic. In fact, a body of ureilite composition needs to be formed in the interior of a large carbonaceous asteroid which underwent significant thermal alteration (Singletary & Grove 2003). This asteroid needs to have undergone a collisional disruption to expose the ureilite material in

space. The same is true for the bodies of Hn composition, with n larger than 3 (Gopel, Manhes & Allegre 1993). But collisional disruptions require large relative velocities, in contrast with the view of a dynamically cold belt. Thus, the asteroid belt could not be overall dynamically cold when the parent body of TC_3 formed.

These considerations suggest that, conversely to what is usually thought, accretion and collisional erosion had to co-exist for some time in the asteroid belt. For this to be possible, presumably there had to be still a significant amount of gas in the system so that, although large asteroids could be on dynamically excited orbits, the orbit of their small fragments were rapidly re-circularized by gas drag. Consequently, the mutual relative velocities of these fragments were small and a new phase of accretion was possible for them.

We remark that the heterogeneity of TC_3 is not at the microscopic level; each of the meteorites delivered to the ground are of a distinct class. Thus, TC_3 seems to be an agglomeration of meteorite-sized (i.e. few dm) pebbles of different nature. Pebbles of this size are strongly coupled with the gas and are extremely sensitive to pressure gradients. They play the key role in the new models of planetesimal formations, based on the concentration of dm-size pebbles in the eddies of a turbulent disc and on the process of streaming instability (Johansen et al. 2007; Johansen, Youdin & Mac Low 2009). These models of planetesimal formation in a turbulent disc seem a priori to be particularly favourable to explain the coexistence of collisional erosion and accretion. Large planetesimals are formed by the concentration of a large number of pebbles, forming self-gravitating clumps. Once formed, the orbits of these large planetesimals are rapidly excited by the stochastic gravitational perturbations exerted by the turbulent disc (Ida, Guillot & Morbidelli 2008; Morbidelli et al. 2009). If the threshold for collisional break-up is achieved, the pebble-size fragments of these large bodies are re-injected into the game: by being concentrated into new eddies they can give origin to new large planetesimals and so forth. Admittedly, quantitative work is needed to support this scenario; also, other more classical planetesimal formation mechanism in presence of gas drag (Wetherill & Stewart 1993; Kenyon & Bromley 2004; Weidenschilling 2011) might explain the co-existence of erosion and accretion as well.

In this respect, it will be important to understand from the observational point of view if macroscopic heterogeneity as that of TC_3 is the exception or the rule among asteroids. TC_3 is the first object of this kind that has ever been observed, but it is also the first fall of an asteroid on Earth documented live and for which an extensive and exhaustive search for meteorites has been done. So, it might not be as rare as one could be tempted to believe. Indeed, a second similar case has just been reported (Spurný, Haloda & Borovicka 2012). Now that the possibility for macroscopic heterogeneity is recognized, careful investigations (also conducted by remote sensing techniques) may reveal additional interesting cases. Understanding which fraction of the asteroids is of primary or secondary accretion will be a fundamental step to constrain the asteroid formation and evolution models.

ACKNOWLEDGMENTS

We thank O. Michel and P. Bendjoya for providing us their method of classification as well as A. Cellino, P. Tanga, M. Müller, H. Campins, B. Carry and P. Vernazza for helpful discussions. Programming tools made available to us by the *Gaia* Data Processing Analysis Consortium (DPAC) have been used within this work. JG-M is also grateful to the Centre National d'Etudes Spatiales (CNES) for financial support.

REFERENCES

Binzel R. P., Xu S., 1993, Sci, 260, 186
Bischoff A., Horstmann M., Pack A., Laubenstein M., Haberer S., 2010, Meteoritics Planet. Sci., 45, 1638
Bottke W. F., Nolan M. C., Greenberg R., Kolvoord R. A., 1994, Icarus, 107, 255
Bottke W. F., Morbidelli A., Jedicke R., Petit J.-M., Levison H. F., Michel P., Metcalfe T. S., 2002, Icarus, 156, 399
Bottke W. F., Durda D. D., Nesvorný D., Jedicke R., Morbidelli A., Vokrouhlicky D., Levison H., 2005, Icarus, 175, 111
Bus S. J., Binzel R. P., 2002, Icarus, 158, 146
Campins H., Morbidelli A., Tsiganis K., de León J., Licandro J., Lauretta D., 2010, ApJ, 721, L53
Cellino A., Zappalà V., Doressoundiram A., di Martino M., Bendjoya P., Dotto E., Migliorini F., 2001, Icarus, 152, 225
Chapman C. R., 2004, Annu. Rev. Earth Planet. Sci., 32, 539
Clark B. E., Hapke B., Pieters C., Britt D., 2002, in Bottke W. F., Cellino A., Paolicchi P., Binzel R. P., eds, Asteroids III. Univ. Arizona Press, Tucson, p. 585
Clark B. E. et al., 2010, J. Geophys. Res. (Planets), 115, 6005
Cloutis E. A., Hudon P., Romanek C. S., Bishop J. L., Reddy V., Gaffey M. J., Hardersen P. S., 2010, Meteoritics Planet. Sci., 45, 1668
De Leon J., Pinilla Alonso N., Licandro J., Campins H., Marzo G. A., 2012, Icarus, 218, 196
Gaffey M. J., 1976, J. Geophys. Res., 81, 905
Gaffey M. J., Burbine T. H., Piatek J. L., Reed K. L., Chaky D. A., Bell J. F., Brown R. H., 1993, Icarus, 106, 573
Galluccio L., Michel O., Bendjoya P., Slezak E., 2008, in AIP Conf. Ser. Vol. 1082, Classification and Discovery in Large Astronomical Surveys. Am. Inst. Phys., New York, p. 165
Galluccio L., Michel O., Comon P., Slezak E., Hero A. O., 2009, Technical Report I3S/RR-2009-08FR, CNRS and Nice-Sophia Antipolis University, France
Gopel C., Manhes G., Allegre C. J., 1993, Meteoritics, 28, 354
Hiroi T., Jenniskens P., Bishop J. L., Shatir T. S. M., Kudoda A. M., Shaddad M. H., 2010, Meteoritics Planet. Sci., 45, 1836
Horstmann M., Bischoff A., Pack A., Laubenstein M., 2010, Meteoritics Planet. Sci., 45, 1657
Ida S., Guillot T., Morbidelli A., 2008, ApJ, 686, 1292
Ivanov A. V., Ulyanov A. A., Skripnic A. Y., Konokona N. N., 1984, Lunar Planet. Inst. Sci. Conf. Abstr., 15, 393
Ivezić Ž., Jurić M., Lupton R. H., Tabachnik S., Quinn T., 2002, in Tyson J. A., Wolff S., eds, Proc. SPIE Vol. 4836, Survey and Other Telescope Technologies and Discoveries. SPIE, Bellingham
Jenniskens P. et al., 2009, Nat, 458, 485
Jenniskens P. et al., 2010, Meteoritics Planet. Sci., 45, 1590
Johansen A., Oishi J. S., MacLow M. M., Klahr H., Henning T., Youdin A., 2007, Nat, 448, 1022
Johansen A., Youdin A., Mac Low M.-M., 2009, ApJ, 704, L75
Jordi C. et al., 2010, A&A, 523, A48
Kenyon S. J., Bromley B. C., 2004, AJ, 127, 513
Marchi S., Paolicchi P., Lazzarin M., Magrin S., 2006, AJ, 131, 1138
Meibom A., Clark B. E., 1999, Meteoritics Planet. Sci., 34, 7
Melosh H. J., 1989, Impact Cratering: A Geologic Process. Oxford Univ. Press, Oxford
Michel O., Bendjoya P., Rojo Guerra P., 2005, Traitement du signal et des images. UCL Presses Universitaires, de Louvain, p. 257
Mignard F. et al., 2007, Earth Moon Planets, 101, 97
Morbidelli A., Nesvorny D., 1999, Icarus, 139, 295
Morbidelli A., Bottke W. F., Jr, Froeschlé C., Michel P., 2002, in Bottke W. F., Cellino A., Paolicchi P., Binzel R. P., eds, Asteroids III. Univ. Arizona Press, Tucson, p. 409
Morbidelli A., Bottke W. F., Nesvorný D., Levison H. F., 2009, Icarus, 204, 558
Nesvorný D., 2010, Nesvorný HCM Asteroid Families V1.0. EAR-A-VARGBDET-5-NESVORNYFAM-V1.0. NASA Planetary Data System

Nesvorný D., Vokrouhlický D., Morbidelli A., Bottke W. F., 2009, Icarus, 200, 698
Paolicchi P., Marchi S., Nesvorný D., Magrin S., Lazzarin M., 2007, A&A, 464, 1139
Parker A., Ivezić Ž., Jurić M., Lupton R., Sekora M. D., Kowalski A., 2008, Icarus, 198, 138
Shaddad M. H. et al., 2010, Meteoritics Planet. Sci., 45, 1557
Singletary S. J., Grove T. L., 2003, Meteoritics Planet. Sci., 38, 95
Spurný P., Haloda J., Borovicka J., 2012, Mistery of the Benesov Bolide Revealed after 20 Years. LPI Contributions (Asteroids, Comets, Meteors Meeting)
Tholen D. J., 1984, PhD thesis, Arizona Univ.
Vernazza P., Binzel R. P., Thomas C. A., DeMeo F. E., Bus S. J., Rivkin A. S., Tokunaga A. T., 2008, Nat, 454, 858
Vokrouhlický D., Brož M., Bottke W. F., Nesvorný D., Morbidelli A., 2006, Icarus, 182, 118
Walsh K. J., Delbo M., Muller M., Binzel R. P., De Meo F., 2012, ApJ, 748, 104
Weidenschilling S. J., 2011, Icarus, 214, 671
Welten K. C. et al., 2010, Meteoritics Planet. Sci., 45, 1728
Wetherill G. W., 1967, J. Geophys. Res., 72, 2429
Wetherill G. W., Stewart G. R., 1993, Icarus, 106, 190

This paper has been typeset from a TEX/LATEX file prepared by the author.

Available online at www.sciencedirect.com
ScienceDirect
Icarus 190 (2007) 236–249
ICARUS
www.elsevier.com/locate/icarus

Thermal inertia of near-Earth asteroids and implications for the magnitude of the Yarkovsky effect

Marco Delbo' [a,b,*], Aldo dell'Oro [a], Alan W. Harris [c], Stefano Mottola [c], Michael Mueller [c]

[a] *INAF – Oss. Astron. di Torino, via Osservatorio 20, 10025 Pino Torinese (TO), Italy*
[b] *Laboratoire Cassiopée, Observatoire de la Côte d'Azur, B.P. 4229, 06034 Nice Cedex 4, France*
[c] *DLR Institute of Planetary Research, Rutherfordstrasse 2, 12489 Berlin, Germany*

Received 26 November 2006; revised 2 March 2007

Available online 30 March 2007

Abstract

Thermal inertia determines the temperature distribution over the surface of an asteroid and therefore governs the magnitude the Yarkovsky effect. The latter causes gradual drifting of the orbits of km-sized asteroids and plays an important role in the delivery of near-Earth asteroids (NEAs) from the main belt and in the dynamical spreading of asteroid families. At present, very little is known about the thermal inertia of asteroids in the km size range. Here we show that the average thermal inertia of a sample of NEAs in the km-size range is $200 \pm 40\ \mathrm{J\,m^{-2}\,s^{-0.5}\,K^{-1}}$. Furthermore, we identify a trend of increasing thermal inertia with decreasing asteroid diameter, D. This indicates that the dependence of the drift rate of the orbital semimajor axis on the size of asteroids due to the Yarkovsky effect is a more complex function than the generally adopted D^{-1} dependence, and that the size distribution of objects injected by Yarkovsky-driven orbital mobility into the NEA source regions is less skewed to smaller sizes than generally assumed. We discuss how this fact may help to explain the small difference in the slope of the size distribution of km-sized NEAs and main-belt asteroids.

Keywords: Asteroids; Near-Earth objects; Infrared observations; Photometry; Asteroids, dynamics

1. Introduction

Observations of asteroids in the wavelength range of their thermal-infrared emission (>5 μm) have been used since the 1970s (Allen, 1970) to determine the sizes and the albedos of these bodies. In recent years, thanks to the advances in detector technology and the availability of 10-m class telescopes on the ground, thermal-infrared observations of asteroids have improved in sensitivity. Increased efforts have consequently been devoted to deriving the sizes and albedos of near-Earth asteroids (NEAs; for reviews see Harris and Lagerros, 2002; Delbo' and Harris, 2002; Delbo', 2004; Harris, 2006 and references therein), in order to better assess the impact hazard these bodies pose to our planet and to improve our understanding of their relation to main-belt asteroids and comets (see Stuart and Binzel, 2004; Morbidelli et al., 2002). Furthermore, improvements in spectral coverage and the possibility of easily obtaining spectrophotometric data through narrow-band filters in the range 5–20 μm have allowed information on the surface temperatures of asteroids to be obtained. The spectrum of the thermal-infrared radiation received from a body is related to the temperature distribution on that part of its surface visible to the observer. Several factors play a role in determining the temperature distribution on the surface of an asteroid, such as the heliocentric distance, albedo, obliquity of the spin vector, rotation rate, and a number of thermal properties of the surface such as its thermal inertia.

Thermal inertia is a measure of the resistance of a material to temperature change. It is defined as $\Gamma = \sqrt{\rho\kappa c}$, where κ is the thermal conductivity, ρ the density and c the specific heat capacity. The thermal inertia of an asteroid depends on regolith particle size and depth, degree of compaction, and exposure of solid rocks and boulders within the top few centimeters of the subsurface (see, e.g., Mellon et al., 2000). At the limit of zero thermal inertia (the most simple temperature distribution model

* Corresponding author. Fax: +33 (0) 4 9200 3121.
E-mail address: delbo@obs-nice.fr (M. Delbo').

0019-1035/$ – see front matter
doi:10.1016/j.icarus.2007.03.007

for asteroids), a body with a smooth surface would display a temperature distribution which depends only on the solar incidence angle i (on a sphere, i is also the angular distance of a point from the subsolar point):

$$T = \begin{cases} T_{SS} \cos^{1/4} i, & i \leqslant \pi/2, \\ 0, & i > \pi/2. \end{cases} \quad (1)$$

The subsolar temperature, T_{SS}, is determined by equating the total energy absorbed by a surface element to that emitted in the thermal infrared, i.e.

$$\frac{S_\odot (1 - A)}{r^2} = \eta \sigma \varepsilon T_{SS}^4, \quad (2)$$

where A is the bolometric Bond albedo, $S_\odot$ is the solar constant, r is the heliocentric distance of the body, ε is the infrared emissivity, σ is the Stefan–Boltzmann constant and η is the so-called "beaming parameter," which is equal to one in the case that each point of the surface is in instantaneous thermal equilibrium with solar radiation. The surface temperature distribution that one obtains for $\eta = 1$ on a spherical surface is that of the so-called Standard Thermal Model (STM; Lebofsky and Spencer, 1989) that was widely used to derive diameters and albedos especially of main-belt asteroids (MBAs). In the more realistic case of a body with finite thermal inertia and rotating with a spin vector not pointing toward the sun, the temperature distribution is no longer symmetric with respect to the subsolar point: each surface element behaves like a capacitor or sink for the solar energy such that the body's diurnal temperature profile becomes more smoothed out in longitude (see Spencer et al., 1989; Delbo' and Harris, 2002; Delbo', 2004). The hottest temperatures during the day decrease, whereas those on the night-side do not drop to zero as in the idealistic case of zero thermal inertia, implying non-zero thermal-infrared emission from the dark side of the body.

However, the effect of thermal inertia is coupled with the rotation rate of the body. An asteroid rotating slowly with a high thermal inertia displays a similar temperature distribution to one rotating more rapidly but with a lower thermal inertia. The degree to which the surface of an asteroid can respond to changes in insolation can be characterized by a single parameter: this is the so-called thermal parameter Θ (e.g., Spencer et al., 1989), which combines rotation period, P, thermal inertia, Γ, and subsolar surface temperature, T_{SS}, and consequently depends on the heliocentric distance of the body. The thermal parameter is given by

$$\Theta = \frac{\Gamma}{\varepsilon \sigma T_{SS}^3} \sqrt{\frac{2\pi}{P}}. \quad (3)$$

Note that objects with the same value of Θ, although with different P or Γ, display the same diurnal temperature profile, provided they have the same shape and spin axis obliquity (the angle formed by the object spin vector and the direction to the Sun). In the case of non-zero thermal inertia, because the temperature distribution is no longer symmetric with respect to the direction to the Sun, the momentum carried off by the photons emitted in the thermal infrared has a component along the orbital velocity vector of the body, causing a decrease or increase of the asteroid orbital energy depending on whether the rotation sense of the body is prograde or retrograde. This phenomenon, known as the Yarkovsky effect (see Bottke et al., 2002), causes a secular variation of the semimajor axis of the orbits of asteroids on a time scale of the order of 10^{-4} AU/Myr for a main-belt asteroid at 2.5 AU from the Sun with a diameter of 1 km. The Yarkovsky effect is responsible for the slow but continuous transport of small asteroids and meteoroids from the zone of their formation into chaotic resonance regions that can deliver them to near-Earth space (Bottke et al., 2002; Morbidelli and Vokrouhlický, 2003). The Yarkovsky effect also offers an explanation for the spreading of asteroid dynamical families (Bottke et al., 2001, 2006; Nesvorný and Bottke, 2004). Moreover, the emission of thermal photons also produces a net torque that alters the spin vector of small bodies in two ways: it accelerates or decelerates the spin rate and also changes the direction of the spin axis. This mechanism was named by Rubincam (2000) as the Yarkovsky–O'Keefe–Radzievskii–Paddack effect, or YORP for short.

Knowledge of the thermal inertia of asteroids is thus important for a number of reasons: (a) It can be used to infer the presence or absence of loose material on the surface: thermal inertia of fine dust is very low: $\sim 30\ \mathrm{J\,m^{-2}\,s^{-0.5}\,K^{-1}}$ (Putzig et al., 2005); lunar regolith, a layer of fragmentary incoherent rocky debris covering the surface of the Moon, also has a low thermal inertia of about $50\ \mathrm{J\,m^{-2}\,s^{-0.5}\,K^{-1}}$ (Spencer et al., 1989). Coarse sand has a higher thermal inertia, i.e., about $400\ \mathrm{J\,m^{-2}\,s^{-0.5}\,K^{-1}}$ (Mellon et al., 2000; Christensen, 2003), that of bare rock is larger than $2500\ \mathrm{J\,m^{-2}\,s^{-0.5}\,K^{-1}}$ (Jakosky, 1986), whereas the thermal inertia of metal rich asteroidal fragments can be larger than $12{,}000\ \mathrm{J\,m^{-2}\,s^{-0.5}\,K^{-1}}$ (Farinella et al., 1998; Table 1). (b) Thermal inertia is the key thermophysical parameter that determines the temperature distribution over the surface of an asteroid and therefore governs the magnitude of the Yarkovsky and YORP effects (Capek and Vokrouhlický, 2004). (c) It allows a better determination of systematic errors in diameters and albedos derived using simple thermal models, which make assumptions about the surface temperature distribution and/or neglect the thermal-infrared flux from the non-illuminated fraction of the body (see Spencer et al., 1989; Delbo', 2004; Harris, 2006). However, at present, very little is known about the thermal inertia of asteroids in general, especially in the case of bodies in the km size range.

The thermal inertia of an asteroid can be derived by comparing measurements of its thermal-infrared emission to synthetic fluxes generated by means of a thermophysical model (TPM; Spencer, 1990; Lagerros, 1996; Emery et al., 1998; Delbo', 2004), which is used to calculate the temperature distribution over the body's surface as a function of a number of parameters, including the thermal inertia Γ. In these models, the asteroid shape is modeled as a mesh of planar facets. The temperature of each facet is determined by numerically solving the one-dimensional heat diffusion equation using assumed values of the thermal inertia, with the boundary condition given by the time-dependent solar energy absorbed at the surface of the facet (see Delbo', 2004). This latter quantity is calculated from

Table 1
Near-Earth asteroids with η-values derived from spectral fitting to multi-wavelength mid-infrared observations

Asteroid		D (km)	p_V	A	η	r (AU)	α (°)	P (h)	Obs. date	Spin axis	Ref.
433	Eros	23.60	0.200	0.079	1.05	1.135	10	5.27	17-01-1975	Y	a
433	Eros	23.60	0.210	0.082	1.07	1.619	31	5.27	29-06-1998	Y	a
1580	Betulia	3.82	0.110	0.043	1.09	1.199	53	6.138	22-06-2002	Y	b
1862	Apollo	1.40	0.260	0.102	1.15	1.063	35	3.065	26-11-1980	–	c
1866	Sisyphus	8.90	0.140	0.055	1.14	1.609	35	2.4	29-06-1998	–	d
1980	Tezcatlipoca	6.60	0.150	0.059	1.64	1.129	63	7.252	31-08-1997	Y	a
2100	Ra-Shalom	2.79	0.080	0.031	2.32	1.174	39	19.8	21-08-2000	Y	e
2100	Ra-Shalom	2.50	0.130	0.051	1.80	1.195	41	19.8	30-08-1997	Y	f
3200	Phaethon	5.10	0.110	0.043	1.60	1.132	48	3.604	20-12-1984	–	c
3554	Amun	2.10	0.170	0.067	1.20	1.243	16	2.53	15-03-1986	–	c
3671	Dionysus	1.50	0.160	0.063	3.10	1.126	58	2.705	02-06-1997	–	a
5381	Sekhmet	1.50	0.220	0.086	1.90	1.213	44	3	22-06-2003	–	d
5381	Sekhmet	1.40	0.240	0.094	1.50	1.119	35	3	14-05-2003	–	d
5587	1990 SB	4.00	0.250	0.098	1.10	1.399	19	5.052	09-04-2001	Y	d
5587	1990 SB	3.57	0.320	0.126	0.84	1.210	42	5.052	10-05-2001	Y	e
6455	1992 HE	3.43	0.280	0.110	0.80	1.641	22	– -	22-03-2002	–	g
6455	1992 HE	3.55	0.240	0.094	0.70	1.364	29	–	29-09-2002	–	g
9856	1991 EE	1.00	0.300	0.118	1.15	1.093	36	3.045	11-09-1991	–	f
14402	1991 DB	0.60	0.140	0.055	1.04	1.025	36	2.266	16-04-2000	–	e
19356	1997 GH_3	0.91	0.340	0.133	0.98	1.406	5	6.714	11-05-2001	–	e
25330	1999 KV_4	2.55	0.080	0.031	1.06	1.392	3	4.919	14-05-2003	–	d
25330	1999 KV_4	2.70	0.080	0.031	1.30	1.495	16	4.919	02-06-2003	–	d
25330	1999 KV_4	3.21	0.050	0.020	1.50	1.197	54	4.919	10-05-2001	–	e
33342	1998 WT_{24}	0.34	0.590	0.232	0.90	0.990	67	3.697	18-12-2001	–	d
33342	1998 WT_{24}	0.44	0.350	0.137	1.50	0.987	79	3.697	19-12-2001	–	d
33342	1998 WT_{24}	0.50	0.270	0.106	1.85	0.981	93	3.697	21-12-2001	–	d
35396	1997 XF_{11}	0.89	0.320	0.126	1.30	1.215	30	3.257	28-11-2002	–	d
35396	1997 XF_{11}	0.91	0.310	0.122	1.20	1.018	53	3.257	03-11-2002	–	d
35396	1997 XF_{11}	1.18	0.180	0.071	1.80	1.034	63	3.257	05-11-2002	–	d
53789	2000 ED_{104}	1.20	0.180	0.071	1.68	1.089	60	–	29-09-2002	–	g
85953	1999 FK_{21}	0.59	0.320	0.126	0.91	1.140	35	–	21-02-2002	–	e
86039	1999 NC_{43}	2.22	0.140	0.055	2.86	1.116	59	34.49	17-03-2000	–	e
99935	2002 AV_4	1.50	0.370	0.145	1.60	1.086	70	–	01-06-2003	–	d
	1999 HF_1	4.74	0.110	0.043	1.68	0.957	91	–	22-03-2002	–	g
	2000 BG_{19}	1.77	0.040	0.016	0.74	1.388	17	–	17-03-2000	–	e
	2001 LF	2.00	0.050	0.020	1.40	1.172	45	–	02-06-2003	–	d
	2002 BM_{26}	0.84	0.020	0.008	3.10	1.023	60	–	21-02-2002	–	e
	2002 HK_{12}	0.80	0.170	0.067	2.84	1.138	33	–	28-09-2002	–	g
	2002 NX_{18}	2.40	0.030	0.012	1.19	1.158	54	–	29-09-2002	–	g
	2002 QE_{15}	1.94	0.150	0.059	1.53	1.131	62	–	28-09-2002	–	g
	2003 YT_1	1.50	0.270	0.106	1.92	1.035	74	–	08-05-2004	–	d

Note. The object effective diameter, D, the geometric visible albedo p_V, and the η-values have been derived by using the NEATM. α is the phase angle at the epoch of the observations, which is given in the "Obs. date" column. P is the rotation period in hours. In the column "Spin axis" a "Y" indicates that the spin axis orientation of the asteroid is known. In the column "Ref." we give the original publication reference: (a) Harris and Davies (1999); (b) Harris et al. (2005); (c) Harris (1998); (d) Delbo' (2004); (e) Delbo' et al. (2003); (f) Harris et al. (1998); (g) Wolters et al. (2005).

the heliocentric distance of the asteroid, the value assumed for the albedo, and the solar incident angle. Macroscopic surface roughness is usually modeled by adding hemispherical section craters of variable opening angle and variable surface density to each facet. Shadowing and multiple reflections of incident solar and thermally emitted radiation inside craters are taken into account as described by Spencer (1990), Emery et al. (1998), and Delbo' (2004). Heat conduction is also accounted for within craters (Spencer et al., 1989; Spencer, 1990; Lagerros, 1996; Delbo', 2004). Surface roughness can be adjusted by changing the opening angle of the craters, the density of the crater distribution, or a combination of both. However, Emery et al. (1998) have shown that if surface roughness is measured in terms of the mean surface slope, $\bar{\theta}$, according to the parameterization introduced by Hapke (1984), emission spectra are a function of $\bar{\theta}$ only and not of the crater opening angle and crater surface density. We recall here that

$$\tan\bar{\theta} = \int_0^{\pi/2} a(\theta)\tan\theta\,\mathrm{d}\theta, \tag{4}$$

where θ is the angle of a given facet from the horizontal, and $a(\theta)$ is the distribution of surface slopes. The total observable thermal emission is calculated by summing the contributions from each facet visible to the observer. Model parameters (e.g., Γ, A, $\bar{\theta}$) are adjusted until the best agreement is obtained with the observational data, i.e., the least-squares residual of the fit, χ^2, is minimized, thereby constraining the physical properties

(albedo, size, macroscopic roughness, and thermal inertia) of the asteroid.

To date, TPMs have been used to derive the thermal inertia of seven large MBAs (Müller and Lagerros, 1998; Müller and Blommaert, 2004; Mueller et al., 2006), and five NEAs (Harris et al., 2005, 2007; Müller et al., 2005; Mueller et al., 2007); values derived lie between 5 and ∼1000 J m^{-2} s$^{-0.5}$ K^{-1}, i.e., Γ varies by more than two orders of magnitude. The applicability of TPMs is limited to the few asteroids for which gross shape, rotation period, and spin axis orientation are known. Multi-epoch observations are also required for obtaining a robust estimation of the thermal properties of asteroids via TPM fit.

There is, however, an extensive set of thermal-infrared observations of NEAs in the km size range for which no TPM fit is possible (e.g., Veeder et al., 1989; Harris, 1998; Harris et al., 1998; Harris and Davies, 1999; Delbo' et al., 2003; Delbo', 2004; Wolters et al., 2005). In order to overcome this limitation, we have developed a statistical inversion method, described in Section 2, enabling the determination of the average value of the thermal inertia of NEAs in the km-size range. Our approach is based on the fact that, even though shapes, rotation periods, and spin axis orientations are not known for every NEA, the distribution of these quantities for the whole population can be inferred from published data (La Spina et al., 2004; Hahn, 2006).

In Section 3 we compare the result from our statistical inversion method with the values of the thermal inertias of asteroids determined by means of thermophysical models, and we identify a trend of increasing thermal inertia with decreasing asteroid diameter, D.

In Section 4 we describe the implications of the trend of increasing thermal inertia with decreasing asteroid diameter, in particular for the size dependence of the Yarkovsky effect and the size distribution of NEAs and MBAs.

2. Determination of the mean thermal inertia of NEAs

The large majority of asteroids for which we have thermal-infrared observations have been observed at a single epoch and/or information about their gross shape and pole orientation is not available, precluding the use of TPMs. In these cases simpler thermal models such as the near-Earth asteroid thermal model (NEATM; Harris, 1998) are used to derive the sizes and the albedos of these objects. The NEATM assumes that the object has a spherical shape, and its surface temperature distribution is described by Eqs. (1) and (2). However, the parameter η is not kept constant, as in the case of the STM, but is adjusted in the fitting procedure to allow the model spectral energy distribution to match the observed data. In order to derive a robust estimate of the η-value the NEATM requires observations at different, ideally well-spaced, wavelengths in the thermal infrared. The parameter η can be seen as a measure of the departure of the asteroid temperature distribution from that of the STM and is a strong function of the surface thermal inertia (Spencer et al., 1989; Harris, 1998; Delbo', 2004). However, η depends also on parameters such as the macroscopic surface roughness, $\bar{\theta}$, the rotation period, P, the bolometric Bond albedo, A, the thermal-infrared emissivity, ε, the heliocentric distance, r, the gross shape of the body, $\mathbb{S}$, the sub-solar latitude, θ_{SS}, the longitude, ϕ_{SE}, and the latitude, θ_{SE}, of the sub-Earth point (Delbo', 2004). In general we can write that

$$\eta \equiv \eta\big(\varepsilon, A, r, \Theta(\Gamma, P), \bar{\theta}, \theta_{SS}, \theta_{SE}, \phi_{SE}, \mathbb{S}\big). \tag{5}$$

These parameters are usually not known for the individual objects, but their distributions can be estimated (or reasonably assumed) for the entire population. Note that a set of θ_{SS}, ϕ_{SE}, and θ_{SE}, which depend on the ecliptic longitude λ_0 and latitude β_0 of the pole of the body, is also related to the value of the solar phase angle, α.

Delbo' et al. (2003) noted that qualitative information about the average thermal properties of a sample of NEAs could be obtained from the distribution of the η-values of the sample as a function of the phase angle, α. In particular, the absence of large η-values (e.g., $\eta > 2$) at small or moderate phase angles (e.g., $\leqslant 45°$), and the fact that η tends to ∼0.8 for α approaching 0°, was interpreted in terms of the NEAs having low thermal inertias in general. In subsequent work (Delbo', 2004) it was found that for a synthetic population of spherical asteroids with constant values of A, r, Γ, P, and $\bar{\theta}$, but with pole directions randomly oriented, the distribution of the points in the (α, η) plane is strongly dependent on Γ. By varying Γ until the distribution of the synthetic points in the (α, η) plane matched the one derived from the observations, Delbo' (2004) obtained a best-fit thermal inertia for the NEAs equal to ∼500 J m^{-2} s$^{-0.5}$ K^{-1}. Harris (2006), using a similar method on a larger database of η-values and neglecting the effects of surface roughness ($\bar{\theta} = 0°$), derived a best-fit thermal inertia of ∼300 J m^{-2} s$^{-0.5}$ K^{-1}.

Here we improve on the above-mentioned work by determining the mean thermal inertia of NEAs using a rigorous statistical inversion method, based on the comparison of the distributions of NEATM η-values from the current NEA database vs α, with that of a synthetic population of asteroids generated through a TPM, using realistic distributions of the input parameters P, θ_{SS}, θ_{SE}, ϕ_{SE}, and A derived from the literature [see Table 1 with published η-values from Harris (1998), Harris et al. (1998), Harris and Davies (1999), Delbo' et al. (2003), Delbo' (2004), and Wolters et al. (2005). La Spina et al. (2004) give the distribution of λ_0 and β_0 for NEAs, and Hahn (2006) that of NEA rotation rates]. In the following section we describe our method in detail.

2.1. Model parameter space

As a first step we studied the dependence of η on the relevant parameters of Eq. (5). This was done by choosing typical parameter values and showing how small perturbations of the assumed values affect η. For the purpose of this analysis we assume $A_0 = 0.073$, $r_0 = 1.2$ AU (as we will show below, these are the average values of A and r for the NEAs in our sample), $\bar{\theta}_0 = 36°$ (the value derived for 433 Eros; Domingue et al., 2002), $\mathbb{S}_0$ = sphere, and $\Theta_0 = 1.0$. Note that $\Theta_0 = 1.0$ corresponds to a thermal inertia of ∼200 J m^{-2} s$^{-0.5}$ K^{-1} for surface temperatures typical of NEAs and $P = 6$ h, a rotation

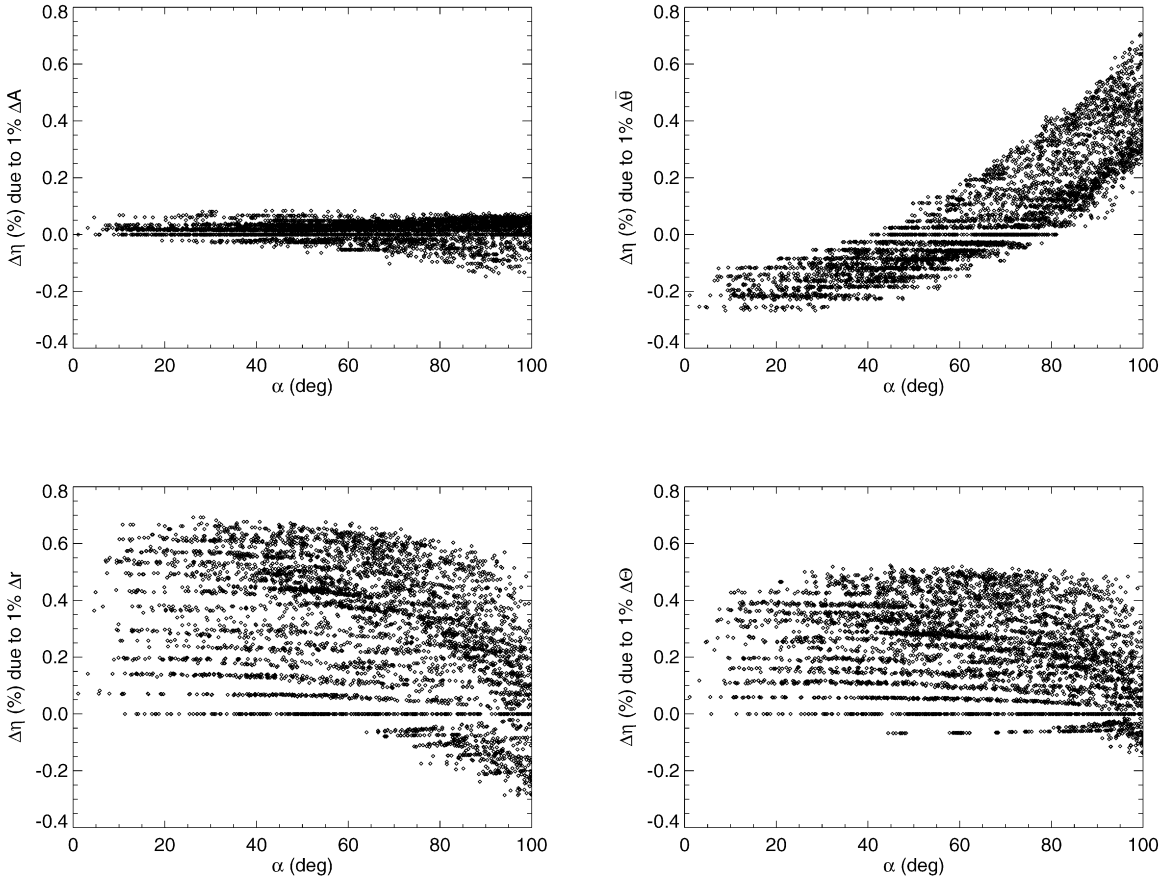

Fig. 1. Sensitivity of η to model parameter variations. $\Delta\eta/\eta$ (%) caused by a change of 1% in the bolometric Bond albedo A (upper left), macroscopic surface roughness $\bar{\theta}_0$ (upper right), heliocentric distance r (lower left), and the thermal parameter Θ (lower right). See text, Section 2.1 for details.

period representative of asteroids with sizes between ∼0.15 and 10 km (Pravec et al., 2002). We will show in Section 2.3 that $\Gamma = 200\ \mathrm{J\,m^{-2}\,s^{-0.5}\,K^{-1}}$ is the mean thermal inertia of NEAs. The illumination and observation geometry was varied such that θ_{SS} was uniformly distributed in the range between 0 and $\pi/2$ and θ_{SE}, ϕ_{SE} were varied in such a manner that the resulting sub-Earth vectors were uniformly distributed over the celestial sphere. The values of θ_{SE}, ϕ_{SE} were further subject to the constraint that the phase angle be $\leqslant 100°$. Fig. 1 shows the sensitivity of η to a change in the model parameters. In particular, for each value of θ_{SS}, θ_{SE}, and ϕ_{SE}, the variation of η due to a 1% change in each parameter is plotted. We have also calculated, for some fixed illumination and observation geometries (e.g., $\theta_{\mathrm{SE}} = 0°$, $\phi_{\mathrm{SE}} = 45°$, and $\theta_{\mathrm{SS}} = 0°$), how the variations $\Delta\eta$ scale with changes in the model parameters. We found that $\Delta\eta$ is proportional to ΔA, $\Delta\bar{\theta}_0$, $\Delta\Theta$, and Δr within a large range of variation (>100%) of each parameter from its nominal value. Because for common asteroidal material the thermal-infrared emissivity is thought to be relatively constant, it has been fixed for this study at $\varepsilon = 0.9$. It is appropriate for objects with surfaces that emit a substantial portion of their thermal-infrared radiation shortward of 8 μm (Lim et al., 2005; Salisbury et al., 1991). Mustard and Hays (1997) have also shown that the reflectances of fine-grained particulate materials, thought to be representative of planetary regoliths, have values around 0.1 and in general smaller than 0.2 in the region 8–24 μm. Because the reflectance, R, and the emissivity are related by Kirchhoff's law ($R = 1 - \varepsilon$), the measurements cited above imply that $\varepsilon = 0.9$ is a reasonable estimate for the thermal-infrared emissivity of NEA surfaces. Moreover, from Eq. (2) one can calculate that $\Delta\eta \approx 1.6\Delta\varepsilon$ for $\varepsilon \approx 0.9$ and $\eta \approx 1.5$ (the average η for the NEAs for which this parameter was derived from observations; see Table 1). This implies that variations of ε in the range 0.8–1.0 cause changes of η that are within the typical uncertainty of ∼20% in the estimation of η from observations. Note that the value of $\Delta\eta/\eta = 20\%$, where $\Delta\eta$ is the uncertainty in η, is based on the reproducibility of η for those objects for which more than one measurement is available from independent data sets. Moreover, 20% is also the mean value of $\Delta\eta/\eta$ of the "Delbo' Thermal Infrared Asteroid Diameters and Albedos" database at the NASA PDS (Delbo', 2006). In this dataset for those observations where $\Delta\eta$ is present, its value was formally calculated from the measurements of the asteroids' thermal infrared fluxes.

The vast majority of the observations in our sample was obtained at a phase angle smaller than 80°, and within this range, Fig. 1 shows that the largest variation of η caused by a 1% change of A (the bolometric Bond albedo) is approximately 0.1%. Because the mean value of A for our sample is $\langle A\rangle = 0.073$ and the standard deviation is 0.04 (see Table 1), the variation of η due to the distribution of the albedos is smaller than 5% and thus small compared to the typical uncertainty of

$\Delta\eta/\eta \sim 20\%$. For this reason we have utilized a constant value of 0.073 for A in our statistical inversion method.

Moreover, the variation of η due to a 1% change in the macroscopic surface roughness is strongly phase angle dependent, but in general smaller than 0.2% for α in the range 0–60°. This implies that even a $\pm 100\%$ change in $\bar{\theta}$ causes a variation of η within the typical 20% uncertainty. Note that a $\pm 100\%$ change in $\bar{\theta}$ corresponds to a large variation of the macroscopic roughness, ranging from that of a completely smooth surface to one oversaturated by hemispherical craters. For those observations carried out at $\alpha > 60°$, η is more sensitive to variations of $\bar{\theta}$. For the reasons above we have treated $\bar{\theta}$ as a free parameter in the inversion method and searched for the value that best fits the observational data.

The sensitivity of η to changes of the objects' heliocentric distances is such that a 1% change of r corresponds to a maximum 0.7% change of η. As calculated for the values in Table 1, the heliocentric distances in our sample have a mean value of 1.2 AU and a standard deviation of 0.1 AU (∼8%). The corresponding variation of η is approximately 6% and therefore small. We thus took a constant value of 1.2 AU for r in our statistical inversion method. Only in two cases, namely those of the 29-06-1998 observation of (433) Eros and for the 22-03-2002 observation of (6455) 1992 HE is the variation of η due to the deviation of the heliocentric distance from the nominal value of 1.2 AU slightly larger than the error bars.

We note here that Eq. (5) implicitly contains the assumption that seasonal effects do not affect asteroid surface temperatures. However, when $\Theta \neq 0$, asteroid temperatures always depend on the previous thermal history of the surface. Since NEAs have in general large orbital eccentricities, these bodies experience large variations of insolation as a function of their orbital position, which may lead to a seasonal component of the variation of their surface temperatures and thus of the corresponding η-values. To demonstrate that our working hypothesis of Eq. (5) is valid (i.e., seasonal components are negligible), we calculated η for several synthetic asteroids with the same physical characteristics, but with different orbits, in order to explore the effect of different levels of insolation. Orbits were chosen with eccentricities in the range 0 to 0.8 but with a common perihelion distance r_p. For different values of the asteroid thermal inertia in the range 200–5000 $\mathrm{J\,m^{-2}\,s^{-0.5}\,K^{-1}}$ and r_p in the range 0.5–1.5 AU, we found variations of only a few percent in the η-values calculated at r_p. This leads us to conclude that seasonal variations in the η-values are small and that Eq. (5) is valid.

In general NEAs have elongated shapes, which may cause their surface temperature distributions to differ from that of a spherical object with the same surface properties and illumination geometry. We studied the sensitivity of η to deviations from the spherical shape by calculating η-values of tri-axial ellipsoids, the semiaxes of which were varied in the ratio $a/(\sqrt{a}/1)$ with $1 \leqslant a \leqslant 6$, assuming $A_0 = 0.073$, $r_0 = 1.2$ AU, $\bar{\theta}_0 = 36°$, $\Theta_0 = 1.0$, and for random orientations of the shape with respect to the Sun and the Earth. We found that the distribution of $\Delta\eta$ is a function of a (with values of $\Delta\eta$ increasing with increasing a), where $\Delta\eta$ is the deviation of η from that calculated using a sphere under the same illumination and viewing geometry. However, the relative error in η, $\Delta\eta/\eta$, is always smaller than $\pm 10\%$ for $a \leqslant 5$ and $\alpha \leqslant 45°$. For $\alpha > 45°$, the mean value of the relative error, $\langle \Delta\eta/\eta \rangle$, is smaller than $+15\%$ and its standard deviation, $\sigma_{\Delta\eta/\eta}$, is smaller than 5% for $a \leqslant 5$. Because the maximum lightcurve amplitude of our model ellipsoid is $L \approx 1.25 \log a$ mag, $\Delta\eta/\eta$ is smaller than 20% if $L \leqslant 0.873$ mag. This condition is in general satisfied for the NEAs in Table 1, for which the average value of L is around 0.6 mag.

We expect that the contributions to $\Delta\eta$ due to variations of the model parameters A, r, $\bar{\theta}$, and the ellipsoid axial ratio a, stack up randomly, since deviations of these parameters from their mean values are fully uncorrelated (e.g., there is no apparent reason that an NEA with an albedo higher than the average is also observed at an heliocentric distance higher than the average value). We performed some numerical experiments in order to cross check this assumption and found that the value of $\Delta\eta$ is in general a good approximation of $[(\partial\eta/\partial A \Delta A)^2 + (\partial\eta/\partial r\,\Delta r)^2 + (\partial\eta/\partial\bar{\theta}\,\Delta\bar{\theta})^2]^{1/2}$. Adding the effect of non-spherical shapes increases the value of $\Delta\eta$, but never systematically at phase angles $< \sim 60°$. It is clear that ellipsoids are highly idealized shapes and larger contributions to $\Delta\eta$ may be expected in the case of real NEAs.

Fig. 1 shows that the sensitivity of η to changes in the thermal parameter is very similar to the sensitivity to changes in r, with variations of η in general no larger than 0.5% for a 1% change of Θ. However, while the value of r for the asteroids in Table 1 is rather constant around the mean value of 1.2 AU, Θ can range between 0.1 and 20 considering that thermal inertia can be anywhere between 10 $\mathrm{J\,m^{-2}\,s^{-0.5}\,K^{-1}}$ (the thermal inertia of large main-belt asteroids) and 2500 $\mathrm{J\,m^{-2}\,s^{-0.5}\,K^{-1}}$ (that of bare rock). This implies that the scatter in the η-values that we observe in the NEAs of Table 1 is mainly a function of α and Θ, which depends on the thermal inertia. If we assume the thermal inertia to be roughly constant within the NEA population for a given size, its value can be inferred from the distribution of the measured η-values versus α. This is the idea on which our statistical inversion method is based.

2.2. Model populations

Our inversion method requires η to be computed for all members of a synthetic population of NEAs as a function of Γ. The calculation of η was performed by numerically generating thermal-infrared spectra by means of a TPM and fitting them with the NEATM. As discussed in the previous sections, the parameters A, ε, r, $\bar{\theta}$, and $\mathbb{S}$ contribute little to the variation of η within the expected parameter ranges. Therefore, they have been kept fixed to their nominal values throughout the modeling process. In order to keep the amount of computing time required for the inversion within reasonable limits, the values of η have been computed only once for all possible combinations of the remaining parameters, and the results have been stored in a four-dimensional look up table. The granularity of the look up table was chosen to be small enough to cause changes of η of about 0.1 between two consecutive parameter steps.

For each value of Γ, we then generated a large number (30,000) of synthetic objects whose parameters have random

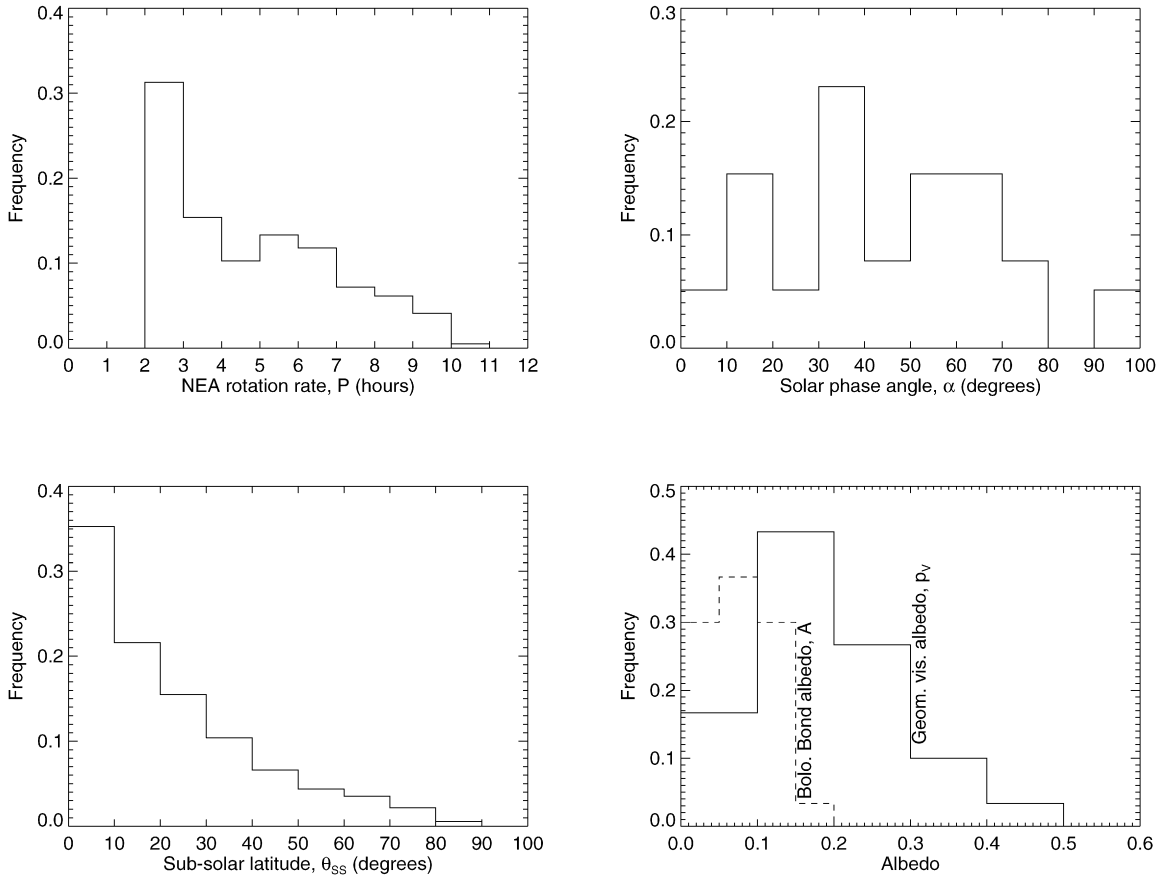

Fig. 2. Distribution of the input parameters used in our statistical inversion method. Upper left: distributions of NEA rotation rates from "Physical parameters of NEOs" (Hahn, 2006; http://earn.dlr.de). Upper right: distribution of NEA phase angles. Lower left: distribution of NEA sub-solar latitudes θ_{SS}. Lower right, solid line: distribution of the geometric albedos (p_V) and, dashed line: the bolometric Bond albedos (A) for the asteroids of Table 1 having η-values determined from observations.

values with distributions that have been chosen to provide a reasonable match to the observed population of NEAs. In particular:

(i) the distributions of the angles θ_{SS}, θ_{SE}, and ϕ_{SE} were computed starting from the distributions of the spin-axis orientation (λ_0, β_0) from La Spina et al. (2004), the phase angle α, the heliocentric ecliptic latitude β_H, and the geocentric ecliptic latitude β_E of the asteroids at the time of the infrared observations (see Table 1 and Fig. 2);
(ii) the distribution of the thermal parameter was calculated starting from the distribution of the NEA rotation periods (Hahn, 2006) and by using a constant value of Γ.

In Fig. 3 three such populations are shown that correspond to the Γ values of 15 (green), 200 (red), and 1000 (blue) $\mathrm{J\,m^{-2}\,s^{-0.5}\,K^{-1}}$, respectively. We have superimposed the η-values for the NEAs in Table 1 on the synthetic data plot.

2.3. Best-fit procedure

Fig. 3 gives a clear visual impression of the dependence of η on Γ. We therefore used a formal best-fit technique to estimate the value of Γ for which a synthetic population best fits the observed data, under the assumption that Γ is constant for all objects in the observed sample. The method that we used to compare the observed data with the bi-dimensional distributions of the synthetic points in the (α, η) plane is based on the two-dimensional Kolmogorov–Smirnov metric (K–S; Press et al., 1992). The distance D of the K–S metric is used as the goodness of fit estimator (Press et al., 1992). Our best-fit procedure consisted of finding the value of Γ that minimizes the K–S distance D. From here on, we indicate this value with the symbol Γ^*. Fig. 4, where we have plotted the K–S distance D as a function of Γ, shows that the function $D(\Gamma)$ has a minimum at $\Gamma = 200\ \mathrm{J\,m^{-2}\,s^{-0.5}\,K^{-1}}$, which is the value of thermal inertia that we take for Γ^*.

We expect Γ^* to depend upon the assumed value for $\bar{\theta}$, the distributions of NEA rotation rates, and also on the spin-axis orientations that we have used to produce the distribution of the input parameters θ_{SS}, θ_{SE}, and ϕ_{SE}. Moreover, the value of Γ^* must be affected by the errors in the measurements of the thermal-infrared fluxes, i.e., by the errors on the η-values taken from the literature. In order to study the sensitivity of Γ^* to changes applied to the nominal values of the input parameters, we first varied $\bar{\theta}$ in the range between 0° (perfectly smooth surface) and 58° (corresponding to the surface completely covered by hemispherical craters). Fig. 4 shows the function $D(\Gamma)$ for

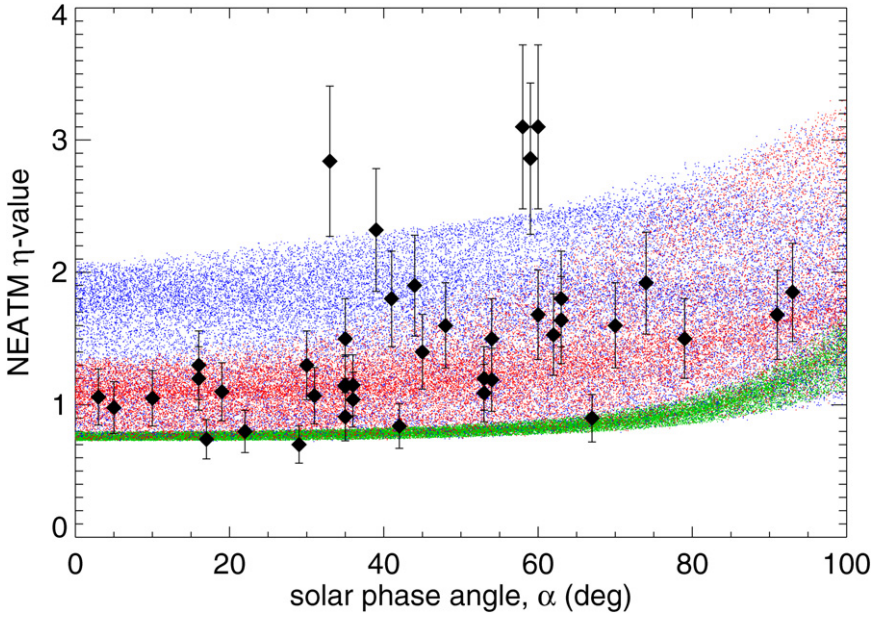

Fig. 3. Dependence of η-value on phase angle, α. Black diamonds: η-values derived from the NEATM for a set of NEAs with adequate multi-filter photometric data to enable η to be derived via spectral fitting (the data set includes multiple values of η for some objects observed at more than one phase angle; for the original data sources see Table 1). The error bars represent a 20% uncertainty, which is based on the reproducibility of η for those objects for which more than one measurement is available from independent data sets. Colored points: distributions of (α, η) calculated by means of our model for different values of thermal inertia: i.e., 15 (green), 200 (red), and 1000 (blue) J m^{-2} s$^{-0.5}$ K^{-1}. The distribution of the measured η-values is best described by the red points.

three different values of $\bar{\theta}$. It clearly demonstrates that the value of Γ^* only weakly depends on $\bar{\theta}$ and that a high degree of surface roughness produces a better fit to the observed data.

We also investigated the sensitivity of Γ^* to changes in the input distributions of asteroids' spin-axis orientations and rotation rates. Fig. 4 shows the function $D(\Gamma)$ obtained by using random spin-axis orientations uniformly distributed over the sphere instead of the nominal distribution. In that case, the best-fit thermal inertia increases to 250 J m^{-2} s$^{-0.5}$ K^{-1}, and to 230 J m^{-2} s$^{-0.5}$ K^{-1} if the distribution of the rotation rates are assumed to be uniformly distributed between 4 and 10 h, a case which we believe to be very extreme.

The sensitivity of Γ^* to the errors affecting the η-values from Table 1 was studied by performing extended Monte Carlo simulations, in which we randomly varied the values of the η-values within their error bars (using normally distributed random numbers), and for each simulation of noise-corrupted data we calculated the best-fit thermal inertia. The standard deviation of Γ^* was found to be 40 J m^{-2} s$^{-0.5}$ K^{-1}.

Of course, we expect that the distribution of the data points in Fig. 3 derives from a population with a range of thermal inertias, and further investigation is required to understand what the relations are between Γ^* and the parameters defining the population, such as the mean value of Γ and the standard deviation of its distribution. In order to answer this question, we applied our inversion method on (α, η) points obtained from synthetic populations of NEAs with known distributions of thermal inertia. We used random values of Γ uniformly and normally distributed, varying both the mean value and the standard deviation of the populations. We found that our fitting procedure, based on the minimization of the K–S distance D, is capable of retrieving a good estimate of the mean value for Γ of the populations in all cases. We conclude that the average value of the thermal inertia for km-sized NEAs is 200 ± 40 J m^{-2} s$^{-0.5}$ K^{-1}, which is about four times that of the lunar soil and corresponds to a surface thermal conductivity of $0.027^{+0.015}_{-0.010}$ W m^{-1} K^{-1} assuming that the surface material density and specific heat capacity are in the range 1500–3500 kg m^{-3} and 500–680 J kg^{-1} K^{-1}, respectively (Britt et al., 2002; Farinella et al., 1998).

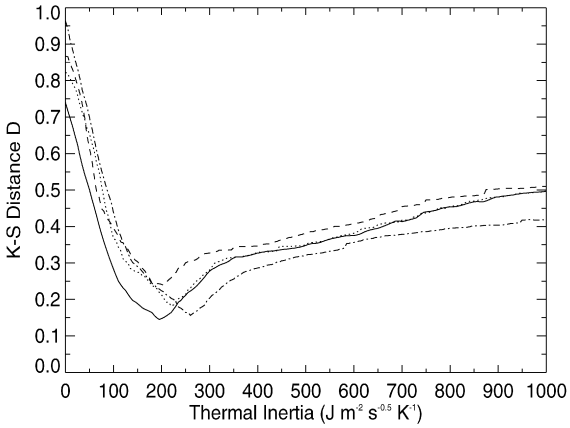

Fig. 4. Plot of the function $D(\Gamma)$, i.e., the distance D of the two-dimensional Kolmogorov–Smirnov best-fit procedure against the thermal inertia Γ. The three curves were generated assuming three different values of the surface roughness: solid line, $\bar{\theta} = 58°$; dotted line, $\bar{\theta} = 36°$; dashed line, $\bar{\theta} = 0°$, i.e., a smooth surface. The dashed–dotted line shows the function $D(\Gamma)$ obtained by using $\bar{\theta} = 58°$ and a random distribution of asteroid spin-axis orientations uniformly distributed over the celestial sphere, instead of the nominal one, as input for our model.

The value of Γ^* that we have derived by means of the best-fit procedure is less than 10% of that expected for a bare-rock surface (Jakosky, 1986). This implies that the surfaces of NEAs have in general significant quantities of thermally insulating regolith. However, Γ^* is also about four times higher than the value that has been determined for the lunar soil and more than ten times higher than the thermal inertia typical of large main-belt asteroids. This effect may be due to the fact that the regolith present on NEA surfaces is less mature and/or less thick than that of the Moon and the largest MBAs. The higher NEA thermal inertia can also be explained in terms of a coarser regolith and the exposure of rocks and boulders on the surface of these bodies, as clearly shown in the high resolution images of (433) Eros and (25143) Itokawa obtained by the NEAR Shoemaker and the Hayabusa missions, respectively.

A population of asteroids with constant $\Gamma = 200$ J m^{-2} s$^{-0.5}$ K^{-1} gives the best fit to the dataset. Fig. 3 shows, however, that five points with $\eta > 2$ are clearly significantly higher than the majority, indicating that these objects presented unusually low color temperatures to the observer, possibly due to higher-than-average thermal inertia (see Delbo' et al., 2003; Delbo', 2004). To gain insights into the *width* of the distribution of the thermal inertia of km-sized NEAs, we fitted the observed distribution of the data points with a synthetic population in which Γ was assumed to be uniformly distributed between 0 and $\Gamma_{\rm MAX}$. The best fit was obtained for $\Gamma_{\rm MAX} \sim 600$ J m^{-2} s$^{-0.5}$ K^{-1}. This suggests that the large majority of km-sized NEAs in our sample have thermal inertia below this value.

The average value of the thermal inertia was derived for a sample of objects whose diameter distribution is shown in Fig. 5. We use here the radiometric diameters as derived by the NEATM. The mean diameter of the sample is 3 km, but if we remove the Asteroid 433 Eros, the mean diameter value decreases to 2 km. 433 Eros is much larger than the average size of the sample (see Fig. 5). In fact the median value of the diameter distribution (including 433 Eros) is 1.8 km. We note that the distribution of log D (where D is the diameter measured in km) is well fitted by a Gaussian distribution with a central value of 1.7 km. The standard deviation of the best-fit Gaussian function is 0.31 (in log D). We can thus conclude that the average value of the thermal inertia is representative of NEAs in the size range 0.8–3.4 km.

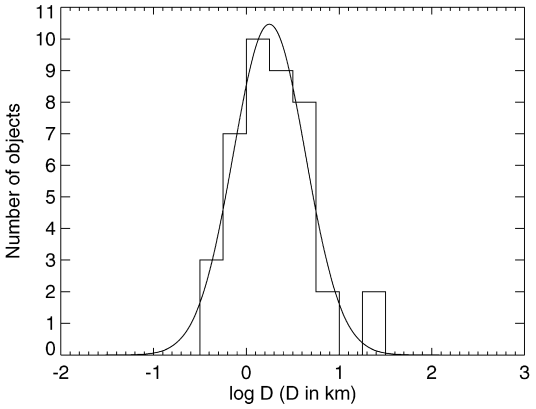

Fig. 5. Histogram of the distribution of the log of the diameters, D, of the NEAs for which we have η-values determined from observations. The best-fit Gaussian function, $0.37\exp(-z^2/2)$, where $z = (\log D - 0.23)/0.31$, with D in km, is also shown.

3. Size dependence of asteroid thermal inertia

The mean thermal inertia for the sample of NEAs with published η-values is consistent with the values derived by means of TPMs for (433) Eros (Mueller et al., 2007), (1580) Betulia (Harris et al., 2005), (25143) Itokawa (Mueller et al., 2007; Müller et al., 2005), and (33342) 1998 WT$_{24}$ (Harris et al., 2007) for which values around 150, 180, 350, 630, and 200 J m^{-2} s$^{-0.5}$ K^{-1} have been obtained respectively. Note that in the case of (25143) Itokawa, Müller et al. (2005) have obtained a thermal inertia value of 750 J m^{-2} s$^{-0.5}$ K^{-1} combining thermal-infrared observations gathered at ESO in 2004 with those obtained by Delbo' (2004) in 2001. On the other hand, from the latter dataset of observations and a series of further observations of (25143) Itokawa obtained at the NASA-IRTF 3-m telescope with MIRSI in 2004, Mueller et al. (2007) derived a thermal inertia of ∼350 or ∼800 J m^{-2} s$^{-0.5}$ K^{-1} depending on whether the size of the body was obtained from the TPM or was forced to the radar value of Ostro et al. (2004). In this work we have taken the mean value and the extreme values of 350, 750, and 800 J m^{-2} s$^{-0.5}$ K^{-1} as our best estimate for the thermal inertia of Itokawa and its uncertainty. Müller et al. (2004) have also attempted to derive the thermal inertia of the small (∼0.28 km) NEA 2002 NY$_{40}$. They obtained a value of 100 J m^{-2} s$^{-0.5}$ K^{-1} in the case that the size of the object was derived from the TPM, or 1000 J m^{-2} s$^{-0.5}$ K^{-1} if the body's size was forced to the value obtained from radar observations. However, it is important to note that the thermal inertia of 2002 NY$_{40}$ was derived by assuming an equator-on view and a spherical shape for this object. The value of the thermal inertia derived from the TPM is in general strongly dependent on the pole orientation of the body. For this reason we expect the value of Γ derived for 2002 NY$_{40}$ to be less reliable than the values obtained for the other NEAs, for which the pole orientation derived from lightcurve inversion was adopted.

From thermophysical modeling, Müller and Lagerros (1998) derived the thermal inertias of a number of the largest MBAs, namely (1) Ceres, (2) Pallas, (3) Juno, (4) Vesta, and (532) Herculina, obtaining the values of 10, 10, 5, 25, and 15 J m^{-2} s$^{-0.5}$ K^{-1}, respectively. Using the same approach, Müller and Blommaert (2004) derived a thermal inertia of 15 J m^{-2} s$^{-0.5}$ K^{-1} for (65) Cybele, and Mueller et al. (2006) obtained $\Gamma \sim 50$ J m^{-2} s$^{-0.5}$ K^{-1} for (21) Lutetia. From the published plots of the goodness of the TPM fit to the thermal-infrared data as a function of Γ it is possible to deduce that the relative uncertainties for the thermal inertias of these asteroids are around 50%.

From the comparison of the values of Γ mentioned above, it is clear that there is an increase in the thermal inertia from that of large MBAs with diameters of several hundred km to that of much smaller km-sized NEAs, and that the values of Γ obtained for km-sized NEAs are about one order of magnitude or more higher than the values derived for large MBAs, but still an

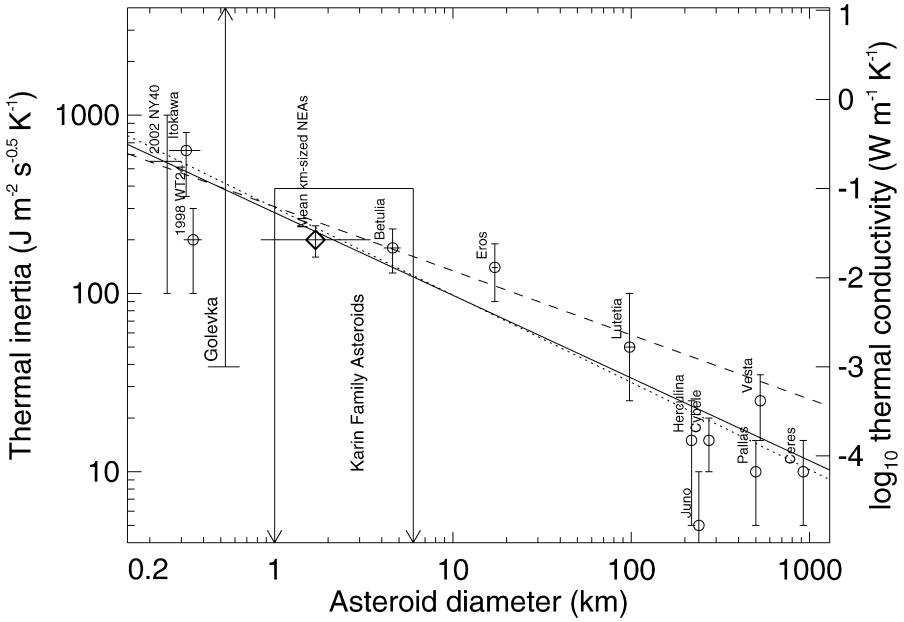

Fig. 6. Thermal inertia as a function of asteroid diameter. Small open circles represent values from the literature derived by means of thermophysical models. The large open *diamond* is the result from this work (see text for details). The straight (continuous) line which gives the best fit to the trend of increasing thermal inertia, Γ, with decreasing asteroid diameter, D, is given by the expression $\Gamma = 300 \times D^{-0.48}$. The axis on the right-hand side gives the asteroid surface thermal conductivity k on the basis of $k = \Gamma^2/(\rho c)$, assuming constant surface density, ρ, equal to 2500 kg m^{-3} and specific heat capacity, c, equal to 600 J kg^{-1} K^{-1}. These values are reasonable assumptions for asteroid surfaces (Britt et al., 2002; Farinella et al., 1998). The thermal conductivities of (6489) Golevka (Chesley et al., 2003) and for Karin cluster asteroids (Nesvorný and Bottke, 2004) are indicated with arrows. The two values of Γ derived for 2002 NY$_{40}$ are indicated as the lower and the upper limits of the error bar on the extreme left of the plot. Dotted line: linear regression of Eq. (6) for MBAs only; dashed line: linear regression of Eq. (6) for NEAs only.

order of magnitude lower than the thermal inertia of bare rock (∼2500 J m^{-2} s$^{-0.5}$ K^{-1}; Jakosky, 1986). In order to highlight the behavior of the thermal inertia of asteroids as a function of their size, we have plotted the mean value of thermal inertia for NEAs and the values of the thermal inertia derived by means of TPMs against object diameters in Fig. 6. Small open circles represent the literature values derived from the application of TPMs. The large open diamond is the result from this work. The axis on the right-hand side gives the asteroid surface thermal conductivity k as a function of size, on the basis of $k = \Gamma^2/(\rho c)$, with constant surface density $\rho = 2500$ kg m^{-3} and specific heat capacity $c = 600$ J kg^{-1} K^{-1}. These values are reasonable assumptions for asteroid surfaces (Britt et al., 2002; Farinella et al., 1998). For the Asteroid 2002 NY$_{40}$ a bar between 100 and 1000 J m^{-2} s$^{-0.5}$ K^{-1} is drawn. The thermal conductivity has also been constrained in the cases of (6489) Golevka (Chesley et al., 2003) and for asteroids in the Karin cluster (Nesvorný and Bottke, 2004). The values of the thermal conductivities derived by these authors have been converted to values of Γ assuming $\rho = 2500$ kg m^{-3} and $c = 600$ J kg^{-1} K^{-1}. Fig. 6 shows that the resulting limits, based on the measurements of the Yarkovsky effect on these bodies, are in general agreement with our results.

Fig. 6 reveals a convincing trend of increasing thermal inertia with decreasing asteroid diameter, D, confirming the intuitive view that large main-belt asteroids, over many hundreds of millions of years, have developed substantial insulating regolith layers, responsible for the low values of their surface thermal inertia. On the other hand, much smaller bodies, with shorter collisional lifetimes, presumably have less regolith, or less mature regolith, and therefore display a larger thermal inertia. Deriving a functional dependence of the thermal inertia as a function of the size of the body has important implications for improving the models of the orbital mobility of asteroids due to the Yarkovsky effect and to better quantify systematic errors in radiometric diameters and albedos of small bodies based on the use of thermal models that neglect the effects of heat conduction, such as the STM. The graph in Fig. 6 suggests that, to the first order, thermal inertia in this size range follows a power law. Expressing Γ as

$$\Gamma = d_0 D^{-\xi} \tag{6}$$

(a linear relation in the $\log \Gamma$–$\log D$ plot), a linear regression gives best-fit values of $\xi = 0.48 \pm 0.04$ and $d_0 = 300 \pm 47$, where D is km and Γ in S.I. units (J m^{-2} s$^{-0.5}$ K^{-1}), and the 1σ uncertainty is based on the assumption that the errors on the thermal inertia and diameter values are normally distributed. (The values of Γ for 2002 NY$_{40}$, 6489 Golevka and the Karin cluster asteroids were excluded from the linear regression analysis.)

However, the slope ξ of Eq. (6) may assume different values in different size ranges, since there are reasons to suspect that the surface properties of large asteroids may be different to those of smaller bodies: for example, Bottke et al. (2005) showed that asteroids with $D > 100$ km and most bodies with $D > 50$ km in size are likely to be primordial objects that have not suffered collisional disruption in the past 4 Gyr. These

large bodies have spent sufficient time in the asteroid belt to build a regolith such that they would display a low thermal inertia independent of size. In this case ξ should be about zero for D larger than about 50 km. In the same study it was shown that asteroids smaller than ~30 km are statistically the remnants of catastrophic collisional disruption of larger parent bodies, and the smaller the object, the fresher the surface. In this latter case one may intuitively expect that a dependence of the thermal inertia on the asteroid diameter would be more likely to occur, implying $\xi > 0$ for $D < 30$ km. For these reasons we tried to fit the data piecewise, separating the NEAs from the MBAs: a linear regression of Eq. (6) for the MBAs only of Fig. 6, gives best-fit values of $\xi = 0.49 \pm 0.27$ and $d_0 = 300 \pm 1504$ (Fig. 6, dotted line) in good agreement with the trend obtained by fitting the whole dataset of thermal inertias. However, we note that the accuracy of this fit is poor and that the value of ξ is strongly influenced by the thermal inertia of 21 Lutetia. On the other hand, a fit of Eq. (6) for near-Earth asteroids only, gives best-fit values of $\xi = 0.36 \pm 0.09$ and $d_0 = 300 \pm 45$ (Fig. 6, dashed line) which corresponds to a shallower dependence of Γ on D for sizes up to 20 km.

A further distinction in the thermal properties of MBAs compared to that of NEAs is given by the different mean heliocentric distances of the two classes of body, causing NEAs to have average temperatures ~200 K higher than those of MBAs. The thermal conductivity in the regolith is temperature dependent (Keihm, 1984), and so is thermal inertia. This temperature dependence of Γ may alter the slope ξ of Eq. (6) when both NEAs and main-belt asteroids are included in the fit. Under the assumption that heat is transported in the regolith mainly by radiative conduction between grains, the thermal conductivity is proportional to T^3, with T being the temperature of the regolith grains (Kührt and Giese, 1989; Jakosky, 1986). In this case $\Gamma \propto T^{3/2}$ and, from Eq. (2), $\Gamma \propto r^{-3/4}$, where r is the heliocentric distance of the body. On the basis of this dependence of Γ with respect to r, we corrected the values of the thermal inertias of the asteroids of Fig. 6 to the mean heliocentric distance $r_{\rm ref}$ of 1.7 AU. Although the correction factors are in general smaller than the errors affecting the values of Γ, the thermal inertia values of NEAs ($r < r_{\rm ref}$) are reduced, whereas those of MBAs ($r > r_{\rm ref}$) are increased, yielding a smaller value of the slope $\xi = 0.37 \pm 0.04$ and $d_0 = 230 \pm 30$.

Furthermore, the make up of NEA surfaces can be modified by processes such as close encounters with planets causing tidal disruption that do not affect asteroids in the main belt. Such processes might have been able to alter or strip off the regolith of some NEAs. Thus, while NEAs may be a good proxy for small main-belt asteroids, more observations are needed to confirm this point.

It is clear that with the present small number of asteroids for which we have an estimate of the thermal inertia it is difficult to reveal possible variations of ξ with respect to the mean trend, $\xi \sim 0.4$, in different size ranges. Nevertheless, Fig. 6 shows a clear correlation of Γ with asteroid size and that asteroids in the 1–30 km size range have values of Γ in general larger than 100 $\mathrm{J\,m^{-2}\,s^{-0.5}\,K^{-1}}$. The fact that thermal inertia increases with decreasing size and that the value of Γ for km and multi-km sized asteroids is at least ten times larger than the value derived for the largest main-belt asteroids, has a number of important implications. First of all, radiometric diameters and albedos of asteroids derived by means of thermal models neglecting the effects of thermal inertia, such as the STM, are likely to be affected by increasing systematic errors with decreasing size. Spencer et al. (1989) have studied systematic biases in radiometric diameter determinations as a result of the effects of thermal inertia, rotation rate, pole orientation, and temperature. They concluded that the STM systematically underestimates the diameters of objects with non-negligible thermal inertia, while overestimating their albedos. Because we find that thermal inertia increases with decreasing asteroid diameter, it is likely that the systematic underestimation of asteroid diameters (and overestimation of asteroid albedos) obtained from the STM increases for decreasing asteroid size.

Moreover, the absolute value and size dependence of the thermal inertia for asteroids with diameters smaller than about 10–20 km have crucial implications for the magnitude of the Yarkovsky effect, which is an important phenomenon that offers an explanation for the dispersion of asteroid dynamical families and the slow but steady injection of bodies into the dynamical resonances that eventually transport them from the main belt to near-Earth space.

4. Implications for the magnitude of the Yarkovsky effect

Current models of Yarkovsky-assisted delivery of NEAs from the main belt (Morbidelli and Vokrouhlický, 2003) and the spreading of asteroids families (Bottke et al., 2001; Nesvorný and Bottke, 2004), assume that thermal inertia is independent of object size. In this case, the theory of the Yarkovsky effect predicts that the orbital semimajor axis drift rate of an asteroid, $\mathrm{d}a/\mathrm{d}t$, is proportional to D^{-1} (Bottke et al., 2002). However, the mean value of the thermal inertia derived for NEAs and the inverse correlation of this thermophysical property with asteroid size, demonstrated in this work, give rise to a different magnitude of the Yarkovsky effect and a modified dependence of $\mathrm{d}a/\mathrm{d}t$ on the object diameter. In order to derive this modification one can directly insert the function $\Gamma = d_0 D^{-\xi}$ in the formulas given by Bottke et al. (2002) and Vokrouhlický (1999) to explicitly calculate $\mathrm{d}a/\mathrm{d}t$ as a function of the relevant parameters.

Here we discuss the case of MBAs with $D < 10$ km, assuming the linearized theory of the diurnal component of the Yarkovsky effect of Vokrouhlický (1999), which yields

$$\frac{\mathrm{d}a}{\mathrm{d}t} \propto \frac{1}{D}\frac{\Theta}{1+\Theta+0.5\Theta^2}. \tag{7}$$

Because Θ is directly proportional to Γ, for $\Theta \gg 1$, $\mathrm{d}a/\mathrm{d}t \propto D^{-1}\Gamma^{-1}$ and hence $\mathrm{d}a/\mathrm{d}t \propto D^{\xi-1}$. We found that this condition holds in general for small asteroids in the main belt: in fact for objects with D smaller than ~10 km Fig. 6 shows that the thermal inertia is in general >100 $\mathrm{J\,m^{-2}\,s^{-0.5}\,K^{-1}}$, and at heliocentric distances >2 AU the surface temperatures of these

bodies are in general smaller than 250 K (see, e.g., Delbo', 2004). Pravec et al. (2002) have also shown that asteroids with sizes between ∼0.15 and 10 km have a typical rotation rate around 6 h. Inserting these values in Eq. (3), we find that Θ is in general larger than ∼2 for main-belt asteroids in this size range. By taking $\xi \sim 0.4$, as derived in the previous section for the $\Gamma = d_0 D^{-\xi}$ relation, we obtain that the size dependence of da/dt due to the diurnal component of the Yarkovsky effect is proportional to $D^{-0.6}$ rather than proportional to D^{-1}, as generally assumed, and which holds for a thermal inertia independent of asteroid size.

We caution, however, that there are currently no reliable estimates of thermal inertia available for any object smaller than Itokawa ($D \sim 350$ m), so the relation derived for $da/dt \propto D^{-0.6}$ should be assumed to hold for objects with diameters in the range between ∼0.35 and ∼10 km. Moreover, for asteroids smaller than 350 m and/or higher values of the thermal inertia, the seasonal component of the Yarkovsky effect may become significant and contribute to the average value of da/dt. From this analysis we conclude that, in the main belt, the drift rate in semimajor axis due to the diurnal component of the Yarkovsky effect increases with decreasing asteroid size more slowly than is normally assumed in models of the origin of NEAs and the spreading of asteroids families.

The shallower dependence of the Yarkovsky effect on the diameter of the bodies caused by the inverse correlation of Γ with D has the important implication that the size distribution of the asteroids injected into the NEA source regions is less skewed to small objects than generally assumed. In the following we briefly discuss some of the consequences of this: there is general consensus that the large majority of NEAs originate from the main belt via well defined "feeding zones" of dynamical instability (Morbidelli et al., 2002). Asteroidal material can gradually drift towards these NEA source regions as a result of Yarkovsky-driven semimajor axis mobility (Morbidelli et al., 2002; Morbidelli and Vokrouhlický, 2003). The cumulative size distribution of a population of asteroids in a given diameter range (e.g., $0.35 < D < 10$ km) can be approximated by a simple exponential function of the form

$$N(> D) = N_0 D^{-\alpha}. \tag{8}$$

Therefore, according to this asteroid delivery model, the difference in the exponent α between the bodies injected into the NEA source regions and the remaining population of asteroids in the main belt is of the order of ∼1 if the semimajor axis mobility is proportional to D^{-1}. The same difference in the value of the exponents holds for the NEA and the MBA populations in a comparable size range, assuming that the large majority of NEAs come from the main belt.

The results of the latest studies that have analyzed the size distributions of NEAs and km-sized MBAs imply that this difference is closer to 0.5–0.7, in favor of a Yarkovsky effect less effective for smaller asteroids, which is consistent with the results of this work. We recall that Eq. (8) can be converted into a cumulative absolute visual magnitude H distribution of a population of asteroids with the form

$$N(< H) = N_0' 10^{\beta H}, \tag{9}$$

where the exponential slope of the absolute magnitude distribution, β, can be converted into the power-law slope of the diameter distribution via $\alpha = 5\beta$ (see, e.g., Stuart and Binzel, 2004). Several authors (Rabinowitz et al., 2000; Bottke et al., 2000; Stuart and Binzel, 2004) agree that β is in the range 0.35–0.39 for the NEA population, which implies a value of $\alpha_{\rm NEA}$ between 1.75 and 1.95. The size distribution of km- and sub-km-sized MBAs is less constrained than that of NEAs, since the known population is still rather incomplete for $H > 14$–15 (corresponding to values of D between 6 and 3 km for a geometric visible albedo of 0.11), so that beyond this threshold only extrapolations of the known distribution can be made. Morbidelli and Vokrouhlický (2003) used the slopes derived by Ivezic et al. (2001) from the Sloan Digital Sky Survey (SDSS), namely, $\beta = 0.61$ for $13 < H < 15.5$ and $\beta = 0.25$ for $15.5 < H < 18$, to extrapolate the observed H cumulative distribution (as given by the Astorb catalog) to km-sized asteroids, and use it in their model of the Yarkovsky-driven origin of near-Earth asteroids. Assuming $\beta = 0.25$ for $15.5 < H < 18$ this would give a value of $\alpha_{\rm MBA} = 1.25$ for the slope of the cumulative size distribution of MBAs in the range $1 < D < 3$ km. This value is in good agreement with the even slightly shallower size distribution ($\alpha_{\rm MBA} \sim 1.2$) of km- and sub-km-sized MBAs (for $0.5 < D < 1$ km) found by the SMBAS survey (Sub-Kilometer Main-Belt Asteroid Survey) obtained by Yoshida et al. (2003). Taking the values of α from the studies above, we find that $\alpha_{\rm NEA} - \alpha_{\rm MBA} = 0.5$–0.7, in good agreement with a drifting population of asteroids with $da/dt \propto D^{-0.6}$.

However, Morbidelli and Vokrouhlický (2003) have also shown that the collisional re-orientation of asteroid spin axes (which resets the drift speed due to the Yarkovsky effect), the collisional disruption of the bodies during their slow drift towards the NEA source regions, and the YORP effect, tend to decrease the difference between $\alpha_{\rm NEA}$ and $\alpha_{\rm MBA}$. The addition of these phenomena along with the revised dependence of $da/dt \propto D^{-0.6}$ due to the Yarkovsky effect may help to explain the even steeper size distribution of small MBAs, and thus a difference between $\alpha_{\rm NEA}$ and $\alpha_{\rm MBA}$ smaller than 0.5–0.7 implied by the recent results of the Sub-Kilometer Asteroid Diameter Survey (SKADS; Davis et al., 2006), which found $\beta_{\rm MBA} = 0.38$, corresponding to $\alpha_{\rm MBA} = 1.9$, for $13 < H < 17$.

The value of the thermal inertia also plays an important role in the YORP effect (Rubincam, 2000; Vokrouhlický and Capek, 2002), which is a torque produced by the thermal radiation emitted by asteroids with irregular shapes causing a slow spin-up/spin-down and a change of the spin axis obliquities of these bodies. In contrast to the Yarkovsky effect, YORP also acts on bodies with zero surface thermal conductivity. However, in the case of a thermal inertia significantly larger than zero (in contrast to the case of zero-conductivity), YORP preferentially drives obliquity toward two asymptotic states perpendicular to the orbital plane, and asymptotically decelerates and accelerates rotation rate in about an equal number of cases (Capek and Vokrouhlický, 2004). Capek and Vokrouhlický (2004) have shown that the acceleration of the rotation rate, $d\omega/dt$, is largely independent of the thermal inertia, whereas the latter significantly affects the rate of change of the obliquity, $d\theta_{\rm SS}/dt$, in

the sense that the higher the thermal inertia the larger the mean value of $d\theta_{SS}/dt$. Capek and Vokrouhlický (2004) found the median value of the distribution of $d\theta_{SS}/dt$ for populations of Gaussian spheres increased from 3.33 deg/Myr for $\Gamma = 0\ J\,m^{-2}\,s^{-0.5}\,K^{-1}$ to 5.94 deg/Myr for $\Gamma = 39\ J\,m^{-2}\,s^{-0.5}\,K^{-1}$ and to 8.60 deg/Myr in the case of $\Gamma = 122\ J\,m^{-2}\,s^{-0.5}\,K^{-1}$, which is a reasonable value for bodies of about 5 km according to our Fig. 6. Because our $\Gamma(D)$ relation predicts an even larger value of surface thermal inertia for asteroids of 1 km in diameter, the YORP reorientation of the spin vector of asteroids becomes a more effective mechanism in the case of km-sized asteroids, capable of driving the rotation axis to the asymptotic state perpendicular to the orbital plane in just a few tens of millions of years.

5. Conclusions

The thermal inertia of an asteroid can be derived by comparing measurements of its thermal-infrared flux, at wavelengths typically between 5 and 20 μm, to synthetic fluxes generated by means of a thermophysical model (TPM). To date TPMs have been used to derive the thermal inertia of seven large MBAs and five NEAs. Although an extensive set of thermal-infrared observations of NEAs exists, application of TPMs is limited to the few asteroids for which the gross shape, the rotation period, and the spin axis orientation are known.

In order to overcome this limitation, we have developed a statistical method enabling the determination of the thermal inertia of a sample of objects for which such information is not available. This method has been applied to a sample of NEAs with diameters generally between 0.8 and 3.4 km. The resulting value, $\Gamma = 200 \pm 40\ J\,m^{-2}\,s^{-0.5}\,K^{-1}$, corresponds to a surface thermal conductivity of about $0.03\ W\,m^{-1}\,K^{-1}$.

This value of thermal inertia and those derived by means of TPMs reveal a significant trend of increasing thermal inertia with decreasing asteroid diameter, D. Assuming that Γ is proportional to $D^{-\xi}$ we derive a best-fit value for the exponent of $\xi \sim 0.4$.

The dependence $\Gamma(D)$ has important implications for the magnitude of the Yarkovsky effect. On the basis of our results, the size dependence of the orbital semimajor axis drift rate da/dt of MBAs for $\sim 0.35 < D < \sim 10$ due to the diurnal component of the Yarkovsky effect is proportional to $D^{-0.6}$, rather than the generally assumed D^{-1} dependence for size-independent thermal inertia.

The modified dependence, $da/dt \propto D^{-0.6}$, implies that the size distribution of the objects injected by Yarkovsky-driven orbital mobility into the NEA source regions is less skewed to smaller sizes than generally assumed. This may help to explain the smaller-than-one difference in the value of the exponents of the cumulative size distribution of NEAs and MBAs.

We stress that the dataset on which our results are based is small and more multi-wavelength, multi-epoch thermal-infrared observations of asteroids with known spin states are required to refine our conclusions on the size dependence of thermal inertia and its consequences.

Acknowledgments

We wish to thank Bill Bottke and David Vokrouhlický for earlier suggestions and comments that inspired us to develop the original concept of this work further, and the referees of the present paper, Stephen Wolters and Bill Bottke, for suggestions that led to significant improvements in the presentation. M.D. wishes to acknowledge fruitful discussions with A. Morbidelli and A. Cellino.

References

Allen, D.A., 1970. Infrared diameter of Vesta. Nature 227, 158.

Bottke, W.F., Jedicke, R., Morbidelli, A., Petit, J.-M., Gladman, B., 2000. Understanding the distribution of near-Earth asteroids. Science 288, 2190–2194.

Bottke, W.F., Vokrouhlický, D., Broz, M., Nesvorný, D., Morbidelli, A., 2001. Dynamical spreading of asteroid families by the Yarkovsky effect. Science 294, 1693–1696.

Bottke, W.F., Vokrouhlický, D., Rubincam, D.P., Broz, M., 2002. The effect of Yarkovsky thermal forces on the dynamical evolution of asteroids and meteoroids. In: Bottke, W.F., Cellino, A., Paolicchi, P., Binzel, R.P. (Eds.), Asteroids III. Univ. of Arizona Press, Tucson, AZ, pp. 395–408.

Bottke, W.F., Durda, D.D., Nesvorný, D., Jedicke, R., Morbidelli, A., Vokrouhlický, D., Levison, H.F., 2005. Linking the collisional history of the main asteroid belt to its dynamical excitation and depletion. Icarus 179, 63–94.

Bottke, W.F., Vokrouhlický, D., Rubincam, D.P., Nesvorný, D., 2006. The Yarkovsky and YORP effects: Implications for asteroid dynamics. Annu. Rev. Earth Planet. Sci. 34, 157–191.

Britt, D.T., Yeomans, D., Housen, K., Consolmagno, G., 2002. Asteroid density, porosity, and structure. In: Bottke, W.F., Cellino, A., Paolicchi, P., Binzel, R.P. (Eds.), Asteroids III. Univ. of Arizona Press, Tucson, AZ, pp. 485–500.

Capek, D., Vokrouhlický, D., 2004. The YORP effect with finite thermal conductivity. Icarus 172, 526–536.

Chesley, S.R., Ostro, S.J., Vokrouhlický, D., Capek, D., Giorgini, J.D., Nolan, M.C., Margot, J.-L., Hine, A.A., Benner, L.A.M., Chamberlin, A.B., 2003. Direct detection of the Yarkovsky effect by radar ranging to Asteroid 6489 Golevka. Science 302, 1739–1742.

Christensen, P.R., and 21 colleagues, 2003. Morphology and composition of the surface of Mars: Mars Odyssey THEMIS results. Science 300, 2056–2061.

Davis, D.R., Gladman, B., Jedicke, R., Williams, G., 2006. The Sub-Kilometer Asteroid Diameter survey. Bull. Am. Astron. Soc. 38. Abstract 53.01.

Delbo', M., 2004. The nature of near-Earth asteroids from the study of their thermal infrared emission. Doctoral thesis, Freie Universität Berlin. http://www.diss.fu-berlin.de/2004/289/indexe.html.

Delbo', M., 2006. Delbo' Thermal Infrared Asteroid Diameters and Albedos V1.0. EAR-A-KECK1LWS/ETAL-5-DELBO-V1.0. NASA Planetary Data System, 2006, http://www.psi.edu/pds/resource/delbo.html.

Delbo', M., Harris, A.W., 2002. Physical properties of near-Earth asteroids from thermal infrared observations and thermal modeling. Meteorit. Planet. Sci. 37, 1929–1936.

Delbo', M., Harris, A.W., Binzel, R.P., Pravec, P., Davies, J.K., 2003. Keck observations of near-Earth asteroids in the thermal infrared. Icarus 166, 116–130.

Domingue, D.L., Robinson, M., Carcich, B., Joseph, J., Thomas, P., Clark, B.E., 2002. Disk-integrated photometry of 433 Eros. Icarus 155, 205–219.

Emery, J.P., Sprague, A.L., Witteborn, F.C., Colwell, J.E., Kozlowski, R.W.H., Wooden, D.H., 1998. Mercury: Thermal modeling and mid-infrared (5–12 μm) observations. Icarus 136, 104–123.

Farinella, P., Vokrouhlický, D., Hartmann, W.K., 1998. Meteorite delivery via Yarkovsky orbital drift. Icarus 140, 369–378.

Hahn, G., 2006. Table on Physical Properties of NEOs. http://earn.dlr.de/nea/table1_new.html.

Hapke, B., 1984. Bidirectional reflectance spectroscopy. 3. Correction for macroscopic roughness. Icarus 59, 41–59.

Harris, A.W., 1998. A thermal model for near-Earth asteroids. Icarus 131, 291–301.

Harris, A.W., 2006. The surface properties of small asteroids from thermal-infrared observations. In: Lazzaro, D., Ferraz-Mello, S., Fernández, J.A. (Eds.), Proc. of IAU Symposium 229. Cambridge Univ. Press, Cambridge, UK, pp. 449–463.

Harris, A.W., Davies, J.K., 1999. Physical characteristics of near-Earth asteroids from thermal infrared spectrophotometry. Icarus 142, 464–475.

Harris, A.W., Lagerros, J.S.V., 2002. Asteroids in the thermal IR. In: Bottke, W.F., Cellino, A., Paolicchi, P., Binzel, R.P. (Eds.), Asteroids III. Univ. of Arizona Press, Tucson, AZ, pp. 205–218.

Harris, A.W., Davies, J.K., Green, S.F., 1998. Thermal infrared spectrophotometry of the near-Earth Asteroids 2100 Ra-Shalom and 1991 EE. Icarus 135, 441–450.

Harris, A.W., Mueller, M., Delbo', M., Bus, S.J., 2005. The surface properties of small asteroids: Peculiar Betulia—A case study. Icarus 179, 95–108.

Harris, A.W., Mueller, M., Delbo', M., Bus, S.J., 2007. Physical characterization of the potentially-hazardous high-albedo Asteroid (33342) 1998 WT24 from thermal-infrared observations. Icarus, in press.

Ivezic, Z., and 31 colleagues, 2001. Solar System objects observed in the Sloan Digital Sky Survey commissioning data. Astron. J. 122, 2749–2784.

Jakosky, B.M., 1986. On the thermal properties of martian fines. Icarus 66, 117–124.

Keihm, S.J., 1984. Interpretation of the lunar microwave brightness temperature spectrum—Feasibility of orbital heat flow mapping. Icarus 60, 568–589.

Kührt, E., Giese, B., 1989. A thermal model of the martian satellites. Icarus 81, 102–112.

Lagerros, J.S.V., 1996. Thermal physics of asteroids. I. Effects of shape, heat conduction and beaming. Astron. Astrophys. 310, 1011–1020.

La Spina, A., Paolicchi, P., Kryszczýnska, A., Pravec, P., 2004. Retrograde spins of near-Earth asteroids from the Yarkovsky effect. Nature 428, 400–401.

Lebofsky, L.A., Spencer, J.R., 1989. Radiometry and thermal modeling of asteroids. In: Binzel, R.P., Gehrels, T., Matthews, M.S. (Eds.), Asteroids II. Univ. of Arizona Press, Tucson, pp. 128–147.

Lim, L.F., McConnochie, T.H., Bell, J.F., Hayward, T.L., 2005. Thermal infrared (8–13 μm) spectra of 29 asteroids: The Cornell Mid-Infrared Asteroid Spectroscopy (MIDAS) survey. Icarus 173, 385–408.

Morbidelli, A., Vokrouhlický, D., 2003. The Yarkovsky-driven origin of near-Earth asteroids. Icarus 163, 120–134.

Morbidelli, A., Bottke, W.F., Froeschlé, Ch., Michel, P., 2002. Origin and evolution of NEOs. In: Bottke, W.F., Cellino, A., Paolicchi, P., Binzel, R.P. (Eds.), Asteroids III. Univ. of Arizona Press, Tucson, pp. 409–422.

Mellon, M.T., Jakosky, B.M., Kieffer, H.H., Christensen, P.R., 2000. High-resolution thermal inertia mapping from the Mars global surveyor thermal emission spectrometer. Icarus 148, 437–455.

Mueller, M., Harris, A.W., Bus, S.J., Hora, J.L., Kassis, M., Adams, J.D., 2006. The size and albedo of Rosetta fly-by target 21 Lutetia from new IRTF measurements and thermal modeling. Astron. Astrophys. 447, 1153–1158.

Mueller, M., Delbo', M., Kaasalainen, M., Di Martino, M., Bus, S.J., Harris, A.W., 2007. Indications for Regolith on Itokawa from Thermal-Infrared Observations. ASP Conference Series, in press.

Müller, T.G., Blommaert, J.A.D.L., 2004. 65 Cybele in the thermal infrared: Multiple observations and thermophysical analysis. Astron. Astrophys. 418, 347–356.

Müller, T.G., Lagerros, J.S.V., 1998. Asteroids as far-infrared photometric standards for ISOPHOT. Astron. Astrophys. 338, 340–352.

Müller, T.G., Sterzik, M.F., Schuetz, O., Pravec, P., Siebenmorgen, R., 2004. Thermal infrared observations of near-Earth Asteroid 2002 NY40. Astron. Astrophys. 424, 1075–1080.

Müller, T.G., Sekiguchi, T., Kaasalainen, M., Abe, M., Hasegawa, S., 2005. Thermal infrared observations of the Hayabusa spacecraft target Asteroid 25143 Itokawa. Astron. Astrophys. 443, 347–355.

Mustard, J.F., Hays, J.E., 1997. Effects of hyperfine particles on reflectance spectra from 0.3 to 25 μm. Icarus 125, 145–163.

Nesvorný, D., Bottke, W.F., 2004. Detection of the Yarkovsky effect for main-belt asteroids. Icarus 170, 324–342.

Ostro, S.J., and 15 colleagues, 2004. Radar observations of Asteroid 25143 Itokawa (1998 SF36). Meteorit. Planet. Sci. 39, 407–424.

Pravec, P., Harris, A.W., Michalowski, T., 2002. Asteroid rotations. In: Bottke, W.F., Cellino, A., Paolicchi, P., Binzel, R.P. (Eds.), Asteroids III. Univ. of Arizona Press, Tucson, AZ, pp. 113–122.

Press, W.H., Teukolsky, S.A., Vetterling, W.T., Flannery, B.P., 1992. Numerical Recipes in C. The Art of Scientific Computing, second ed. Cambridge Univ. Press, Cambridge, UK.

Putzig, N.E., Mellon, M.T., Kretke, K.A., Arvidson, R.E., 2005. Global thermal inertia and surface properties of Mars from the MGS mapping mission. Icarus 173, 325–341.

Rabinowitz, D.L., Helin, E., Lawrence, K., Pravdo, S., 2000. A reduced estimate of the number of kilometer-sized near-Earth asteroids. Nature 403, 165–166.

Rubincam, D.P., 2000. Radiative spin-up and spin-down of small asteroids. Icarus 148, 2–11.

Salisbury, J.W., D'Aria, D.M., Jarosewich, E., 1991. Mid-infrared (2.5–13.5 microns) reflectance spectra of powdered stony meteorites. Icarus 92, 280–297.

Spencer, J.R., 1990. A rough-surface thermophysical model for airless planets. Icarus 83, 27–38.

Spencer, J.R., Lebofsky, L.A., Sykes, M.V., 1989. Systematic biases in radiometric diameter determinations. Icarus 78, 337–354.

Stuart, J.S., Binzel, R.P., 2004. Bias-corrected population, size distribution, and impact hazard for the near-Earth objects. Icarus 170, 295–311.

Veeder, G.J., Hanner, M.S., Matson, D.L., Tedesco, E.F., Lebofsky, L.A., Tokunaga, A.T., 1989. Radiometry of near-Earth asteroids. Astron. J. 97, 1211–1219.

Vokrouhlický, D., 1999. A complete linear model for the Yarkovsky thermal force on spherical asteroid fragments. Astron. Astrophys. 344, 362–366.

Vokrouhlický, D., Capek, D., 2002. YORP-induced long-term evolution of the spin state of small asteroids and meteoroids: Rubincam's approximation. Icarus 159, 449–467.

Wolters, S.D., Green, S.F., McBride, N., Davies, J.K., 2005. Optical and thermal infrared observations of six near-Earth asteroids in 2002. Icarus 175, 92–110.

Yoshida, F., Nakamura, T., Watanabe, J.-I., Kinoshita, D., Yamamoto, N., Fuse, T., 2003. Size and spatial distributions of sub-km main-belt asteroids. Publ. Astron. Soc. Jpn. 55, 701–715.

LETTER

doi:10.1038/nature13153

Thermal fatigue as the origin of regolith on small asteroids

Marco Delbo[1], Guy Libourel[2,3], Justin Wilkerson[4], Naomi Murdoch[1,5], Patrick Michel[1], K. T. Ramesh[4], Clément Ganino[3], Chrystele Verati[3] & Simone Marchi[6]

Space missions[1,2] and thermal infrared observations[3] have shown that small asteroids (kilometre-sized or smaller) are covered by a layer of centimetre-sized or smaller particles, which constitute the regolith. Regolith generation has traditionally been attributed to the fall back of impact ejecta and by the break-up of boulders by micrometeoroid impact[4,5]. Laboratory experiments[6] and impact models[4], however, show that crater ejecta velocities are typically greater than several tens of centimetres per second, which corresponds to the gravitational escape velocity of kilometre-sized asteroids. Therefore, impact debris cannot be the main source of regolith on small asteroids[4]. Here we report that thermal fatigue[7–9], a mechanism of rock weathering and fragmentation with no subsequent ejection, is the dominant process governing regolith generation on small asteroids. We find that thermal fragmentation induced by the diurnal temperature variations breaks up rocks larger than a few centimetres more quickly than do micrometeoroid impacts. Because thermal fragmentation is independent of asteroid size, this process can also contribute to regolith production on larger asteroids. Production of fresh regolith originating in thermal fatigue fragmentation may be an important process for the rejuvenation of the surfaces of near-Earth asteroids, and may explain the observed lack of low-perihelion, carbonaceous, near-Earth asteroids[10].

The collisional and gravitational re-accumulation processes by which small asteroids are formed probably result in the creation of surfaces composed of boulders[11]. These boulders are broken up by micrometeoroid impacts into the smaller particles constituting the regolith[4,5]. A standard model[12] that calculates the time required to form regolith by fragmenting rocks of sizes between 1 and 10 cm by micrometeoroid impacts shows that these rocks on the Moon's surface will be broken down into smaller rocks in several million years[5,12]. Using the known[13] orbital distribution of micrometeoroids and a method[14] to calculate the impact probability of micrometeoroids with the Moon and asteroids (Methods), we find that the breakdown of surface rocks requires about the same amount of time on near-Earth asteroids (NEAs; asteroids with a perihelion distance of $q < 1.3$ AU, where 1 AU is the Earth–Sun distance) and on the Moon, whereas on main-belt asteroids (MBAs) this time is about ten times longer than on the Moon (Fig. 1).

Boulders on the surfaces of asteroids are also exposed to cyclic diurnal temperature variations, which cause mechanical stresses. To answer the question of whether these stresses are large enough to induce thermal

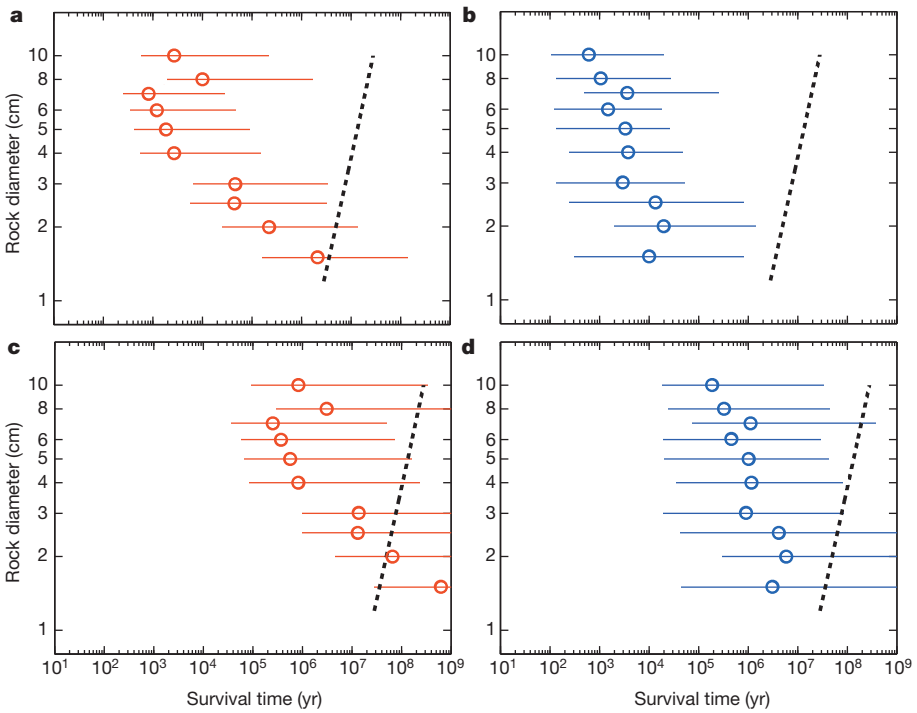

Figure 1 | Time required to break rocks on asteroids. Symbols show the time required to thermally fragment 90% of rocks for the nominal values of the model parameters. The thick dashed lines show the times at which 90% of these same rocks are broken by micrometeoroid impacts. **a**, Ordinary chondrite-like asteroid 1 AU from the Sun; **b**, carbonaceous chondrite-like asteroid at 1 AU; **c**, ordinary chondrite-like asteroid at 2.5 AU; **d**, carbonaceous chondrite-like asteroid at 2.5 AU. Error bars show the change in the thermal fragmentation time when model parameters are varied within their uncertainties (Methods).

[1]Laboratoire Lagrange, UNS-CNRS, Observatoire de la Côte d'Azur, Boulevard de l'Observatoire-CS 34229, 06304 Nice Cedex 4, France. [2]Université de Lorraine, CRPG-CNRS, 15 Rue Notre-Dame des Pauvres, BP 20, 54501 Vandoeuvre les Nancy, France. [3]Laboratoire Géoazur, UNS-CNRS, Observatoire de la Côte d'Azur, 250 rue Albert Einstein, Les Lucioles 1, Sophia-Antipolis, 06560 Valbonne, France. [4]Hopkins Extreme Materials Institute, Johns Hopkins University, Latrobe 122, 3400 North Charles Street, Baltimore, Maryland 21218, USA. [5]Institut Supérieur de l'Aéronautique et de l'Espace, 10 avenue Edouard-Belin, BP 54032, 31055 Toulouse Cedex 4, France. [6]Solar System Exploration Research Virtual Institute, Institute for the Science of Exploration Targets, Southwest Research Institute, 1050 Walnut Street, Suite 300 Boulder, Colorado 80302, USA.

fatigue crack growth, we perform laboratory experiments (Methods) on two meteorites: a carbonaceous chondrite (CM2 Murchison) and an ordinary chondrite (L/LL3.2 Sahara 97210) considered the closest available analogues of the broad asteroid spectroscopic classes C and S, respectively. Our protocol (Extended Data Fig. 1) consists of using a climatic chamber to subject these meteorites to temperature cycles that approximate the day–night temperature variations experienced on NEA surfaces. The temperature cycle period was taken to be 2.2 h, the fastest period permitted by our climatic chamber, allowing us to have a reasonable number of cycles within a month (still subjecting meteorites to temperature rates of change typical of NEA surfaces). The magnitude of the temperature excursion, ΔT, was taken to be 190 K, equal of the ΔT of C-type NEAs at ~0.7 AU from the Sun (Methods and Extended Data Fig. 2).

After subjecting the meteorites to as few as 407 temperature cycles, we use X-ray tomography to observe (Fig. 2) and measure (Methods) an increase in the length and in the width of several of the pre-existing cracks in both Murchison and Sahara 97210, thus confirming thermal fatigue (measurements for 21 cracks for each meteorite are shown in Extended Data Figs 3 and 4). Additionally, we found particles in the sample holder of Murchison that had broken off from its surface as a result of temperature cycling (Fig. 3). Crack growth and fragmentation due to either the manipulation of the samples or the freeze–thaw of water are both ruled out (Methods and Extended Data Fig. 5).

A second question is how much time is required for pre-existing cracks to propagate enough to break the rocks and contribute to the generation of finer regolith. Our measurements show that, under laboratory conditions, pre-existing cracks are extending in length at a rate of about 0.5 mm yr^{-1} (average of Murchison and Sahara 97210). A constant crack propagation rate would suggest that a 1-cm rock on the surface of an NEA could fragment into smaller pieces in less than 20 yr, several orders of magnitude faster than comminution by micrometeoroid impacts, which requires about 2 Myr on NEAs and about 20 Myr on MBAs. However, the crack propagation rate is typically a nonlinear function of crack size, thus requiring a detailed fracture mechanics analysis to investigate whether such a rapid growth rate would be maintained to the point of fragmentation and whether thermal fragmentation can also occur for different cycle periods, for larger rocks and at lower temperatures (for example for MBAs).

To investigate this question, we develop a micromechanical model (Methods) based on well-established thermal diffusion[15], thermomechanical[16] (Extended Data Fig. 6) and fracture mechanics[17] models in order to analyse the progressive crack growth from the early stages to final fragmentation (model parameter values are in Extended Data Table 1).

First we compare the crack growth measured in our laboratory experiments with model predictions. We use thermal boundary conditions simulating those of the laboratory experiments: the entire surface of a

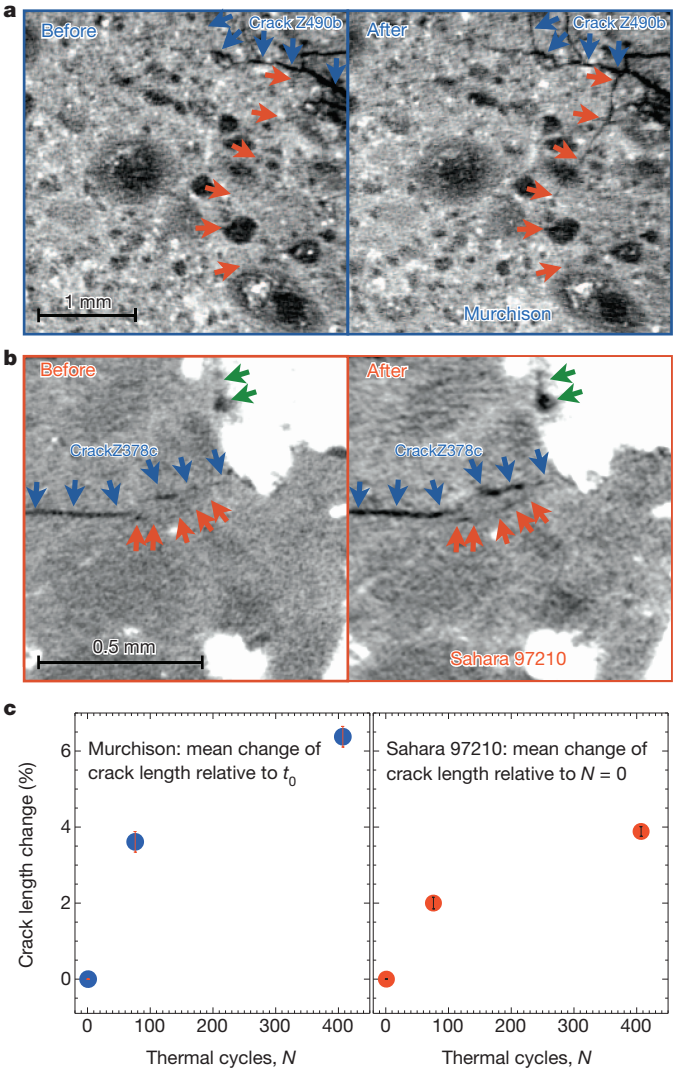

Figure 2 | Crack growth in meteorites due to laboratory temperature cycling. Arrows of the same colour mark growing cracks in the pictures before and after temperature cycling. **a**, Murchison; **b**, Sahara 97210. The cracks volume and length growth are given in the Extended Data Figs 3 and 4, respectively. **c**, The mean change of the length of the 21 measured cracks for each meteorite as a function of the number of thermal cycles. Statistical errors are 1σ.

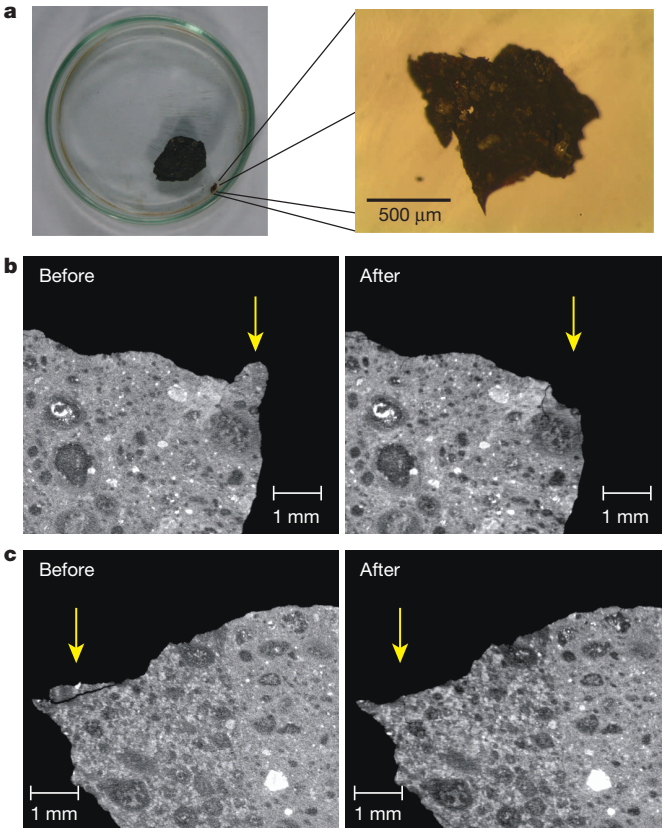

Figure 3 | Regolith formation from Murchison in the laboratory. **a**, The sample of Murchison and (enlarged) one of its small fragments, containing several visible chondrules, found in the sample holder after temperature cycling. **b**, **c**, Tomographic slices of regions of the same sample of Murchison before and after temperature cycling. The arrows indicate fragments that broke off from Murchison.

rock 1 cm in diameter is forced to follow sinusoidal temperature oscillations with $\Delta T = 190$ K and a period of 2.2 h. Considering the idealized nature of the model, the agreement with the experimental measurements is satisfactory (the average model-to-experiment discrepancy is 20%; see Methods and Extended Data Fig. 7) and indicates that we have captured the essential aspects of thermal fatigue crack growth.

Next we use the model to provide predictions for the time (number of day–night temperature cycles) required to achieve thermal fragmentation for surface rocks with sizes between 1 and 10 cm (Extended Data Fig. 8) on C- and S-type asteroids at 1 and 2.5 AU from the Sun. Here the cycle period is taken to be 6 h, which is more appropriate than 2.2 h for most small asteroids. The day–night temperature variations, temperature gradients and mechanical stresses are calculated using boundary conditions appropriate for asteroid surfaces radiatively heated by the Sun (Methods). We use a conservative definition of rock fragmentation in our model, namely that an initial 30-μm-long crack grows to a length equal to the rock diameter. Shorter cracks can still produce fragments, either by merging with other growing cracks or by a flaking mechanism (as in the case of Fig. 3).

Our results (Fig. 1) demonstrate that, at 1 AU from the Sun, centimetre-sized rocks fragment on asteroids at least an order of magnitude faster by thermal fragmentation than by comminution by micrometeoroid impacts, the previously assumed dominant mechanism. We also find (Fig. 1) that although larger rocks require more time to fragment by micrometeoroid impact, the trend is reversed for thermal fragmentation. Therefore, thermal fragmentation of a 10-cm rock is predicted to occur orders of magnitude faster than fragmentation due to micrometeoroid impact. Although the speed of thermal fatigue is reduced at larger heliocentric distances (Extended Data Fig. 2), we still find (Fig. 1) that in the main belt, 2.5 AU from the Sun, thermal fatigue fragmentation is, in general, and within the errors of our model (Methods and Extended Data Fig. 9), more quickly than rock break-up by micrometeoroid impacts.

Because regolith formation by thermal fragmentation does not depend on asteroid size, this process occurs also on larger asteroids (for example, those varying in size from several tens to several hundreds of kilometres).

We argue that asteroid rock thermal fragmentation has observable implications: by breaking down rocks into smaller pieces and thus exposing new surface area, thermal fragmentation can provide a mechanism to make fresh regolith. Because the process of thermal fragmentation is strongly dependent on the value of ΔT, the rate of thermal fragmentation increases with decreasing perihelion distance (Extended Data Fig. 2). Observations show that the fraction of NEAs with fresh surfaces, whose reflectance spectra resemble those of ordinary chondrites ('Q-type' asteroids), is increasing with decreasing perihelion distance with a dependence[18] that mimics the curves of the NEA ΔT. From this result, a concrete, testable prediction is that more regolith should be found on NEAs that, during their chaotic dynamical evolution, are likely to have spent more time with smaller perihelion distances[19].

We also predict that small NEAs (for example those 100 m in radius) with low perihelion distances ($q < 0.3$ AU) could be eroded by thermal fragmentation and radiation pressure sweeping[20] on timescales shorter than their dynamical lifetime. For instance, at 0.3 AU the solar radiation pressure can remove grains with radii of the order of millimetres from the surface of an asteroid with a radius of 100 m (ref. 20); these grains can be produced by thermal fragmentation of centimetre-sized rocks in less than ~200 yr. Therefore, low-perihelion NEAs loose regolith at a rate of roughly 5×10^{-5} m yr^{-1}, implying that an object with a radius of 100 m would be completely eroded in about 2 Myr. Because thermal fragmentation is faster for C-type NEAs than for S-type NEAs (Fig. 1), we predict that erosion would be faster for carbonaceous NEAs, providing an explanation for the shortage of low-albedo, carbonaceous Aten-type NEAs[10].

METHODS SUMMARY

Rock comminution by micrometeoroid impacts on asteroids. We calculate the impact probability of micrometeoroids of the zodiacal dust cloud[13] on the Moon, on a typical NEA and on MBAs using the method of ref. 14 but without imposing any impact velocity cut-off. The ratio of the rock survival times on NEAs and MBAs to the known lunar value[12] is proportional to the respective impact probability ratios.

Thermal fatigue laboratory experiments. We perform two sets of temperature cycles (respectively 76 and 331, for a total of 407) on centimetre-sized samples of the meteorites Murchison (CM2) and Sahara 97210 (L/LL3.2). Before and after the first set of cycles, and after the second set, meteorites are imaged using a computed tomographic scanner. The scanned volumes are aligned and the increases in volume and length of several (21) cracks are measured.

Thermomechanical and fatigue crack growth model. Asteroid rock (Extended Data Fig. 8) temperatures are calculated for heliocentric distances between 0.3 and 2.5 AU. We use a well-established one-dimensional thermal model[15]. Model parameters are as follows[21]: rotational period, 6 h; thermal inertia, $\Gamma = 640$ J m^{-2} s$^{-0.5}$ K^{-1} (carbonaceous chondrite) or $\Gamma = 1{,}800$ J m^{-2} s$^{-0.5}$ K^{-1} (ordinary chondrite); bolometric albedo, $A = 0.02$ (carbonaceous) or $A = 0.1$ (ordinary). The cyclic spatial and temporal temperature fields are used to calculate the strains and stresses in the rocks and the stress intensity factors at the tip of surface cracks that, following Paris's law[17], grow downwards through the rocks in the direction perpendicular to the asteroid surface. The time needed to propagate a crack from 30 μm to a length equal to the rock diameter is then compared with the rock survival time against micrometeoroid impact (Fig. 1).

Online Content Any additional Methods, Extended Data display items and Source Data are available in the online version of the paper; references unique to these sections appear only in the online paper.

Received 28 June 2013; accepted 11 February 2014.
Published online 2 April 2014.

1. Veverka, J. *et al.* The landing of the NEAR-Shoemaker spacecraft on asteroid 433 Eros. *Nature* **413,** 390–393 (2001).
2. Yano, H. *et al.* Touchdown of the Hayabusa spacecraft at the Muses Sea on Itokawa. *Science* **312,** 1350–1353 (2006).
3. Gundlach, B. & Blum, J. A new method to determine the grain size of planetary regolith. *Icarus* **223,** 479–492 (2013).
4. Housen, K. R., Wilkening, L. L., Chapman, C. R. & Greenberg, R. Asteroidal regoliths. *Icarus* **39,** 317–351 (1979).
5. Hörz, F. & Cintala, M. Impact experiments related to the evolution of planetary regoliths. *Meteorit. Planet. Sci.* **32,** 179–209 (1997).
6. Housen, K. R. & Holsapple, K. A. Ejecta from impact craters. *Icarus* **211,** 856–875 (2011).
7. McFadden, L., Eppes, M., Gillespie, A. & Hallet, B. Physical weathering in arid landscapes due to diurnal variation in the direction of solar heating. *Geol. Soc. Am. Bull.* **117,** 161–173 (2005).
8. Luque, A., Ruiz-Agudo, E., Cultrone, G., Sebastián, E. & Siegesmund, S. Direct observation of microcrack development in marble caused by thermal weathering. *Environ. Earth Sci.* **62,** 1375–1386 (2011).
9. Viles, H. *et al.* Simulating weathering of basalt on mars and earth by thermal cycling. *Geophys. Res. Lett.* **37,** L18201 (2010).
10. Mainzer, A. *et al.* Characterizing subpopulations within the near-earth objects with NEOWISE: preliminary results. *Astrophys. J.* **752,** 110–126 (2012).
11. Michel, P. & Richardson, D. C. Collision and gravitational reaccumulation: possible formation mechanism of the asteroid Itokawa. *Astron. Astrophys.* **554,** L1 (2013).
12. Hoerz, F., Schneider, E., Gault, D. E., Hartung, J. B. & Brownlee, D. E. Catastrophic rupture of lunar rocks: a Monte Carlo simulation. *Moon* **13,** 235–258 (1975).
13. Nesvorný, D. *et al.* Cometary origin of the zodiacal cloud and carbonaceous micrometeorites. implications for hot debris disks. *Astrophys. J.* **713,** 816–836 (2010).
14. Briani, G., Morbidelli, A., Gounelle, M. & Nesvorný, D. Evidence for an asteroid-comet continuum from simulations of carbonaceous microxenolith dynamical evolution. *Meteorit. Planet. Sci.* **46,** 1863–1877 (2011).
15. Spencer, J. R., Lebofsky, L. A. & Sykes, M. V. Systematic biases in radiometric diameter determinations. *Icarus* **78,** 337–354 (1989).
16. Čapek, D. & Vokrouhlický, D. Thermal stresses in small meteoroids. *Astron. Astrophys.* **519,** A75 (2010).
17. Janssen, M., Zuidema, J. & Wanhill, R. *Fracture Mechanics* 2nd edn, 207–213 (Spon, 2004).
18. Marchi, S., Magrin, S., Nesvorný, D., Paolicchi, P. & Lazzarin, M. A spectral slope versus perihelion distance correlation for planet-crossing asteroids. *Mon. Not. R. Astron. Soc. Lett.* **368,** L39–L42 (2006).
19. Marchi, S., Delbo, M., Morbidelli, A., Paolicchi, P. & Lazzarin, M. Heating of near-Earth objects and meteoroids due to close approaches to the sun. *Mon. Not. R. Astron. Soc.* **400,** 147–153 (2009).
20. Jewitt, D. The active asteroids. *Astron. J.* **143,** 66–80 (2012).
21. Opeil, C. P., Consolmagno, G. J. & Britt, D. T. The thermal conductivity of meteorites: new measurements and analysis. *Icarus* **208,** 449–454 (2010).

Acknowledgements This work was supported by the French Agence National de la Recherche (ANR) SHOCKS, the BQR of the Observatoire de la Côte d'Azur (OCA), the University of Nice-Sophia Antipolis, the Laboratory GeoAzur and the French National

Program of Planetology (PNP). We benefited from discussions with K. J. Walsh and W. F. Bottke. A. Morbidelli helped with the dynamical model. M. Moumni, J.-M. Hiver and G. Thomas helped with the experiments, X-ray tomography and early data analysis. G.L. conducted part of his work as an INSU-CNRS delegate. S.M. acknowledges support from NASA SSERVI. The comments of S. Byrne improved this work fundamentally. Computations and data analysis were done on the CRIMSON cluster at OCA.

Author Contributions M.D. and S.M. inspired the laboratory experiments, which were designed by G.L., C.G., P.M., C.V. and M.D. Experiments were carried out by G.L. N.M. and M.D. developed the methods of crack volume and length measurement. N.M. and M.D. applied the methods to the experimental data. J.W., K.T.R. and M.D. worked on the thermomechanical model that was mostly developed and used by J.W. The scientific analysis was directed by M.D. with frequent discussions with G.L., P.M., J.W., K.T.R. and C.G. Computer codes were developed by M.D., J.W. and N.M. M.D., J.W., G.L., P.M., N.M., K.T.R. and C.G. jointly drafted the manuscript, with all authors reviewing it and contributing to its final form.

Author Information Reprints and permissions information is available at www.nature.com/reprints. The authors declare no competing financial interests. Readers are welcome to comment on the online version of the paper. Correspondence and requests for materials should be addressed to M.D. (delbo@oca.eu) or G.L. (libou@oca.eu).

METHODS

Rock comminution by micrometeoroid impacts on asteroids. On asteroids, like on the Moon, regolith formation via break-up of rocks by micrometeoroid impacts is accomplished by two mechanisms: rupture and erosion[5]. On the Moon, rock survival time against micrometeoroid rupture is in the range between 2 and 20 Myr for rock diameters between 1 and 10 cm (ref. 12). This survival time on asteroids can be calculated by the following method.

First, given the relation between the rock diameter and the meteoroid impact energy required for the rock rupture[12], and assuming densities of 1 g cm^{-3} for cometary meteorids and 3.5 g cm^{-3} for asteroidal meteoroids, one can find that rocks 1–10 cm in size are broken up by sub-millimetre meteoroids[5]. Meteoroids of this size dominate the zodiacal dust cloud[13,14], 90% of which is constituted by cometary dust[13].

Next, given the orbital distribution of these cometary particles[13], we use a classical method[14], but without imposing an impact velocity cut-off, to calculate the average intrinsic impact probabilities (p, for example, the number of impacts per meteoroid on a circular cross-section of radius 1 km per year) and the average impact velocity (v_i) of meteoroids on the Moon, a typical NEA ($a = 1$ AU, $e = 0.3$, $i = 0.15$ rad; where a is the semimajor axis of the orbit, e is its eccentricity and i is its inclination) and an average MBA. We find that $p = 8.0 \times 10^{-18}$ and $v_i = 11$ km s^{-1} for the Moon, that $p = 9.5 \times 10^{-18}$ and $v_i = 15$ km s^{-1} for a typical NEA, and that $p \approx 1 \times 10^{-18}$ and $v_i = 10$ km s^{-1} for an average MBA. Neglecting the different impact velocities (because the energy for rock break-up, E_b, is a shallow function of the impact velocity[12]: $E_b \propto v_i^{0.7}$), the rate of meteoroid impacts per unit time and unit surface, Φ, on the Moon, NEAs and MBAs is proportional to p. We thus have $\Phi_{NEA} \approx \Phi_{Moon} \approx 10\Phi_{MBA}$.

Hence, the rock survival time on NEAs is similar to that on the Moon (we assume that they are the same in Fig. 1), whereas on MBAs rocks survive about ten times longer. For rocks in the size range 1–10 cm, erosion removes surface material at a rate of order 1 mm Myr^{-1} (refs 5,12), requiring at least ~10–100 Myr to comminute rocks on the Moon and on NEAs, and 0.1–1 Gyr on MBAs.

Thermal fatigue laboratory experiments. Our experimental protocol is presented in Extended Data Fig. 1. To 'image' the cracks in the meteorites at three stages of thermal fatigue (before the temperature cycles, t_0; after 76 cycles, t_1; and after 407 cycles, t_2), we use a Phoenix Nanotom computed tomography scanner that produces three-dimensional data cubes of approximately 1,000^3 voxels or 2,000^3 voxels depending on the spatial resolution, $\Delta\lambda$. Specifically, for Murchison $\Delta\lambda = 12.5$, 13, 13 μm, and for Sahara 97210 $\Delta\lambda = 3.75$, 4, 4.5 μm, at t_0, t_1 and t_2, respectively. The higher spatial resolution for Sahara 97210 is necessary because this meteorite has fewer and thinner cracks than Murchison. The orientation of each sample within the scanned volume varies between t_0, t_1 and t_2. Because the determination of crack growth requires the comparison of sizes of same cracks at t_0, t_1 and t_2, we precisely align and scale the meteorites within the computed tomography scans. To do this, several distinctive features in the meteorites, such as metal-rich inclusions of a few voxels in volume, are visually identified at t_0, t_1 and t_2, and used as position markers. Because the objects are not initially aligned, the same marker does not necessarily have the same coordinates at t_0, t_1 and t_2. For each meteorite, we determine the matrices that best transform the marker coordinates at t_1 and at t_2 to those at t_0. A Monte Carlo method is used to calculate the best transformation matrix by minimizing the square of the distance between the marker coordinates at t_0 and the transformed ones. We then use the procedure TRANSFORM_VOLUME, written in IDL by Martin Downing, to apply the transformations to align the computed tomography volumes at t_1 and t_2 with those at t_0 (see www.idlcoyote.com/programs/transform_volume.pro; IDL is developed by Exelis Visual Information Solutions Incorporated (http://www.exelisvis.com/ProductsServices/IDL.aspx)). The accuracy of the final alignment is, in general, of the order of 1 voxel.

We develop a method for the determination of the volume and length of the cracks that is not sensitive to the absolute value of the voxel intensity. This is because the X-ray intensity is not constant between different computed tomography scans, causing variability of the meteorite voxel counts, the background counts and the noise level among scans of the same meteorite. We measure the crack width at all voxels along the crack length, and the crack height, within a volume of interest of the meteorite that includes the crack or a portion thereof. We use the same volume of interest for the same crack at t_0, t_1 and t_2 on the aligned computed tomography scans. The volume of interest, different for each different crack, is defined as follows. We chose a plane (for example, the x–y plane) along which the crack mainly extends, and we extract several slices from the computed tomography volume parallel to the considered plane. Typically, we consider ten slices. For each slice, we draw a segmented line that follows the crack as closely as possible; the same number of segments is used for each slice. For each segment and for each slice, we determine the width of the crack and the width uncertainty in the direction perpendicular to the segment at every point. We calculate the volume of the crack portion from

$$V = \sum_{i=n}^{N} \sum_{j=1}^{M_i} \sum_{k=1}^{L_{i,j}} W_{i,j,k} g_{i,j,k} (\Delta\lambda)^3 \quad (1)$$

where $W_{i,j,k}$ is the crack width at the kth position along the jth segment of length $L_{i,j}$ on the ith slice of the volume of interest. The initial and final slices are n and N, respectively, and M is the number of segments. The value of $g_{i,j,k}$ is equal to 1 or 0 depending on whether the width determination was accepted or deemed invalid using the procedure described in the next paragraph. As for the width of the crack, we use the full-width at half-maximum of the Gaussian function that best fits the intensity profile of the meteorite perpendicular to the segment. We prefer to give the volume of the crack instead of its average width. This is because cracks typically have large width variations throughout their volume. The accuracy of the crack width determination is estimated at each point by a Monte Carlo method: we attempt to fit a Gaussian function up to 9,000 times to the meteorite intensity profile to have at least 30 valid fits. Gaussian random noise (with a standard deviation given by noise in the computed tomography data) is added to the voxel counts in each iteration. If at t_0, t_1 or t_2 the dispersions of the widths, centres or amplitudes of the Gaussian fits are larger than some threshold values that, once tuned, are kept constant for both meteorites at all times, the point is deemed not to contain a crack and is excluded from the sums of equation (1) at t_0, t_1 and t_2 (by setting the corresponding value of g to zero).

The crack length measurement method is similar to the one used for the crack volume determination, but with two main differences. First we select a volume of interest that includes one or more crack tips, typically by constructing the segments such that they partly extend beyond the crack tips. This is because any potential increase in the length of the crack due to temperature cycling must happen at the crack tip. Next, for each slice, we count the number of voxels where $g = 1$, that is, where a valid crack width is found. We note that, contrary to the method used for the measurement of the crack volume, we do not set $g = 0$ at t_0, t_1 and t_2 if $g = 0$ at t_0, t_1 or t_2. We observe that our method fails to fit a Gaussian function to the meteorite intensity profile beyond the crack tip and that the dispersions of the Gaussian parameters can become very large, indicating the absence of a crack. The length of the crack averaged over the slices of interest is given by

$$L = \frac{1}{N-n} \sum_{i=n}^{N} \sum_{j=1}^{M_i} \sum_{k=1}^{L_{i,j}} g_{i,j,k} \Delta\lambda$$

We take the standard error of the mean as the error in the length of the crack. This same process is applied to the computed tomography scans of the meteorites at t_0, t_1 and t_2 to measure the evolution of crack length as a function of the number of the cycles.

We were concerned that processes other than thermal fatigue could affect crack growth in our experiments. For example, the water freeze–thaw effect has an important role in the opening of cracks in terrestrial rocks. Atmospheric moisture in the cracks of our specimens could, in principle, have been present and may have facilitated the opening and the lengthening of cracks. However, we rule out this mechanism in our experiments in two ways. First, temperature cycling of our samples is carried out under an anhydrous atmosphere at a pressure of 1 bar. Next, before the temperature cycling begin, the meteorite specimens are exposed to a vacuum of ~10^{-2} bar and later immersed in an argon–nitrogen gas for several hours to eliminate potential traces of humidity.

We were also concerned that the transport of the meteorites from the climatic chamber to the computed tomography scanner may have stressed the samples and affected the crack growth. We rule out this effect by obtaining scans of a sample of Murchison that was transported from the climatic chamber to the scanner, but not subjected to temperature cycles. We repeat this procedure twice. Visual inspection of the scan images shows no obvious change in the position, width and length of the cracks, and no formation of new cracks. Also, no fragments flaking off from the surface of the Murchison specimen were found (analysis of the scans shows no obvious change in the surface of the specimen). Volume measurements of several cracks in the specimen of Murchison that was transported but not subjected to temperature cycles show no variation within the error bars (Extended Data Fig. 5).

Thermomechanical and fatigue crack growth model. Our thermomechanical and crack growth model is based on the coupling of a well-established thermal diffusion model[15], linear elastic fracture mechanics and a well-established fatigue crack growth law (Paris's law[17]). Paris's law relates the rate at which the crack length, a, grows as a function of the number of cycles, N, to the maximum stress intensity factor[17] excursion, ΔK_I:

$$\frac{da}{dN} = C[\Delta K_I(a)]^n \quad (2)$$

where C and n are material properties fitted to experimental fatigue data[22].

First, we use a well-established thermal model[15] to solve the one-dimensional heat diffusion problem and calculate the temperature, $\bar{T}(x,t)$, as a function of time, t, and depth, x, in a layer of rocks of different sizes at the asteroid surface (Extended Data Fig. 8). We use the same boundary conditions and finite-difference implementation as in ref. 15, but we adopt a higher spatial resolution of 0.025 times the heat penetration depth[15], and a maximum depth is set at 1,024 resolution elements. We model a surface area at the equator. We set the initial temperatures to zero, and we let the model evolve until the mid-day temperature of the surface at the asteroid rotation $N+1$ is within 0.1 K of the temperature at the rotation N. The parameters that control the values of $\bar{T}(x,t)$ are the thermal inertia, Γ, the bolometric albedo, A, and the asteroid rotation period, P. We model two cases whose thermal parameters, taken from ref. 21, are $\Gamma = 640\,\mathrm{J\,m^{-2}\,s^{-0.5}\,K^{-1}}$, $A = 0.02$ and $\Gamma = 1{,}800\,\mathrm{J\,m^{-2}\,s^{-0.5}\,K^{-1}}$, $A = 0.1$, corresponding to those of carbonaceous and ordinary chondrites, respectively (Extended Data Table 1). We set $P = 6$ h, which is appropriate for small asteroids. The thermal model does not account for the rock boundaries, which increase the porosity of the medium, resulting in lower thermal inertia and probably increasing the thermal gradients.

To model the temperatures in the meteorites in our laboratory experiments, we modify the thermal model by solving the heat diffusion problem for an idealized spherical, homogeneous and isotropic body (with the thermal properties of a carbonaceous or an ordinary chondrite, as above) whose surface temperature is forced to follow a sinusoidal function in time with a period of 2.2 h and an amplitude of 190 K, independently of the mineralogy and equal to those imposed on the meteorites in the climatic chamber.

Next we compute the time-dependent macroscopic stress field, $\Sigma(x,t)$, associated with the transient thermal gradients following established methods[16]. Additionally, we account for the microscopic stress fields, $\sigma(x;y,t)$, that develop as a result of the heterogeneous microstructure of the material, assuming different thermal expansion coefficients for the matrix and the chondrules (the two main components of those meteorites). Finally, the maximum stress intensity excursion experienced over a temperature cycle is used in Paris's law to compute the growth rate of a planar crack originating from the surface of rock (a flow chart of the procedure is shown in Extended Data Fig. 6).

Consider a two-scale body (Extended Data Fig. 6) with two macroscale observable quantities, namely macroscopic stress, $\Sigma(x,t)$, and macroscopic temperature, $\bar{T}(x,t)$, which are functions of the macroscale material coordinate x. Likewise, the microscale quantities $\sigma(x;y,t)$ and $T(x;y,t)$ are functions of the microscale material coordinate y. The macroscale quantities are related to the microscale quantities through a suitable volumetric average, that is, $\Sigma(x,t) = v^{-1}\int_v \sigma(x;y,t)\,\mathrm{d}v$ and $\bar{T}(x,t) = v^{-1}\int_v T(x;y,t)\,\mathrm{d}v$. The microscale is heterogeneous, approximated by spherical inclusions embedded in a matrix. The linear thermoelastic properties of the inclusions are as follows: bulk modulus, K_i; shear modulus, μ_i; thermal expansion coefficient, α_i. Likewise, the linear thermoelastic properties of the matrix are K_m, μ_m and α_m. The macroscale is homogenized with effective linear thermoelastic properties of $\bar{K}$, $\bar{\mu}$ and $\bar{\alpha}$ (Extended Data Table 1).

The macroscopic stresses, $\Sigma(x,t)$, develop as a result of spatial gradients in the macroscopic transient temperature field, $\bar{T}(x,t)$. The formulation of our macroscopic stress field is very similar to that in ref. 16. We confirm that the macroscopic stress fields used in this study agree with finite-element analysis.

In general, additional microscale stresses in excess of the macroscale stresses are generated by both the heterogeneous microstructure, that is, $\alpha_\mathrm{i} \neq \alpha_\mathrm{m}$, as well as microscale gradients in the microscale temperature field, that is, $\nabla_y T(x;y,t)$. For simplicity, we assume that the microscale temperature field is equal to the macroscopic temperature field at a particular macroscale location, that is, $T(x;y,t) = \bar{T}(x,t)$, thus neglecting any microscopic gradients in the microscopic temperature field.

Let the spherical inclusions of radii r_c be located on a cubic lattice with lattice parameter 2ℓ. The microscopic stress tensor associated with the thermal mismatch, σ^TM, is defined such that $\sigma(x;y,t) = \Sigma(x,t) + \sigma^\mathrm{TM}(x;y,t)$ and is calculated through a self-consistent, two-phase composite spheres approach. The method approximates the periodic array of spherical inclusions as a two-phase spherical assemblage with appropriate boundary conditions[23]. This approach approximates the stress-field interactions between inclusions[23]. The thermoelastic constitutive relations for both the inner solid sphere and outer spherical shell are expressed as

$$\sigma^\mathrm{TM} = \begin{cases} \left(K_\mathrm{i} - \frac{2}{3}\mu_\mathrm{i}\right)(I:\varepsilon^\mathrm{TM})I \\ \quad + 2\mu_\mathrm{i}\varepsilon^\mathrm{TM} - 3K_\mathrm{i}\alpha_\mathrm{i}\Delta\bar{T}I & 0 \le \|y\| \le r_\mathrm{c} \\ \left(K_\mathrm{m} - \frac{2}{3}\mu_\mathrm{m}\right)(I:\varepsilon^\mathrm{TM})I \\ \quad + 2\mu_\mathrm{m}\varepsilon^\mathrm{TM} - 3K_\mathrm{m}\alpha_\mathrm{m}\Delta\bar{T}I & r_\mathrm{c} < \|y\| \le \ell \end{cases}$$

where tensorial notation is used, ε^TM is the total microscopic linear strain associated with the thermal mismatch, and I is the identity (where the tensor product $A:B$ is defined as $A_{ij}B_{ij}$).

The microscopic equilibrium equation yields the following solution for the microscopic hoop stresses associated with thermal mismatch:

$$\sigma^\mathrm{TM}_{\theta\theta}(x;y,t) = \begin{cases} K^\mathrm{TM}\Delta\alpha\Delta\bar{T}(x,t)(r_\mathrm{c}^3\ell^{-3} - 1) & 0 \le \|y\| \le r_\mathrm{c} \\ \frac{1}{2}K^\mathrm{TM}\Delta\alpha\Delta\bar{T}(x,t)(r_\mathrm{c}^3\|y\|^{-3} + r_\mathrm{c}^3\ell^{-3}) & r_\mathrm{c} < \|y\| \le \ell \end{cases}$$

where $\Delta\alpha = \alpha_\mathrm{i} - \alpha_\mathrm{m}$, $\Delta\bar{T}(x,t) = \bar{T}(x,t) - \bar{T}_0$, and K^TM is defined as

$$K^\mathrm{TM} = \frac{12\mu_\mathrm{m}K_\mathrm{i}K_\mathrm{m}}{3K_\mathrm{i}K_\mathrm{m} + 4\mu_\mathrm{m}K_\mathrm{m} + 4\mu_\mathrm{m}(K_\mathrm{i} - K_\mathrm{m})r_\mathrm{c}^3\ell^{-3}}$$

Returning to the body shown in Extended Data Fig. 6, we now consider the introduction of a planar crack originating from the surface of this body. On the macroscale the crack cuts through the diameter of the rock, and on the microscale the crack is assumed to cut through the array of chondrules. To perform the fatigue crack propagation analysis, it is necessary to obtain an expression for the stress intensity factor, K_I, which is dependent on both the loading and the geometry[17].

The stress intensity factor most closely associated with our geometry and loading conditions was obtained by ref. 24 as

$$K_\mathrm{I}(a,t) = \int_0^a \mathrm{d}\xi\, \frac{2e_\mathrm{n}^c \bullet \sigma(\xi,t)e_\mathrm{n}^c}{\sqrt{2\pi(a-\xi)}} \sum_{i=0}^{3} M_i \left(1 - \frac{\xi}{a}\right)^{i/2} \qquad (3)$$

where σ is the total microscopic tensorial stress field that would develop along the crack plane if the crack were not present, e_n^c is the unit normal to the crack plane and M_i are geometric parameters that may be found in ref. 24. To make use of the transient stress intensity factor of equation (3) in the solution of equation (2), it is necessary to obtain the maximum stress intensity factor excursion, $\Delta K_\mathrm{I}(a)$, experienced over a particular cycle. Because we are dealing with thermal cyclic stress, the crack tip experiences both tensile and compressive stresses over a full cycle; therefore, ignoring crack closure[25], the lowest stress intensity factor that the crack tip experiences is simply zero. The resulting nonlinear ordinary differential equation—equation (2) after substitution of equation (3)—is solved numerically by an adaptive fourth-order Runge–Kutta method, providing the crack size as a function of the number of thermal cycles.

Lastly, we develop a method for providing some degree of model validation and uncertainty quantification. The chondrule size, r_c, and spacing, ℓ, are known with a high degree of accuracy because these are measured from our computed tomography scans. However, we expect a ~30% relative uncertainty in the values of the thermophysical parameters because their values were obtained through direct measurement of meteorites[16,26–30]. We thus calculate our model for several sets of values of the thermophysical parameters that we choose to within 30% of the nominal parameter values, and find an order-of-magnitude change in the predicted number of thermal cycles required to achieve rock fragmentation. This implies an order-of-magnitude change in the survival time of rocks in Fig. 1 and, therefore, that thermal fragmentation remains dominant over meteoroid impacts as a regolith generation mechanism.

To the best of our knowledge, no systematic fatigue crack growth experiments have been conducted on asteroid or meteorite materials. Therefore, we took the Paris's law parameters of Carrara marble[22], which satisfactorily predict the fatigue crack growth observed in our experiments (inset of Extended Data Fig. 7). Paris's law parameters dramatically different from those of Carrara marble will result in greater model–experiment discrepancy (Extended Data Fig. 9), which is defined as

$$\left| \frac{a_\mathrm{model}(N) - a_\mathrm{exp}(N)}{a_\mathrm{exp}(N) - a_\mathrm{exp}(N=0)} \right| \qquad (4)$$

where a_model and a_exp are the crack lengths predicted by the model and those measured from our laboratory experiments, respectively. Even if the Paris's law exponent were 30% larger than the assumed value (Extended Data Fig. 9), the model would still predict that thermal fragmentation is the dominant regolith generation mechanism over comminution by micrometeoroid impact.

22. Migliazza, M., Ferrero, A. & Spagnoli, A. Experimental investigation on crack propagation in Carrara marble subjected to cyclic loads. *Int. J. Rock Mech. Min. Sci.* **48,** 1038–1044 (2011).
23. Christensen, R. M. *Mechanics of Composite Materials* 31–58 (Krieger, 1979).
24. Glinka, G. & Shen, G. Universal features of weight functions for cracks in mode I. *Eng. Fract. Mech.* **40,** 1135–1146 (1991).
25. Suresh, S. *Fatigue of Materials* 2nd edn, 505–507 (Cambridge Univ. Press, 1998).

26. Medvedev, R. V., Gorbatsevich, F. I. & Zotkin, I. T. Determination of the physical properties of stony meteorites with application to the study of processes of their destruction. *Meteoritika* **44,** 105–110 (1985).
27. Flynn, G. J. Physical properties of meteorites and interplanetary dust particles: clues to the properties of the meteors and their parent bodies. *Earth Moon Planets* **95,** 361–374 (2004).
28. Hazen, R. M. Temperature, pressure and composition: structurally analogous variables. *Phys. Chem. Miner.* **1,** 83–94 (1977).
29. Anderson, O., Isaak, D. & Oda, H. Thermoelastic parameters for six minerals at high temperature. *J. Geophys. Res.* **96,** 18037–18046 (1991).
30. Smyth, J. R. High temperature crystal chemistry of fayalite. *Am. Mineral.* **60,** 1092–1097 (1975).

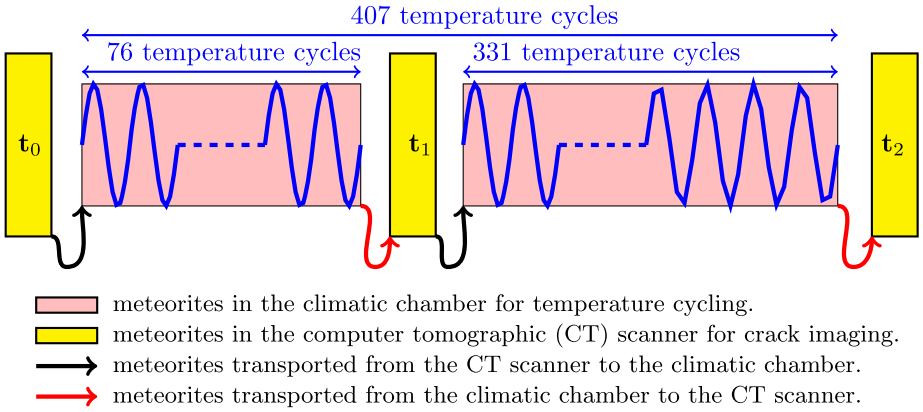

Extended Data Figure 1 | Protocol of the thermal fatigue laboratory experiments. We place samples of Murchison and Sahara 97210 ~1 cm in size in a climatic chamber where the air temperature is forced to follow cycles between 250 and 440 K with a period of 2.2 h. The air is anhydrous and at a pressure of 1 bar. Meteorites are analysed by X-ray computed tomography before the temperature cycles begin (t_0), after 76 cycles (t_1) and after 407 cycles (t_2). From the scans, we measure (Methods) the increases in the volume and length of cracks as functions of the number of temperature cycles.

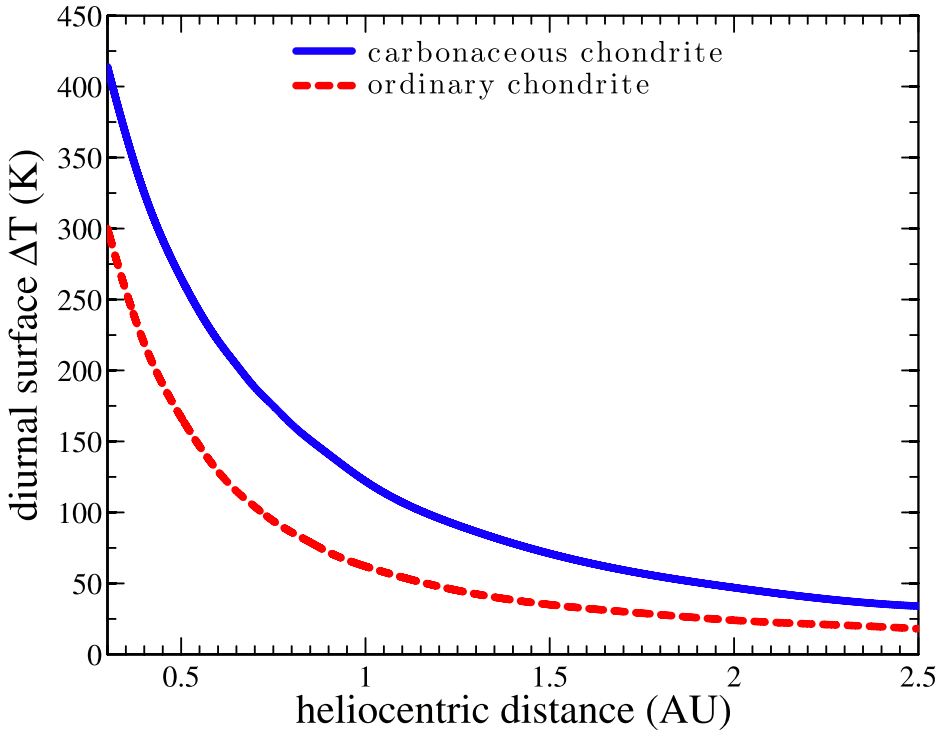

Extended Data Figure 2 | Diurnal surface temperature excursions on asteroids as a function of the distance to the Sun. Temperatures are calculated at the equator of a spherical asteroid by means of an asteroid thermophysical model[15] (Methods), assuming the thermal properties (Extended Data Table 1) of a carbonaceous chondrite (the CM2 Cold-Bokkevel) and that of an ordinary chondrite (the H5 Cronstad). The asteroid rotation period is set to 6 h. The bolometric albedo is assumed to equal 0.02 for the carbonaceous chondrite and 0.1 for the ordinary chondrite.

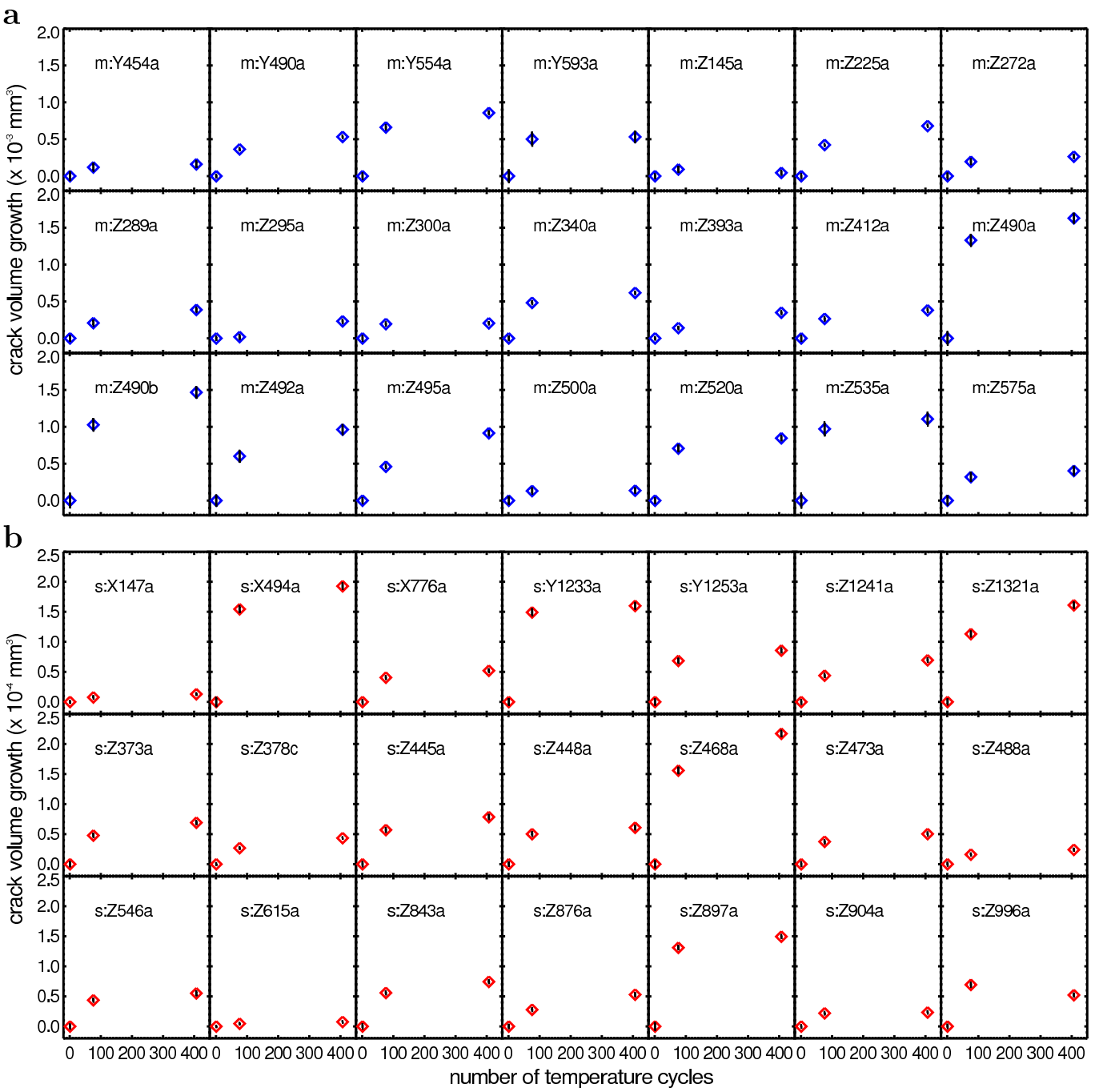

Extended Data Figure 3 | Volume growth of individual cracks as a function of the number of temperature cycles. **a**, Murchison; **b**, Sahara 97210. Statistical errors are 1σ and are in general smaller than the plot symbols. The crack volume is measured by the procedure described in Methods. Cracks are labelled with the value of the initial slice of the corresponding volume of interest. If different volumes of interest are defined with the same initial tomographic slice, the last letter of the crack label is used to identify the crack (for example Z387a, Z378b, Z378c).

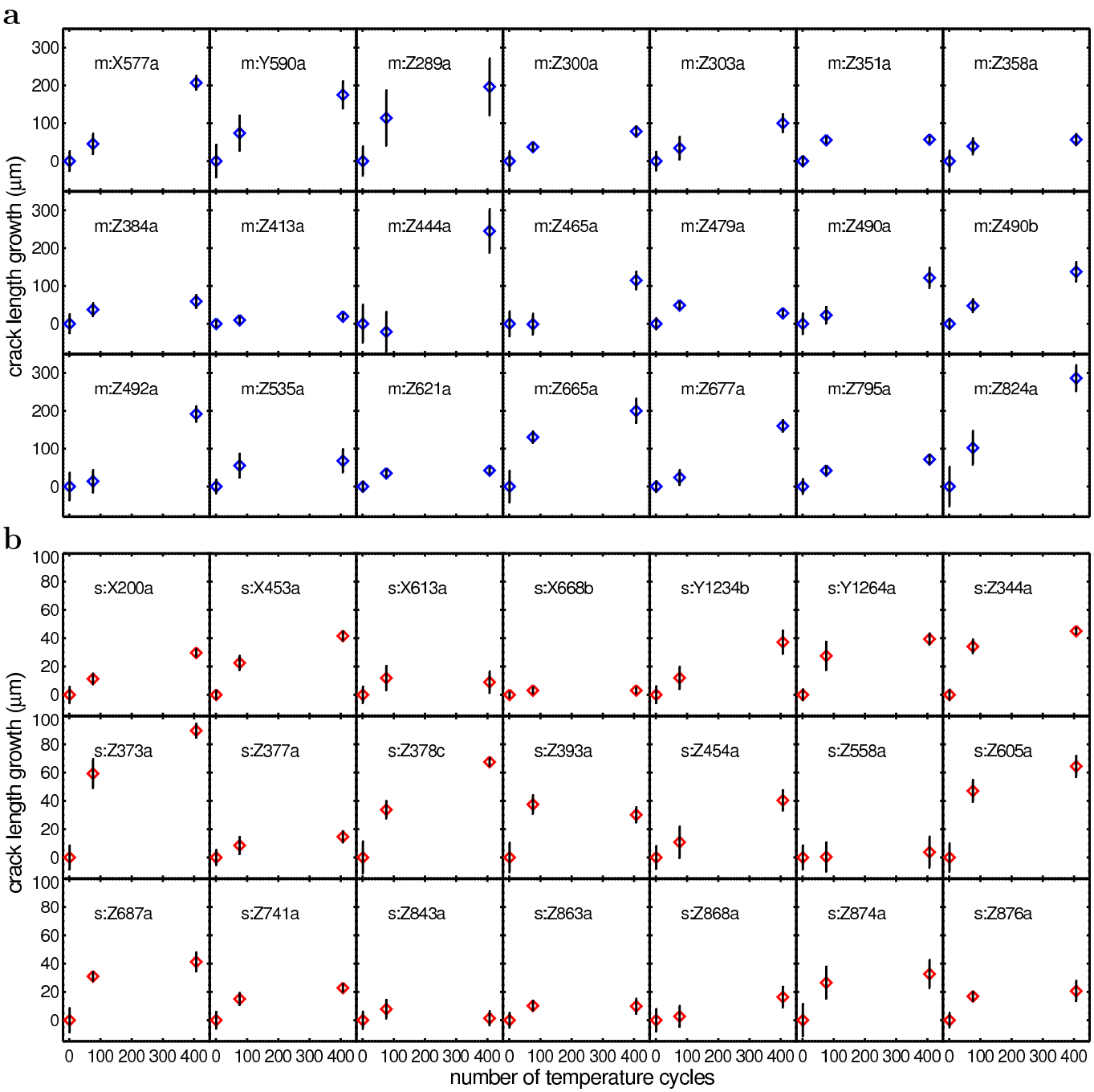

Extended Data Figure 4 | Length growth of individual cracks as a function of the number of temperature cycles. **a**, Murchison; **b**, Sahara 97210. Statistical errors are 1σ. The crack length is measured by the procedure described in Methods. See Extended Data Fig. 3 for crack labelling.

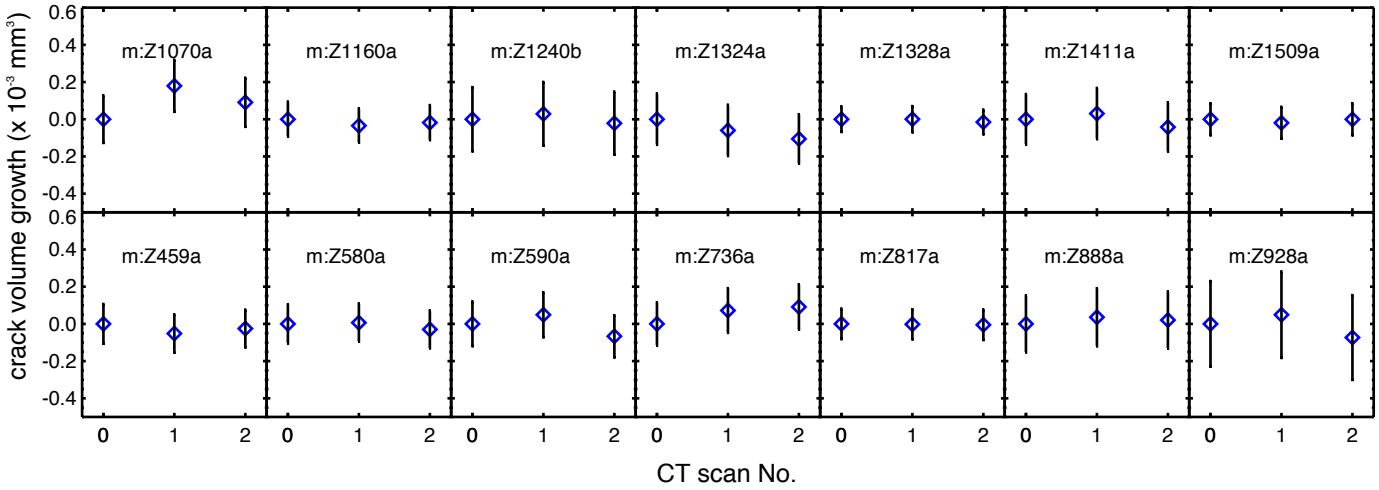

Extended Data Figure 5 | No crack growth with no temperature cycles. Volume growth of individual cracks in a specimen of Murchison that was transported from the climatic chamber to the computed tomography scanner without temperature cycling. Statistical errors are 1σ. The crack volume is measured by the procedure described in Methods. We performed three computed tomography scans: scan no. 0 (the label on the *x* axis) was obtained on the sample of the meteorite as it was received; scan no. 1 was carried out after the meteorite was transported from the computed tomography scanner to the climatic chamber and back; and scan no. 2 was obtained after a second transportation of the meteorite.

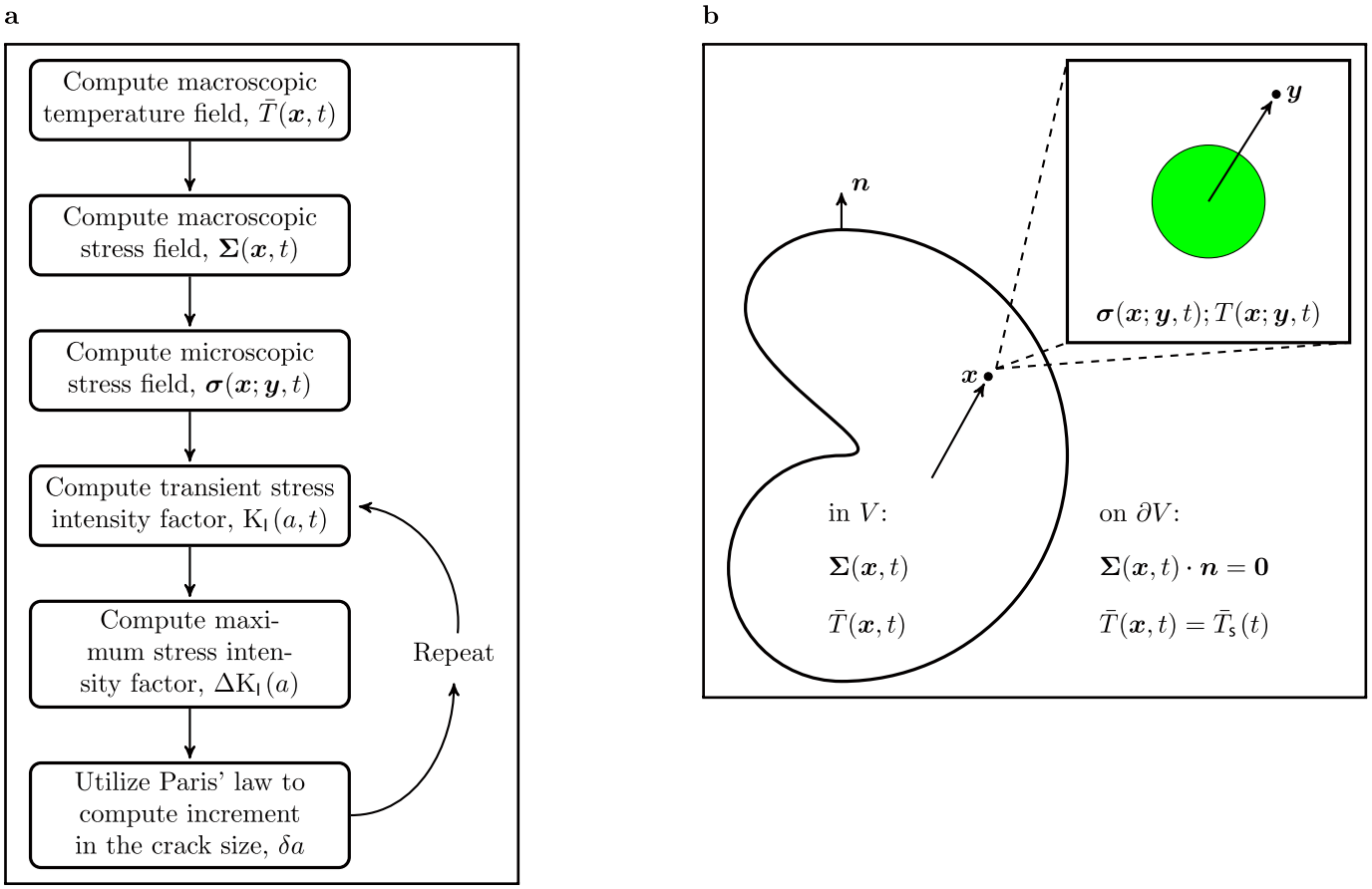

Extended Data Figure 6 | Schematics of our micromechanical model. **a**, Flow chart; **b**, schematic of the two-scale representation (Methods). ∂V is the surface of a body of volume V. A microscopic spherical inclusion, centred at the macroscopic point x is embedded in an infinite, effectively homogenized matrix. A general microscopic material point is located at a distance y measured from the centre of its nearest spherical inclusion located at x. The spherical inclusions of radius r_c are located at the vertices of a cubic lattice with lattice parameter 2ℓ.

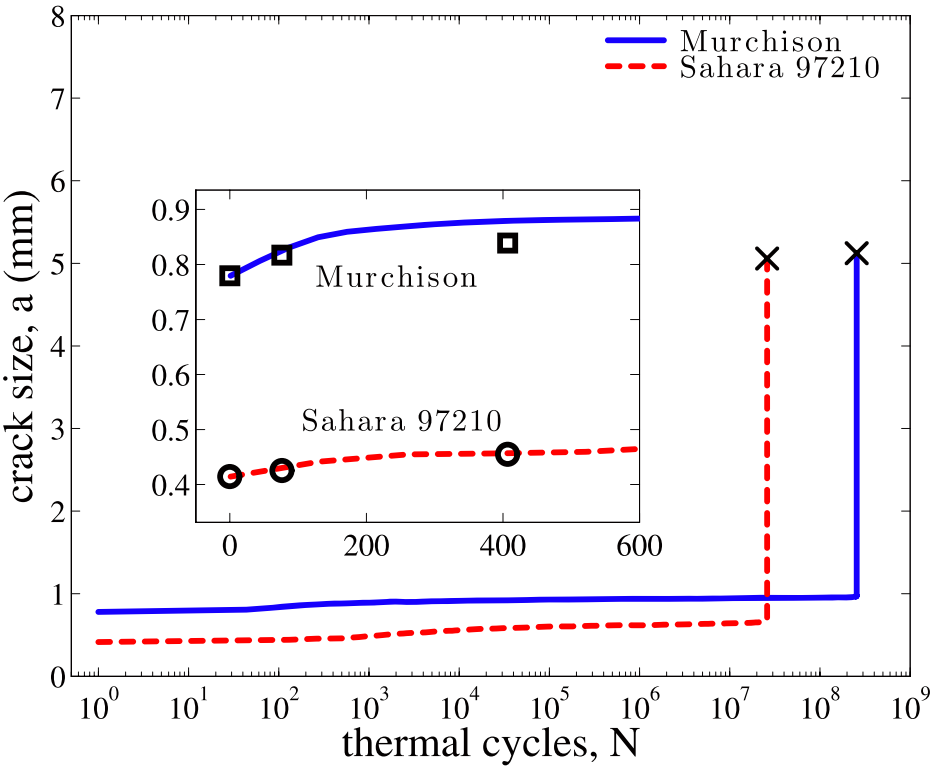

Extended Data Figure 7 | Comparison of theoretical and measured crack growth. Crack size is shown as a function of the number of temperature cycles predicted by our model and compared with experimental data for two particular cracks. Main plot: pre-existing cracks of 0.76 mm for Murchison and 0.41 mm for Sahara 97210 originating at the surface of the samples progressively propagate through the respective meteorites. The crosses indicate that the crack has reached a length equal to the meteorite diameter; therefore, full fragmentation occurs. Inset: comparison of the model with the length growth measured in our experiments for the same two cracks.

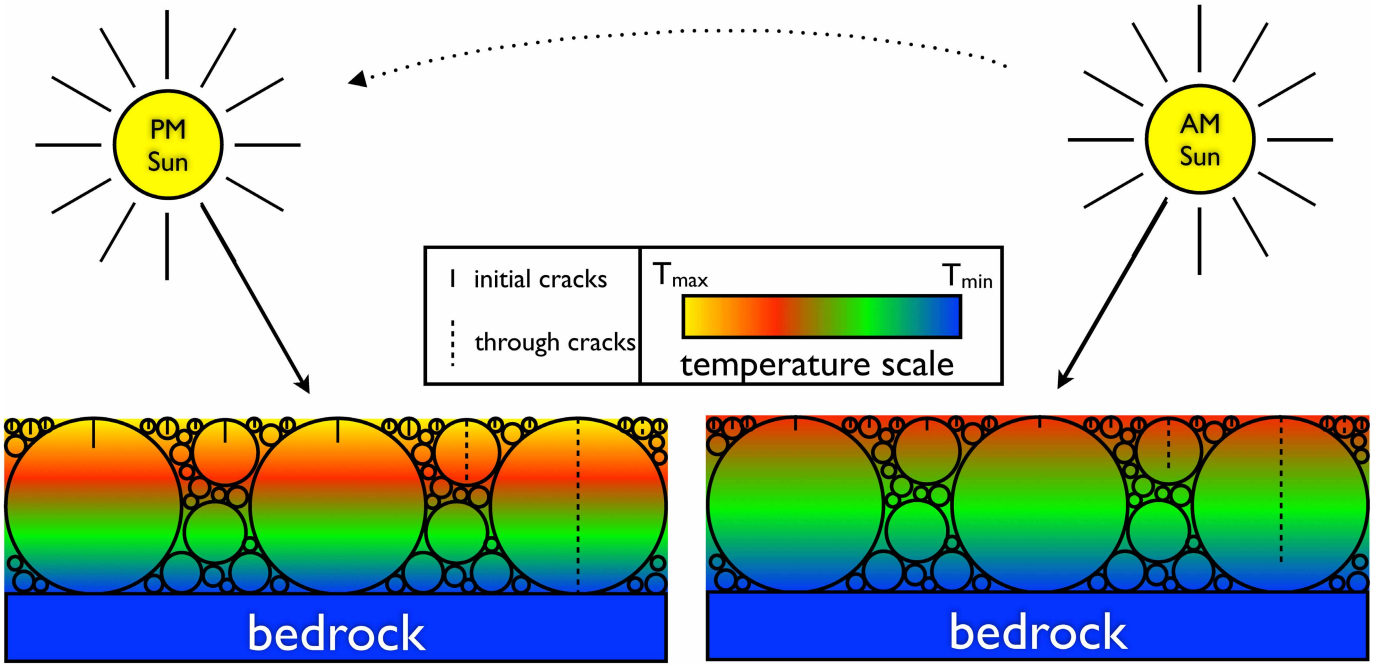

Extended Data Figure 8 | Schematic of the surface layer of rocks modelled in this work. The schematic is inspired by Fig. 3 of ref. 7. The layer is composed of rocks with different sizes. The rocks are subjected to spatial and temporal temperature gradients at the surface of the asteroid due to changes in the diurnal solar heating. The bottom of the rock layer is assumed to be in contact with bedrock that is deep enough to have a constant temperature. Temperatures are calculated assuming a uniform medium (no rock boundaries). This is probably a conservative approximation, because the presence of voids between rocks may enhance the temperature gradients owing to a reduction in the thermal conductivity. When the model starts, all rocks have a surface crack of the same length (30 μm), represented by the thin vertical line. It is very likely that cracks of this size, similar to the grain size of meteorites, are present in asteroidal material. Crack growth is from top to bottom. Crack growth is modelled until the time (survival time) the crack reaches the diameter of the rock (through-crack), and the rock is broken into two pieces. Rock survival times are shown in Fig. 1.

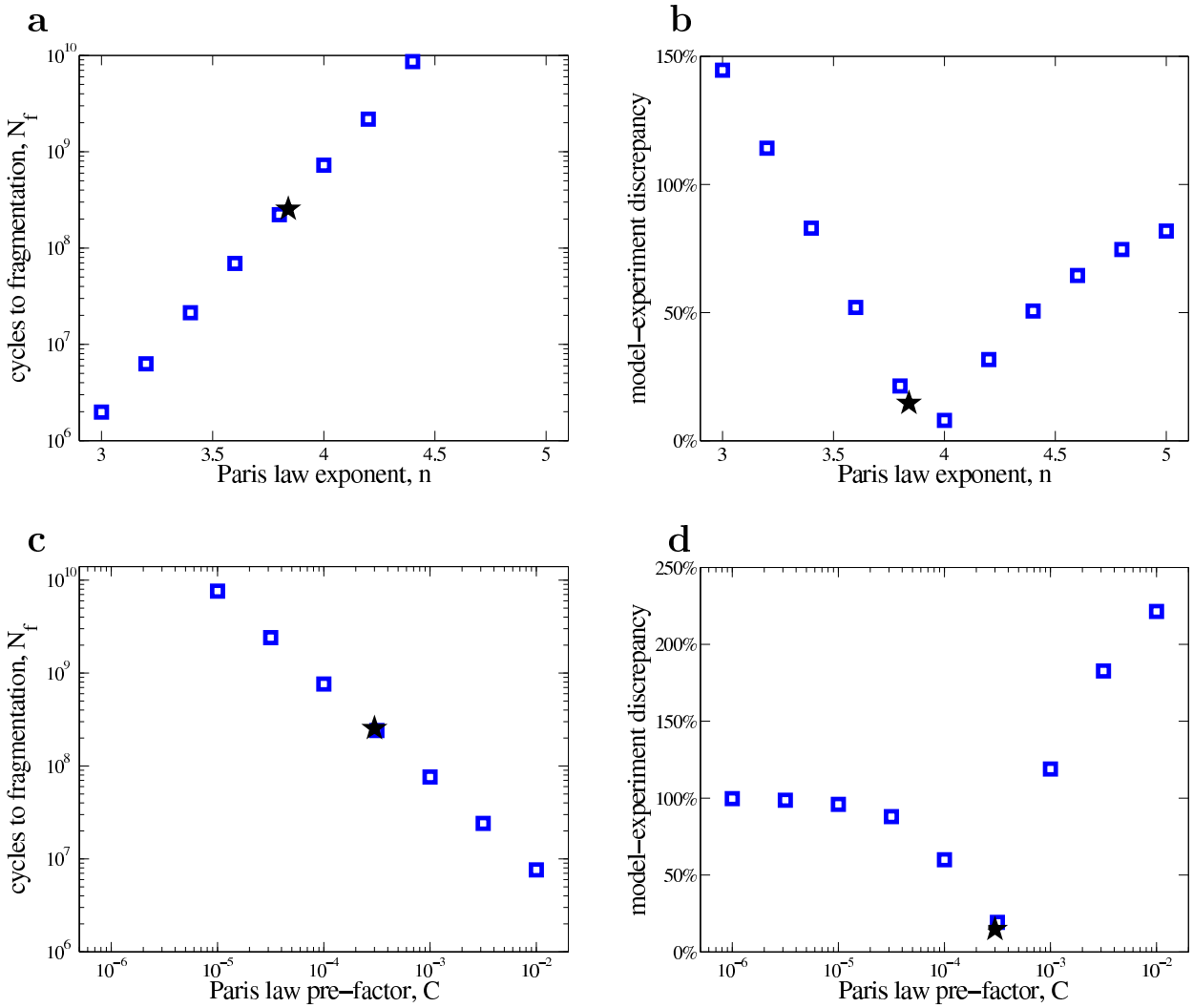

Extended Data Figure 9 | Sensitivity of the model results to variations in Paris's law parameters. The stars indicate model results for the nominal values of the parameters given in Extended Data Table 1. **a**, Number of temperature cycles until fragmentation for a rock 1 cm in diameter as a function of the Paris's law exponent, *n*. **b**, Discrepancy between the model and the experimental crack growth, defined by equation (4) in Methods, as a function of the Paris's law exponent. The model–experiment discrepancy is of the order of 20% for the nominal values of the *C* and *n*. A 100% discrepancy would be clearly visible in Extended Data Fig. 7. **c**, Same as **a**, but here the number of cycles until rock fragmentation is plotted as a function of the Paris's law factor *C*. **d**, Same as **b**, but here the discrepancy between the model and the experimental crack growth is plotted as a function of the Paris's law factor *C*.

Extended Data Table 1 | Physical properties of materials and their default values used in this work

	Units	Carbonaceous chondrite	Ordinary chondrite	Reference
Paris exponent, n		3.84	3.84	[23]
Paris pre-factor, C	$\mathrm{m\,[MPa\,\sqrt{m}]^{-n}}$	3×10^{-4}	3×10^{-4}	[23]
Bulk modulus, $\bar{K}$	GPa	29	56	[27, 26]
Chondrule modulus K_i	GPa	113	113	[28]
Shear modulus, $\bar{\mu}$	GPa	18	29	[27, 26]
Bulk expansion coefficient, $\bar{\alpha}$	$\mathrm{K^{-1}}$	8.5×10^{-6}	8.5×10^{-6}	[28]
Chondrule expansion coefficient, α_i	$\mathrm{K^{-1}}$	10.4×10^{-6}	10.4×10^{-6}	[30]
Thermal conductivity, κ	$\mathrm{W\,m^{-1}\,K^{-1}}$	0.5	1.88	[21]
Heat capacity, C	$\mathrm{J\,kg^{-1}\,K^{-1}}$	500	550	[21]
Bulk density, ρ	$\mathrm{kg\,m^{-3}}$	1662	3150	[21]
Average chondrule radius	mm	0.78	1.16	this work
Average chondrule spacing	mm	1.6	1.4	this work
Thermal inertia, Γ	$\mathrm{J\,m^{-2}\,s^{-0.5}\,K^{-1}}$	640	1800	[21]
Bolometric albedo, A		0.02	0.1	-
Asteroid rotation period, P	hours	6	6	-
Laboratory temperature cycle period, P	hours	2.2	2.2	-

Asteroid thermophysical modeling

Marco Delbo
Laboratoire Lagrange, UNS-CNRS, Observatoire de la Côte d'Azur

Michael Mueller
SRON Netherlands Institute for Space Research

Joshua P. Emery
Dept. of Earth and Planetary Sciences - University of Tennessee

Ben Rozitis
Dept. of Earth and Planetary Sciences - University of Tennessee

Maria Teresa Capria
Istituto di Astrofisica e Planetologia Spaziali, INAF

The field of asteroid thermophysical modeling has experienced an extraordinary growth in the last ten years, as new thermal infrared data became available for hundreds of thousands of asteroids. The infrared emission of asteroids depends on the body's size, shape, albedo, thermal inertia, roughness and rotational properties. These parameters can therefore be derived by thermophysical modeling of infrared data. Thermophysical modeling led to asteroid size estimates that were confirmed at the few-percent level by later spacecraft visits. We discuss how instrumentation advances now allow mid-infrared interferometric observations as well as high-accuracy spectro-photometry, posing their own set of thermal-modeling challenges. We present major breakthroughs achieved in studies of the thermal inertia, a sensitive indicator for the nature of asteroids soils, allowing us, for instance, to determine the grain size of asteroidal regoliths. Thermal inertia also governs non-gravitational effects on asteroid orbits, requiring thermophysical modeling for precise asteroid dynamical studies. The radiative heating of asteroids, meteoroids, and comets from the Sun also governs the thermal stress in surface material; only recently has it been recognized as a significant weathering process. Asteroid space missions with thermal infrared instruments are currently undergoing study at all major space agencies. This will require a high level of sophistication of thermophysical models in order to analyze high-quality spacecraft data.

1. INTRODUCTION

Asteroid thermophysical modeling is about calculating the temperature of asteroids' surface and immediate subsurface, which depend on absorption of sunlight, multiple scattering of reflected and thermally emitted photons, and heat conduction. Physical parameters such as albedo (or reflectivity), thermal conductivity, heat capacity, emissivity, density and roughness, along with the shape (e.g., elevation model) of the body, its orientation in space, and its previous thermal history are taken into account. From the synthetic surface temperatures, thermally emitted fluxes (typically in the infrared) can be calculated. Physical properties are constrained by fitting model fluxes to observational data.

One differentiates between sophisticated *thermophysical models* (*TPMs;* Lebofsky and Spencer, 1989; Spencer, 1990; Spencer et al., 1989; Lagerros, 1997, 1996a, 1998; Delbo, 2004; Mueller, 2007; Rozitis and Green, 2011) and *simple thermal models*, which typically assume spherical shape, neglect heat conduction (or simplify its treatment), and do not treat surface roughness (see Harris and Lagerros, 2002; Delbo and Harris, 2002, for reviews). In the past, usage of TPMs was reserved to the few exceptional asteroids for which detailed shape models and high quality thermal infrared data existed (Harris and Lagerros, 2002). In the last ten years, however, TPMs became significantly more applicable (see § 6), thanks both to new spaceborn infrared telescopes (*Spitzer*, *WISE* and *AKARI;* see Mainzer et al., 2015) and to the availability of an ever-growing number of asteroid shape models (Durech et al., 2015).

After introducing the motivations and the different contexts for calculating asteroid temperatures (§ 2), we provide an overview of simple thermal models (§ 3) and of TPMs (§ 4). We describe data analysis techniques based on TPMs (§ 5), then we present the latest results and implications on the physics of asteroids (§ 6). In § 7, we discuss temperature-induced surface changes on asteroids; see

also the chapter "Asteroid surface geophysics" by Murdoch et al. (2015). All used symbols are summarized in Tab. 1.

Note that we do not discuss here the so-called asteroid *thermal evolution models* that are generally used to compute the temperature throughout the body as a function of time, typically taking into account internal heat sources such as the decay of the radiogenic ^{26}Al. Such models allow one to estimate the degree of metamorphism, aqueous alteration, melting and differentiation that asteroids experienced during the early phases of the solar system formation (see McSween et al., 2002, for a review).

2. MOTIVATIONS AND APPLICATIONS OF TPMs

Thermophysical modeling of observations of asteroids in the thermal infrared ($\lambda \gtrsim 4$ μm) is a powerful technique to determine the values of physical parameters of asteroids such as their sizes (e.g., Müller et al., 2014a), the thermal inertia and the roughness of their soils (e.g., Müller and Lagerros, 1998; Mueller, 2007; Delbo and Tanga, 2009; Matter et al., 2011; Rozitis and Green, 2014; Capria et al., 2014) and in some particular cases also of their bulk density and their bulk porosity (Rozitis et al., 2013, 2014; Emery et al., 2014; Chesley et al., 2014)

Knowledge of physical properties is crucial to understand asteroids: for instance, size information is fundamental to constrain the asteroid size frequency distribution that informs us about the collisional evolution of these bodies (Bottke et al., 2005); is paramount for the study of asteroid families, for the Earth-impact risk assessment of near-Earth asteroids (NEAs; see Harris et al., 2015, for a review), and for the development of asteroid space mission scenarios (§ 5.7). Accurate sizes are also a prerequisite to calculate the volumes of asteroids for which we know the mass, allowing us to derive the bulk density, which inform us about the internal structure of these bodies (e.g., Carry, 2012).

Thermal inertia, the resistance of a material to temperature change (§ 5.2), is a sensitive indicator for the properties of the grainy soil (regolith, Murdoch et al., 2015) on asteroids, e.g., the typical grain size (Gundlach and Blum, 2013) and their degree of cementation (Piqueux and Christensen, 2009a,b) can be inferred from thermal-inertia measurements. In most cases, the regolith is what we study by means of remote-sensing observations. It therefore moderates our understanding of the underlying body. Regolith informs us about the geological processes occurring on asteroids (Murdoch et al., 2015) such as impacts, micrometeoroid bombardment (Hörz and Cintala, 1997), and thermal cracking (Delbo et al., 2014). Regolith contains records of elements implanted by the solar wind and cosmic radiation, and therefore informs us about the sources of those materials (Lucey, 2006). Regolith porosity can shed light on the role of electrostatic and van-der-Waals forces acting on the surface of these bodies (e.g., Rozitis et al., 2014; Vernazza et al., 2012).

Knowledge of surface temperatures is also essential for the design of the instruments and for the near-surface operation of space missions, as in the case of the sample-return missions Hayabusa-II and OSIRIS-REx of JAXA and NASA, respectively, In the future, knowledge of asteroid temperatures will be crucial for planning human interaction with asteroids.

Another reason to model asteroid surface temperatures is that they affect its orbital and spin state evolution via the Yarkovsky and YORP effects, respectively (§ 5.8 and Vokrouhlický et al., 2015). In particular, thermal inertia dictates the strength of the asteroid Yarkovsky effect. This influences the dispersion of members of asteroid families, the orbital evolution of potentially hazardous asteroids, and the delivery of $D \lesssim 40$ km asteroids and meteoroids from the main belt into dynamical resonance zones capable of transporting them to Earth-crossing orbits (see Vokrouhlický et al., 2015, and the references therein).

The YORP effect is believed to be shaping the distribution of rotation rates (Bottke et al., 2006) and spin vector orientation (Vokrouhlický et al., 2003; Hanuš et al., 2011, 2013); small gravitationally bound aggregates could be spun up so fast (Vokrouhlický et al., 2015; Bottke et al., 2006, and references therein) that they are forced to change shape and/or undergo mass shedding (Holsapple, 2010). Approximately 15% of near-Earth asteroids are observed to be binaries (Pravec et al., 2006), and YORP spin up is proposed as a viable formation mechanism (Walsh et al., 2008; Scheeres, 2007; Jacobson and Scheeres, 2011).

A further motivation to apply TPM techniques is to constrain the spin-axis orientation and the sense of rotation of asteroids (examples are 101955 Bennu and 2005 YU_{55}, Müller et al., 2012, 2013). Durech et al. (2015) describe how to use optical and thermal infrared data simultaneously to derive more reliable asteroid shapes and spin properties.

The temperature and its evolution through the entire life of an asteroid can alter its surface composition and nature of the regolith (§ 7). For example, when the temperature rises above a certain threshold for a sustained period, certain volatiles can be lost via sublimation (Schorghofer, 2008; Capria et al., 2012), dehydration (Marchi et al., 2009), or desiccation (Delbo and Michel, 2011; Jewitt et al., 2015, and references therein).

There can be pronounced and fast temperature variations between day and night. Modeling these temperature variations is fundamental to studying the effect of thermal cracking of asteroid surface material (§ 7.1), which was found to be an important source of fresh regolith production (Delbo et al., 2014).

3. SIMPLE THERMAL MODELS

We start by introducing the near-Earth asteroid thermal model (NEATM, Harris, 1998) that is typically used where the data quality and/or the available knowledge about asteroid shape and spin preclude the usage of TPMs. Typically, the NEATM allows a robust estimation of asteroid diameter and albedo, but does not provide any direct information on thermal inertia or surface roughness (see Harris

and Lagerros, 2002, for a review). The recent large-scale thermal-emission surveys of asteroids and trans-Neptunian objects (see Mainzer et al., 2015; Lellouch et al., 2013, and references therein) typically use the NEATM in their data analysis, thereby establishing it as the de-facto default among the simple thermal models. The typical NEATM accuracy is 15% in diameter and roughly 30% in albedo (Harris, 2006). Other simple thermal models are the "Standard Thermal Model" (STM; Lebofsky et al., 1986), the "Isothermal Latitude Model" (ILM, also known as the Fast Rotating Model or FRM, Lebofsky and Spencer, 1989), and the night emission simulated thermal model (NESTM by Wolters and Green, 2009). The STM and the ILM, reviewed by, e.g., Harris and Lagerros (2002), have largely fallen out of use.

The NEATM assumes that the asteroid has a spherical shape and does not directly account for thermal inertia nor surface roughness. The surface temperature is given by the instantaneous equilibrium with the insolation, which is proportional to the cosine of the angular distance between local zenith and the Sun and zero at the night side. The maximum temperature occurs at the subsolar point and it reads:

$$(1 - A)S_{\odot}r^{-2} = \eta\sigma\epsilon\, T_{\rm SS}^4 \qquad (1)$$

(nomenclature is provided in Tab. 1). The parameter η was introduced in the STM of Lebofsky et al. (1986) as a means of changing the model temperature distribution to take account of the observed enhancement of thermal emission at small solar phase angles due to surface roughness. This is known as the beaming effect. For this reason η is also called the *beaming parameter*. The η formalism, in the NEATM, allows a first-order description of the effect of a number of geometrical and physical parameters, in particular the thermal inertia and surface roughness on the spectral energy distribution of an asteroid (Delbo et al., 2007). For a large thermal inertia, one would expect η-values significantly larger than unity (e.g., 1.5–3; with theoretical maximum values around 3.5; Delbo et al., 2007), whereas for low thermal inertia $\eta \simeq 1$ (for $\Gamma = 0$ and zero surface roughness). Roughness, on the other hand, tends to lower the value of η (for observations at low or moderate phase angles). For instance, a value of $\eta \sim 0.8$ for a main belt asteroid indicates that this body has low thermal inertia and significant roughness (with minimum theoretical values of 0.6 - 0.7; Spencer, 1990; Delbo et al., 2007). We note, however, that η is not a physical property of an asteroid, as it can vary due to changing observing and illumination geometry, aspect angle, heliocentric distance of the body, phase angle and wavelength of observation.

4. THERMOPHYSICAL MODELS

4.1. Overview

Different TPMs have been proposed to study the thermal emission of asteroids, comets, planets, and satellites. The first models were motivated by thermal observations of the lunar surface, which revealed an almost thermally insulating surface that emitted thermal radiation in a non-Lambertian way (Pettit and Nicholson, 1930; Wesselink, 1948a). Heat conduction and radiation scattering models of various rough surfaces were able to reproduce the lunar observations to a good degree (e.g., Smith, 1967; Buhl et al., 1968b,a; Sexl et al., 1971; Winter and Krupp, 1971), and the derived thermal inertia and surface roughness values matched *in situ* measurements by Apollo astronauts (see Rozitis and Green, 2011, and references therein). These early lunar models were adapted to general planetary bodies, albeit with an assumed spherical shape, by Spencer et al. (1989) and Spencer (1990). The most commonly used asteroid TPMs of Lagerros (1996a, 1997, 1998), Delbo (2004), Mueller (2007), and Rozitis and Green (2011) are all based on Spencer et al. (1989) and Spencer (1990). Here we present the basic principles utilized in TPMs; for implementation details, the reader is referred to the quoted works.

All TPMs represent the global asteroid shape as a mesh of (triangular) facets (see Fig. 1) that rotates around a given spin vector with rotation period P. In general, utilized shape models are derived from radar observations, inversion of optical light-curves, in-situ spacecraft images, or stellar occultation timing (see Durech et al., 2015, for a review of asteroid shape modeling). If no shape model is available, one typically falls back to a sphere or an ellipsoid (e.g., Müller et al., 2013, 2014a; Emery et al., 2014).

The goal is to calculate the thermal emission of each facet of the shape model at a given illumination and observation geometry. To this end, the temperature of the surface and, in the presence of thermal inertia, the immediate subsurface need to be calculated. Generally, lateral heat conduction can be neglected as the shape model facets are much larger than the penetration depth of the diurnal heat wave (i.e., the thermal skin depth), and only 1D heat conduction perpendicular to and into the surface needs to be considered. For temperature T, time t, and depth z, 1D heat conduction is described by:

$$\rho C\frac{\partial T}{\partial t} = \frac{\partial}{\partial z}\kappa\frac{\partial T}{\partial z} \qquad (2)$$

where κ is the thermal conductivity, ρ is the material density, and C is the heat capacity. If κ is independent of depth (and, implicitly, temperature independent, see §5.3), Eq. 2 reduces to the diffusion equation:

$$\frac{\partial T}{\partial t} = \frac{\kappa}{\rho C}\frac{\partial T^2}{\partial^2 z} \qquad (3)$$

It is useful to define the thermal inertia Γ and the thermal skin depth l_s

$$\Gamma = \sqrt{\kappa\rho C} \qquad (4)$$

$$l_s = \sqrt{\kappa P/2\pi\rho C}. \qquad (5)$$

These material properties are generally assumed to be constant with depth and temperature in asteroid TPMs, but varying properties has been considered in some Moon, Mars, planetary satellites, and asteroids models (e.g Giese

TABLE 1
NOMENCLATURE

Symbol	Quantity	Unit	Symbol	Quantity	Unit
T	Temperature	K	$\bar{\theta}$	Mean surface slope	deg
$T_{\rm SS}$	Subsolar temperature	K	l_s	Thermal skin depth	m
σ	Stefan-Boltzmann constant	(5.67051 10^{-8}) W m^{-2} K^{-4}	P	Rotation period	s
$S_\odot$	Solar constant at r=1 au	(1329) W m^{-1}	ω	= $2\pi/P$	s^{-1}
r	Distance to the Sun	au	λ_p	ecliptic longitude of the pole	deg
$\vec{r}$	Vector to the Sun	m	β_p	ecliptic latitude of the pole	deg
Δ	Distance to the observer	au	ϕ_0	Initial rotational phase at epoch	deg
ϵ	Emissivity	-	α	(Phase) angle between asteroid-sun-observer	deg
η	Beaming parameter	-	a	Area of a facet	m^2
κ	Thermal conductivity	W m^{-1} K^{-1}	S	Shadowing function	
C	Heat capacity	J kg^{-1} K^{-1}	$F_{\vec{i},\vec{j}}$	View factor	
Γ	Thermal inertia	J m^{-2}s$^{-1/2}$K^{-1}	$J_V(\vec{j})$	Visible radiosity	
Θ	Thermal parameter	-	$J_{IR}(\vec{j})$	Infrared radiosity	
ρ	Material density	kg m^{-3}	$\hat{n}$	Local normal	m
H	Absolute magnitude of the H, G system		$\vec{i}$	Vector to the local facet	m
G	Slope parameter of the H, G system		$\vec{j}$	Vector to the remote facet	m
V	Actual magntude in the V-band		γ_C	Crater opening angle	deg
D	Diameter	m (or km)	ρ_C or f	Area density of craters	
A	Bolometric Bond albedo	-	ϕ	Emission angle	rad
p_V	Geometric visible albedo	-	$f_\lambda(\tau)$	Infrared flux	W m^{-2} μm^{-1}
z	Depth in the subsoil	m	λ	Wavelength	μm
t	Time	s			
r_p	Pore radius of regolith	m			

and Kuehrt, 1990; Urquhart and Jakosky, 1997; Piqueux and Christensen, 2011; Keihm, 1984; Keihm et al., 2012; Capria et al., 2014, see also section 5.3).

TPM implementations typically employ dimensionless time and depth variables: $\tau = 2\pi t/P$ and $Z = z/l_s$. Then, the only remaining free parameter is the dimensionless thermal parameter ($\Theta = \Gamma\sqrt{\omega}/\epsilon\sigma T_{SS}^3$, Spencer, 1990) describing the combined effect of thermal inertia, rotation period, and heat emission into space on the surface temperature distribution (see Fig. 2).

A numerical finite-difference technique is used to solve the 1D heat conduction equation, and an iterative technique is used to solve the surface boundary condition. This requires a suitable number of time and depth steps to fully resolve the temperature variations and to ensure model stability (typically, at least 360 time steps and 40 depth steps over 8 thermal skin depths are required). TPMs are run until specified convergence criteria are met (e.g., until temperature variations between successive model iterations are below a specified level) and/or until a specified number of model iterations have been made.

For applications such as the study of the sublimation of water ice from the shallow subsurface of asteroids (e.g., the *Main Belt Comets* or 24 Themis) the heat conduction equation must be coupled with a gas diffusion equation (Schorghofer, 2008; Capria et al., 2012; Prialnik and Rosenberg, 2009). See also Huebner et al. (2006) for a review.

The 1D heat conduction equation is solved with internal and surface boundary conditions to ensure conservation of energy. Since the amplitude of subsurface temperature variations decreases exponentially with depth, an internal boundary condition is required to give zero temperature gradient at a specified large depth

$$\left(\frac{\partial T}{\partial z}\right)_{z\gg l_s} = 0. \tag{6}$$

A typical surface boundary condition for a facet at point $\vec{i}$ with respect to the asteroid origin, at point $\vec{r}$ with respect to the Sun, and with surface normal $\hat{n}$ is then given by

$$\begin{aligned} &\epsilon\sigma T^4(\vec{i},t) - \left(\frac{\partial T(\vec{i},t)}{\partial z}\right)_{z=0} = \\ &\frac{(1-A)S_\odot}{\vec{r}^{\,3}}(\vec{r}\cdot\hat{n})(1-S(\vec{r},\vec{i}))+ \\ &(1-A)\int J_V(\vec{j})F_{\vec{i},\vec{j}}\,da'+ \\ &\epsilon\sigma(1-\epsilon)\int J_{IR}(\vec{j})F_{\vec{i},\vec{j}}\,da' \end{aligned} \tag{7}$$

The left-hand side of Eq. (7) gives the thermal energy radiated to space and the heat conducted into the subsurface, and the right-hand side gives the input radiation from three different sources: direct solar radiation, multiply scattered solar radiation (i.e., self-illumination), and reabsorbed thermal radiation (i.e., self-irradiation). The two last components are also known as mutual heating (see Fig. 3).

The amount of solar radiation absorbed by a facet depends on the Bond albedo A and any shadows projected on it, which is dictated by $S(\vec{r},\vec{i})$ (i.e., $S(\vec{r},\vec{i}) = 1$ or 0, depending on the presence or absence of a shadow). Projected shadows occur on globally non-convex shapes only, which can be determined by ray-triangle intersection tests of the solar illumination ray (e.g., Rozitis and Green, 2011) or by local horizon mapping (e.g., Statler, 2009). Related to shadowing are the self-heating effects arising from interfacing

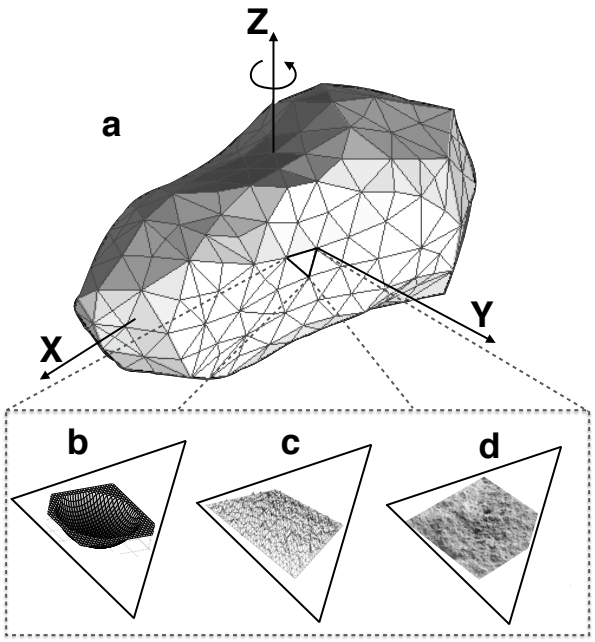

Fig. 1.— (a) example of a triangulated 3D shape model as typically used in TPMs (asteroid (2063) Bacchus from http://echo.jpl.nasa.gov/asteroids/shapes/shapes.html). Temperatures are color coded: white corresponds to the maximum and dark-gray corresponds to minimum temperature. Three different roughness models are sketched in the bottom of the figure: (b) hemispherical section craters; (c) Gaussian surface; (d) fractal surface. Sub-figures b and d are adapted from Davidsson et al. (2015), c is from Rozitis and Green (2011).

facets, which tend to reduce the temperature contrast produced inside concavities. The problem here is to determine which facets see other facets, and to calculate the amount of radiation exchanged between them. The former can be determined by ray-triangle intersection tests again, and the latter can be solved using view factors. The view factor $F_{\vec{i},\vec{j}}$ is defined as the fraction of the radiative energy leaving the local facet $\vec{i}$ that is received by the remote facet $\vec{j}$ assuming Lambertian emission (Lagerros, 1998). $J_V(\vec{j})$ and $J_{IR}(\vec{j})$ are then the visible and thermal-infrared radiosities of remote facet $\vec{j}$. Either single or multiple scattering can be taken into account, and the latter can be efficiently solved using Gauss-Seidel iterations (Vasavada et al., 1999). Most TPMs neglect shadowing and self-heating effects resulting from the global shape for simplicity, but they can be significant on asteroids with large shape concavities (e.g., the south pole of (6489) Golevka: Rozitis and Green, 2013).

4.2. Modeling asteroid thermal emission

Once the surface temperature distribution across an asteroid surface has been computed, the emission spectrum (Fig. 4) at a given observation geometry and a specified time can be calculated. The monochromatic flux density can also be calculated at wavelengths of interest. When these model fluxes are plotted as a function of the asteroid rotational

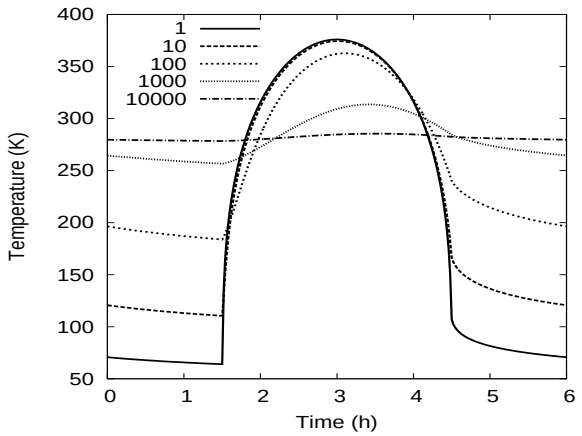

Fig. 2.— Synthetic diurnal temperature curves on the equator of a model asteroid for different values of thermal inertia (in units of J $m^{-2}s^{-1/2}K^{-1}$). Increasing thermal inertia smooths temperature contrasts and causes the temperature peak to occur after the insolation peak at 3 h. The asteroid is situated at a heliocentric distance of r = 1.1 au, has a spin period of 6 h, a Bond albedo of A = 0.1, and its spin axis is perpendicular to the orbital plane.

phase, one obtains the so-called thermal lightcurves (e.g. Fig. 5), which can be used to test the fidelity of shape and albedo models typically used as input in the TPM.

When the temperature for a facet is known, the intensity $I_\lambda(\tau)$ at which it emits at wavelength λ is given by the Planck function. Assuming Lambertian emission, the spectral flux of the facet seen by an observer is then

$$f_\lambda(\tau) = I_\lambda(\tau)\frac{a}{\Delta^2}\cos\phi \tag{8}$$

where a is area of the facet, Δ is the distance to the observer, and ϕ is the emission angle. The total observed flux is obtained by summing the thermal fluxes of all visible shape model facets including any contributions from surface roughness elements contained within them. For disk-integrated measurements, this summation is performed across the entire visible side of the asteroid, whilst for spatially resolved measurements it is summed across facets contained within the detector pixel's field of view.

The assumption of Lambertian emission depends on no directionality induced by surface irregularities at scales below the thermal skin depth. Davidsson and Rickman (2014) show that surface roughness at sub-thermal-skin-depth scales is quasi-isothermal and is therefore not likely to deviate from Lambertian emission overall. However, radiative transfer processes between the regolith grains could contribute up to 20% of the observed beaming effects (Hapke, 1996). Rozitis and Green (2011, 2012) investigated combined microscopic (regolith grain induced) and macroscopic (surface roughness induced) beaming effects, and demonstrated that the macroscopic effects dominated overall. This was previously found to be the case in directional thermal emission measurements of lava flows on Earth (Jakosky et al., 1990).

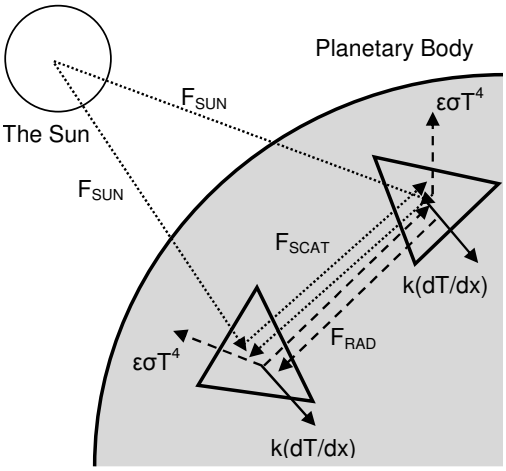

Fig. 3.— Diagram illustrating the energy balance and radiation transfer between facets (copied from Rozitis and Green, 2011). The terms F_{SUN}, F_{SCAT}, F_{RAD}, $k(dT/dx)$ and $\epsilon\sigma T^4$ are the direct sunlight, multiply scattered sunlight, reabsorbed thermal radiation, conducted heat and thermal radiation lost to space, respectively.

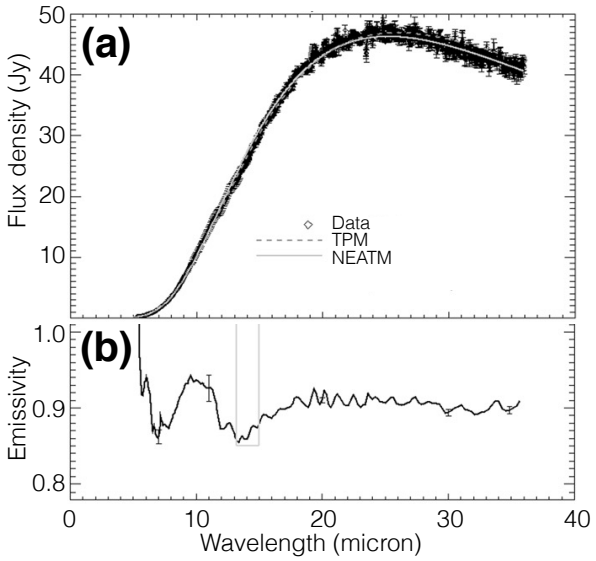

Fig. 4.— (a) Example of SED calculated from a TPM and the NEATM compared to a Spitzer spectrum of (87) Sylvia. (b) Spectral emissivity derived from the above: data divided by the NEATM continuum. Figure from Marchis et al. (2012).

As wavelengths increase to the submillimeter range and above, asteroid regolith becomes increasingly transparent and the observed flux is integrated over increasing depths (Chamberlain et al., 2009; Keihm et al., 2013). Modeling such fluxes with typical thermal models (which derive fluxes from surface temperatures, only) requires a significant reduction in effective spectral emissivity. For example, 3.2 mm flux measurements of (4) Vesta require an emissivity of ∼0.6 to match model predictions (Müller and Barnes, 2007). The reduction in emissivity can be explained by lower subsurface emission temperatures (Lagerros, 1996b) and by different subsurface scattering processes dependent on grain size (Redman et al., 1992; Müller and Lagerros, 1998). Keihm et al. (2012, 2013) attribute the reduced emissivity at submm/mm wavelengths to a higher thermal inertia value of the subsurface layers. Reduction in emissivity has also been determined at wavelengths shorter than 4.9 μm for disk-resolved regions of (4) Vesta (Tosi et al., 2014).

4.3. Surface Roughness

Roughness causes an asteroid surface to thermally emit in a non-Lambertian way with a tendency to reradiate the absorbed solar radiation back towards the Sun, an effect known as thermal infrared beaming (Lagerros, 1998; Rozitis and Green, 2011). It is thought to be the result of two different processes: a rough surface will have elements orientated towards the Sun that become significantly hotter than a flat surface, and multiple scattering of radiation between rough surface elements increases the total amount of solar radiation absorbed by the surface. The relevant size scale ranges from the thermal skin depth to the linear size of the facets in the shape model. It is included in thermophysical models by typically modeling an areal fractional coverage (f) of spherical-section craters (of opening angle γ_C) within each shape model facet. Other more complex forms have been considered, such as Gaussian random (Lagerros, 1998) or fractal (Groussin et al., 2013) surfaces or parallel sinusoidal trenches (see sketch of Fig. 1) , but the spherical-section crater produces similar results (in terms of the disk-integrated beaming effect Lagerros, 1998) and accurately reproduces the directionality of the lunar thermal infrared beaming effect (Rozitis and Green, 2011). However, it has been shown that the thermal emission depends also on roughness type in addition to roughness level, for disk resolved data Davidsson et al. (2015).

Spherical-section craters are typically implemented, as the required shadowing and view-factor calculations can be performed analytically (Emery et al., 1998; Lagerros, 1998). Heat conduction can be included by dividing the crater into several tens of surface elements where the same equations listed above can be applied. Alternatively, the temperature distribution within the crater resulting from heat conduction, $T_{\rm crater}(\Gamma)$, can be approximated using

$$\frac{T_{\rm rough}(\Gamma)}{T_{\rm rough}(0)} = \frac{T_{\rm smooth}(\Gamma)}{T_{\rm smooth}(0)} \quad (9)$$

where $T_{\rm rough}(0)$ can be calculated analytically assuming instantaneous equilibrium (Lagerros, 1998). $T_{\rm smooth}(0)$ and $T_{\rm smooth}(\Gamma)$ are the corresponding smooth-surface temperatures, which can be calculated exactly. This approximation is computationally much cheaper than the full implementation. However, it does not work on the night side of the asteroid and temperature ratios diverge near the terminator (Mueller, 2007). An even simpler alternative is to multiply the smooth-surface temperatures by a NEATM-like η

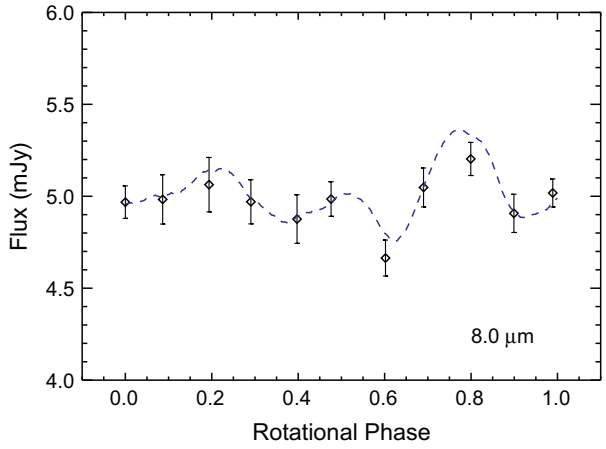

Fig. 5.— Example of a TPM generated thermal lightcurve (dashed line) and real data for (101955) Bennu. From Emery et al. (2014).

value (e.g. Groussin et al., 2011). Whilst this alternative might produce the correct disk-integrated color temperature of the asteroid, it does not reproduce the directionality of the beaming effect. Indeed, roughness models predict a limb-brightening effect (Rozitis and Green, 2011), which is seen in spatially-resolved measurements of (21) Lutetia by Rosetta (Keihm et al., 2012).

The above implementations neglect lateral heat conduction, although the spatial scales representing surface roughness can, in some cases, become comparable to the thermal skin depth. Modeling of 3D heat conduction inside rocks the size of the thermal skin depth has demonstrated that their western sides (for a prograde rotator; eastern sides for a retrograde rotator) are generally warmer than their eastern sides, which could result in a tangential-YORP effect that predominantly spins up asteroids (Golubov and Krugly, 2012). Other than this, it appears that the 1D heat conduction approximation still produces satisfactory results.

In thermophysical models, the degree of surface roughness can be quantified in terms of the Hapke mean surface slope

$$\tan\bar{\theta} = \frac{2}{\pi}\int_0^{\pi/2} a(\theta)\tan\theta\, d\theta \qquad (10)$$

where θ is the angle of a given facet from horizontal, and $a(\theta)$ is the distribution of surface slopes (Hapke, 1984). Alternatively, it can be measured in terms of the RMS surface slope (Spencer, 1990). This then allows comparison of results derived using different surface roughness representations (e.g., craters of different opening angles and fractional coverages, or different Gaussian random surfaces: Davidsson et al., 2015), and comparison against roughness measured by other means. It has been demonstrated that different roughness representations produce similar degrees of thermal infrared beaming when they have the same degree of roughness measured in terms of these values (Spencer, 1990; Emery et al., 1998; Lagerros, 1998; Rozitis and Green, 2011).

5. DATA ANALYSIS USING A TPM

5.1. Thermal infrared spectro-photometry

Physical properties than can be derived from TPM fits to disk-integrated thermal observations include the diameter, geometric albedo, thermal inertia and roughness. In practically all cases, the absolute visual magnitude H is known, establishing a link between D and p_V and reducing the number of TPM fit parameters by one:

$$D(\mathrm{km}) = 1329\, p_V^{-1/2}\, 10^{-H/5}, \qquad (11)$$

(Fowler and Chillemi, 1992; Vilenius et al., 2012). Frequently, the rotational phase during the thermal observations is not sufficiently well known and has to be fitted to the thermal data (e.g., Harris et al., 2005; Alí-Lagoa et al., 2014). In some cases, TPMs can be used to constrain the orientation of the spin vector of an asteroid, with λ_p and β_p treated as free parameters (as demonstrated e.g., by Müller et al., 2013, 2012, note that in the case of 101955 Bennu the radar-constrained pole solution was not yet known). Moreover, Müller et al. (2014b) successfully performed a TPM analysis of an asteroid (99942 Apophis) in a non-principal axis rotation state for the first time.

The thermal effects of thermal inertia and surface roughness are difficult to tell apart. A commonly used approach is to use four different roughness models corresponding to no, low, medium, and high roughness, with each model leading to a different thermal-inertia fit (Mueller, 2007; Delbo and Tanga, 2009); frequently, the scatter between these four solutions accounts for the bulk of the uncertainty in thermal inertia. However, in some lucky cases, data do allow the effects of roughness and thermal inertia to be disentangled. This requires good wavelength coverage straddling the thermal emission peak and good coverage in solar phase angle, such that both the morning and afternoon sides of the asteroid are seen. See Fig. 6 for an illustration.

The best-fitting model parameters are those that minimize χ^2. Their uncertainty range is spanned by the values that lead to χ^2 within a specified threshold of the best fit, depending on the number of free fit parameters. Ideally, the reduced χ^2 of the best fit should be around unity. However, due to systematic uncertainties introduced in thermal infrared observations (e.g., flux offsets between different instruments), and/or in the thermophysical modeling, it is not uncommon to get large reduced χ^2 values. Large χ^2 values are also obtained when the assumed shape model differs significantly from the asteroid's true shape (Rozitis and Green, 2014). In particular, if the spatial extent of the shape model's z-axis is wrong, this can lead to diameter determinations that are inconsistent with radar observations (e.g., for 2002 NY_{40} and (308635) 2005 YU_{55} in Müller et al., 2004, 2013, respectively), and/or two different thermal inertia determinations (e.g., the two different results produced for (101955) Bennu by Emery et al., 2014; Müller et al.,

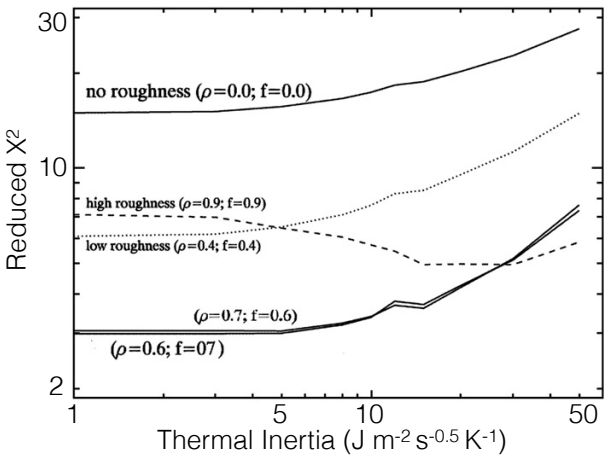

Fig. 6.— (21) Lutetia: a TPM fit that allows surface roughness to be constrained. The quantity ρ here is not the bulk density of the body, but it is the r.m.s. of the slopes on the surface. It is related to the ratio between the diameter and the depth of spherical section craters (Lagerros, 1998) in this particular case. f is the areal fraction of each facet covered with craters. From O'Rourke et al. (2012).

2012). In some works, the asteroid shape model has also been optimized during the thermophysical fitting to resolve inconsistencies with radar observations (e.g., (1862) Apollo and (1620) Geographos in Rozitis et al., 2013; Rozitis and Green, 2014, respectively).

We remind the reader that the accuracy of the physical properties (in particular the value of Γ) of asteroids derived from TPM depends on the quality of the thermal infrared data, coverage in wavelength, phase, rotational, and aspect angle. The accuracy of the shape model and of the H and G values are also important (see e.g. Rozitis and Green, 2014). The derived thermal inertia value often depends on the assumed degree of roughness and it is usually affected by large errors (e.g. 50 or 100 %, see Tab. 2). Care must be used in accepting TPM solutions purely based on the goodness of fit (e.g. the value of the χ^2), as they can be dominated by one or few measurements with unreliable small errors or calibration offsets between measurements from different sources.

5.2. Thermal Inertia and Thermal Conductivity

As asteroids rotate, the day-night cycle causes cyclic temperature variations that are controlled by the thermal inertia (defined by Eq. 4) of the soil and the rotation rate of the body. In the limit of vanishing thermal inertia, the surface temperature would be in instantaneous equilibrium with the incoming flux, depending only on the solar incidence angle (as long as self heating can be neglected); surface temperatures would peak at local noon and would be zero at night. In reality, thermal conduction into and from the subsoil causes a certain thermal memory, referred to as *thermal inertia*. This smoothens the diurnal temperature profile, leads to non-zero night-side temperatures, and causes the surface temperature to peak on the afternoon side, as shown in Fig. 2, thereby causing the Yarkovsky effect (§ 5.8).

The mass density ρ, the specific heat capacity c, and the thermal conductivity κ, and correspondingly Γ itself, must be thought of as effective values representative of the depth range sampled by the heat wave, which is typically in the few-cm range. In turn, thermal-inertia values inform us about the physical properties of the top few centimeters of the surface, not about bulk properties of the object.

As will be discussed below (§ 6.5), ρ and c of an asteroid surface can plausibly vary within a factor of several, while plausible values of κ span a range of more than 4 orders of magnitude. It is therefore not unjustified to convert from Γ to κ and back using reference values for ρ and c (note that Yarkovsky/YORP models tend to phrase the thermal-conduction problem in units of κ, while TPMs tend to be formulated in units of Γ, which is the observable quantity).

Importantly, the κ of finely powdered lunar regolith is 3 orders of magnitude lower than that of compact rock (compact metal is even more conductive by another order of magnitude). This is because radiative thermal conduction between regolith grains is significantly less efficient than phononic heat transfer within a grain. A fine regolith, an aggregate of very small grains, is a poor thermal conductor and displays a low Γ. Thermal inertia can therefore be used to infer the presence or absence of thermally insulating powdered surface material. In extension, thermal inertia can be used as a proxy of regolith grain size. The required calibration under Mars conditions (where the tenuous atmosphere enhances thermal conduction within pores compared to a vacuum) was obtained by Presley and Christensen (1997a,b) and used in the analysis of thermal-inertia maps of Mars (see Mellon et al., 2000; Putzig and Mellon, 2007). Similar progress in asteroid science was slowed down by the lack of corresponding laboratory measurements under vacuum conditions (but see below for recent lab measurements of meteorites). However, Gundlach and Blum (2013) provided a calibration relation based on heat-transfer modeling in a granular medium.

5.3. Temperature dependence of thermal inertia

Thermal inertia is a function of temperature (Keihm, 1984), chiefly because the thermal conductivity is. In general, for a lunar-like regolith the thermal conductivity is given by:

$$\kappa = \kappa_b + 4\sigma r_p T^3 \tag{12}$$

where κ_b is the solid-state thermal conductivity (heat conduction by phonons) and r_p is the radius of the pores of the regolith. The term proportional to T^3 is due to the heat conduction by photons. Equation 12 is often written in the form $\kappa = \kappa_0(1 + \chi T^3)$ (e.g., Vasavada et al., 1999). Note that κ_b is itself a function of T (Opeil et al., 2010). There is extensive literature on the T-dependence of the conductivity of lunar regolith (e.g., Vasavada et al., 1999, and references therein). A theoretical description of the temperature de-

pendence of κ in regoliths is given by Gundlach and Blum (2013).

Asteroid TPMs typically neglect the temperature dependence of Γ. This is uncritical for typical remote observations, which are dominated by the warm sunlit hemisphere (see Fig. 7 and Capria et al., 2014; Vasavada et al., 2012). In the analysis of highly spatially resolved observations, however, the temperature dependence must be considered, certainly when analyzing night-time observations on low-Γ asteroids. Note that for temperature-dependent κ, Eq. 2 must be used instead of Eq. 3 (see, e.g., Capria et al., 2014).

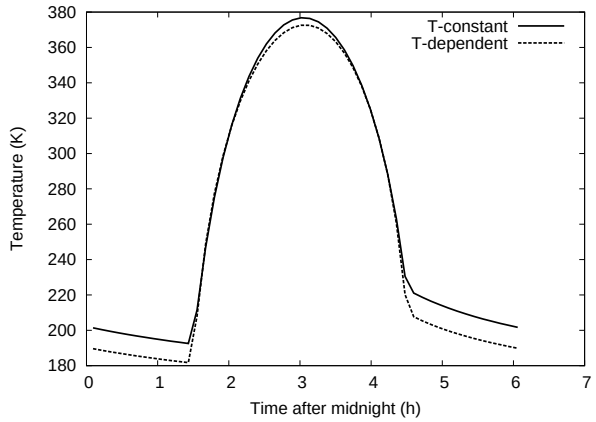

Fig. 7.— Diurnal temperature curves at the equator of an asteroid with A=0.1, P=6h, ϵ=1.0 at a heliocentric distance of 1.0 au. Solid curve: constant thermal conductivity κ=0.02 W K^{-1} m^{-1}. Dashed-curved: temperature-dependent heat conductivity $\kappa = 10^{-2}(1 + 0.5(T/250)^3)$ W K^{-1} m^{-1}.

Caution must be exercised when comparing thermal-inertia results obtained at different heliocentric distances r, i.e., at different temperatures. All other things being equal, $T^4 \propto r^{-2}$. Assuming that the T^3 term dominates in Eq. 12, the thermal inertia of a test object scales with (see also Mueller et al., 2010):

$$\Gamma \propto \sqrt{\kappa} \propto T^{3/2} \propto r^{-3/4}. \quad (13)$$

5.4. Binary Asteroid TPM

A rather direct determination of thermal inertia can be obtained by observing the thermal response to eclipses and their aftermath, allowing one to see temperature changes in real time. Such observations have been carried out for planetary satellites such as the Galilean satellites (Morrison and Cruikshank, 1973), and our Moon (Pettit, 1940; Shorthill, 1973; Lawson et al., 2003; Lucey, 2000; Fountain et al., 1976). Mueller et al. (2010) report the first thermal observations of eclipse events in a binary Trojan asteroid system, (617) Patroclus, where one component casts shadow on the other while not blocking the line of sight toward the observer.

The thermophysical modeling of eclipse events is relatively straightforward, assuming the system is in a tidally locked rotation state typical of evolved binary systems. In that case, the components' spin rates match one another, and their spin axes are aligned with that of the mutual orbit. The system is therefore at rest in a co-rotating frame and can be modeled like a single object with a non-convex (disjoint!) global shape. Eclipse effects are fully captured, provided that shadowing between facets is accounted for. The two hemispheres that face one another can, in principle, exchange heat radiatively. This is negligible for typical binary systems, however.

As discussed above, the thermal effects of roughness and thermal inertia can be hard to disentangle. In the case of eclipse measurements, which happen at essentially constant solar phase angle, the effect of surface roughness is much less of a confounding factor. This is because the variation in the thermal signal is dominated by the temperature change induced by the passing shadow, which is a strong function of thermal inertia.

It must be kept in mind that the duration of an eclipse event is short compared to the rotation period. The eclipse-induced heat wave therefore probes the subsoil less deeply than the diurnal heat wave does (the typical heat penetration depth is given by Eq. 5 with P equal to the duration of the eclipse event). A depth dependence of thermal inertia (see § 6.6) could manifest itself in different thermal-inertia determinations using the two different measurement methods.

5.5. Thermal-infrared interferometry

Interferometric observations of asteroids in the thermal infrared measure the spatial distribution of the thermal emission along different directions on the plane of sky, thereby constraining the distribution in surface temperature and hence thermal inertia and roughness. Provided the asteroid shape is known, interferometry can be used to break the aforementioned degeneracy between thermal inertia and roughness from a single-epoch observation (Matter et al., 2011, 2013). Interferometry also allows a precise determination of the size of an asteroid (Delbo et al., 2009).

Spatial resolutions between 20 and 200 milli-arcseconds can be obtained from the ground (see Durech et al., 2015, for a review and future perspectives of the application of this technique).

While for the determination of asteroid sizes and shapes from interferometric observations in the thermal infrared, simple thermal models can be used (Delbo et al., 2009; Carry et al., 2015), a TPM was utilized to calculate interferometric visibilities of asteroids in the thermal infrared for the observations of (41) Daphne (Matter et al., 2011) and (16) Psyche (Matter et al., 2013).

Mid-infrared interferometric instruments measure the total flux and the visibility of a source, the latter being related to the intensity of the Fourier Transform (FT) of the spatial flux distribution along the interferometer's baseline projected on the plane of sky. Thus, the data analysis procedure consisted in generating images of the thermal infrared emission of the asteroids at different wavelengths as viewed by the interferometer and then in obtaining the model visi-

bility and flux for each image. The former is related to the FT of the image, the latter is simply the sum of the pixels. The free parameters of the TPM (size, thermal inertia value and roughness) are adjusted in order to minimize the distance between the disk integrated flux and visibility of the model, and the corresponding observed quantities (see Matter et al., 2011, 2013; Durech et al., 2015, for further information). Some results from these observational programs are discussed in § 6 and in the chapter by Durech et al. (2015).

5.6. Disk-resolved data and retrieval of temperatures

The availability of disk-resolved thermal-infrared observation has been increasingly steadily over the years: the ESA mission *Rosetta* performed two successful flybys to the asteroids (2867) Steins (in 2008) and (21) Lutetia (in 2010) (Barucci et al., 2015). In 2011, the NASA mission *Dawn* began its one-year orbiting of (4) Vesta (Russell et al., 2012); Dawn is reaching (1) Ceres at the time of writing. JAXA's *Hayabusa II* sample-return mission will map its target asteroid (162173) 1999 JU_3 using the thermal infrared imager (TIR) aboard the spacecraft (Okada et al., 2013); NASA's *OSIRIS-REx* mission and its thermal spectrometer OTES will do likewise for its target asteroid (101955) Bennu (in 2018-2019). These data can be used to derive surface-temperature maps, from which maps of thermal inertia and roughness can be derived.

Three different methods are used to measure surface temperatures from orbiting spacecraft: bolometry, mid-infrared spectroscopy, and near-infrared spectroscopy. In the following, we will elaborate on the challenges posed by these different methods, and on their dependence on spectral features, surface roughness, illumination geometry, and viewing geometry.

Bolometers measure thermal flux within a broad bandpass in the infrared, approximating the integral of the Planck function, $U = \sigma T_e^4$ (e.g., Kieffer et al., 1977; Paige et al., 2010). The temperature derived in this way (**effective temperature**) is directly relevant to the energy balance on the surface. Since the bolometric flux is spectrally integrated, the resulting temperature is fairly insensitive to spectral emissivity variations, as long as the bolometric emissivity (weighted spectrally averaged emissivity) is known or can be reasonably approximated.

Temperatures derived from mid-infrared spectrometry, on the other hand, are typically **brightness temperatures,** i.e., the temperature of a black body emitting at the wavelength in question. It is generally assumed that at some wavelength, the spectral emissivity is very close to 1.0, and the brightness temperature at this wavelength is taken as the surface temperature.

Spacecraft sent to asteroids (and/or comets) have more commonly been instrumented with near-infrared spectrometers (e.g., $\lambda < 5$ μm) rather than mid-infrared spectrometers. The long-wavelength ends of these spectrometers often extend into the range where thermal emission dominates the measured flux (for the daytime surface temperatures of most asteroids). At these wavelengths, one cannot assume that the emissivity is close to 1.0. It is therefore not practical to derive brightness temperatures. Instead, the **color temperature** is derived, that is the temperature of a black body that emits with the same spectral shape. Such derivations have to separate temperature from spectral emissivity. The problem is under-constrained (N+1 unknowns, but only N data points), so there is no deterministic solution. Spectral emissivities for fine-grained silicates trend in the same direction as the blackbody curve, so it would be very easy to mistake spectral emissivity variations for different temperatures. The most statistically rigorous approach that has been applied to separating temperature and spectral emissivity in the 3 – 5 μm region is that of Keihm et al. (2012) and Tosi et al. (2014) for Rosetta/VIRTIS data of Lutetia and Dawn/VIR data of Vesta.

Temperatures thus measured represent an average temperature in the field of view of a given pixel: illuminated hot zones and shadowed colder parts will both contribute. They do not directly correspond to a physical temperature of the soil; rather, they depend sensitively on the observation and illumination geometry (see Rozitis and Green, 2011, in particular their Fig. 9), especially in the case of large illumination angles.

Microwave spectrometers such as MIRO (Gulkis et al., 2007) can provide both day and nightside thermal flux measurements. At sub-mm, mm, and longer wavelengths, asteroid soils become moderately transparent. Subsurface layers contribute significantly to the observable thermal emission, thus providing information on the subsurface temperature. Observable fluxes depend on the subsurface temperature profile, weighted by the wavelength-dependent electrical skin depths, so both a thermal and an electrical model are required to interpret such data (Keihm et al., 2012).

We remind here that thermal infrared fluxes should be used as input data for TPMs and not (effective, color, or brightness) temperatures derived from radiometric methods, because of their dependence on illumination and observation angles !

5.7. Sample-return missions

Space agencies across the planet are developing space missions to asteroids, notably sample-return missions to primitive (C and B type) near-Earth asteroids: Hayabusa-2, was launched by JAXA towards (162173) 1999 JU_3 on December 3, 2014, and OSIRIS-REx is to be launched by NASA in 2016 (Lauretta et al., 2012). A good understanding of the expected thermal environment, which is governed by thermal inertia, is a key factor in planning spacecraft operations on or near asteroid surfaces. E.g., OSIRIS-REx is constrained to sampling a regolith not hotter than 350 K, severely constraining the choice of the latitude of the sample selection area on the body, the local time, and the arrival date on the asteroid.

Both Hayabusa-2 and OSIRIS-REx are required to take

regolith samples from the asteroid surface back to Earth. Obviously, this requires that regolith be present in the first place, which needs to be ascertained by means of ground-based thermal-inertia measurements. The sampling mechanism of OSIRIS-REx, in particular, requires relatively fine (cm-sized or smaller) regolith.

5.8. Accurate Yarkovsky and YORP modeling from TPMs

Scattered and thermally emitted photons carry momentum. Any asymmetry in the distribution of outgoing photons can, after averaging over an orbital period, impart a net recoil force (Yarkovsky effect) and/or a net torque (YORP effect) on the asteroid. Both effects are more noticeable as the object gets smaller. For small enough objects, the orbits can be significantly affected by the Yarkovsky effect, and their rotation state by YORP (Bottke et al., 2006; Vokrouhlický et al., 2015).

The strength of the Yarkovsky effect is strongly influenced by thermal inertia (Bottke et al., 2006, and references therein) and by the degree of surface roughness (Rozitis and Green, 2012). However, the strength and sign of the YORP rotational acceleration on an asteroid is independent of thermal inertia (Čapek and Vokrouhlický, 2004), but it is highly sensitive to the shadowing (Breiter et al., 2009), self-heating (Rozitis and Green, 2013), and surface roughness effects (Rozitis and Green, 2013) that are incorporated in thermophysical models.

Accurate calculations of the instantaneous recoil forces and torques require an accurate calculation of surface temperatures as afforded by TPMs; Rozitis and Green (2012, 2013) report on such models. Other than on thermal inertia, the Yarkovsky-induced orbital drift depends on the bulk mass density. Therefore, Yarkovsky measurements combined with thermal-inertia measurements can be used to infer the elusive mass density (Mommert et al., 2014b,a; Rozitis and Green, 2014; Rozitis et al., 2014, 2013). In the case of (101955) Bennu, the uncertainties in published values of thermal inertia (Emery et al., 2014) and measured Yarkovsky drift (Chesley et al., 2014) are so small that the accuracy of the inferred mass density rivals that of the expected in-situ spacecraft result (1260 ± 70 kg m^{-3}, i.e., a nominal uncertainty of only 6%). Rozitis et al. (2014) derived the bulk density of (29075) 1950 DA and used it to reveal the presence of cohesive forces stabilizing the object against the centrifugal force.

In turn, the measured Yarkovsky drift can be used to infer constraints on thermal inertia. This was first done by Chesley et al. (2003) studying the Yarkovsky effect on (6489) Golevka and by Bottke et al. (2001) studying the Koronis family in the main asteroid belt; both studies revealed thermal inertias consistent with expectations based on the observed correlation between thermal inertia and diameter (see § 6.2).

Whilst the YORP effect is highly sensitive to small-scale uncertainties in an asteroid's shape model (Statler, 2009), it can be used to place constraints on the internal bulk density distribution of an asteroid (Scheeres and Gaskell, 2008). For instance, Lowry et al. (2014) explain the YORP detection on (25143) Itokawa, which was opposite in sign to that predicted, by Itokawa's two lobes having substantially different bulk densities. However, unaccounted lateral heat conduction in thermal skin depth sized rocks could also explain, at least partially, this opposite sign result (Golubov and Krugly, 2012).

6. LATEST RESULTS FROM TPMs

In the *Asteroid III* era, thermal properties were known for only a few asteroids, i.e., (1) Ceres, (2) Pallas, (3) Juno, (4) Vesta, (532) Herculina from Müller and Lagerros (2002), and (433) Eros from Lebofsky and Rieke (1979). Since then, the number of asteroids with known thermal properties has increased steadily. We count 59 minor bodies with known value of Γ (see Tab. 2). Of these, 16 are near-Earth asteroids (NEAs), 27 main-belt asteroids (MBAs), 4 Jupiter Trojans, 5 Centaurs, and 7 trans-Neptunian objects (TNOs).

These classes of objects present very different physical properties such as sizes, regolith grain size, average value of the thermal inertia, and composition. Other important differences are their average surface temperature due to their very different heliocentric distances and orbital elements. The illumination and observation geometry are also diverse for different classes of objects. For instance, for TNOs and MBAs the phase angle of observation from Earth and Earth-like orbits is typically between a few and a few tens of degrees, respectively. On the other hand, NEAs can be observed under a much wider range of phase angles than can approach hundred degrees and more Müller (see also 2002). A special care should be used in these cases to explicitly calculate the heat diffusion in craters instead of using the approximation of Eq. 9.

6.1. Ground truth from space missions to asteroids

A number of asteroids have been, or will be, visited by spacecraft, providing ground-truth for the application of TPMs to remote-sensing thermal-infrared data.

(21) Lutetia: based on ground-based data and a TPM, Mueller et al. (2006) measured Lutetia's effective diameter and p_V to within a few percent of the later Rosetta result (Sierks et al., 2011). Their thermal-inertia constraint ($\Gamma < 50$ J m^{-2}s$^{-1/2}$K^{-1}) was refined by O'Rourke et al. (2012) based on the Rosetta shape model and more than 70 thermal-infrared observations obtained from the ground, *Spitzer, Akari*, and *Herschel*: $\Gamma = 5$ J m^{-2}s$^{-1/2}$K^{-1}with a high degree of surface roughness. Keihm et al. (2012) used MIRO aboard Rosetta to obtain a surface thermal inertia $\lesssim 30$ J m^{-2}s$^{-1/2}$K^{-1}. The low thermal inertia can be explained by a surface covered in fine regolith; Gundlach and Blum (2013) infer a regolith grain size of about 200 μm. The study of the morphology of craters by Vincent et al. (2012) indicates abundant, thick (600 m), and very fine re-

TABLE 2

PUBLISED THERMAL INERTIA VALUES

Number	Name	D (km)	Δ_D (km)	Γ (SI)	Δ_Γ (SI)	Tax	r (au)	Ref.	Number	Name	D (km)	Δ_D (km)	Γ (SI)	Δ_Γ (SI)	Tax	r (au)	Ref.
1	Ceres	923	20	10	10	C	2.767	1	1620	Geographos	5.04	0.07	340	120	S	1.1	12
2	Pallas	544	43	10	10	B	2.772	1	1862	Apollo	1.55	0.07	140	100	Q	1.0	13
3	Juno	234	11	5	5	S	2.671	1	2060	Chiron	142	10	4	4	B/Cb	8-15	14
4	Vesta	525	1	20	15	V	2.3	2	2060	Chiron	218	20	5	5	B/Cb	13	15
16	Psyche	244	25	125	40	M	2.7	3	2363	Cebriones	82	5	7	7	D	5.2	16
21	Lutetia	96	1	5	5	M	2.8	4	2867	Steins	4.92	0.4	150	60	E	2.1	17
22	Kalliope	167	17	125	125	M	2.3	5	2867	Steins	5.2	1	210	30	E	2.1	18
32	Pomona	85	1	70	50	S	2.8	6	8405	Asbolus	66	4	5	5	-	7.9	19
41	Daphne	202	7	25	25	Ch	2.1	7	3063	Makhaon	116	4	15	15	D	4.7	16
44	Nysa	81	1	120	40	E	2.5	6	10199	Chariklo	236	12	1	1	D	13	14
45	Eugenia	198	20	45	45	C	2.6	5	10199	Chariklo	248	18	16	14	D	13	13
87	Sylvia	300	30	70	60	P	2.7	5	25143	Itokawa	0.32	0.03	700	100	S	1.1	8
107	Camilla	245	25	25	10	P	3.2	5	25143	Itokawa	0.320	0.029	700	200	S	1.1	20
110	Lydia	93.5	3.5	135	65	M	2.9	6	29075	1950 DA	1.30	0.13	24	20	M	1.7	21
115	Thyra	92	2	62	38	S	2.5	6	33342	1998 WT_{24}	0.35	0.04	200	100	E	1.0	8
121	Hermione	220	22	30	25	Ch	2.9	5	50000	Quaoar	1082	67	6	4	-	43	15
130	Elektra	197	20	30	30	Ch	2.9	5	54509	YORP	0.092	0.010	700	500	S	1.1	8
277	Elvira	38	2	250	150	S	2.6	6	55565	2002 AW_{197}	700	50	10	10	-	47	22
283	Emma	135	14	105	100	P	2.6	5	90377	Sedna	995	80	0.1	0.1	-	87	23
306	Unitas	56	1	180	80	S	2.2	6	90482	Orcus	968	63	1	1	-	48	13
382	Dodona	75	1	80	65	M	2.6	6	99942	Apophis	0.375	0.014	600	300	Sq	1.05	24
433	Eros	17.8	1	150	50	S	1.6	8	101955	Bennu	0.495	0.015	650	300	B	1.1	25
532	Herculina	203	14	10	10	S	2.772	1	101955	Bennu	0.49	0.02	310	70	B	1.1	26
617	Patroclus	106	11	20	15	P	5.9	9	136108	Haumea	1240	70	0.3	0.2	-	51	27
694	Ekard	109.5	1.5	120	20	-	1.8	6	162173	1999 JU_3	0.87	0.03	400	200	C	1.4	28
720	Bohlinia	41	1	135	65	S	2.9	6	175706	1996 FG_3	1.71	0.07	120	50	C	1.4	29
956	Elisa	10.4	0.8	90	60	-	1.8	10	208996	2003 AZ_{84}	480	20	1.2	0.6	-	45	27
1173	Anchises	136	15	50	20	P	5.0	11	308635	2005 YU_{55}	0.306	0.006	575	225	C	1.0	30
1580	Betulia	4.57	0.46	180	50	C	1.1	8	341843	2008 EV_5	0.370	0.006	450	60	C	1.0	31

References: [1] Müller and Lagerros (1998), [2] Leyrat et al. (2012), [3] Matter et al. (2013), [4] O'Rourke et al. (2012), [5] Marchis et al. (2012), [6] Delbo and Tanga (2009), [7] Matter et al. (2011), [8] Mueller (2007), [9] Mueller et al. (2010), [10] Lim et al. (2011), [11] Horner et al. (2012), [12] Rozitis and Green (2014), [13] Rozitis et al. (2013), [14] Groussin et al. (2004), [15] Fornasier et al. (2013), [16] Fernández et al. (2003), [17] Lamy et al. (2008), [18] Leyrat et al. (2011), [19] Fernández et al. (2002), [20] Müller et al. (2014a), [21] Rozitis et al. (2014), [22] Cruikshank et al. (2005), [23] Pál et al. (2012), [24] Müller et al. (2014b), [25] Müller et al. (2012), [26] Emery et al. (2014), [27] Lellouch et al. (2013), [28] Müller et al. (2011), [29] Wolters et al. (2011), [30] Müller et al. (2013), [31] Alí-Lagoa et al. (2014), Note: for Ceres, Pallas, Juno, and Herculina r is assumed equal to the semimajor asxis of the orbit.

golith, confirming the TPM results.

(433) Eros was studied by the NASA NEAR-Shoemaker space mission that allowed determination of the shape and size of this asteroid (mean radius of 8.46 km with a mean error of 16 m; Thomas et al., 2002). Mueller (2007) performed a TPM analysis of the ground-based thermal infrared data by Harris and Davies (1999), obtaining a best-fit diameter of 17.8 km that is within 5% of the Thomas et al. (2002) result of 16.9 km, and Γ in the range 100 - 200 J m^{-2}s$^{-1/2}$K^{-1}. The latter value, in agreement with TPM results of Lebofsky and Rieke (1979), implies coarser surface regolith than that on the Moon and larger asteroids (see, e.g., Mueller, 2007; Delbo et al., 2007). From the value of Γ of Mueller (2007), Gundlach and Blum (2013) calculated a 1-3 mm typical regolith grain size for Eros. Optical images of the NEAR-Schoemaker landing site at a resolution of about 1 cm/pixel (Veverka et al., 2001) show very smooth areas at the scale of the camera spatial resolution (Fig. 8), likely implying mm or sub-mm grain size regolith, consistent with TPM results.

(25143) Itokawa physical properties were derived *in-situ* by the JAXA sample-return mission Hayabusa, allowing us to compare the size, albedo and regolith nature derived from the TPMs with spacecraft results. Müller et al. (2014a) show an agreement within 2% between the size and the geometric visible albedo inferred from TPM analysis of thermal-infrared data and the value of the corresponding parameters from Hayabusa data. The TPM thermal inertia value for Itokawa is around 750 J m^{-2}s$^{-1/2}$K^{-1}, significantly higher than the value of our Moon (about 50 J m^{-2}s$^{-1/2}$K^{-1}) and of other large main belt asteroids including (21) Lutetia, implying a coarser regolith on this small NEA. The corresponding average regolith grain size according to Gundlach and Blum (2013) is $\sim$ 2 cm. Hayabusa observations from the optical navigation camera (ONC-T), obtained during the descent of the spacecraft to the "Muses Sea" region of the asteroid, reveal similar grain sizes, at a spatial resolution of up to 6 mm/pixel. In particular, Yano et al. (2006) describe "Muses Sea" as composed of numerous size-sorted granular materials ranging from several centimeters to subcentimeter scales. Itokawa's regolith material can be classified as "gravel", larger than submillimeter regolith powders filling in ponds on (433) Eros (Fig. 8).

It is worth pointing out, however, that "Muses Sea" is not representative of Itokawa's surface as a whole. Rather, it was selected as a touchdown site because, in earlier Hayabusa imaging, it appeared as particularly smooth (minimizing operational danger for the spacecraft upon touchdown) and apparently regolith rich (maximizing the chance of sampling regolith). Grain sizes measured at "Muses Sea" are therefore lower limits on typical grain sizes rather than values typical for the surface as a whole.

6.2. Thermal inertia of large and small asteroids

An inverse correlation between Γ and D was noticed by Delbo et al. (2007), then updated Delbo and Tanga (2009) and Capria et al. (2014). This supported the intuitive view that large asteroids have, over many hundreds of millions of years, developed substantial insulating regolith layers, responsible for the low values of their surface thermal inertia. On the other hand, much smaller bodies, with shorter collisional lifetimes (Marchi et al., 2006; Bottke et al., 2005, and references therein), have less regolith, and or larger regolith grains (less mature regolith), and therefore display a larger thermal inertia.

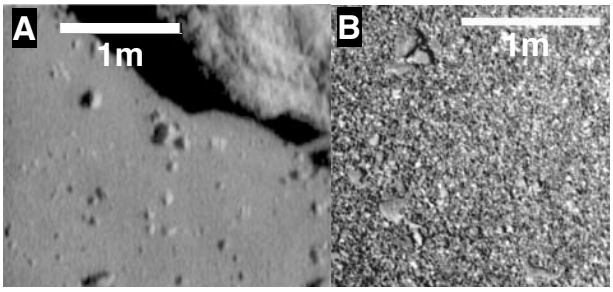

Fig. 8.— Higher Γ-values correspond to coarser regoliths. (A) Close-up image of (433) Eros from the NASA *NEAR Shoemaker* mission reveals coarse regolith with grain size in the mm-range (adapted from Veverka et al., 2001). The value of Γ is $\sim$150 J m^{-2}s$^{-1/2}$K^{-1} for Eros. (B) Image from the JAXA *Hayabusa* mission (from Yano et al., 2006) of the surface of (25143) Itokawa displaying gravel-like regolith. The value of Γ is $\sim$750 J m^{-2}s$^{-1/2}$K^{-1} for Itokawa.

In the light of the recently published values of Γ (Tab. 2), said inversion correlation between Γ and D is less clear, in particular, when the values of the thermal inertia are temperature corrected (Fig. 9). However, the Γ vs D distribution of $D > 100$ km (large) asteroids is different than that of $D < 100$ km (small) asteroids. Small asteroids typically have higher Γ-values than large asteroids, which present a large scatter of Γ-values, ranging from a few to a few hundreds J m^{-2}s$^{-1/2}$K^{-1}. This is a clear indication of a diverse regolith nature amongst these large bodies. A shortage of low Γ values for small asteroids is also clear, with the notable exception of 1950 DA, which has an anomalously low Γ-value compared to other NEAs of similar size (Rozitis et al., 2014).

Fig. 9 also shows previously unnoticed high-thermal-inertia C types, maybe related to CR carbonaceous chondrites, which contain abundant metal phases. We also note that all E types in our sample appear to have a size-independent thermal inertia.

6.3. Very low Γ-values

We also note that the some of the C-complex outer main-belt asteroids and Jupiter Trojans have very low thermal inertia in the range between a few and a few tens of J m^{-2}s$^{-1/2}$K^{-1}. In order to reduce the thermal inertia of a material by at least one order of magnitude (from the lowest measured thermal inertia of a meteorite, $\sim$650 J m^{-2}s$^{-1/2}$K^{-1} at 200 K (Opeil et al., 2010), to the typical values for these

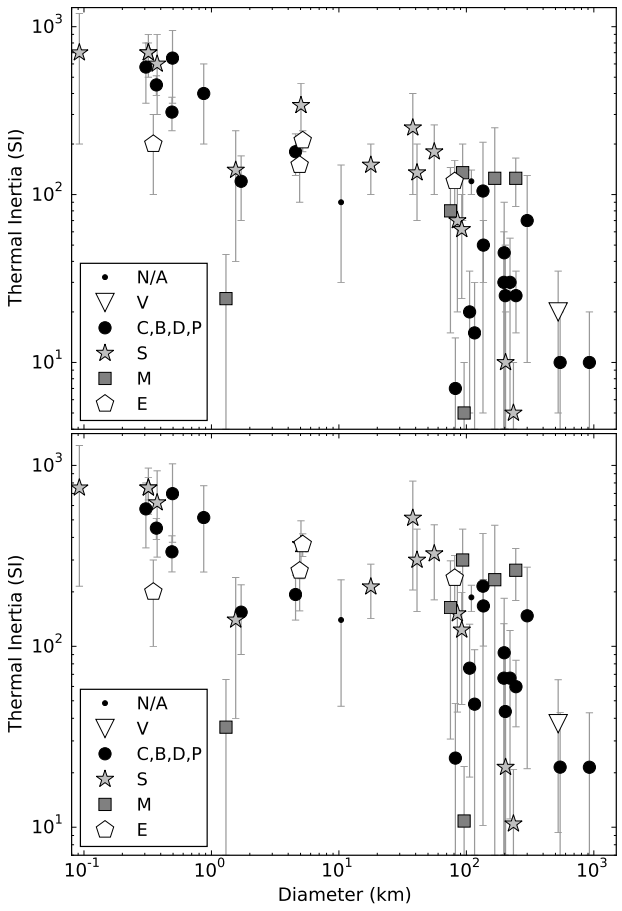

Fig. 9.— Γ values vs. D from Tab. 2 for different taxonomic types (see key). Top plot: original measurements, bottom plot: Γ corrected to 1 au heliocentric distance for temperature dependent thermal inertia assuming Eq. 13 and the heliocentric distance at the time of thermal infrared observations reported in Tab. 2. Trojans, Centaurs and trans-Neptunian objects are not displayed.

large asteroids (Tab. 2 and Fig. 9), a very large porosity (>90%) of the first few mm of the regolith is required (Vernazza et al., 2012). This is consistent with the discovery that emission features in the mid-infrared domain (7–25 μm, Fig. 4) are rather universal among large asteroids and Jupiter Trojans (Vernazza et al., 2012), and that said features can be reproduced in the laboratory by suspending meteorite and/or mineral powder (with grain sizes < 30 μm) in IR-transparent KBr (potassium bromide) powder (Vernazza et al., 2012). As KBr is not supposed to be present on the surfaces of these minor bodies, regolith grains must be "suspended" in void space likely due to cohesive forces and/or dust levitation. On the other hand, radar data indicate a significant porosity (40-50 %) of the first $\sim$1 m of regolith (Magri et al., 2001; Vernazza et al., 2012), indicating decreasing porosity with increasing depth (see Fig. 5 of Vernazza et al., 2012, for a regolith schematics).

6.4. Average thermal inertia of asteroid populations

As described before, the thermal inertia of an asteroid can be directly derived by comparing measurements of its thermal-infrared emission to model fluxes generated by means of a TPM. Typically, more than one observation epoch is required to derive the thermal inertia, in order to "see" the thermal emission from different parts of the asteroid's diurnal temperature distribution. Unfortunately, the large majority of minor bodies for which we have thermal-infrared observations have been observed at a single epoch and/or information about their gross shape and pole orientation is not available, precluding the use of TPMs. However, if one assumes the thermal inertia to be roughly constant within a population of asteroids (e.g., NEAs) one can use observations of different asteroids under non-identical illumination and viewing geometries, as if they were from a unique object. Delbo et al. (2003) noted that qualitative information about the average thermal properties of a sample of NEAs could be obtained from the distribution of the η-values of the sample as a function of the phase angle, α. Delbo et al. (2007) and Lellouch et al. (2013) developed a rigorous statistical inversion method, based on the comparison of the distributions of published NEATM η-values vs α, or vs. r with that of a synthetic population of asteroids generated through a TPM, using realistic distributions of the input TPM parameters such as the rotation period, the aspect angle etc. Delbo et al. (2007) found that the average thermal inertia value for km-sized NEAs is around 200 J m^{-2}s$^{-1/2}$K^{-1}. The average thermal inertia of binary NEAs is higher than that of non-binary NEAs, possibly indicating a regolith-depriving mechanism for the formation of these bodies (Delbo et al., 2011). The same authors also found that NEAs with slow rotational periods (P >10 h) have higher-than-average thermal inertia. From a sample of 85 Centaurs and trans-Neptunian objects observed with Spitzer/MIPS and Herschel/PACS, Lellouch et al. (2013) found that surface roughness is significant, a mean thermal inertia $\Gamma = 2.5 \pm 0.5$ J m^{-2}s$^{-1/2}$K^{-1}, and a trend toward decreasing Γ with increasing heliocentric distance. The thermal inertias derived by Lellouch et al. (2013) are 2-3 orders of magnitude lower than expected for compact ices, and generally lower than on Saturn's satellites or in the Pluto/Charon system. These results are suggestive of highly porous surfaces.

6.5. Relevant astronomical and laboratory data

Physical interpretations of thermal-inertia estimates depend strongly on laboratory and ground-truth measurements of relevant material properties. While in the *Asteroid III* era, we based interpretation of thermal inertia on Earth analog materials, in the last few years laboratory measurements were performed on asteroid analog materials, i.e., meteorites. Meteorite grain densities range from $\sim$2800 kg m^{-3} for CM carbonaceous chondrites to $\sim$3700 kg m^{-3} for enstatite chondrites (Consolmagno et al., 2006; Macke et al., 2010, 2011a,b). Heat capacities have been measured

for a wide sampling of meteorites by Consolmagno et al. (2013), who find that values for stony meteorites are between 450 and 550 J kg^{-2} K^{-1}, whereas C for irons tends to be smaller (330 – 380 J kg^{-2} K^{-1}). Opeil et al. (2012, 2010) present thermal conductivity measurements of stony meteorites, finding values of 0.5 W K^{-1} m^{-1} for the carbonaceous chondrite Cold Bokkeveld to 5.5 W K^{-1} m^{-1} for the enstatite chondrite Pillistfer. Their one iron meteorite sample has a κ of 22.4 W K^{-1} m^{-1}. They also find a linear correlation between and the inverse of the porosity, from which Opeil et al. (2012) conclude that the measured κ of the samples is controlled more by micro-fractures than by composition.

Grain size and packing, more than compositional heterogeneity, are responsible for different thermal inertias of different surfaces. This also explains why TPMs are capable of deriving asteroid physical parameters independently of the asteroid mineralogy. Conduction between grains is limited by the area of the grain contact (Piqueux and Christensen, 2009b,a). As grain size decreases to diameters less than about a thermal skin depth (few cm on most asteroids), conduction is more and more limited (e.g., Presley and Christensen, 1997b). On bodies with atmospheres, conduction through the air in pores can often efficiently transport heat. On airless bodies, however, radiation between grains, which is not very efficient, particularly at low T (e.g., Gundlach and Blum, 2012), is the only alternative to conduction across contacts (Fig. 10). Considering these two modes of energy transport and their dependence on grain size, Gundlach and Blum (2013) developed an analytical approach for determining grain size from thermal inertia measurements. They incorporated the measurements of material properties of meteorites measured above along with results of their own laboratory of heat transport in dusty layers. Additional laboratory measurements of conductivities of powdered meteorites under high vacuum would be valuable for more precise interpretation of asteroid thermal inertias.

The classic opportunity for ground-truth thermal measurements came with the Apollo missions. Astronauts on Apollo 15 and 17 carried out bore-hole style temperature measurements to depths of 1.4 m below the surface on Apollo 15 and 2.3 m below the surface on Apollo 17 (Langeseth and Keihm, 1977; Vaniman et al., 1991). Thermal conductivity of about 0.001 W K^{-1} m^{-1} was found in the top 2 to 3 cm of the lunar regolith, increasing to about 0.01 W K^{-1} m^{-1} over the next few cm, then to values as high as 2 W K^{-1} m^{-1} deeper into the surface where the regolith appears to have been very compacted (Langeseth and Keihm, 1977). Low thermal inertias derived from remote thermal infrared measurements (e.g. Wesselink, 1948b; Vasavada et al., 2012) agree with the very low κ in the topmost few cm of the lunar surface, and the Apollo measurements provide the necessary ground-truth for interpreting such low thermal inertias as very fine-grained, "fluffy" regolith. These measurements fostered, for instance, development of detailed models of lunar regolith (Keihm, 1984). Detailed

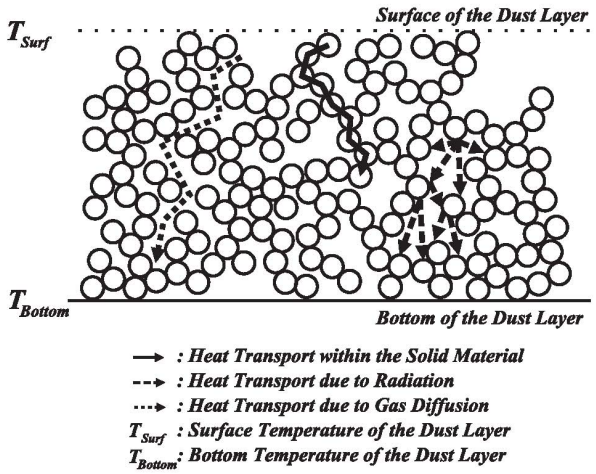

Fig. 10.— Diagram of the modes of heat transport in regoliths. On airless bodies, heat can flow by conduction through grain boundaries (solid line) or by radiation between grains (dashed line). The dotted line showing transport by gas diffusion is not relevant to asteroid surfaces. From Gundlach and Blum (2012).

thermal infrared observations and thermal models of the lunar regolith allows today estimating the subsurface rock abundance (e.g., Bandfield et al., 2011), allowing geological studies of the regolith production rate.

6.6. Dependence of Γ with depth

The depth dependence of typical asteroid regolith properties is poorly constrained at this point, which is why physical constants are typically assumed to be constant with depth. MIRO observations of (21) Lutetia, however, showed the existence of a top layer with $\Gamma < 30$ J m^{-2}s$^{-1/2}$K^{-1}, while the thermal inertia of subsurface material appears to increase with depth much like on the Moon (Keihm et al., 2012).

6.7. Infrared limb brightening

Recent modeling and observations show that, contrary to expectation, the flux enhancement measured in disk-integrated observations of the sunlit side of an asteroid (e.g., Lebofsky et al., 1986) is dominated by limb surfaces rather than the subsolar region (Rozitis and Green, 2011; Keihm et al., 2012). This suggests that for the sunlit side of an asteroid, sunlit surfaces directly facing the observer in situations where they would not be if the surface was a smooth flat one are more important than mutual self-heating between interfacing facets raising their temperatures. Figure 9 of Rozitis and Green (2011) pictures this effect for a Gaussian random surface during sunrise viewed from different directions. The thermal flux observed is enhanced when viewing hot sunlit surfaces (i.e., Sun behind the observer), and is reduced when viewing cold shadowed surfaces (i.e., Sun in front of the observer).

Jakosky et al. (1990) also studied the directional thermal emission of Earth-based lava flows exhibiting macroscopic

roughness. They found that enhancements in thermal emission were caused by viewing hot sunlit sides of rocks and reductions were caused by viewing cold shadowed sides of rocks. This agrees precisely with the model and adds further evidence that thermal infrared beaming is caused by macroscopic roughness rather than microscopic roughness.

The effect of limb brightening has also been measured from disk-resolved thermal infrared data (<5 μm) acquired during sunrise on the nucleus of the comet 9P/Tempel 1 by the *Deep Impact* NASA space mission (Davidsson et al., 2013), and from VIRTIS and MIRO measurements of the asteroid (21) Lutetia (Keihm et al., 2012).

6.8. Asteroid thermal inertia maps

Disk-resolved thermal infrared observations, in the range between 4.5 – 5.1 μm, were provided by the instrument VIR (De Sanctis et al., 2012) on board of the NASA DAWN (Russell et al., 2012) spacecraft (Capria et al., 2014, and references therein). Form TPM analysis of VIR measurements, Capria et al. (2014) obtained a map of the roughness and the thermal inertia of Vesta. The average thermal inertia of Vesta is 30 ± 10 J m^{-2}s$^{-1/2}$K^{-1}, which is in good agreement with the values found by ground-based observations (Müller and Lagerros, 1998; Chamberlain et al., 2007; Leyrat et al., 2012). The best analog is probably the surface of the Moon, as depicted by Vasavada et al. (2012) and Bandfield et al. (2011): a surface whose thermal response is determined by a widespread layer of dust and regolith with different grain sizes and density increasing toward the interior. Exposed rocks are probably scarce or even absent. Capria et al. (2014) also show that Vesta cannot be considered uniform from the point of view of thermal properties. In particular, they found that the thermal inertia spatial distribution follows the global surface exposure age distribution, as determined by crater counting in Raymond et al. (2011), with higher thermal inertia displayed by younger terrains and lower thermal inertia in older soils.

Capria et al. (2014) also found higher-than-average thermal inertia terrain units located in low-albedo regions that contain highest abundance of OH, as determined by the 2.8 μm band depth (De Sanctis et al., 2012). These terrains are associated with the dark material, thought to be delivered by carbonaceous chondrite like asteroids that have impacted Vesta at low velocity. Note that in general (carbonaceous chondrites) have lower densities and lower thermal conductivity (Opeil et al., 2010) than basaltic material, which constitute the average Vestan terrain. This consideration would point to a lower thermal inertia rather than a higher one, as observed on Vesta. Capria et al. (2014) conclude that the factor controlling the thermal inertia in these areas could be the degree of compaction of the uppermost surface layers, which is higher than in other parts of the surface.

6.9. Thermal inertia of metal-rich regoliths

In principle, the composition of the regolith and not only its average grain size and the degree of compaction also affects the thermal inertia of the soil (Gundlach and Blum, 2013). For instance iron meteorites have a higher thermal conductivity than ordinary and carbonaceous chondrites (Opeil et al., 2010). We thus expect that a metal iron rich regolith displays a higher thermal inertia than a soil poor of this component. Harris and Drube (2014) compared values of the NEATM η-parameter derived from WISE data with asteroid taxonomic classifications and radar data, and showed that the η-value appears to be a useful indicator of asteroids containing metal. Matter et al. (2013) performed interferometric observations with MIDI of the ESO-VLTI in thermal infrared of (16) Psyche and showed that Psyche has a low surface roughness and a thermal inertia value around 120 ± 40 J m^{-2}s$^{-1/2}$K^{-1}, which is one of the higher values for an asteroid of the size of Psyche ($\sim$ 200 km). This higher than average thermal inertia supports the evidence of a metal-rich surface for this body.

7. EFFECTS OF TEMPERATURES ON THE SURFACE OF ASTEROIDS

7.1. Thermal cracking

The surface temperature of asteroids follows a diurnal cycle (see Fig. 2) with typically dramatic temperature changes as the Sun rises or sets. The resulting, repeated thermal stress can produce cumulative damage on surface material due to opening and extension of microscopic cracks. This phenomenon is known as *thermal fatigue* (Delbo et al., 2014).

Growing cracks can lead to rock break-up when the number of temperature cycles is large enough. For typical asteroid properties, this process is a very effective mechanism for comminuting rocks and to form fresh regolith (Delbo et al., 2014). For cm-sized rocks on an asteroid 1 au from the Sun, thermal fragmentation is at least an order of magnitude faster than comminution by micrometeoroid impacts, the only regolith-production mechanism previously considered relevant (Hörz and Cintala, 1997; Hoerz et al., 1975).

The efficiency of thermal fragmentation is dominated by the amplitude of the temperature cycles and by the temperature change rate (Hall and André, 2001), which in turn depend on heliocentric distance, rotation period, and the surface thermal inertia. The rate of thermal fragmentation increases with decreasing perihelion distance: at 0.14 au from the Sun, thermal fragmentation may erode asteroids such as (3200) Phaethon and produce the Geminids (Jewitt and Li, 2010), whereas in the outer Main Belt this process might be irrelevant. Thermal fragmentation of surface boulders is claimed by Dombard et al. (2010) to be source of fine regolith in the so-called "ponds" on the asteroid (433) Eros. Production of fresh regolith originating in thermal fatigue fragmentation may be an important process for the rejuvenation of the surfaces of near-Earth asteroids (Delbo et al., 2014).

Thermal cracking is reported on other bodies, too: on Earth, particularly in super-arid environments (Hall, 1999; Hall and André, 2001), on the Moon (Levi, 1973; Duen-

nebier and Sutton, 1974), Mercury (Molaro and Byrne, 2012), Mars (Viles et al., 2010), and on meteorites (Levi, 1973). Moreover, Tambovtseva and Shestakova (1999) suggest that thermal cracking could be an important process in the fragmentation and splitting of kilometer-sized comets while in the inner solar system. Furthermore, Čapek and Vokrouhlický (2010) initially proposed that slowly rotating meteoroids or meteoroids that have spin vector pointing towards the sun can be broken up by thermal cracking. In a further development of their model, Čapek and Vokrouhlický (2012) showed that as the meteoroid approaches the Sun, the stresses first exceed the material strength at the surface and create a fractured layer. If inter-molecular forces (e.g., Rozitis et al., 2014) are able to retain the surface layer, despite the competing effects of thermal lifting and centrifugal forces, the particulate surface layer is able to thermally shield the core, preventing any further damage by thermal stresses.

7.2. Sun-driven heating of near-Earth asteroids and meteoroids

It is known that heating processes can affect the physical properties of asteroids and their fragments, the meteorites (see, e.g., Keil, 2000).

Internal heating due to the decay of short-lived radionuclides was considered early on (Grimm and McSween, 1993). Marchi et al. (2009) discuss close approaches to the Sun as an additional surface-altering heating mechanism. In the present near-Earth asteroid population, the fraction of bodies with relatively small perihelion (q) is very small: about 1/2, 1/10, and 1/100 of the population of currently known near-Earth objects (11,000 as of the time of writing) have a perihelion distance below 1, 0.5, and 0.25 au, where maximum temperature are exceeding 400, 550, and 780 K, respectively (see Fig. 11). However, dynamical simulations show that a much larger fraction of asteroids had small perihelion distances for some time, hence experiencing episodes of strong heating in their past (Marchi et al., 2009). For instance, the asteroid 2004 LG was approaching the Sun to within only $\sim$5.6 solar radii some 3 ky ago, and its surface was baked at temperatures of 2500 K (Vokrouhlický and Nesvorný, 2012).

Solar heating has a penetration depth of typically a few cm (see Eq. 5 and Spencer et al., 1989). Organic components found on meteorites break up at temperatures as low as 300–670 K (see Fig. 11 and Kebukawa et al., 2010; Frost et al., 2000; Huang et al., 1994), thus solar heating can remove these components from asteroid surfaces.

7.3. Thermal metamorphism of meteorites

Radiative heating from the Sun has been invoked as a mechanism for the thermal metamorphism of metamorphic CK carbonaceous chondrites (Chaumard et al., 2012). The matrix of these chondrites shows textures consistent with a transient thermal event during which temperatures rose between 550 and 950 K. The inferred duration of these events

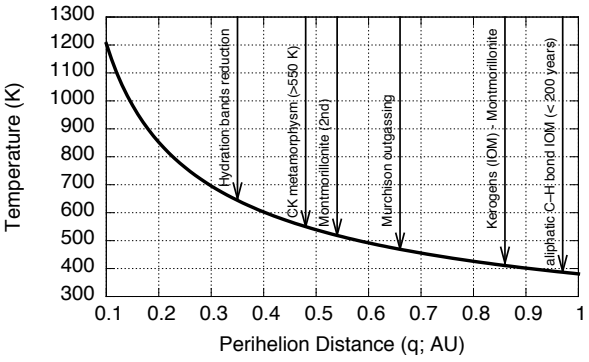

Fig. 11.— Surface temperature of an asteroid or meteoroid as a function of the distance from the Sun. Vertical arrows indicate the threshold temperature for the thermal alteration/desiccation for a variety of chemical compounds discussed in the text (see Delbo and Michel, 2011, and references therein for further information). The temperature range for thermal metamorphism of the CK chondrites is from Chaumard et al. (2012).

is of the order of days to years, much longer than the time scale of shock events but shorter than the time scale for heating by the decay of radiogenic species such as ^{26}Al (e.g., Kallemeyn et al., 1991).

7.4. Subsurface ice sublimation

Observational evidence for the presence of ice on asteroid surfaces stems from the discovery of main belt comets (MBCs; Hsieh and Jewitt, 2006), the localized release of water vapor from the surface of (1) Ceres (Küppers et al., 2014), and the detection of spectroscopic signatures interpreted as water ice frost on the surface of (24) Themis (Rivkin and Emery, 2010; Campins et al., 2010) and of (65) Cybele (Licandro et al., 2011).

The lifetime of ices on the surface and in the subsurface depends strongly on temperature. TPMs have been used to estimate these temperatures. This requires a modification of the "classical" TPM as presented in section 4, such that heat conduction is coupled with gas diffusion (Schorghofer, 2008; Capria et al., 2012; Prialnik and Rosenberg, 2009). The referenced models assume a spherical shape. As for the interior structure, Capria et al. (2012); Prialnik and Rosenberg (2009) assume a comet-like structure, i.e., an intimate mixture of ice and dust throughout the entire body, while Schorghofer (2008) consider an ice layer underneath a rocky regolith cover. Sublimation of ice and the transport of water molecules through the fine-grained regolith is modeled in all cases.

All authors agree that water ice exposed on asteroid surfaces sublimates completely on timescales much shorter than the age of the Solar System. Therefore, asteroid surfaces were expected to be devoid of water ice, contrary to the observational evidence quoted above. However, water ice can be stable over 4.5 Gy in the shallow subsurface, at a depth of $\sim$1–10 m. In particular, Fanale and Salvail (1989) showed that ice could have survived in the subsurface at the

polar regions of Ceres. Large heliocentric distances, slow rotation, and a fine-grained regolith leading to low thermal conductivity and short molecular free path, all favor the stabilization of subsurface water ice (Schorghofer, 2008). The same authors conclude that rocky surfaces, in contrast to dusty surfaces, are rarely able to retain ice in the shallow subsurface.

To be observable on the surface, buried ice most be exposed. Campins et al. (2010) describe several plausible mechanisms such as impacts, recent change in the obliquity of the spin pole, and daily or orbital thermal pulses reaching a subsurface ice layer.

8. FUTURE CHALLENGES FOR TPMs

The *Spitzer* and *WISE* telescopes have opened a new era of asteroid thermal-infrared observations and the exploitation of their data through TPMs has just begun (e.g., Alí-Lagoa et al., 2014; Rozitis et al., 2014; Emery et al., 2014). At the moment, the limiting factor is the availability of accurate asteroid shape models. However, optical-wavelength all-sky surveys such as PanSTARRS, LSST, and Gaia are expected to produce enormous photometric data sets leading to thousands of asteroid models. We envision the availability of thousands of thermal-inertia values in some years from now, enabling more statistically robust studies of thermal inertia as a function of asteroid size, spectral class, albedo, rotation period, etc.

For instance, the distribution of Γ within asteroid families will be crucial in the search of evidence of asteroid differentiation: asteroid formation models and meteorite studies suggest that hundreds of planetesimals experienced complete or partial differentiation. An asteroid family formed from the catastrophic disruption of such a differentiated asteroid should contain members corresponding to the crust, the mantel and the iron core. However, the observed spectra and albedos are very homogeneous across asteroid families. Thermal inertia might help in separating iron rich from iron poor family members, supposedly originating respectively from the core and mantle of the differentiated parent body (e.g., Matter et al., 2013; Harris and Drube, 2014).

At any size range, Fig. 9 shows an almost tenfold variability in thermal inertia, corresponding to difference in average regolith grain size of almost two orders of magnitude Gundlach and Blum (2013). For small near-Earth asteroids, this could be due to a combination of thermal cracking (Delbo et al., 2014), regolith motion (Murdoch et al., 2015), and cohesive forces (Rozitis et al., 2014). Faster rotation periods allow more thermal cycles, which then enhances thermal fracturing. It also encourages regolith to move towards the equator where the gravitational potential is at its lowest (Walsh et al., 2008). And for the extremely fast rotators, large boulders/rocks could be selectively lofted away, because they stick less well to the surface than smaller particles. For $D > 100$ km sized asteroids, Γ-values might be help to distinguish between primordial and more recently re-accumulated asteroids. The former had ~ 4 Gy of regolith evolution, the latter have a less developed and therefore coarser regolith.

The high-precision thermal-infrared data of WISE and Spitzer pose new challenges to TPMs, as model uncertainties are now comparable to the uncertainty of the measured flux. This will become even more important with the launch of the James Webb Space Telescope (JWST). In particular, the accuracy of the shape models might represent a limiting factor (e.g., Rozitis and Green, 2014). The next challenge will be to allow the TPM to optimize the asteroid shape. This seems to be possible as the infrared photometry is also sensitive to shape, provided good-quality thermal data are available (Durech et al., 2015).

New interferometric facilities, such as MATISSE, LBTI, and ALMA, will become available in the next years requiring TPMs to calculate precise disk-resolved thermal fluxes (Durech et al., 2015). The wavelengths of ALMA, similar to those of MIRO, will allow to measure the thermal-infrared radiation from the subsoil of asteroids, thus providing further information about how thermal inertia varies with depth.

Certainly, constraining roughness is one of the future challenges for TPMs. To do so from disk-integrated data requires a range of wavelengths and solar phase angles. Low phase angle measurements are enhanced by beaming whilst high phase angle measurements are reduced by beaming. In particular, shorter wavelengths are affected more than longer wavelengths.

Moreover, the future availability of precise sizes and cross sections of asteroids from stellar occultation timing (Tanga and Delbo, 2007), combined with shape information derived from lightcurve inversion (Durech et al., 2015) will allow to remove the need to constrain the object size from TPM analysis. Iinfrared fluxes will thus be converted into highly reliable thermal inertia and roughness values.

Acknowledgments

We are grateful to S. Green and to an anonymous referee for their thorough reviews. MD thanks J. Hanus and the support from the French Agence National de la Recherche (ANR) SHOCKS.

REFERENCES

Alí-Lagoa V., Lionni L., Delbo M., et al. (2014). Thermophysical properties of near-Earth asteroid (341843) 2008 EV5 from WISE data. *Astronomy & Astrophysics*, *561*, A45.

Bandfield J. L., Ghent R. R., Vasavada A. R., et al. (2011). Lunar surface rock abundance and regolith fines temperatures derived from LRO Diviner Radiometer data. *Journal of Geophysical Research*, *116*.

Barucci A. M., Fulchignoni M., Ji J., et al. (2015). The Steins, Lutetia, and Toutatis fly-bys. In *Asteroids IV*. this book.

Bottke W. F., Durda D. D., Nesvorný D., et al. (2005). The fossilized size distribution of the main asteroid belt. *Icarus*, *175*, 111–140.

Bottke W. F., Vokrouhlický D., Broz M., et al. (2001). Dynamical Spreading of Asteroid Families by the Yarkovsky Effect. *Science*, *294*, 1693–1696.

Bottke W. F. J., Vokrouhlický D., Rubincam D. P., et al. (2006). The Yarkovsky and Yorp Effects: Implications for Asteroid Dynamics. *Annual Review of Earth and Planetary Sciences*, *34*, 157–191.

Breiter S., Bartczak P., Czekaj M., et al. (2009). The YORP effect on 25143 Itokawa. *Astronomy & Astrophysics*, *507*, 1073–1081.

Buhl D., Welch W. J., and Rea D. G. (1968a). Anomalous Cooling of a Cratered Lunar Surface. *Journal of Geophysical Research*, *73*, 7593–7608.

Buhl D., Welch W. J., and Rea D. G. (1968b). Reradiation and Thermal Emission from Illuminated Craters on the Lunar Surface. *Journal of Geophysical Research*, *73*, 5281–5295.

Campins H., Hargrove K., Pinilla-Alonso N., et al. (2010). Water ice and organics on the surface of the asteroid 24 Themis. *Nature*, *464*, 1320–1321.

Čapek D. and Vokrouhlický D. (2004). The YORP effect with finite thermal conductivity. *Icarus*, *172*, 526–536.

Čapek D. and Vokrouhlický D. (2010). Thermal stresses in small meteoroids. *Astronomy and Astrophysics*, *519*, A75.

Čapek D. and Vokrouhlický D. (2012). Thermal stresses in small meteoroids. II. Effects of an insulating surface layer. *Astronomy & Astrophysics*, *539*, A25.

Capria M. T., Marchi S., De Sanctis M. C., et al. (2012). The activity of main belt comets. *Astronomy & Astrophysics*, *537*, A71.

Capria M. T., Tosi F., De Sanctis M. C., et al. (2014). Vesta surface thermal properties map. *Geophysical Research Letters*, *41*, 1438–1443.

Carry B. (2012). Density of asteroids. *Planetary and Space Science*, *73*, 98–118.

Carry B., Matter A., Scheirich P., et al. (2015). The small binary asteroid (939) Isberga. *Icarus*, *248*, 516–525.

Chamberlain M. A., Lovell A. J., and Sykes M. V. (2007). Submillimeter lightcurves of Vesta. *Icarus*, *192*, 448–459.

Chamberlain M. A., Lovell A. J., and Sykes M. V. (2009). Submillimeter photometry and lightcurves of Ceres and other large asteroids. *Icarus*, *202*, 487–501.

Chaumard N., Devouard B., Delbo M., et al. (2012). Radiative heating of carbonaceous near-Earth objects as a cause of thermal metamorphism for CK chondrites. *Icarus*, *220*, 65–73.

Chesley S. R., Farnocchia D., Nolan M. C., et al. (2014). Orbit and bulk density of the OSIRIS-REx target Asteroid (101955) Bennu. *Icarus*, *235*, 5–22.

Chesley S. R., Ostro S. J., Vokrouhlický D., et al. (2003). Direct Detection of the Yarkovsky Effect by Radar Ranging to Asteroid 6489 Golevka. *Science*, *302*, 1739–1742.

Consolmagno G. J., Macke R. J., Rochette P., et al. (2006). Density, magnetic susceptibility, and the characterization of ordinary chondrite falls and showers. *Meteoritics & Planetary Science*, *41*, 331–342.

Consolmagno G. J., Schaefer M. W., Schaefer B. E., et al. (2013). The measurement of meteorite heat capacity at low temperatures using liquid nitrogen vaporization. *Planetary and Space Science*, *87*, 146–156.

Cruikshank D. P., Stansberry J. A., Emery J. P., et al. (2005). The High-Albedo Kuiper Belt Object (55565) 2002 AW197. *The Astrophysical Journal Letters*, *624*, L53–L56.

Davidsson B., Rickman H., Bandfield J. L., et al. (2015). *Interpretation of thermal emission. I. The effect of roughness for spatially resolved atmosphereless bodies*. Icarus (in press).

Davidsson B. J. R., Gutiérrez P. J., Groussin O., et al. (2013). Thermal inertia and surface roughness of Comet 9P/Tempel 1. *Icarus*, *224*, 154–171.

Davidsson B. J. R. and Rickman H. (2014). Surface roughness and three-dimensional heat conduction in thermophysical models. *Icarus*, *243*, 58–77.

De Sanctis M. C., Ammannito E., Capria M. T., et al. (2012). Spectroscopic Characterization of Mineralogy and Its Diversity Across Vesta. *Science*, *336*, 697–700.

Delbo M. (2004). The nature of near-Earth asteroids from the study of their thermal infrared emission. *PhD thesis*, pp. 1–210.

Delbo M., dell'Oro A., Harris A. W., et al. (2007). Thermal inertia of near-Earth asteroids and implications for the magnitude of the Yarkovsky effect. *Icarus*, *190*, 236–249.

Delbo M. and Harris A. W. (2002). Physical properties of near-Earth asteroids from thermal infrared observations and thermal modeling. *Meteoritics & Planetary Science*, *37*, 1929–1936.

Delbo M., Harris A. W., Binzel R. P., et al. (2003). Keck observations of near-Earth asteroids in the thermal infrared. *Icarus*, *166*, 116–130.

Delbo M., Libourel G., Wilkerson J., et al. (2014). Thermal fatigue as the origin of regolith on small asteroids. *Nature*, *508*, 233–236.

Delbo M., Ligori S., Matter A., et al. (2009). First VLTI-MIDI Direct Determinations of Asteroid Sizes. *The Astrophysical Journal*, *694*, 1228–1236.

Delbo M. and Michel P. (2011). Temperature History and Dynamical Evolution of (101955) 1999 RQ 36: A Potential Target for Sample Return from a Primitive Asteroid. *The Astrophysical Journal Letters*, *728*, L42.

Delbo M. and Tanga P. (2009). Thermal inertia of main belt asteroids smaller than 100 km from IRAS data. *Planetary and Space Science*, *57*, 259–265.

Delbo M., Walsh K., Mueller M., et al. (2011). The cool surfaces of binary near-Earth asteroids. *Icarus*, *212*, 138–148.

Dombard A. J., Barnouin O. S., Prockter L. M., et al. (2010). Boulders and ponds on the Asteroid 433 Eros. *Icarus*, *210*, 713–721.

Duennebier F. and Sutton G. H. (1974). Thermal moonquakes. *Journal of Geophysical Research*, *79*, 4351–4363.

Durech J., Carry B., Delbo M., et al. (2015). Asteroid Models from Multiple Data Sources. In *Asteroids IV*. University of Arizona Press, Tucson, AZ.

Emery J. P., Fernández Y. R., Kelley M. S. P., et al. (2014). Thermal infrared observations and thermophysical characterization of OSIRIS-REx target asteroid (101955) Bennu. *Icarus*, *234*, 17–35.

Emery J. P., Sprague A. L., Witteborn F. C., et al. (1998). Mercury: Thermal Modeling and Mid-infrared (5-12 μm) Observations. *Icarus*, *136*, 104–123.

Fanale F. P. and Salvail J. R. (1989). The water regime of asteroid (1) Ceres. *Icarus*, *82*, 97–110.

Fernández Y. R., Jewitt D. C., and Sheppard S. S. (2002). Thermal Properties of Centaurs Asbolus and Chiron. *The Astronomical Journal*, *123*, 1050–1055.

Fernández Y. R., Sheppard S. S., and Jewitt D. C. (2003). The Albedo Distribution of Jovian Trojan Asteroids. *The Astronomical Journal*, *126*, 1563–1574.

Fornasier S., Lellouch E., Müller T., et al. (2013). TNOs are Cool: A survey of the trans-Neptunian region. VIII. Combined Herschel PACS and SPIRE observations of nine bright targets at 70-500 μm. *Astronomy and Astrophysics*, *555*, A15.

Fountain W. F., Fountain J. A., Jones B. P., et al. (1976). Observational and theoretical temperatures for a total lunar eclipse. *The moon*, *15*, 421–437.

Fowler J. W. and Chillemi J. R. (1992). *IRAS asteroid data processing*. The IRAS Minor Planet Survey.

Frost R. L., Ruan H., Kloprogge J. T., et al. (2000). Dehydration and dehydroxylation of nontronites and ferruginous smectite. *Thermochimica Acta*, *346*, 63–72.

Giese B. and Kuehrt E. (1990). Theoretical interpretation of infrared measurements at Deimos in the framework of crater radiation. *Icarus*, *88*, 372–379.

Golubov O. and Krugly Y. N. (2012). Tangential Component of the YORP Effect. *The Astrophysical Journal Letters*, *752*, L11.

Grimm R. E. and McSween H. Y. (1993). Heliocentric zoning of the asteroid belt by aluminum-26 heating. *Science (ISSN 0036-8075)*, *259*, 653–655.

Groussin O., Lamy P., Fornasier S., et al. (2011). The properties of asteroid (2867) Steins from Spitzer Space Telescope observations and OSIRIS shape reconstruction. *Astronomy & Astrophysics*, *529*, A73.

Groussin O., Lamy P., and Jorda L. (2004). Properties of the nuclei of Centaurs Chiron and Chariklo. *Astronomy & Astrophysics*, *413*, 1163–1175.

Groussin O., Sunshine J. M., Feaga L. M., et al. (2013). The temperature, thermal inertia, roughness and color of the nuclei of Comets 103P/Hartley 2 and 9P/Tempel 1. *Icarus*, *222*, 580–594.

Gulkis S., Frerking M., Crovisier J., et al. (2007). MIRO: Microwave Instrument for Rosetta Orbiter. *Space Science Reviews*, *128*, 561–597.

Gundlach B. and Blum J. (2012). Outgassing of icy bodies in the Solar System - II: Heat transport in dry, porous surface dust layers. *Icarus*, *219*, 618–629.

Gundlach B. and Blum J. (2013). A new method to determine the grain size of planetary regolith. *Icarus*, *223*, 479–492.

Hall K. (1999). The role of thermal stress fatigue in the breakdown of rock in cold regions. *Geomorphology*, *31*, 47–63.

Hall K. and André M.-F. (2001). New insights into rock weathering from high-frequency rock temperature data: an Antarctic study of weathering by thermal stress. *Geomorphology*, *41*, 23–35.

Hanuš J., Brož M., Durech J., et al. (2013). An anisotropic distribution of spin vectors in asteroid families. *Astronomy & Astrophysics*, *559*, A134.

Hanuš J., Durech J., Brož M., et al. (2011). A study of asteroid pole-latitude distribution based on an extended set of shape models derived by the lightcurve inversion method. *Astronomy & Astrophysics*, *530*, 134.

Hapke B. (1984). Bidirectional reflectance spectroscopy. III - Correction for macroscopic roughness. *Icarus*, *59*, 41–59.

Hapke B. (1996). A model of radiative and conductive energy transfer in planetary regoliths. *Journal of Geophysical Research*, *101*, 16817–16832.

Harris A., Boslough M., Chapman C. R., et al. (2015). Asteroid Impacts and Modern Civilization: Can we Prevent a Catastrophe? In *Asteroids IV*. University of Arizona Press, Tucson, AZ.

Harris A. W. (1998). A Thermal Model for Near-Earth Asteroids. *Icarus*, *131*, 291–301.

Harris A. W. (2006). The surface properties of small asteroids from thermal-infrared observations. *Asteroids, Comets, Meteors. Proceedings IAU Symposium No. 229, 2005 D. Lazzaro, S. Ferraz-Mello & J.A. Fernandez, eds*, *229*, 449–463.

Harris A. W. and Davies J. K. (1999). Physical Characteristics of Near-Earth Asteroids from Thermal Infrared Spectrophotometry. *Icarus*, *142*, 464–475.

Harris A. W. and Drube L. (2014). How to Find Metal-rich Asteroids. *The Astrophysical Journal Letters*, *785*, L4.

Harris A. W. and Lagerros J. S. V. (2002). Asteroids in the Thermal Infrared. *Asteroids III, W. F. Bottke Jr., A. Cellino, P. Paolicchi, and R. P. Binzel (eds), University of Arizona Press, Tucson.*, pp. 205–218.

Harris A. W., Mueller M., Delbo M., et al. (2005). The surface properties of small asteroids: Peculiar Betulia—A case study. *Icarus*, *179*, 95–108.

Hoerz F., Schneider E., Gault D. E., et al. (1975). Catastrophic rupture of lunar rocks - A Monte Carlo simulation. *Lunar Science Institute*, *13*, 235–258.

Holsapple K. A. (2010). On YORP-induced spin deformations of asteroids. *Icarus*, *205*, 430–442.

Horner J., Müller T. G., and Lykawka P. S. (2012). (1173) Anchises - thermophysical and dynamical studies of a dynamically unstable Jovian Trojan. *Monthly Notices of the Royal Astronomical Society*, *423*, 2587–2596.

Hörz F. and Cintala M. (1997). Impact experiments related to the evolution of planetary regoliths. *Meteoritics & Planetary Science*, *32*, 179–209.

Hsieh H. H. and Jewitt D. (2006). A Population of Comets in the Main Asteroid Belt. *Science*, *312*, 561–563.

Huang W. L., Bassett W. A., and Wu T. C. (1994). Dehydration and hydration of montmorillonite at elevated temperatures and pressures monitored using synchrotron radiation. *American Mineralogist*, *79*, 683–691.

Huebner W. F., Benkhoff J., Capria M. T., et al. (2006). Heat and Gas Diffusion in Comet Nuclei. ISSI Scientific report SR-004, vol. 4. International Space Science Institute.

Jacobson S. A. and Scheeres D. J. (2011). Dynamics of rotationally fissioned asteroids: Source of observed small asteroid systems. *Icarus*, *214*, 161–178.

Jakosky B. M., Finiol G. W., and Henderson B. G. (1990). Directional variations in thermal emission from geologic surfaces. *Geophysical Research Letters*, *17*, 985–988.

Jewitt D., Hsieh H., and Agarwal J. (2015). The Active Asteroids. In *Asteroids IV*. University of Arizona Press, Tucson, AZ.

Jewitt D. and Li J. (2010). Activity in Geminid Parent (3200) Phaethon. *The Astronomical Journal*, *140*, 1519–1527.

Kallemeyn G. W., Rubin A. E., and Wasson J. T. (1991). The compositional classification of chondrites. V - The Karoonda (CK) group of carbonaceous chondrites. *Geochimica et Cosmochimica Acta*, *55*, 881–892.

Kebukawa Y., Nakashima S., and Zolensky M. E. (2010). Kinetics of organic matter degradation in the Murchison meteorite for the evaluation of parent-body temperature history. *Meteoritics & Planetary Science*, *45*, 99–113.

Keihm S., Kamp L., Gulkis S., et al. (2013). Reconciling main belt asteroid spectral flux density measurements with a self-consistent thermophysical model. *Icarus*, *226*, 1086–1102.

Keihm S., Tosi F., Kamp L., et al. (2012). Interpretation of combined infrared, submillimeter, and millimeter thermal flux data obtained during the Rosetta fly-by of Asteroid (21) Lutetia. *Icarus*, *221*, 395–404.

Keihm S. J. (1984). Interpretation of the lunar microwave brightness temperature spectrum - Feasibility of orbital heat flow mapping. *Icarus*, *60*, 568–589.

Keil K. (2000). Thermal alteration of asteroids: evidence from meteorites. *Planetary and Space Science*, *48*, 887–903.

Kieffer H. H., Martin T. Z., Peterfreund A. R., et al. (1977). Thermal and albedo mapping of Mars during the Viking primary mission. *Journal of Geophysical Research*, *82*, 4249–4291.

Küppers M., O'Rourke L., Bockelée-Morvan D., et al. (2014). Localized sources of water vapour on the dwarf planet (1) Ceres. *Nature*, *505*, 525–527.

Lagerros J. S. V. (1996a). Thermal physics of asteroids. I. Effects of shape, heat conduction and beaming. *Astronomy and Astrophysics*, *310*, 1011–1020.

Lagerros J. S. V. (1996b). Thermal physics of asteroids. II. Polarization of the thermal microwave emission from asteroids. *Astronomy & Astrophysics*, *315*, 625–632.

Lagerros J. S. V. (1997). Thermal physics of asteroids. III. Irregular shapes and albedo variegations. *Astronomy & Astrophysics*, *325*, 1226–1236.

Lagerros J. S. V. (1998). Thermal physics of asteroids. IV. Thermal infrared beaming. *Astronomy & Astrophysics*, *332*, 1123–1132.

Lamy P. L., Jorda L., Fornasier S., et al. (2008). Asteroid 2867 Steins. III. Spitzer Space Telescope observations, size determination, and thermal properties. *Astronomy & Astrophysics*, *487*, 1187–1193.

Langeseth M. G. and Keihm S. J. (1977). Lunar Heat-Flow Experiment. *NASA Technical Report NASA-CR-151619; CU-4-77*, pp. 1–289.

Lauretta D. S., Barucci M. A., Bierhaus E. B., et al. (2012). The OSIRIS-REx Mission — Sample Acquisition Strategy and Evidence for the Nature of Regolith on Asteroid (101955) 1999 RQ36. *Asteroids, Comets, Meteors. Proceedings IAU Symposium No. 229, 2005 D. Lazzaro, S. Ferraz-Mello & J.A. Fernandez, eds*, *1667*, 6291.

Lawson S. L. S. L., Rodger A. P. A. P., Bender S. C. S. C., et al. (2003). Multispectral thermal imager observations of the moon during total eclipse. *Lunar and Planetary Science XXXIV*.

Lebofsky L. A. and Rieke G. H. (1979). Thermal properties of 433 Eros. *Icarus*, *40*, 297–308.

Lebofsky L. A. and Spencer J. R. (1989). Radiometry and a thermal modeling of asteroids. In *Asteroids II*, pp. 128–147. University of Arizona Press, Tucson, AZ.

Lebofsky L. A., Sykes M. V., Tedesco E. F., et al. (1986). A refined 'standard' thermal model for asteroids based on observations of 1 Ceres and 2 Pallas. *Icarus*, *68*, 239–251.

Lellouch E., Santos-Sanz P., Lacerda P., et al. (2013). "TNOs are Cool": A survey of the trans-Neptunian region. IX. Thermal properties of Kuiper belt objects and Centaurs from combined Herschel and Spitzer observations. *Astronomy & Astrophysics*, *557*, 60.

Levi F. A. (1973). Thermal Fatigue: A Possible Source of Structural Modifications in Meteorites. *Meteoritics & Planetary Science*, *8*, 209–221.

Leyrat C., Barucci A., Mueller T., et al. (2012). Thermal properties of (4) Vesta derived from Herschel measurements. *Astronomy & Astrophysics*, *539*, A154.

Leyrat C., Coradini A., Erard S., et al. (2011). Thermal properties of the asteroid (2867) Steins as observed by VIRTIS/Rosetta. *Astronomy & Astrophysics*, *531*, A168.

Licandro J., Campins H., Kelley M., et al. (2011). (65) Cybele: detection of small silicate grains, water-ice, and organics. *Astronomy & Astrophysics*, *525*, A34.

Lim L. F., Emery J. P., and Moskovitz N. A. (2011). Mineralogy and thermal properties of V-type Asteroid 956 Elisa: Evidence for diogenitic material from the Spitzer IRS (5-35 μm) spectrum. *Icarus*, *213*, 510–523.

Lowry S. C., Weissman P. R., Duddy S. R., et al. (2014). The internal structure of asteroid (25143) Itokawa as revealed by detection of YORP spin-up. *Astronomy & Astrophysics*, *562*, A48.

Lucey P. G. (2000). Observations of the moon using the Air Force Maui Space Surveillance Complex. *Proc. SPIE Vol. 4091*, *4091*, 216–224.

Lucey P. G. (2006). Radiative transfer modeling of the effect of mineralogy on some empirical methods for estimating iron concentration from multispectral imaging of the Moon. *Journal of Geophysical Research*, *111*, 8003.

Macke R. J., BRITT D. T., and Consolmagno G. J. (2011a). Density, porosity, and magnetic susceptibility of achondritic meteorites. *Meteoritics & Planetary Science*, *46*, 311–326.

Macke R. J., Consolmagno G. J., and BRITT D. T. (2011b). Density, porosity, and magnetic susceptibility of carbonaceous chondrites. *Meteoritics & Planetary Science*, *46*, 1842–1862.

Macke R. J., Consolmagno G. J., BRITT D. T., et al. (2010). Enstatite chondrite density, magnetic susceptibility, and porosity. *Meteoritics & Planetary Science*, *45*, 1513–1526.

Magri C., Consolmagno G. J., Ostro S. J., et al. (2001). Radar constraints on asteroid regolith compositions using 433 Eros as ground truth. *Meteoritics & Planetary Science*, *36*, 1697–1709.

Mainzer A., Trilling D., and Usui F. (2015). Space-Based Infrared Studies of Asteroids. In *Asteroids IV*. University of Arizona Press, Tucson, AZ.

Marchi S., Delbo M., Morbidelli A., et al. (2009). Heating of near-Earth objects and meteoroids due to close approaches to the Sun. *Monthly Notices of the Royal Astronomical Society*, *400*, 147–153.

Marchi S., Paolicchi P., Lazzarin M., et al. (2006). A General Spectral Slope-Exposure Relation for S-Type Main Belt and Near-Earth Asteroids. *The Astronomical Journal*, *131*, 1138–1141.

Marchis F., Enriquez J. E., Emery J. P., et al. (2012). Multiple asteroid systems: Dimensions and thermal properties from Spitzer Space Telescope and ground-based observations. *Icarus*, *221*, 1130–1161.

Matter A., Delbo M., Carry B., et al. (2013). Evidence of a metal-rich surface for the Asteroid (16) Psyche from interferometric observations in the thermal infrared. *Icarus*, *226*, 419–427.

Matter A., Delbo M., Ligori S., et al. (2011). Determination of physical properties of the Asteroid (41) Daphne from interferometric observations in the thermal infrared. *Icarus*, *215*, 47–56.

McSween H. Y. J., Ghosh A., Grimm R. E., et al. (2002). Thermal Evolution Models of Asteroids. *Asteroids III, W. F. Bottke Jr., A. Cellino, P. Paolicchi, and R. P. Binzel (eds), University of Arizona Press, Tucson.*, pp. 559–571.

Mellon M. T., Jakosky B. M., Kieffer H. H., et al. (2000). High-Resolution Thermal Inertia Mapping from the Mars Global Surveyor Thermal Emission Spectrometer. *Icarus*, *148*, 437–455.

Molaro J. and Byrne S. (2012). Rates of temperature change of airless landscapes and implications for thermal stress weathering. *Journal of Geophysical Research*, *117*, 10011.

Mommert M., Farnocchia D., Hora J. L., et al. (2014a). Physical Properties of Near-Earth Asteroid 2011 MD. *The Astrophysical Journal Letters*, *789*, L22.

Mommert M., Hora J. L., Farnocchia D., et al. (2014b). Constraining the Physical Properties of Near-Earth Object 2009 BD. *The Astrophysical Journal*, *786*, 148.

Morrison D. and Cruikshank D. P. (1973). Thermal Properties of the Galilean Satellites. *Icarus*, *18*, 224–236.

Mueller M. (2007). *Surface Properties of Asteroids from Mid-Infrared Observations and Thermophysical Modeling*. PhD thesis, PhD thesis on arXiv.org.

Mueller M., Harris A. W., Bus S. J., et al. (2006). The size and albedo of Rosetta fly-by target 21 Lutetia from new IRTF measurements and thermal modeling. *Astronomy & Astrophysics*, *447*, 1153–1158.

Mueller M., Marchis F., Emery J. P., et al. (2010). Eclipsing binary Trojan asteroid Patroclus: Thermal inertia from Spitzer observations. *Icarus*, *205*, 505–515.

Müller T. G. (2002). Thermophysical analysis of infrared observations of asteroids. *Meteoritics & Planetary Science*, *37*, 1919–1928.

Müller T. G. and Barnes P. J. (2007). 3.2 mm lightcurve observations of (4) Vesta and (9) Metis with the Australia Telescope Compact Array. *Astronomy & Astrophysics*, *467*, 737–747.

Müller T. G., Durech J., Hasegawa S., et al. (2011). Thermophysical properties of 162173 (1999 JU3), a potential flyby and rendezvous target for interplanetary missions. *Astronomy and Astrophysics*, *525*, 145.

Müller T. G., Hasegawa S., and Usui F. (2014a). (25143) Itokawa: The power of radiometric techniques for the interpretation of remote thermal observations in the light of the Hayabusa rendezvous results*. *Publications of the Astronomical Society of Japan*, *66*, 52.

Müller T. G., Kiss C., Scheirich P., et al. (2014b). Thermal infrared observations of asteroid (99942) Apophis with Herschel. *Astronomy & Astrophysics*, *566*, A22.

Müller T. G. and Lagerros J. S. V. (1998). Asteroids as far-infrared photometric standards for ISOPHOT. *Astronomy & Astrophysics*, *338*, 340–352.

Müller T. G. and Lagerros J. S. V. (2002). Asteroids as calibration standards in the thermal infrared for space observatories. *Astronomy & Astrophysics*, *381*, 324–339.

Müller T. G., Miyata T., Kiss C., et al. (2013). Physical properties of asteroid 308635 (2005 YU55) derived from multi-instrument infrared observations during a very close Earth approach. *Astronomy & Astrophysics*, *558*, A97.

Müller T. G., O'Rourke L., Barucci A. M., et al. (2012). Physical properties of OSIRIS-REx target asteroid (101955) 1999 RQ36. Derived from Herschel, VLT/ VISIR, and Spitzer observations. *Astronomy & Astrophysics*, *548*, A36.

Müller T. G., Sterzik M. F., Schütz O., et al. (2004). Thermal infrared observations of near-Earth asteroid 2002 NY40. *Astronomy & Astrophysics*, *424*, 1075–1080.

Murdoch N., sanchez P., Schwartz S. R., et al. (2015). Asteroid Surface Geophysics. In *Asteroids IV*. University of Arizona Press, Tucson, AZ.

Okada T., Fukuhara T., Tanaka S., et al. (2013). Thermal-Infrared Imager TIR on Hayabusa2: Science and Instrumentation. *44th Lunar and Planetary Science Conference*, *44*, 1954.

Opeil C. P., Consolmagno G. J., and Britt D. T. (2010). The thermal conductivity of meteorites: New measurements and analysis. *Icarus*, *208*, 449–454.

Opeil C. P., Consolmagno G. J., Safarik D. J., et al. (2012). Stony meteorite thermal properties and their relationship with meteorite chemical and physical states. *Meteoritics & Planetary Science*, *47*, 319–329.

O'Rourke L., Müller T., Valtchanov I., et al. (2012). Thermal and shape properties of asteroid (21) Lutetia from Herschel observations around the Rosetta flyby. *Planetary and Space Science*, *66*, 192–199.

Paige D. A., Foote M. C., Greenhagen B. T., et al. (2010). The Lunar Reconnaissance Orbiter Diviner Lunar Radiometer Experiment. *Space Science Reviews*, *150*, 125–160.

Pál A., Kiss C., Müller T. G., et al. (2012). "TNOs are Cool": A survey of the trans-Neptunian region. VII. Size and surface characteristics of (90377) Sedna and 2010 EK139. *Astronomy and Astrophysics*, *541*, L6.

Pettit E. (1940). Radiation Measurements on the Eclipsed Moon. *Astrophysical Journal*, *91*, 408–421.

Pettit E. and Nicholson S. B. (1930). Lunar radiation and temperatures. *The Astrophysical Journal*, *71*, 102–135.

Piqueux S. and Christensen P. R. (2009a). A model of thermal conductivity for planetary soils: 1. Theory for unconsolidated soils. *Journal of Geophysical Research*, *114*, 9005.

Piqueux S. and Christensen P. R. (2009b). A model of thermal conductivity for planetary soils: 2. Theory for cemented soils. *Journal of Geophysical Research*, *114*, 9006.

Piqueux S. and Christensen P. R. (2011). Temperature-dependent thermal inertia of homogeneous Martian regolith. *Journal of Geophysical Research*, *116*, 7004.

Pravec P., Scheirich P., KUSNIRAK P., et al. (2006). Photometric survey of binary near-Earth asteroids. *Icarus*, *181*, 63–93.

Presley M. A. and Christensen P. R. (1997a). Thermal conductivity measurements of particulate materials 1. A review. *Journal of Geophysical Research*, *102*, 6535–6550.

Presley M. A. and Christensen P. R. (1997b). Thermal conductivity measurements of particulate materials 2. results. *Journal of Geophysical Research*, *102*, 6551–6566.

Prialnik D. and Rosenberg E. D. (2009). Can ice survive in main-belt comets? Long-term evolution models of comet 133P/Elst-Pizarro. *Monthly Notices of the Royal Astronomical Society (ISSN 0035-8711)*, *399*, L79–L83.

Putzig N. E. and Mellon M. T. (2007). Apparent thermal inertia and the surface heterogeneity of Mars. *Icarus*, *191*, 68–94.

Raymond C. A., Jaumann R., Nathues A., et al. (2011). The Dawn Topography Investigation. *Space Science Reviews*, *163*, 487–510.

Redman R. O., Feldman P. A., Matthews H. E., et al. (1992). Millimeter and submillimeter observations of the asteroid 4 Vesta. *Astronomical Journal (ISSN 0004-6256)*, *104*, 405–411.

Rivkin A. S. and Emery J. P. (2010). Detection of ice and organics on an asteroidal surface. *Nature*, *464*, 1322–1323.

Rozitis B., Duddy S. R., Green S. F., et al. (2013). A thermophysical analysis of the (1862) Apollo Yarkovsky and YORP effects. *Astronomy and Astrophysics*, *555*, A20.

Rozitis B. and Green S. F. (2011). Directional characteristics of thermal-infrared beaming from atmosphereless planetary surfaces - a new thermophysical model. *Monthly Notices of the Royal Astronomical Society*, *415*, 2042–2062.

Rozitis B. and Green S. F. (2012). The influence of rough surface thermal-infrared beaming on the Yarkovsky and YORP effects. *Monthly Notices of the Royal Astronomical Society*, *423*, 367–388.

Rozitis B. and Green S. F. (2013). The influence of global self-heating on the Yarkovsky and YORP effects. *Monthly Notices of the Royal Astronomical Society*, *433*, 603–621.

Rozitis B. and Green S. F. (2014). Physical characterisation of near-Earth asteroid (1620) Geographos. Reconciling radar and thermal-infrared observations. *Astronomy & Astrophysics*, *568*, A43.

Rozitis B., MacLennan E., and Emery J. P. (2014). Cohesive forces prevent the rotational breakup of rubble-pile asteroid (29075) 1950 DA. *Nature*, *512*, 174–176.

Russell C. T., Raymond C. A., Coradini A., et al. (2012). Dawn at Vesta: Testing the Protoplanetary Paradigm. *Science*, *336*, 684–686.

Scheeres D. J. (2007). Rotational fission of contact binary asteroids. *Icarus*, *189*, 370–385.

Scheeres D. J. and Gaskell R. W. (2008). Effect of density inhomogeneity on YORP: The case of Itokawa. *Icarus*, *198*, 125–129.

Schorghofer N. (2008). The Lifetime of Ice on Main Belt Asteroids. *The Astrophysical Journal*, *682*, 697–705.

Sexl R. U., Sexl H., Stremnitzer H., et al. (1971). The directional characteristics of lunar infrared radiation. *The moon*, *3*, 189–213.

Shorthill R. W. (1973). Infrared Atlas Charts of the Eclipsed Moon. *The moon*, *7*, 22–45.

Sierks H., Lamy P., Barbieri C., et al. (2011). Images of Asteroid 21 Lutetia: A Remnant Planetesimal from the Early Solar System. *Science*, *334*, 487–490.

Smith B. G. (1967). Lunar surface roughness: Shadowing and thermal emission. *Journal of Geophysical Research*.

Spencer J. R. (1990). A rough-surface thermophysical model for airless planets. *Icarus*, *83*, 27–38.

Spencer J. R., Lebofsky L. A., and Sykes M. V. (1989). Systematic biases in radiometric diameter determinations. *Icarus*, *78*, 337–354.

Statler T. S. (2009). Extreme sensitivity of the YORP effect to small-scale topography. *Icarus*, *202*, 502–513.

Tambovtseva L. V. and Shestakova L. i. (1999). Cometary splitting due to thermal stresses. *Planetary and Space Science*, *47*, 319–326.

Tanga P. and Delbo M. (2007). Asteroid occultations today and tomorrow: toward the GAIA era. *Astronomy and Astrophysics*, *474*, 1015–1022.

Thomas P. C., Joseph J., Carcich B., et al. (2002). Eros: Shape, Topography, and Slope Processes. *Icarus*, *155*, 18–37.

Tosi F., Capria M. T., De Sanctis M. C., et al. (2014). Thermal measurements of dark and bright surface features on Vesta as derived from Dawn/VIR. *Icarus*, *240*, 36–57.

Urquhart M. L. and Jakosky B. M. (1997). Lunar thermal emission and remote determination of surface properties. *Journal of Geophysical Research*, *102*, 10959–10970.

Vaniman D., Reddy R., Heiken G., et al. (1991). The Lunar Environment. In *Lunat Sourcebook* (Heiken G. H., Vaniman D., and French K. L., editors), pp. 27–60. Cambridge University Press., Cambridge, UK.

Vasavada A. R., Bandfield J. L., Greenhagen B. T., et al. (2012). Lunar equatorial surface temperatures and regolith properties from the Diviner Lunar Radiometer Experiment. *Journal of Geophysical Research*, *117*.

Vasavada A. R., Paige D. A., and Wood S. E. (1999). Near-Surface Temperatures on Mercury and the Moon and the Stability of Polar Ice Deposits. *Icarus*, *141*, 179–193.

Vernazza P., Delbo M., King P. L., et al. (2012). High surface porosity as the origin of emissivity features in asteroid spectra. *Icarus*, *221*, 1162–1172.

Veverka J., Farquhar B., Robinson M., et al. (2001). The landing of the NEAR-Shoemaker spacecraft on asteroid 433 Eros. *Nature*, *413*, 390–393.

Vilenius E., Kiss C., Mommert M., et al. (2012). "TNOs are Cool": A survey of the trans-Neptunian region. VI. Herschel/PACS observations and thermal modeling of 19 classical Kuiper belt objects. *Astronomy & Astrophysics*, *541*, A94.

Viles H., Ehlmann B., Wilson C. F., et al. (2010). Simulating weathering of basalt on Mars and Earth by thermal cycling. *Geophysical Research Letters*, *37*, 18201.

Vincent J.-B., Besse S., Marchi S., et al. (2012). Physical properties of craters on asteroid (21) Lutetia. *Planetary and Space Science*, *66*, 79–86.

Vokrouhlický D., Bottke W. F., Chesley S. R., et al. (2015). The Yarkovsky and YORP effects. In *Asteroids IV*. University of Arizona Press, Tucson, AZ.

Vokrouhlický D. and Nesvorný D. (2012). Sun-grazing orbit of the unusual near-Earth object 2004 LG. *Astronomy & Astrophysics*, *541*, A109.

Vokrouhlický D., Nesvorný D., and Bottke W. F. (2003). The vector alignments of asteroid spins by thermal torques. *Nature*, *425*, 147–151.

Walsh K. J., Richardson D. C., and Michel P. (2008). Rotational breakup as the origin of small binary asteroids. *Nature*, *454*, 188–191.

Wesselink A. J. (1948a). Heat conductivity and nature of the lunar surface material. *Bulletin of the Astronomical Institutes of the Netherlands*, *10*, 351–363.

Wesselink A. J. (1948b). Heat conductivity and nature of the lunar surface material. *Bulletin of the Astronomical Institutes of the Netherlands*, *10*, 351–363.

Winter D. F. and Krupp J. A. (1971). Directional characteristics of infrared emission from the moon. *The moon*, *2*, 279–292.

Wolters S. D. and Green S. F. (2009). Investigation of systematic bias in radiometric diameter determination of near-Earth asteroids: the night emission simulated thermal model (NESTM). *Monthly Notices of the Royal Astronomical Society*, *400*, 204–218.

Wolters S. D., Rozitis B., Duddy S. R., et al. (2011). Physical characterization of low delta-V asteroid (175706) 1996 FG3. *Monthly Notices of the Royal Astronomical Society*, *418*, 1246–1257.

Yano H., Kubota T., Miyamoto H., et al. (2006). Touchdown of the Hayabusa Spacecraft at the Muses Sea on Itokawa. *Science*, *312*, 1350–1353.

This 2-column preprint was prepared with the AAS LaTeX macros v5.2.

3

Perspectives

SURFACES are where exploration and planetary science intersect. A key challenge for solar system science is to establish a comprehensive time line for understanding the variety of processes that create, evolve, and shape the surfaces of small bodies. One future development for the physical studies of minor bodies is to tackle this issue by surveying the physical nature of the surfaces of many asteroids. There are two ways of doing this: (i) by sending many space missions, or (ii) from remote sensing observations. While the former solution is clearly very expensive and quite impractical, we explore here the future perspectives to the latter approach.

3.1 Asteroid spectroscopy and mineralogy with Gaia

Presentation of Gaia

The ESA cornerstone mission Gaia, that started its 5-years all-sky survey in July 2014, will characterize all astrophysical sources down to V=20, including about 300,000 asteroids, by measuring their position, motion and spectral properties. The ultra-precise astrometry ($\sim$25 μas at V=15) is the unbeatable driver for Gaia science, promising a revolution in astrophysics, with the first data release in 2016.

Gaia's instruments: focal plane's CCDs

Gaia consists of two telescopes with a rectangular aperture of 1.45×0.5 m^2 observing simultaneously two fields separated by a basic angle of 106.5°. The two telescopes have a common focal plane composed of 106 CCDs: 77 of them will collect the data for the astrometry and the photometry of the observed sources; 14 CCDs will measure the light dispersed by two prisms, in order to

obtain the colour of all sources observed by the astrometric focal plane; 12 CCDs will collect the data coming from the high resolution spectrometer (RVS) to measure the objects radial velocity; the remaining CCDs are needed for calibration purposes. The two low resolution spectrophotometers are called the Blue Photometer – BP for short – and Red Photometer – RP for short. The first optimised in the blue, and the second in the red.

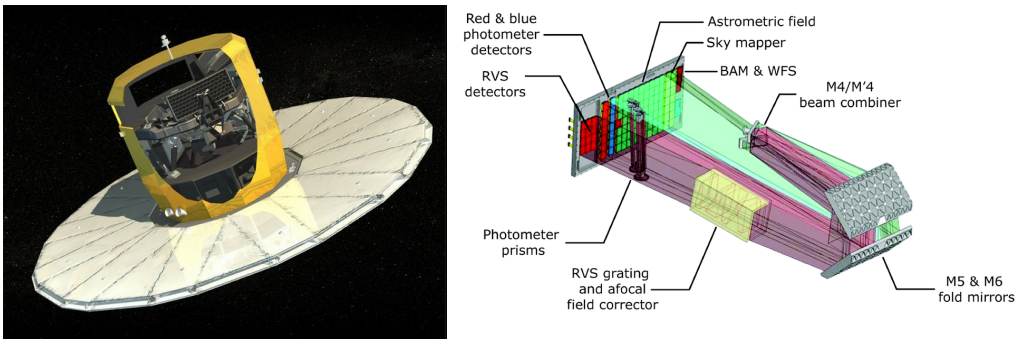

Figure 3.1: LEFT: Gaia spacecraft with deployed sun shield and view of the optical bench that carries the mirrors and the focal plane CCDs. RIGHT: schematics of the focal plane CCDs and of the optical paths.

Asteroid spectroscopy with Gaia

The low-resolution spectrophotometric observations (hereafter BP-RP observations) of asteroids from Gaia will be used to determine the surface reflectivity of asteroids and to produce a spectral classification for 100,000 – 150,000 of these bodies [43], to be compared to the 3,000 asteroid spectra available today. This large number statistic will allow compositional studies of the whole asteroid belt down to very small sizes (it is estimated that there are about 100,000 asteroids larger than 5–7 km in the Main Belt; [18]) and of sub-population of asteroids, such as the different dynamical and collisional families present in the asteroid belt. Moreover, all spectra will be acquired by the same instrument in a very stable space-based environment.

It is estimated [43] that a singal-to-noise ratio good enough to perform spectral classification can be obtained for about 100,000 – 150,000 asteroids with H<15 if the data are averaged over five years of observations (i.e. roughly 60 transits on the focal plane per asteroid). On the other hand, for all observed asteroids ($\sim$ 400,000) the eight-color magnitudes calculated by means of the Spectral Shape Coefficients (SSCs) [43] averaged over the mission duration will allow us to calculate eight-point reflectancies of quality good enough for a robust spectral classification. SSCs are coefficients of spline functions allowing to

reproduce the shape of the BP-RP spectrophometry with a limited number of basis functions with the aim of describing the overall shape of BP-RP spectra. SSCs give more information than just the integrated BP and RP fluxes and can be used to calculate simple pseudo-colours of the observed sources. SSCs will provide four colors for each spectrophotometer, for all sources observed by Gaia [43].

Gaia asteroid spectral taxonomy

Asteroid reflectivities will be used to determine the asteroid spectral class by means of an unsupervised clustering algorithm. The use of this latter method will produce a new asteroid "Gaia" taxonomic classification. The clustering method is based on a Minimal Spanning Tree (MST) algorithm and was developed by ref. [59].

Moreover, the combination of Gaia spectrophotometric observations with auxiliary data (e.g. albedos from the WISE space mission or the Spitzer Space Telescope), will make possible to remove some spectral class degeneracies and build a mineralogical map of the asteroids of the main belt down to sizes of few kilometers in diameter (the diameter of an asteroid with H$\sim$15 and geometric visible albedo $\sim$0.1 is about 4 km).

The DPAC

These analysis are performed by the Data Processing and Analysis Consortium of Gaia (DPAC) gathers $\sim$450 scientists and engineers from all over Europe tasked with the mass processing of the mission[1]. The goal of DPAC is to produce a calibrated, first-level data product containing the main properties (positions, proper motions, statistics, classifications, etc.) of the largest possible number of astrophysical objects, as observed by Gaia.

3.2 Interferometry

Mass, density and internal structure of asteroids

Among the most important characteristics of asteroids are their density and internal structures, which are also some of the least constrained. When compared with the densities of meteorites - a partial sample of the building blocks of asteroids that survive the passage through the Earth's atmosphere - one can deduce the nature of asteroid interiors.

[1] I have responsibilities in the development of algorithms and software for the treatment and scientific exploitation of the data from the Gaia space mission, with which my department – the Laboratoire Lagrange – is strongly engaged. I am in charge of the spectrophotometry of small bodies and I am member of the Radiation Damage Task Force that studies the effects of the damage of the CCD sensors due to cosmic and solar protons bombardment.

Binary asteroids with interferometry

Recent technological advances in high spatial resolution astronomy offer a unique opportunity to study the densities and internal structures of asteroids in unprecedented detail. In particular, interferometry can be used to measure the semimajor axis of the orbits of asteroid satellites. This method can provide very accurate masses since, by Kepler's third law, the orbital period and semi-major axis of the system uniquely determine the mass of the bodies. The orbital periods of small binary asteroid targets are already known from photometric lightcurve observations; accurate measurements of their sizes are now also available from WISE data.

Going to smaller and fainter binary asteroids can revolutionize our understanding, because we will be sampling a new regime in physical properties. Moreover, up to now densities have been determined for only 30 asteroids; the known sample is strongly biased because it includes only the largest asteroids - such as 1 Ceres, 2 Pallas, 4 Vesta - few binaries with sizes >100 km, and a handful of small near NEAs two of them visited in situ by space missions and the others accurately studied by radar, by high precision astrometry, and thermal infrared that allow the determination of their densities from the measurement and modelling of the Yarkovsky effect.

From the bulk density of asteroids one can estimate their macroporosity and assess their internal structure. To do this, three sources of data are required for each individual asteroid: (1) its bulk density, (2) its reflectance spectrum, to indicate a meteoritic compositional analogue, and (3) the grain density and average porosity of that analogue meteorite.

Scientific impact

Any deviation of the asteroid's bulk density from its potential meteorite analog's grain density provides an estimate of the bulk porosity of the asteroid. The macroporosity of asteroids is directly linked to the past collisional evolution of the asteroid belt. In fact, current models [11, 90] predict that most asteroids larger than a few ∼100 m are fractured aggregates held together by gravity only. Their gravitational reaccumulation follows the catastrophic disruption of a parent body, due to a collision [120]. Checking these models is highly required because our knowledge of the collisional process is still poor and needs to be confronted to a large variety of validation tests (e.g. impact experiments at small scale, asteroid family formation at large scale, confrontation with macroporosity measurements through linkage with meteorite analogs). Furthermore, collisional processes play a major role in all phases of planetary system formation and evolution, from the formation of planets through collisional accretion to later stages when small bodies undergo collisional disruptions. Moreover,

knowledge of macroporosity allows us to estimate the lifetime of small bodies, because their response to impacts depends highly on their internal structure. A final need for knowing the internal structure of asteroids concerns mitigation strategies. In order to efficiently deflect a potentially hazardous asteroid by means of a kinetic impactor, it is fundamental to know its internal structure, such that the projectile can be given adequate impact energy. Binaries among the larger main-belt asteroids are probably formed by collisions: catastrophic collisions, followed by mutual capture of individual fragments, can form binaries; large cratering events (sub-catastrophic collisions), with reaccumulation of some ejecta can yield moons orbiting a large primary body [120, 52]. Furthermore, the knowledge of the presence and amount of marcoporosity is an important discriminator for models of binary formation. Indeed, formation mechanisms involving rotational fragmentation due to the YORP spin-up assumes that the progenitor at the origin of the final binary is a gravitational aggregate. In this model [182], while the spin of the progenitor increases slowly due to the YORP thermal effect, particles from the equator (which undergo the largest centrifugal force, and lowest gravity) start being ejected from the surface, those from the pole go to the equator to be eventually ejected, and under certain conditions ejected particles reaccumulate to form a secondary. This mechanism only works if the original asteroid is a rubble pile, so that individual particles can leave the surface and on the same time the shape of the primary remains oblate enough that a secondary is not destabilized by a too irregular potential over which it orbits.

The instruments

These observational techniques require achieving spatial resolutions well below ∼100 mas by making use of interferometers such as the ESO Very Large Telescope Interferometer (VLTI), the Large Binocular Telescope Interferometer (LBTI), or ALMA.

Figure 3.2 shows all asteroids with satellites known in the Main Belt. Only asteroids in the upper left corner, bright and with primary-secondary separation in excess of 100 mas, can be resolved today using direct imaging. Interferometries can be used to target those asteroids, with separation <100 mas, that cannot be resolved that way. These asteroids are known to have a satellite from photometric lightcurve studies. With nominal spatial resolution varying between 2 and 12 mas in the near-IR and 20 and 200 mas in the thermal IR, the VLTI of the ESO can be used to characterize binary asteroids that are too compact to be imaged with other techniques. The spatial resolution of the LBTI at around 3 μm (using the LMIRcam) is about 20 mas. The measurement

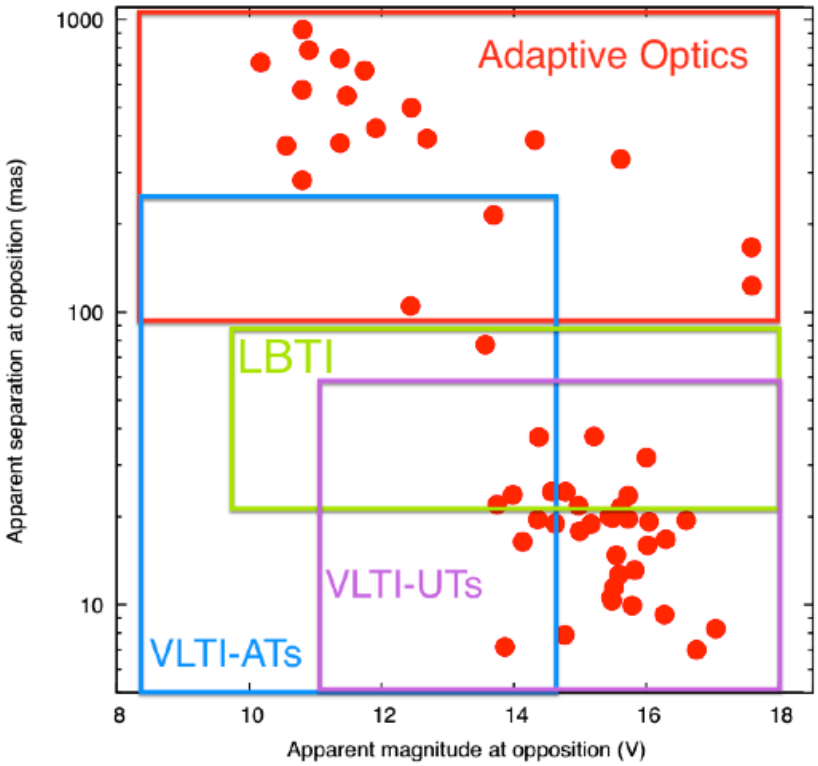

Figure 3.2: LEFT: Gaia spacecraft with deployed sun shield and view of the optical bench that carries the mirrors and the focal plane CCDs. RIGHT: schematics of the focal plane CCDs and of the optical paths.

of the separation of a binary astronomical source is a classical application of interferometry, and [47] and [36] describe the application of this technique in the case of asteroids observed with MIDI at the VLTI. A binary source produces a modulation of the contrast of the interferometric fringes proportional to $\sqrt{\cos(2\pi\lambda/B\rho)}$ where B is the projected length of the interferometer baseline, λ the wavelength of the light and ρ the angular separation of the binary components in the plane of the sky projected along B.

The Multi AperTure mid-Infrared SpectroScopic Experiment (MATISSE) is the mid-infrared spectrograph and imager under construction for the VLTI [105][2]. This is a second generation interferometric instrument will significantly

[2]I was invited to join the MATISSE Science Team in 2011. This international team was mostly devoted to the definition of the science cases for the instrument and now to the

contribute to several fundamental research topics in astro- physics, focussing, for instance, on the inner regions of discs around young stars where planets form and evolve, the surface structure and mass loss of stars at different evolutionary stages and the environment of black holes in active galactic nuclei (AGN). MATISSE is a combined imager and spectrograph for interferometry in the 3–5 μm region (L- and M-bands) and the 8–13 μm window (N-band).

MATISSE will provide simultaneous observations with four different baselines, leading to six simultaneous visibility points. In the case of binary asteroid studies, this will lead to a much better constraint on the angular separation of the system, and will allow us to determine, in one single observation, the "true" angular separation as projected onto the plane of the sky (and not only along the baseline direction). An efficient and reliable measurement of the semi-major axis of the system is thus expected.

The Atacama Large Millimeter/submillimeter Array (ALMA) is also a very promising instrument for high spatial resolution studies of asteroids. Recent images [82] of the asteroid (3) Juno were obtained with an angular resolution of 0.042 arc sec (60 km at 1.97 au). With the unprecedented resolution of ALMA, it is shown that it is possible to study the brightness temperature variation across the surface of the body. These results demonstrate ALMA?s potential to resolve thermal emission from the surface of main belt asteroids, and to measure accurately their position, geometric shape, rotational period, and soil characteristics.

3.3 NEA space exploration & sample return

OSIRIS-REx

The NASA's Origins, Spectral Interpretation, Resource Identification, and Security–Regolith Explorer (OSIRIS-REx) asteroid sample return mission[3] of the NASA will survey near-Earth asteroid (101955) Bennu to understand its physical, mineralogical, and chemical properties; assess its resource potential; refine the impact hazard; and return a sample of this body to Earth. This mission is scheduled for launch in 2016, rendezvous in 2018, and departure in 2021.

preparation of the GTO time and the data exploitation.

[3]I was invited to be Co-I of the mission with the task of thermophsyical modelling. One of my task is to put forward a methodology of developing the asteroid Bennu surface temperature maps for OSIRIS-REx spacecraft and instrument thermal design and analyses.

The measurements made at the asteroid during our encounter will allow us to critically test our pre-encounter understanding of Bennu, built from astronomical observations. The most interesting results will be obtained in areas where the ground-based observations proved inaccurate.

OSIRIS-REx will also develop a comprehensive thermophysical model of the asteroid using data obtained during the asteroid encounter. Comparison of the Yarkovsky and YORP effects predicted from this first-principles approach to the direct measurement of the resulting asteroid acceleration and change in rotation state will test our understanding of these phenomena and lead to a substantial improvement in our knowledge of the fundamental parameters that give rise to these effects. Finally, the thermal conductivity and heat capacity of the returned samples will be directly measured in the laboratory. These fundamental physical parameters, combined with the state of the regolith on the asteroid surface, drive the thermal inertia and the resulting strength of the YORP and Yarkovsky effects. Thus, OSIRIS-REx will benefit future studies of near-Earth objects as well as Main Belt asteroids in many different ways.

AIDA

The Asteroid Impact & Deflection Assessment (AIDA) mission will be the first space experiment to investigate a binary NEA and to demonstrate asteroid impact hazard mitigation by using a kinetic impactor. AIDA[4] is a joint ESA-NASA cooperative project, which includes the ESA Asteroid Impact Mission (AIM) rendezvous spacecraft and the NASA Double Asteroid Redirection Test (DART) mission. The primary goals of AIDA are (i) to investigate the binary NEA (65803) Didymos, (ii) to test our ability to impact its moon by an hypervelocity projectile in 2022 and (iii) to measure and characterize the impact deflection both from space with AIM and from ground based observatories.

The AIM study entered Phase A/B1 at ESA in early 2015 and will proceed through summer 2016. The DART study entered NASA Phase A in late spring 2015 and will also proceed through summer 2016.

3.4 Thermal inertia and nature of asteroid surfaces

Limitation of spectroscopic and albedo data

Most of our knowledge of asteroid physical properties is hitherto based on the determination of their albedos and reflectance spectra as tools to investigate their compositions and mineralogy. However, these parameters are insensitive to geological quantities of asteroid surfaces such as the presence of rocks or

[4] I am a member of the AIDA science team.

fine regolith, which still remain poorly constrained despite being a key parameter for planetary science. The surface is indeed what we sense with remote observations, and it thus shapes our understanding of the underlying body.

Thermal inertia and rockyness

The physical nature of airless surfaces can be investigated from remote observations by measuring the value of the thermal inertia (Γ), which is very sensitive to the "rockiness" of the soil. For instance, fine-grained-soil has a Γ-value lower than that of a solid rock with the same composition [64].

The value of the thermal inertia depends on the composition and physical nature of the soil: e.g., a metal-rich soil has a higher Γ-value than a metal-poor one (this is because the value of the thermal conductivity of metal is much higher than that of silicates or carbonaceous compounds [140, 141].

Determination of thermal inertia

As we saw in chapter 2, asteroid thermal inertias can be determined by analysing thermal infrared and optical data by the so-called asteroid TPMs. Physical parameters such as albedo (or reflectivity), thermal conductivity, heat capacity, emissivity, density and roughness, along with the shape (e.g., elevation model) of the body, its orientation in space, and its previous thermal history are taken into account by TPMs to calculate surface temperatures. From the synthetic surface temperatures, thermally emitted fluxes (typically in the medium-infrared) can be calculated. Physical properties are constrained by fitting model fluxes to observational data. Typically TPMs produce the value of the thermal inertia averaged over the whole surface of the body.

Current limitations

Due to the relative scarcity of both requisites for TPM, namely high-quality IR data and asteroid shapes and rotation states, it is not surprising that only a meagre set of 27 values of thermal inertias have been determined to date for asteroids in the main belt [49] (see also Fig. 2.5). Part of the problem has recently improved tremendously with the release of NASA's WISE enormous thermal infrared catalogue. Simple thermal models that assume spherical surfaces and neglect the thermal mechanisms described above have already been used to exploit WISE's large database. While more sophisticated modeling requires better quality and more numerous data, there are still $\sim$50,000 asteroids which have more than ten measurements in both W3 and W4 bands amenable to TPM. On the other hand, only three works that take advantage of WISE data and TPM have been published so far [2, 154, 67]. Thus, the bottleneck now hindering significant advancement in the field is thus the small number of asteroids with known shapes.

Shapes of asteroids from lightcurve inversion

The lightcurve inversion method [92, 93] is a powerful tool that allows us to derive basic physical properties of asteroids (the sidereal rotation period, spin

vector orientation and the shape) from their disk-integrated photometry. These shape models are used as inputs for the TPM[5]. In March 2015, models of almost 400 asteroids were included in DAMIT[6]. about a hundred based only on dense data. Recently, another 400 new asteroid models were recently derived from sparse data. These unpublished models are much coarser than those based on classical dense lightcurves and additional photometry needs to be obtained prior any further application. However, it is estimated (Hanus, private communication) that shapes for almost 1,000 are almost available. In addition, Gaia data analysis in 2019 will provide shapes for ∼10,000 asteroids, allowing us to obtain the same number of thermal inertias.

This allows to build a new tool for the reconnaissance of the rockiness of asteroid surfaces from remote sensing that, in addition to albedo and spectral data, will add a new dimension to the maps of the physical properties of asteroids throughout the Main Belt, with obvious benefits for various types of space missions (Figs. 3.3,3.4).

Scientific impact

This will have far reaching implications. For example, knowledge of thermal inertia is fundamental for modeling thermal forces affecting the orbits of small asteroids, including those that are close to Earth. Furthermore, rockiness is a key parameter for space missions designed to interact with the surface to, for instance, collect samples, land, or even put an astronaut on an asteroid. These results will give us unprecedented insights into the asteroid population from a completely unexplored point of view. For instance, finding asteroids of similar sizes within the same families but with different thermal inertias might indicate

[5]This photometry can be dense-in-time, sparse-in-time or combination of both. To obtain a unique spin and shape solution, one needs a set of at least a few tens of dense lightcurves observed during three or more apparitions for an asteroid: this is the first/classical approach. But, it has been shown [91] that one can also use only sparse data for the inversion technique. In such case, a unique model can be derived from more than about one hundred calibrated measurements observed during 3-5 years if the photometric accuracy is better than ∼5% [53]. Sparse data available so far are not that accurate. Nevertheless, for many asteroids with high lightcurve amplitudes, it is possible to derive their shape models from contemporary sparse data (covering usually time of ∼15 years). First results coming from this approach were based on sparse data from the US Naval Observatory in Flagstaff (USNO-Flagstaff station) [55]. If one combines sparse and dense data together, the shape model can be already derived from few dense lightcurves and about 100 sparse data points. This approach led to a significant increase of derived shape models from ∼100 to ∼400 [66, 68].

[6]Most of the asteroid models are publicly available in the Database of Asteroid Models from Inversion Techniques (DAMIT, http://astro.troja.mff.cuni.cz/projects/asteroids3D).

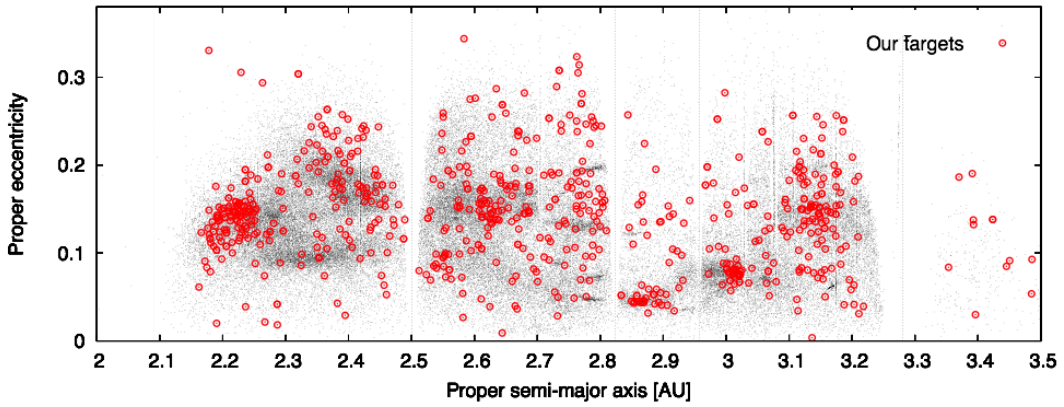

Figure 3.3: Orbital distribution of asteroids throughout the belt. We highlight the asteroids that we are currently attempting to derive thermal inertia from shape models of the DAMIT and unpublished shape models.

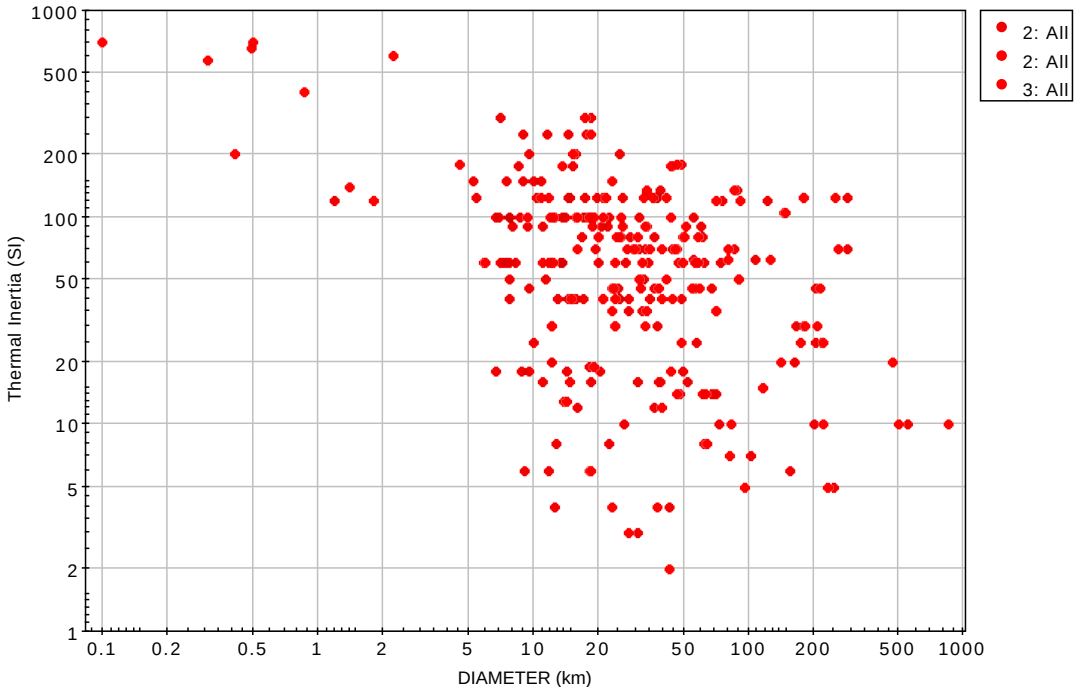

Figure 3.4: Thermal inertia vs diameter. This is an update of Fig. 2.5 including unpublished results from Hanus, Delbo et al. in preparation (since 2014).

different composition, which in turn could provide hints of differentiation of the parent body. Clues of asteroid differentiation come from the meteorite record but have never been found in the asteroid Main Belt; e.g., no trace of family members corresponding to the metallic core, olive mantle and silicate crust have ever been found nor there is any clear evidence of the olivine rich mantle in (4) Vesta, despite the fact that asteroid formation models suggest it should be differentiated. Reliable values of thermal inertias typical of particular asteroid families are highly desired inputs for accurate modeling of Yarkovsky force causing the spreading of the semi/major axes of the family members over time.

An original perspective is the utilization of thermal inertia as a clock. The rockiness, i.e., the fractional area of the surface covered by ∼10 cm-sized rocks and larger compared to the area covered with fine regolith [8], can be derived form thermal inertia data. The rockiness can then be used as a clock to time how long a surface has been exposed to space and weathered by micrometeorite impacts and thermal fatigue fragmentation [46]. These processes result in the gradual fragmentation of the surface material, which will be used to establish a novel approach to set a unified asteroid chronology of evolutionary processes of asteroids with different mineralogy and ages throughout the Main Belt

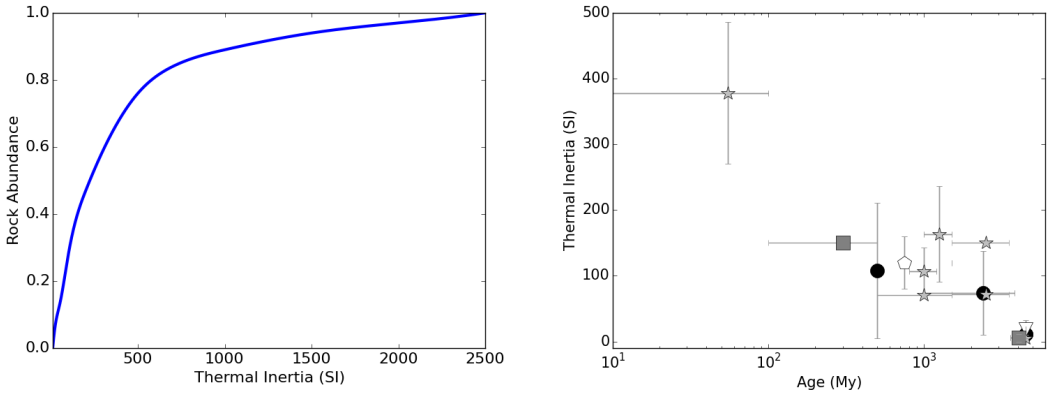

Figure 3.5: Left: rock abundance as a function of thermal inertia derived using our preliminary method described in part B2 of the proposal. Right: thermal inertia versus age for some asteroids with estimated ages (preliminary, unpublished results).

A field-changing discovery would be the confirmation of the primordial age (∼4.6 Ga) of main belt asteroids with very low thermal inertia value (e.g., 10-50 J $m^{-2}s^{-1/2}K^{-1}$) in the size range 10-40 km, which have been identified in prelim-

inary results from our group (Hanus, Delbo, Durech, Al-Lagoa in preparation. See also Fig. 3.4). If these objects were the direct result of primordial material accretion in the nebula, their existence could be explained only by certain models of planetesimal accretion, e.g., by the so-called pebble accretion (Kretke, K. A. & Levison H. F. (2014), DPS abstract; Levison, H. F. (2014), Nature, submitted). On the other hand, if these were products of collisions, we would be looking at the remnants of the first collisional processes in our Solar System, which have been long sought after without success.

Planetary and Space Science 73 (2012) 86–94

Contents lists available at SciVerse ScienceDirect

Planetary and Space Science

journal homepage: www.elsevier.com/locate/pss

Asteroid spectroscopy with Gaia

Marco Delbo' [a,*], Julie Gayon-Markt [a], Giorgia Busso [b], Antony Brown [b], Laurent Galluccio [a], Christophe Ordenovic [a], Philippe Bendjoya [a], Paolo Tanga [a]

[a] Université Nice Sophia-Antipolis – CNRS UMR 7293 – Observatoire de la Côte d'Azur, BP 4229, Nice Cedex-4, France
[b] Leiden Observatory, P.O. Box 9513, 2300 RA Leiden, The Netherlands

ARTICLE INFO

Article history:
Received 31 January 2012
Received in revised form
2 July 2012
Accepted 24 July 2012
Available online 14 August 2012

Keywords:
Asteroids
Photometry
Space missions
Spectroscopy

ABSTRACT

The Gaia space mission of the European Space Agency (ESA) will survey the entire sky with a limiting magnitude of about 20 in the V-band. Gaia is expected to be launched in the summer of 2013. Gaia will also observe about 400,000 asteroids, for which high precision astrometry and photometry will be obtained. Here we discuss Gaia spectrophotometric observations of asteroids, the methods for the treatment of the data, the expected performances of the spectrophotometers and the spectral classification of asteroids. We estimate that a robust spectral classification can be obtained for at least 100,000 asteroids from the low-resolution spectra obtained by Gaia.

1. Introduction

In 2013 the European Space Agency (ESA) will launch the Gaia space mission to the Earth's Lagrangian Point L2. Gaia is mainly devoted to the precise measurement of the positions of about 10^9 stars repeatedly over 5 years (see Perryman et al., 2001; Mignard et al., 2007, and references therein). These measurements will produce the most complete and accurate catalogue of parallaxes and proper motions of the stars of our galaxy with unprecedented astrometric accuracy. Gaia consists of two telescopes with a rectangular aperture of 1.45×0.5 m^2 observing simultaneously two fields separated by a basic angle of 106.5°. The two telescopes have a common focal plane composed of 106 CCDs: 77 of them will collect the data for the astrometry and the photometry of the observed sources; 14 CCDs will measure the light dispersed by two prisms, in order to obtain the color of all sources observed by the astrometric focal plane; 12 CCDs will collect the data coming from the high resolution spectrometer (RVS) to measure the objects radial velocity; the remaining CCDs are needed for calibration purposes. The two low resolution spectrophotometers are called the *Blue Photometer* – BP for short – and *Red Photometer* – RP for short. The first optimised in the blue, and the second in the red.

On one hand, the spectrophotometric data will provide fundamental information about the physical characteristics of the observed sources (e.g. the photospheric temperature of stars); on the other hand, color spectrophotometry is needed to select the color-dependent instrument point spread function (PSF) in the analysis of the astrometric focal plane data.[1]

Gaia will also serendipitously observe about 400,000 asteroids on average 60 times over 5 years (Tanga and Mignard, this issue). The main products of Gaia solar system objects observations will be orbital and physical properties of asteroids (Mignard et al., 2007). In this paper we focus on the low-resolution spectrophotometric observations (hereafter BP-RP observations) of asteroids from Gaia. These data will be used to determine the surface reflectivity of asteroids and to produce a spectral classification for 100,000 – 150,000 of these bodies (see Section 4.1), to be compared to the 3,000 asteroid spectra available today. This large number statistic will allow compositional studies of the whole asteroid belt down to very small sizes (it is estimated that there are about 100,000 asteroids larger than 5–7 km in the Main Belt; Bottke et al., 2005) and of sub-population of asteroids such as the different dynamical families present in the asteroid belt. Moreover, all spectra will be acquired by the same instrument in a very stable space-based environment.

This paper gives a short overview of the asteroid spectrophotometry with Gaia and is structured as follows: after an introduction devoted to asteroid spectral classification (Section 2) and the interpretation of these classes in terms of composition of these bodies, Section 3 will shortly describe the BP-RP instruments; Section 4 describes their performances in terms of asteroid observations as well as the products of the BP-RP data reduction pipeline for

* Corresponding author. Tel./fax: +33 4 9200 1944.
E-mail addresses: delbo@oca.eu, delbo@obs-nice.fr (M. Delbo').

0032-0633/$ - see front matter © 2012 Elsevier Ltd. All rights reserved.
http://dx.doi.org/10.1016/j.pss.2012.07.029

[1] Although Gaia's telescopes are based on a full reflective optical system, chromatic aberrations cause displacements of the PSF larger than the astrometric specifications and dependent on the color of the source.

asteroid; in Section 5, the classification method adopted and a verification test of the latter are presented; Section 6 is devoted to synergies of Gaia asteroid spectrophotometry with other complementary data.

2. Asteroid spectral classes and mineralogy

A spectral class is assigned to asteroids based on the shape of the object's surface reflectivity as a function of the wavelength. The reflectivity is determined by the ratio of the spectral energy distribution of the asteroid (SED) measured in visible and/or near-infrared light and the spectrum of the Sun. Fig. 1 shows examples of asteroid reflectivities in the visible. In general each spectral class is thought to correspond to an asteroid's surface composition/mineralogy.[2] In particular, asteroid spectral classification was initiated by Chapman et al. (1975) with three main groups: the C-type for dark carbonaceous objects, S-type for stony (silicaceous) objects, and U-type for those that did not fit into either C or S. This classification has since been expanded by several works (see Tholen, 1989; Bus et al., 2002; DeMeo et al., 2009, and references therein). Most recent visible spectroscopic classification schemes are based on spectra acquired by means of CCD spectrographs covering the wavelength range between $\sim$450 and $\sim$1000 nm (Bus and Binzel, 2002; Bus et al., 2002). In the latest years, the growing availability of near-infrared (NIR) spectrographs at 3–4 m class and 8–10 m class telescopes allowed asteroid spectroscopy and their spectral classification to be extended in the NIR (DeMeo et al., 2009). The NIR spectral range is rich of silicate absorption bands diagnostic of the asteroid mineralogical composition.

2.1. Modern CCD based asteroid spectroscopy and its limitations

Early asteroid classifications were based on measurements obtained by photoelectric photometers: this is the case of the Eight Colour Asteroid Survey (ECAS) by Zellner et al. (1985). ECAS was based on asteroid magnitudes measured in eight filters in the 330–1,050 nm range. Visible spectra of asteroids taken today with CCD-based spectrographs allow the observations of much fainter objects, but usually do not include data at wavelength less then 450 nm, and most available data in the blue region (340–550 nm) are in general of poor quality. We note that the paucity of data for wavelength $<$450 nm is not only related to the lower CCD efficiency in this region, but also to the choice of many observers in getting low resolution spectroscopy in the largest wavelength range: often an order sorter filter is inserted at 400–450 nm to avoid second order overlapping in the 800–900 nm where some interesting absorption bands may be seen.

Recent classifications have been thus increasingly based on the red part of the visible spectrum. As a consequence some spectral classes of Bus and Binzel (2002) cannot distinguish among previously identified classes of low-albedo, primitive bodies, which could be separated in the past based on their spectroscopic properties in the ultraviolet (roughly between 330 and 400 nm) and in the blue region (roughly between 400 and 500 nm). For instance, the F-class, in the classification of Tholen (1989) can be distinguished from the Tholen's B-class from a much weaker UV drop-off in the spectra of the former compared to the latter and also because B-class asteroids show a moderately higher average albedo than F-class bodies. However, in the Bus classification these two classes are merged in a unique class (the B-class).

[2] However, there are few classes, such as the X-class in the Bus et al. (2002) taxonomy that can correspond to more than one asteroid mineralogy.

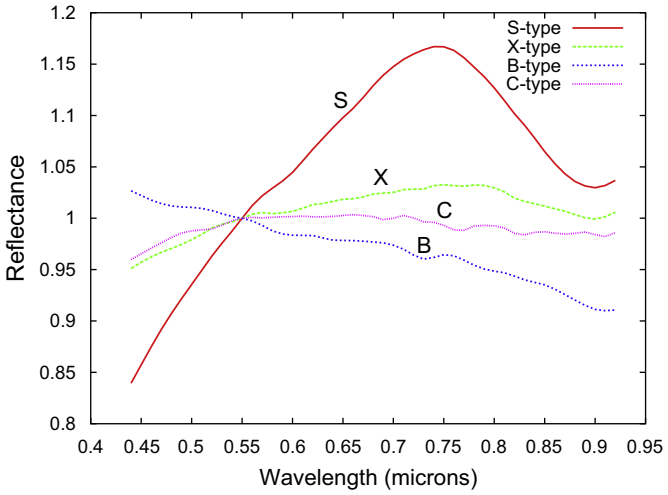

Fig. 1. Example of reflectancies of asteroids in the visible from the Small Main Belt Asteroid Spectroscopic Survey (SMASS, by R. Binzel and collaborators at the MIT, USA; www.smass.mit.edu). The spectral class of each asteroid is indicated with a letter near the corresponding spectrum.

In terms of the number of objects observed, the Moving Object Catalogue (MOC) of the Sloan Digital Sky Survey (SDSS) (Ivezić et al., 2002, 2001; Parker et al., 2008) is the largest survey of visible colors of asteroids. SDSS observations allow the determination of reflectivities in five bands (centered at u′ : 354, g′ : 477, r′ : 623, i′ : 763, z′ : 913 nm). These data are available (in the MOC4 http://www.astro.washington.edu/users/ivezic/sdssmoc/sdssmoc.html) for more than 100,000 asteroids and allowed the investigation of the composition of several asteroid families (Ivezić et al., 2002; Parker et al., 2008). However, a limitation of asteroid data in the SDSS is the in general low quality of the photometry for the faintest bodies (e.g. there are $\sim$87,000 asteroids with SNR $\gtrsim$ 10 and $\sim$57,000 with SNR $\gtrsim$ 20). We recall here that an SNR of at least 20 in the 400–1000 nm range is in general required for a robust spectral classification of an asteroid (F. Demeo, private communication).

By observing a larger number of asteroids with higher sensitivity and more stable conditions (from space), Gaia BP-RP observations will allow a new compositional map of the asteroid population and its different sub-populations (e.g. asteroid families). In the next sections we describe the BP-RP instruments devoted to acquire spectrophometric measurements and the expected results.

3. BP-RP: the low-resolution spectrophotometers of Gaia

Spectrophotometry will be obtained for every asteroid brighter than $G\sim 20$ at the epoch of observation from the Earth's Lagrangian Point L2 (G is the apparent magnitude of a source in the unfiltered broad band of Gaia CCDs: $G\sim V-0.234$ for a solar like spectrum). From an extended set of simulations of observations of asteroids from Gaia, under realistic conditions, it is possible to show that the expected G-magnitude distribution will have a median value of $H-4$ (where H is the absolute magnitude of the asteroid) and a width of the distribution at full half maximum of about 1 magnitude (see Tanga and Mignard, this issue, for more details) This implies that Gaia will be roughly limited to $H\lesssim 16$ for asteroids. Our knowledge of the population of asteroids at $H=16$ is not yet complete. However, Tanga and Mignard (this issue) estimates that the total number of asteroids that will be observed by Gaia should be around 400,000. Spectrophotometry will be obtained for all these bodies. After presenting the

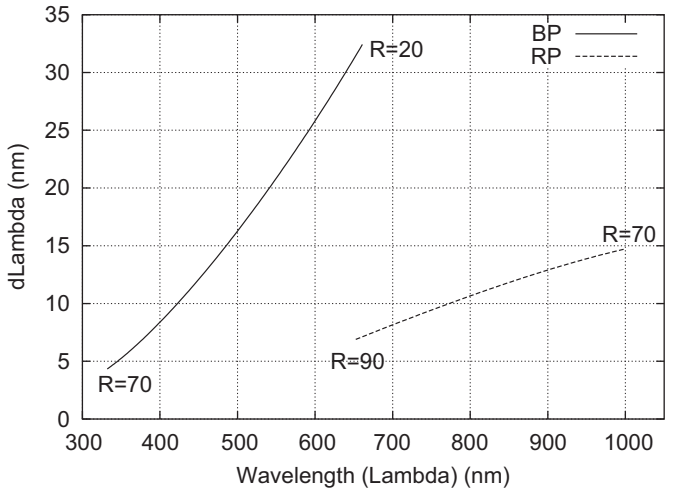

Fig. 2. The spectral resolution of BP and RP: The letter R indicate the equivalent resolving power ($R=\lambda/\Delta\lambda$) at each end of the instrument range.

spectrophotometers, in the next sections we estimate the SNR of the BP-RP observations as a function of the magnitude and the number of asteroids for which we expect to obtain robust spectral classes.

The spectrophotometers are based on two low-resolution prisms (for the instrument layout see Jordi et al., 2010, and in particular their Figure 2). One spectrophotometer (BP) is optimised for the blue wavelengths (330–680 nm) and one (RP) for the red wavelengths (640–1000 nm). Fig. 2 shows the spectral resolution of each spectrophotometer.

The dispersion direction corresponds to the scan of the satellite (along scan direction or "AL"). For both BP and RP, the spectrum is in general contained within 40 AL pixels. Sampling is such to have about 18 spectrophotometric independent bands in the BP-RP domain (Brown, 2006).

4. Gaia BP-RP asteroid observations

BP and RP observations – including asteroids – will be treated by the Photometric pipeline (PhotPipe), which will calculate the calibrated spectrum (the SED) and also the Spectral Shape Coefficients (SSCs). The latter are coefficients of spline functions allowing to reproduce the shape of the BP-RP spectrophometry with a limited number of basis functions with the aim of describing the overall shape of BP-RP spectra. SSCs give more information than just the integrated BP and RP fluxes and can be used to calculate simple pseudo-colours of the observed sources. SSCs will provide four colors for each spectrophotometer, for all sources observed by Gaia (Marrese and Brown, 2009). As proposed in the latter report, the knots of the spline used for the determination of the SSCs are at the wavelengths of 327.9924, 386.9469, 501.7551, 623.7873, 656.4977, 710.0429 nm for BP and 623.7873, 656.4977, 710.0429, 816.6522, 888.0572, 1042.2987 nm for RP. Note that the last three knots for BP and the first three knots for RP coincide, and that the SSCs and the asteroid reflectancies derived from BP-RP spectrophometric data will be both published in the Gaia catalogue.

It is worthy of note to mention that the colors derived from the SSCs, are refined using updated spacecraft/telescopes/detectors calibrations at every data treatment cycle (i.e. every $\sim$6 months) and are potentially very interesting for a color survey of asteroids similar to ECAS and the more recent SDSS (see also Section 4.1 for an estimate of the SNR of asteroid observations in the SSCs bands).

Asteroids are moving objects and, as such, require a special data treatment compared to "fixed" stars. In particular, knowledge of their proper motion at the time of the transit on the Gaia focal plane is necessary to propagate their position from the astrometric field to the BP and RP CCDs.[3] An accurate *a priori* position on the BP and RP CCDs is required for the wavelength calibration of the spectra.

A second effect of asteroids' rapid proper motions is the smearing of their spectra. Because a CCD transit lasts about four seconds, a smearing of the PSF $\lesssim 1$ pixel is expected. This value is not of concern for an accurate extraction of the asteroid reflectivity from BP-RP data.

4.1. Expected performances of the BP-RP

In order to estimate the signal to noise ratio (SNR) of BP-RP asteroid observations as a function of the magnitude, we evaluated the BP-RP response for point like sources assuming a solar like spectrum using an instrument model (see Fig. 3).

Because the BP and the RP provide in general photon noise limited observations, the SNR for asteroid observations of different magnitudes can be easily calculated as $\mathrm{SNR}=\sqrt{N_{phelectrons}}$ (where $N_{phelectrons}$ is the number of photoelectrons within the exposure time) as a function of the wavelength (see Fig. 4). Fig. 5 shows the minimum and the peak SNR in the range between 400 and 1000 nm per observation (i.e. asteroid transit on the Gaia focal plane). Note that the minimum of the SNR always occurs in the blue end of the BP range.

Because an SNR of at least 20 in the 400–1000 nm range (F. Demeo, private communication) is in general required for a robust spectral classification of an asteroid, Fig. 5 shows that asteroids observed by Gaia with a magnitude $G<15$ can be classified from a single transit. For faintest asteroids, it is required to build a higher SNR spectrum by averaging over observations at different epochs.

Due to the Gaia scanning law of the sky, the large majority of asteroids (in the Main Belt) are observed on average 60 times (Mignard et al., 2007; Tanga and Mignard, this issue) over 5 years. The SNR of the accumulated (also called the average) spectrophotometry is thus roughly equals to the SNR of the single-transit BP-RP signal times the square root of the number of transits. Fig. 6 shows the SNR of BP-RP observations at the end of mission assuming an average of 60 observations per asteroids. It can be clearly seen that the SNR is large enough for an accurate spectrophotometric classification over a large range of magnitudes. However, for the faintest magnitudes, in the range of magnitudes $19\lesssim G\lesssim 20$ even the SNR of the accumulated BP-RP signal will be not large enough for an accurate spectral classification if the criterion $\mathrm{SNR}>20$ in the range 400–1000 nm is adopted. If this latter criterion is somehow relaxed (e.g. $\mathrm{SNR}>10$ in the range 400–1000 nm) then spectral classification from BP–RP data will be possible for all asteroids observed by Gaia ($\sim$400,000).

Figure 4 of Tanga and Mignard (this issue) shows that Gaia will observe between 100,000 and 150,000 asteroids with $H\lesssim 15$ (corresponding to $G\lesssim 19$), for which the quality of the data will

[3] Simulations by Mignard et al. (2007) show that 80% of asteroids are observed with proper motions $\lesssim$15 mas/s. Because BP–RP observations take place about 40 s after the source position is detected, the wavelength calibration can be off by several pixels (the along scan pixel size is 60 mas) if the proper motion of ;the asteroid is not taken into account. Asteroid ephemerides will be used to calculate the on-the-sky velocity of the asteroid at the time of the detection in order to propagate its position from the measured position on the astro focal plane to the BP and RP CCDs.

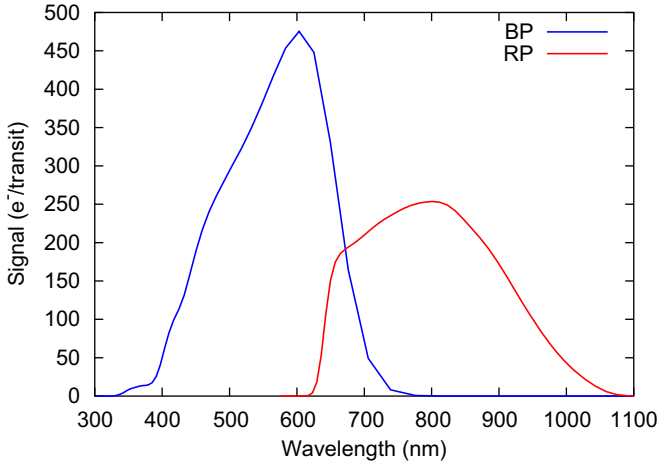

Fig. 3. Response (signal) of the BP (left; blue line) and RB (right; red line) for a magnitude G=17 point like source with a solar like spectrum. (For interpretation of the references to color in this figure caption, the reader is referred to the web version of this article.)

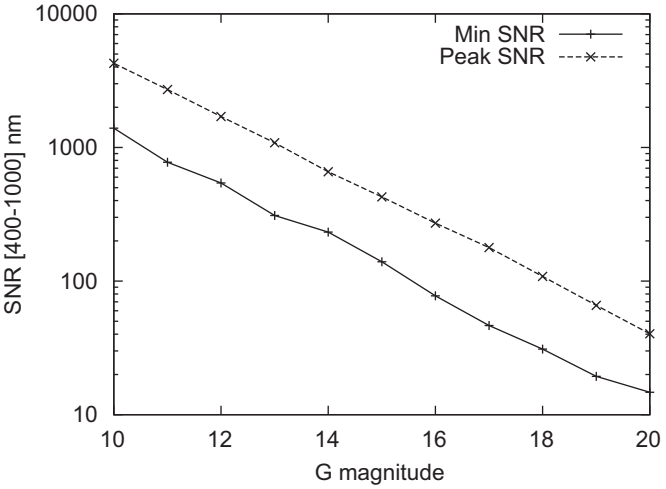

Fig. 6. Minimum and peak BP-RP SNR in the range 400–1000 nm as a function of the G magnitude at the end of the mission assuming 60 transit/asteroid.

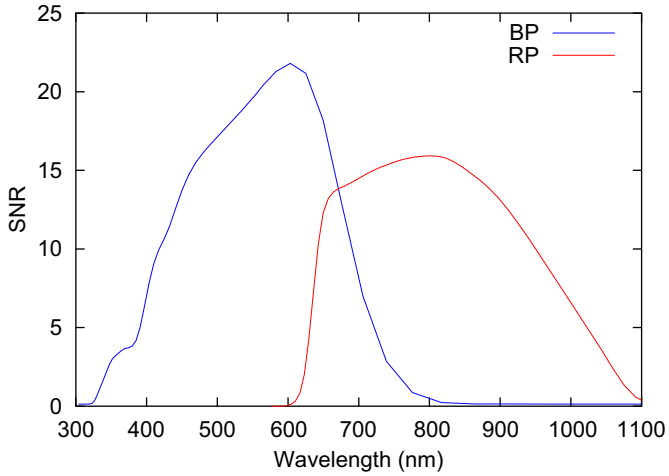

Fig. 4. Signal to noise ratio for a magnitude G=17 asteroid as a function of the wavelength in the BP (left; blue line) and RP (right; red line) domain. Note that the exposure time is fixed by the scanning law of the satellite. (For interpretation of the references to color in this figure legend, the reader is referred to the web version of this article.)

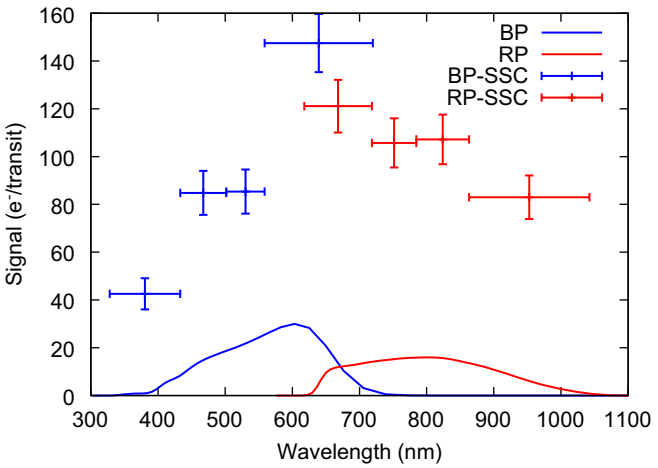

Fig. 7. Example of SSC values calculated for a BP-RP signal of a G=20 asteroid (solar-like spectrum). See text and Marrese and Brown (2009) for more details.

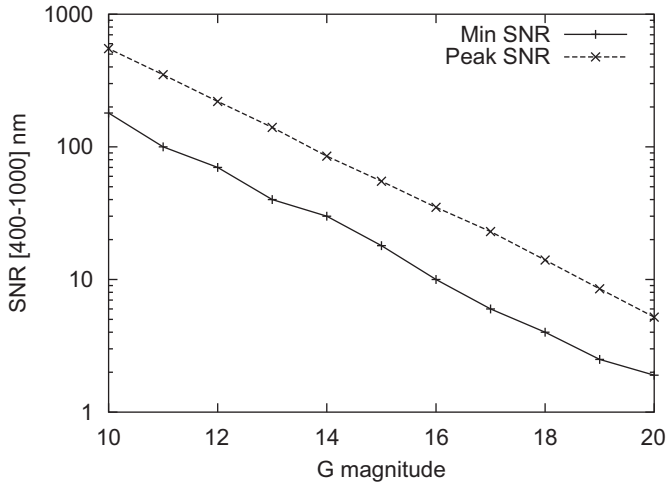

Fig. 5. BP-RP SNR as a function of the G magnitude (one transit) Minimum and Peak SNR in the range 400–1000 nm are shown. Best fit to min SNR: $\mathrm{SNR}=17\,631\times10^{-0.201317*G}$.

be good enough to obtain a robust spectral classification. It is also worth mentioning that the SNR of the BP-RP data after one single transit will be good enough for those asteroids with $G\lesssim15$, i.e. $H\lesssim11$ and Figure 4 of Tanga and Mignard (this issue) shows that about 2000 asteroids meet this condition. This imply that for $H\lesssim11$ asteroids Gaia will produce data at about 60–80 different epochs with each signal with SNR $\geq$ 20 or better. This implies that spectrophotometry of good enough signal-to-noise ratio will be obtained for these asteroids at different rotational phases and/or aspect angles. Such data will be very valuable to study possible spectra heterogeneity of the surface of these bodies.

For very faint asteroids ($19\lesssim G\lesssim20$), the use of SSCs to calculate the eight-color reflectivity might be more robust than the accumulated spectrum. In order to estimate the SNR of the eight colors spectrophotometry as a function of the magnitude, we integrated the response of RP and BP of Fig. 3 in the SSC bands. We used rectangular bands. Fig. 7 shows the flux in each of the SSC colors for a source of magnitude G=20. It is clear that even for the faintest sources, the eight-color fluxes, accumulated over 60 observations epochs will yield to an SNR of 40 or better over the whole spectral range.

4.2. Products of the data treatment pipeline

BP and RP data will mainly results in the publication of two products in the Gaia catalogue of asteroid observations: namely surface reflectivities (in the range 330–1000 nm), averaged over the whole set of observations, and the asteroid spectral classes. In order to produce the above mentioned products, the following procedure has put forward: first the spectral energy distribution of the source (SED in physical units: e.g. $W/m^2/\mu m$ as a function of the wavelength) is obtained from accumulated BP-RP data; epoch SEDs might be also produced for those asteroids bright enough to have SNR > 20 in the range 400–1000 nm after one transit on the focal plane. Fig. 5 shows that this corresponds to asteroids brighter than magnitude $G=15$ or $H=11$. Asteroid reflectivities are then calculated from the SEDs: BP and RP SEDs (calculated separately by the PhotPipe) are combined into one SED and the latter is divided by the solar spectrum and the results normalised to 1 at 550 nm. Asteroid reflectivities will be used to determine the asteroid spectral class by means of an unsupervised clustering algorithm. The use of this latter method will produce a new asteroid "Gaia" taxonomic classification.

The clustering method is based on a Minimal Spanning Tree (MST) algorithm and was developed by Galluccio et al. (2008). The algorithm is based on a method for partitioning a set V of N data points ($V \in \mathbb{R}^L$), where L in our case is the number of spectral bands, into K non-overlapping clusters such that (a) the inter-cluster variance is maximized and (b) the intra-cluster variance is minimized. Each spectrum is considered as a vertex of tree. A tree is a graph that is connected (i.e. every vertex is connected to at least another vertex) and acyclic (i.e. the graph has no loops).

The spanning tree (i.e. the tree passing through each vertex of the set) with the minimal length, namely the MST, is calculated using the Prim's algorithm (see Galluccio et al., 2008, and references therein). The length of each edge of the tree (i.e. the distance between two spectra) is determined using the Kullback–Leibler metric: let $v_i = \{v_{i1}, \ldots, v_{iL}\}$ be the feature vector corresponding to a reflectance spectrum (L being the number of wavelengths or spectral bands); at a given wavelength λ_i, each spectrum is associated with a (positive) normalized quantity: $\tilde{v}_{ij} = v_{ij} / \sum_{j=1}^{L} v_{ij}$, which can be interpreted as the probability distribution that a certain amount of information has been measured around the wavelength λ_i. To measure the similarity between two probability density functions, we compute the symmetrized Kullback–Leibler divergence:

$$d_{kl}(v_i || v_k) = \sum_{j=1}^{L} (\tilde{v}_{ij} - \tilde{v}_{kj}) \log \frac{\tilde{v}_{ij}}{\tilde{v}_{kj}}.$$

The identification of the clusters is performed by first computing, at each step of the MST construction, the length of the newly connected edge and then by identifying valleys in the curve obtained by plotting the MST edge length as a function of the iteration of the construction (see Fig. 8; an example of how to use Fig. 8 for the identification of spectral groups will be given in Section 5). The valleys in this curve identify the number and the position of high density region of points, i.e. the clusters (see Galluccio et al., 2008, for a more thorough description of the algorithm). The clusters represent, in our case, the different asteroid spectral classes. In the next section we present a test of this classification algorithm using SDSS data.

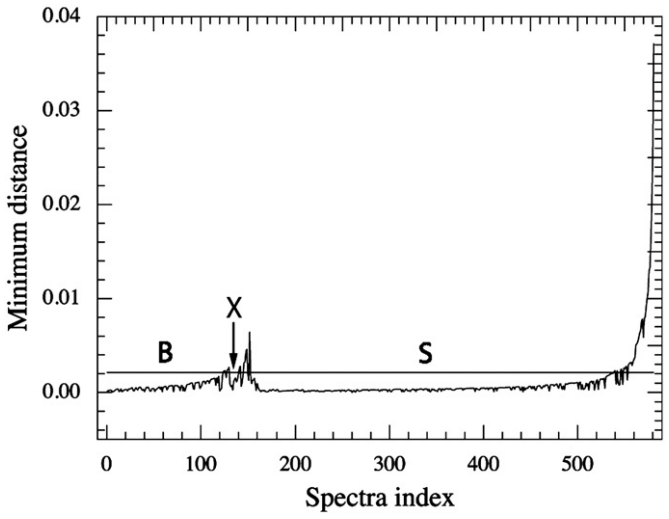

Fig. 8. Edge-length of the MST as a function of the number of the spectrum (spectrophotometry) added to the tree. A class is defined anytime the graph makes a valley below the horizontal threshold line. Each valley corresponds to a group of points (spectrophotometric data) that have a small distance between them. Th B- and S- groups can be clearly identified in the plot. The X-types constitute a small group of asteroid and are separated by a small distance – though statistically significant – from the B-types.

5. Test of the classification algorithm

In order to test our spectral classification algorithm we performed the identification of the asteroid spectral classes in the Nysa–Polana dynamical family. This is a group of asteroids located in the inner main belt, at low orbital inclination ($i \lesssim 5^\circ$) between the ν_6 secular resonance (at heliocentric distance ≈ 2.1 AU) and the 3:1 mean motion resonance with Jupiter (at heliocentric distance of 2.5 AU). A spectroscopy study by Cellino et al. (2001) of this group of asteroids suggested that there are at least two populations of bodies of different physical characteristics overlapping in orbital element space. SDSS colors of the members of the Nysa–Polana family also show the presence of two compositional groups (Campins et al., 2010, Fig. 1).

This suggests that the Nysa–Polana group was formed by two major collisional break-up events, one related to asteroid (142) Polana and the other one possibly related to asteroid (878) Mildred, as originally proposed by Cellino et al. (2001). The same work also found a few X-type objects in the Nysa–Polana group, which suggests the possibility of a third, minor, collisional break-up event in the region or the presence of interloper asteroids in the Nysa–Polana family assuming the members identification of Nesvorny (2010). We note that the Nysa–Polana family includes also other large asteroids that are classified as X-types (in the Bus taxonomy) such as (44) Nysa and (135) Herta. However, Cellino et al. (2001) followed the Tholen's taxonomy, so that (44) Nysa and (135) Herta are an E- and M-type, respectively.

In order to increase the sample statistics compared to the relatively small number of asteroids observed by Cellino et al. (2001) and identify meaningful spectral groups within the Nysa–Polana family, we used our spectral classification algorithm on the observations contained in the SDSS MOC4 (Ivezić et al., 2002, 2001).

To obtain the surface reflectivity of the asteroids, we subtracted the solar contribution ($u_\odot$, $g_\odot$, $r_\odot$, $i_\odot$, $z_\odot$) to the observed asteroids magnitudes. The solar contribution is calculated from transformation equations between the SDSS u′g′r′i′z′ magnitudes and the usual $UBVR_cI_c$ system: i.e.: $u_\odot = 6.55$, $g_\odot = 5.12$, $r_\odot = 4.68$, $i_\odot = 4.57$, $z_\odot = 4.54$. (for more details, see the SDSS website http://www.sdss.org). In order to calculate the symmetrized Kullback–Leibler divergence between asteroid spectral reflectancies and be able to use our classification algorithm, we chose to normalize each spectrum relatively to the r' band ($\lambda_{r'} = 623$ nm). Finally, we obtained the following asteroid reflectivity for the λ_i wavelength:

$$v_i = 10^{-0.4(C_i - C_{r'})}$$

with $C_i = i - i_\odot$ and $C_{r'} = r' - r_\odot$

the reflectivity colors at λ_i and $\lambda_{r'}$ respectively; where the index i runs over the g', i', and z' wavelengths.

We searched in the MOC4 database for all asteroids belonging to the Nysa–Polana family. Concerning the family members identification, we used the definition of dynamical families of Nesvorny (2010). Among this family, 4134 objects have been observed at least once by the SDSS (as a comparison, the number of spectra obtained in the visible light or near-infra red, for the Nysa–Polana family, in the SMASS, ECAS and 52-Color catalogs are : 15, 13, and 2, respectively).

However, likely due to non-photometric conditions and the faintness of the asteroids, some of our objects have high uncertainties in the magnitudes published in the MOC4. Thus, we selected only the less noisy observations: namely, we required that all data have a relative uncertainty $\lesssim 10\%$ in the in-band photometric flux, in order for an observations to be included in our analysis. If an asteroid has multiple valid observations, we computed the average reflectivity and its standard deviation in the five bands. In the end, the taxonomic classification of the Nysa–Polana group was performed over 579 objects.

Fig. 8 shows the edge length as a function of the number of added spectra when processing the MST construction on SDSS-MOC4 photometric data of the asteroid of the Nysa–Polana family. The figure clearly shows three main valleys corresponding to three groups composed of 378, 118, and 13 asteroids, respectively. The remaining objects (70 of which makes about 12% of the total sample) do not belong to any group because both the "distance" between these objects and the three groups and also the "distance" between each pair of spectra is larger than the threshold. We conclude that we cannot find similarities between these spectra and the main three groups. These asteroids are likely interlopers in the Nysa–Polana family. From the hierarchical clustering method (HCM) of family members identification, it is in general expected that about 10% of the family members are interlopers (D. Nesvorny, private communication). As a consequence, in the following, we do not take into account these 70 unclassified asteroids.

Also, in order to estimate the probability of misclassification of our method, we used a Monte-Carlo analysis. We generated a random set of B-, X- and S-type reflectivities on the bands of the SDSS, normally distributed around the mean value of the respective groups previously found in the Nysa–Polana family (see Fig. 9). We applied our classification method on the simulated spectrophotometric data and found that between 2 and 5% of the objects are misclassified depending on the choice of the value of the threshold line (see Fig. 8 and the corresponding text).

Fig. 9 shows asteroid spectra of each group and their associated mean spectrum. Error bars are the 1-sigma standard deviation. We also compared our results with the mean spectrum of different spectral classes from the Bus-DeMeo classification (http://smass.mit.edu/busdemeoclass.html). In each panel, we only plot the Bus-DeMeo mean spectra which present the closer similarity with the mean spectra of each group:

1. For the first group (top panel of Fig. 9, 378 objects), we find that all spectra resemble the *S*-type mean spectra of Bus-DeMeo.
2. In the middle panel of Fig. 9, the 118 spectra of the second group fits with *B*-type asteroids (such as 142 Polana, for instance).
3. The bottom panel shows the third more populous group containing 13 asteroids. Comparing the spectra of this group and the mean spectrum of *X*-types, X_c-types, X_k-types, and X_e-types, we find that the third group of 13 objects corresponds to asteroids of the *X*-complex and its subtypes.

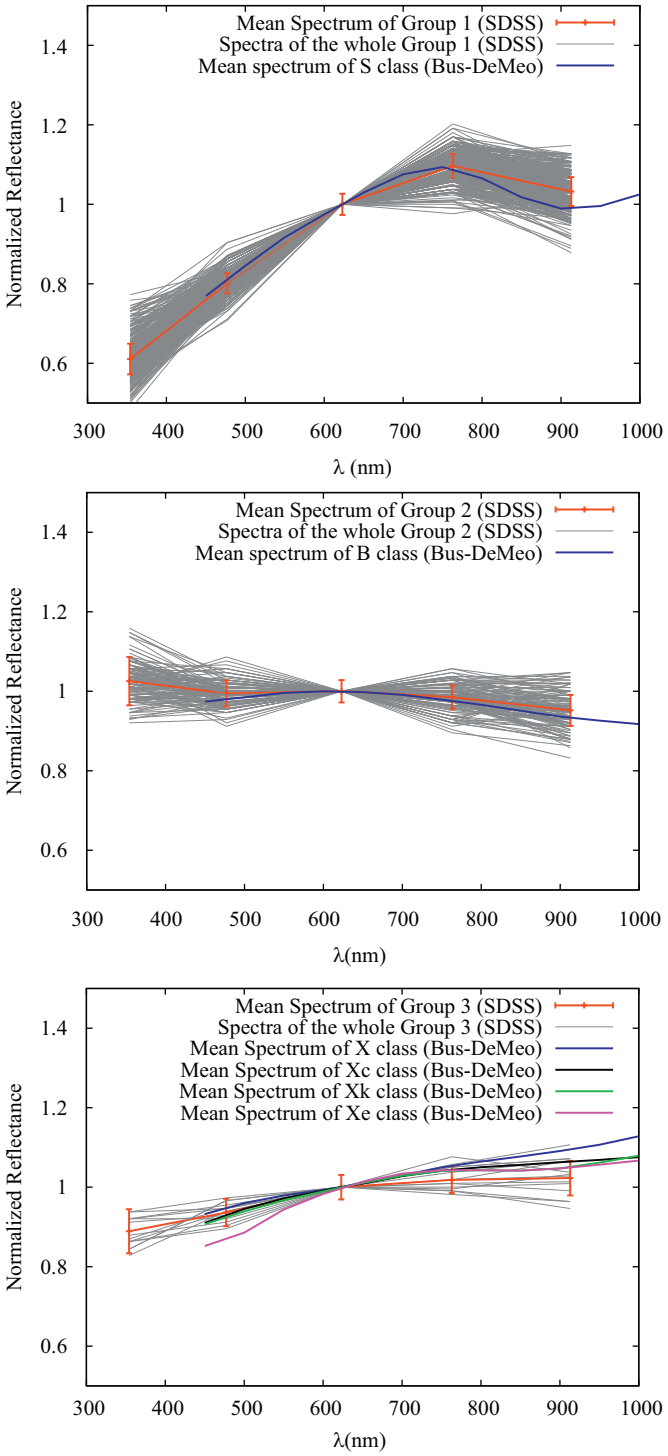

Fig. 9. Panels (a), (b), and (c) represent the spectra for each group with their mean spectrum. A comparison with several spectra types from the Bus and Binzel (2002) taxonomy is also performed. We compare the *S*-type spectrum with Group 1, the *B*-type spectrum with Group 2 and *X*-type (and sub-types) spectrum with Group 3.

We note that groups (1) and (2) are also consistent with the two main spectral classes found by Cellino et al. (2001). Moreover, the same authors had already identified the presence of asteroids with *X*-type spectral reflectancies. They also noted that two of the largest asteroids, (44) Nysa and (135) Herta have spectra consistent with an *X*-type classification. This shows that (1) our classification algorithm is capable of retrieving the three

classes already identified by Cellino et al. (2001); (2) our classification algorithm is able to retrieve robust spectral classes from five-points asteroid spectral reflectivities; (3) our classification algorithm can operate effectively on a large number of asteroid spectra.

6. Combination of BP-RP spectroscopy with auxiliary data

The application of the classification method presented here to BP-RP spectrophotometric asteroid data will produce a new asteroid taxomomy. The latter will be published in the Gaia observational catalogs. Plans are also in place to assign spectral classes from an existing taxonomy (e.g. the Bus taxonomy) to asteroids observed by Gaia by comparing accumulated (end of mission) BP-RP spectrophotomertic reflectivities to the average classes of an asteroid taxonomy.

Gaia spectrophotometric observations will help us to refine the mineralogical map of the Main Belt to an unprecedented detail. However, it is well known that classes of asteroids built from visible spectroscopy are affected by degeneracies in their compositional interpretation. For instance, the X-class (in the Bus taxonomy) does not define a compositional class nor has a unique meteorite analog. It is known that asteroids of the X-class can have very different albedos from low (defining the P-class), to moderate (defining the M-class), to high (defining the E-class). Another example is given by B-type asteroids: while in the visible the asteroids belonging to the B-type have very similar spectra, the extension of their spectra in the near infrared shows different behaviours that can be interpreted with different processes that have affected the surfaces of these bodies (Clark et al., 2010; de León et al., 2012).

In order to remove degeneracies in the Gaia classification of asteroids, one can add auxiliary data to the BP-RP spectrophometry. These data can come from telescopic surveys in the near infrared, or more likely from the catalogue of asteroid observations of the NASA WISE mission (Wright et al., 2010; Mainzer et al., 2011a; Masiero et al., 2011, and references there in). WISE has surveyed the whole sky in four bands, centered at 3.4, 4.6, 12, and 22 microns, in the thermal infrared. From WISE thermal infrared observations, it is possible to derive asteroid sizes and geometric visible albedos (p_V) by means of the so-called asteroids thermal models (see Harris and Lagerros, 2002; Delbó and Harris, 2002, and references therein). The first release of diameters and values of p_V for asteroids from the cryogenic phase of the mission contains results for 129,750 main belt asteroids (Masiero et al., 2011). The value of p_V provides strong constrain to the asteroid mineralogy when used together with the spectral information. Other space missions have been obtained data of a large number of asteroids in the medium infrared from which physical properties such as diameters, albedo and thermal properties such as the surface thermal inertia (see e.g. Delbo' and Tanga, 2009) can be obtained. We remind here: the Supplemental IRAS Minor Planet Survey (Tedesco et al., 2002, SIMPS), the Akari (Usui et al., 2011) and the Asteroid Spitzer Survey (Enga et al., 2009). The SIMPS contains 2228 different multiply observed asteroids (measured infrared fluxes as well as resulting asteroid diameters and albedos are available in the catalogue); the Akari catalog include 4953 main belt asteroids, 58 near-Earth asteroids, and 109 Jovian Trojan asteroids. The catalog is publicly available via the Internet; the Spitzer Asteroid Catalog contains flux measurements of asteroids serendipitously observed in publicly available Spitzer data. To the best of our knowledge the Spitzer Asteroid Survey was never released for public use.

In order to show the importance of the albedo information to constrain the mineralogy of the asteroids members of the Nysa–Polana family, we plot in Fig. 10 the distributions of the geometric visible albedos of asteroids in the B-, S-, and X-groups as identified in Section 5. We obtained the WISE albedos from Masiero et al. (2011). The albedo distribution of S-type asteroids in our sample is consistent with S-type asteroids in general in the asteroid main belt (Mainzer et al., 2011b). The albedo distribution of B-types in our sample is strongly concentrated below a value of 0.1. This is an indication that the B-type asteroids of the Nysa–Polana family have dark surfaces and are primitive, likely carbonaceous rich asteroids. On the other hand, albeit limited by a small number statistics, asteroids with X-type spectra have in the 64% of the cases albedos below 0.1. This is indicative that some of the asteroids of the Nysa–Polana family with X-type spectra have also primitive compositions (maybe P-types). An interesting question is whether these bodies are genetically related to the B-type asteroids also present in the family.

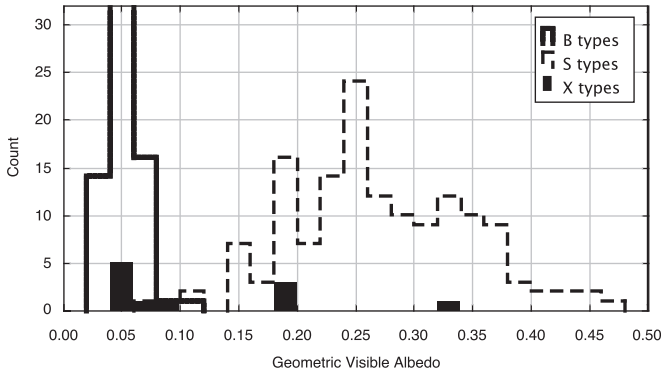

Fig. 10. The distribution of the geometric visible albedos (from Masiero et al., 2011) of the asteroids of B-, S-, and X-type identified using our classification method in the Nysa–Polana family. Continuous line: B-types; dashed line: S-types; filled bars: X-types.

While WISE has mainly observed main belt asteroids, the determination of the diameters and albedos for also 428 near-Earth asteroids have been obtained from thermal modeling of WISE data (Mainzer et al., 2011c). Moreover, it is worth reminding that at the time of writing there are other observational programs specifically devoted to the size and albedo determination of near-Earth asteroids: the ExploreNEOs (PI D. Trilling) is one of the most important. It makes use of the Warm Spitzer NASA telescope. Sizes and albedos of more than 100 NEOs from the ExploreNEOs program have already been published (Trilling et al., 2010), whereas results for 450 NEOs have been obtained as of March 2011. It is expected that the final database of ExploreNEOs will include sizes and albedos for about 700 NEOs (Trilling et al., 2010).

7. Conclusions

Gaia will be launched in 2013 and will obtain astrometric and photometric observations of abut 400,000 asteroids in the visible light. Gaia will also obtain low resolution ($R \sim 20-90$) visible spectra (or spectrophometry) of asteroids using two instruments: one spectrophotometer (BP) is optimized in the blue, the other (RP) in the red.

The catalogue of Gaia observations of asteroids will contain reflectancies (averaged over all observations during the mission) and spectral classes of asteroids, and likely epoch spectrophotometry for the brighter asteroids. Because the data reduction pipeline will also calculate magnitudes in six bands on each photometer (with three bands overlapping on BP-RP spectra), a proposal is also in place to publish the eight-point spectral reflectivities derived from this data for each asteroid.

Gaia asteroid spectrophotometry will be obtained throughout the duration of the mission under very stable conditions in space. In this work we have calculated the expected SNR for spectrophometry observations for asteroids. We recall here that a spectrum with an SNR > 20 is required in the range (400–1000 nm) for a robust spectral classification. We found that a SNR > 20 in the range (400–1000 nm) can be obtained for $G \lesssim 15$ asteroids from one single transit of the body on the Gaia's focal plane. It is expected that this corresponds to $H \lesssim 11$ asteroids, whose population includes about 2000 objects.

An SNR > 20 in the range (400–1000 nm) can be obtained for about 100,000 – 150,000 asteroids with $H \lesssim 15$ if the data are averaged over five years of observations (i.e. roughly 60 transits on the focal plane per asteroid).

For all observed asteroids ($\sim$400,000) the eight-color magnitudes calculated by means of the Spectral Shape Coefficients (SSCs) averaged over the mission duration will allow us to calculate eight-point reflectancies of quality good enough for a robust spectral classification.

Here we also have presented and tested on a real case (the Nysa–Polana asteroid family) the asteroid spectral classification algorithm adopted by the data reduction pipeline.

Moreover, the combination of Gaia spectrophotometric observations with auxiliary data (e.g. albedos from the WISE space mission or the Spitzer Space Telescope), will make possible to remove some spectral class degeneracies and build a mineralogical map of the asteroids of the main belt down to sizes of few kilometers in diameter (the diameter of an asteroid with $H=15$ and $p_V=0.1$ is 4.2 km).

Acknowledgments

We thank O. Michel, A. Cellino, H. Campins and P. Sartoretti for useful discussion. Programming tools made available to us by the Gaia Data Processing Analysis Consortium (DPAC) have been used to complete this work. J. Gayon-Markt is also grateful to the Centre National d'Etudes Spatiales (CNES) for financial support. We thank the reviewers Mirel Birlan and Sonia Fornasier for their thorough feedback, which helped improving the manuscript.

This work is partially based on data from the SDSS: Funding for the creation and distribution of the SDSS Archive has been provided by the Alfred P. Sloan Foundation, the Participating Institutions, the National Aeronautics and Space Administration, the National Science Foundation, the U.S. Department of Energy, the Japanese Monbukagakusho, and the Max Planck Society. The SDSS Web site is http://www.sdss.org.

The SDSS is managed by the Astrophysical Research Consortium (ARC) for the Participating Institutions. The Participating Institutions are The University of Chicago, Fermilab, the Institute for Advanced Study, the Japan Participation Group, The Johns Hopkins University, the Korean Scientist Group, Los Alamos National Laboratory, the Max-Planck-Institute for Astronomy (MPIA), the Max-Planck-Institute for Astrophysics (MPA), New Mexico State University, University of Pittsburgh, University of Portsmouth, Princeton University, the United States Naval Observatory, and the University of Washington.

References

Bottke, W.F., Durda, D.D., Nesvorný, D., Jedicke, R., Morbidelli, A., Vokrouhlický, D., Levison, H., 2005. The fossilized size distribution of the main asteroid belt. Icarus 175, 111–140.

Brown, A., 2006. Simulating Prism Spectra for the EADS-Astrium Gaia Design. DPAC-Livelink Technical Note GAIA-CA-TN-LEI-AB-005-7, 1–40.

Bus, S.J., Binzel, R.P., 2002. Phase ii of the small main-belt asteroid spectroscopic survey a feature-based taxonomy. Icarus 158, 146.

Bus, S.J., Vilas, F., Barucci, M.A., 2002. Visible-Wavelength Spectroscopy of Asteroids. Asteroids III, 169.

Campins, H., Morbidelli, A., Tsiganis, K., León, J., Licandro, J., Lauretta, D., 2010. The origin of asteroid 101955 (1999 rq36). The Astrophysical Journal Letters 721, L53.

Cellino, A., Zappalà, V., Doressoundiram, A., di Martino, M., Bendjoya, P., Dotto, E., Migliorini, F., 2001. The puzzling case of the Nysa–Polana family. Icarus 152, 225.

Chapman, C., Morrison, D., Zellner, B., 1975. Surface properties of asteroids—a synthesis of polarimetry, radiometry, and spectrophotometry. Icarus 25, 104–130.

Clark, B.E., Ziffer, J., Nesvorny, D., Campins, H., Rivkin, A.S., Hiroi, T., Barucci, M.A., Fulchignoni, M., Binzel, R.P., Fornasier, S., DeMeo, F., Ockert-Bell, M.E., Licandro, J., Mothé-Diniz, T., 2010. Spectroscopy of B-type asteroids: subgroups and meteorite analogs. Journal of Geophysical Research (Planets) 115, 6005.

de León, J., Pinilla-Alonso, N., Campins, H., Licandro, J., Marzo, G.A., 2012. Near-infrared spectroscopic survey of B-type asteroids: compositional analysis. Icarus 218, 196–206.

Delbó, M., Harris, A.W., 2002. Physical properties of near-earth asteroids from thermal infrared observations and thermal modeling. Meteoritics & Planetary Science 37, 1929.

Delbo', M., Tanga, P., 2009. Thermal inertia of main belt asteroids smaller than 100 km from IRAS data. Planetary and Space Science 57, 259–265.

DeMeo, F., Binzel, R., Slivan, S., Bus, S., 2009. An extension of the bus asteroid taxonomy into the near-infrared. Icarus.

Enga, M.-T., Trilling, D., Mueller, M., Wasserman, L., Sykes, M., Blaylock, M., Stansberry, J., Bhattacharya, B., Spahr, T., 2009. Albedo and Diameter Distributions of Asteroid Families Using the Spitzer Asteroid Catalog AAS/Division for Planetary Sciences Meeting Abstracts #41, 41, #34.02.

Galluccio, L., Michel, O., Bendjoya, P., 2008. Unsupervised clustering on astrophysics data: asteroids reflectance spectra surveys and hyperspectral images. American Institute of Physics Conference Series 1082, 165.

Harris, A.W., Lagerros, J.S.V., 2002. Asteroids in the Thermal Infrared. Asteroids III, 205.

Ivezić, Ž., Lupton, R., Jurić, M., Tabachnik, S., Quinn, T., Gunn, J., Knapp, G., Rockosi, C., Brinkmann, J., 2002. Color confirmation of asteroid families. The Astronomical Journal 124, 2943.

Ivezić, Ž., Tabachnik, S., Rafikov, R., Lupton, R.H., Quinn, T., Hammergren, M., Eyer, L., Chu, J., Armstrong, J.C., Fan, X., Finlator, K., Geballe, T.R., Gunn, J.E., Hennessy, G.S., Knapp, G.R., Leggett, S.K., Munn, J.A., Pier, J.R., Rockosi, C.M., Schneider, D.P., Strauss, M.A., Yanny, B., Brinkmann, J., Csabai, I., Hindsley, R.B., Kent, S., Lamb, D.Q., Margon, B., McKay, T.A., Smith, J.A., Waddel, P., York, D.G., 2001. the SDSS Collaboration, 2001. Solar system objects observed in the sloan digital sky survey commissioning data. The Astronomical Journal 122, 2749.

Jordi, C., Gebran, M., Carrasco, J.M., Bruijne, J.D., Voss, H., Fabricius, C., Knude, J., Vallenari, A., Kohley, R., Mora, A., 2010. Gaia broad band photometry. A&A 523, 48.

Mainzer, A., Grav, T., Masiero, J., Bauer, J., Wright, E., Cutri, R.M., Walker, R., McMillan, R.S., 2011a. thermal model calibration for minor planets observed with WISE/NEOWISE: comparison with infrared astronomical satellite. The Astrophysical Journal 737, L9.

Mainzer, A., Grav, T., Masiero, J., Hand, E., Bauer, J., Tholen, D., McMillan, R.S., Spahr, T., Cutri, R.M., Wright, E., Watkins, J., Mo, W., Maleszewski, C., 2011b. NEOWISE studies of spectrophotometrically classified asteroids: preliminary results. The Astrophysical Journal 741, 90.

Mainzer, A., Grav, T., Bauer, J., Masiero, J., McMillan, R.S., Cutri, R.M., Walker, R., Wright, E., Eisenhardt, P., Tholen, D.J., Spahr, T., Jedicke, R., Denneau, L., DeBaun, E., Elsbury, D., Gautier, T., Gomillion, S., Hand, E., Mo, W., Watkins, J., Wilkins, A., Bryngelson, G.L., DelPinoMolina, A., Desai, S., GómezCamus, M., Hidalgo, S.L., Konstantopoulos, I., Larsen, J.A., Maleszewski, C., Malkan, M.A., Mauduit, J.-C., Mullan, B.L., Olszewski, E.W., Pforr, J., Saro, A., Scotti, J.V., Wasserman, L.H., 2011c. NEOWISE observations of near-Earth objects: preliminary results. The Astrophysical Journal 743, 156.

Marrese, P., Brown, A., 2009. Describing the bp/rp Measurements With Spectrum Shape Coefficients. DPAC-Livelink Technical Note GAIA-CA-TN-LEI-AB-005-7, 1–36.

Masiero, J.R., Mainzer, A.K., Grav, T., Bauer, J.M., Cutri, R.M., Dailey, J., Eisenhardt, P.R.M., McMillan, R.S., Spahr, T.B., Skrutskie, M.F., Tholen, D., Walker, R.G., Wright, E.L., DeBaun, E., Elsbury, D., Gautier Jr., T., Gomillion, S., Wilkins, A., 2011. Main belt asteroids with WISE/NEOWISE. I. Preliminary albedos and diameters. The Astrophysical Journal 741, 68.

Mignard, F., Cellino, A., Muinonen, K., Tanga, P., Delbo, M., Dell'oro, A., Granvik, M., Hestroffer, D., Mouret, S., Thuillot, W., 2007. The gaia mission: expected applications to asteroid science. Earth Moon Planet 101, 97–125.

Nesvorny, D., 2010. Nesvorny HCM Asteroid Families v1.0. NASA Planetary Data System EAR-A-VARGBDET-5-NESVORNYFAM-V1.0.

Parker, A., Ivezić, Ž., Jurić, M., Lupton, R., Sekora, M.D., Kowalski, A., 2008. The size distributions of asteroid families in the SDSS moving object catalog 4. Icarus 198, 138.

Perryman, M.A.C., de Boer, K.S., Gilmore, G., Høg, E., Lattanzi, M.G., Lindegren, L., Luri, X., Mignard, F., Pace, O., de Zeeuw, P.T., 2001. GAIA composition formation and evolution of the galaxy. Astronomy and Astrophysics 369, 339–363.

Tanga, P., Mignard, F. The solar system as seen by Gaia. Planetary and Space Science, this issue.

Tedesco, E.F., Noah, P.V., Noah, M., Price, S.D., 2002. The supplemental IRAS minor planet survey. The Astronomical Journal 123, 1056–1085.

Tholen, 1989. Asteroids taxonomic classification. In: Binzel, R.P., Gehrels, T., Matthews, M.S. (Eds.), Asteroids II. University of Arizona Press, Tucson, pp. 1139–1153.
Trilling, D., Mueller, M., Hora, J., Harris, A., Bhattacharya, B., Bottke, W., Chesley, S., Delbo, M., Emery, J., Fazio, G., 2010. Exploreneos. I. Description and first results from the warm spitzer near-earth object survey. The Astronomical Journal 140, 770.
Usui, F., Kuroda, D., Müller, T.G., Hasagawa, S., Ishiguro, M., Ootsubo, T., Ishihara, D., Kataza, H., Takita, S., Oyabu, S., Ueno, M., Matsuhara, H., Onaka, T., 2011. Asteroid Catalog Using Akari: AKARI/IRC Mid-Infrared Asteroid Survey Publications of the Astronomical Society of Japan, 63, 1117–1138.
Wright, E., Eisenhardt, P., Mainzer, A., Ressler, M., Cutri, R., Jarrett, T., Kirkpatrick, J., Padgett, D., McMillan, R., Skrutskie, M., 2010. The wide-field infrared survey explorer (wise): mission description and initial on-orbit performance. The Astronomical Journal 140, 1868.
Zellner, B., Tholen, D., Tedesco, E., 1985. The eight-color asteroid survey: results for 589 minor planets. Icarus 61, 355–416.

Bibliography

[1] V. Alí-Lagoa, J. de León, J. Licandro, M. Delbo, H. Campins, N. Pinilla-Alonso, and M. S. Kelley. Physical properties of B-type asteroids from WISE data. *Astronomy & Astrophysics*, 554:71, June 2013.

[2] V. Alí-Lagoa, L. Lionni, M. Delbo, B. Gundlach, J. Blum, and J. Licandro. Thermophysical properties of near-Earth asteroid (341843) 2008 EV5 from WISE data. *Astronomy & Astrophysics*, 561:A45, Jan. 2014.

[3] K. Altwegg, H. Balsiger, A. Bar-Nun, J. J. Berthelier, A. Bieler, P. Bochsler, C. Briois, U. Calmonte, M. Combi, J. De Keyser, P. Eberhardt, B. Fiethe, S. Fuselier, S. Gasc, T. I. Gombosi, K. C. Hansen, M. Hässig, A. Jäckel, E. Kopp, A. Korth, L. LeRoy, U. Mall, B. Marty, O. Mousis, E. Neefs, T. Owen, H. Rème, M. Rubin, T. Sémon, C. Y. Tzou, H. Waite, and P. Wurz. 67P/Churyumov-Gerasimenko, a Jupiter family comet with a high D/H ratio. *Science*, 347(6):1261952–1261952, Jan. 2015.

[4] Y. Amelin, A. N. Krot, I. D. Hutcheon, and A. A. Ulyanov. Lead Isotopic Ages of Chondrules and Calcium-Aluminum-Rich Inclusions. *Science*, 297(5):1678–1683, Sept. 2002.

[5] E. Ammannito, M. C. De Sanctis, E. Palomba, A. Longobardo, D. W. Mittlefehldt, H. Y. McSween, S. Marchi, M. T. Capria, F. Capaccioni, A. Frigeri, C. M. Pieters, O. Ruesch, F. Tosi, F. Zambon, F. Carraro, S. Fonte, H. Hiesinger, G. Magni, L. A. McFadden, C. A. Raymond, C. T. Russell, and J. M. Sunshine. Olivine in an unexpected location on Vesta's surface. *Nature*, 504(7):122–125, Dec. 2013.

[6] C. Avdellidou, M. C. Price, and M. J. Cole. Survival of the impactor during hypervelocity collisions. An analogue for icy bodies. *EPSC Meeting 2015*, pages 1–2, May 2015.

[7] C. Avdellidou, M. C. Price, M. Delbo, P. Ioannidis, and M. J. Cole. Survival of the impactor during hypervelocity collisions. An analogue for icy bodies. *Monthly Notice of the Royal Astronomical Society*, pages 1–5, May 2015.

[8] J. L. Bandfield, R. R. Ghent, A. R. Vasavada, D. A. Paige, S. J. Lawrence, and M. S. Robinson. Lunar surface rock abundance and regolith fines temperatures derived from LRO Diviner Radiometer data. *Journal of Geophysical Research*, 116, Dec. 2011.

[9] M. A. Barucci, S. Fornasier, E. Dotto, P. L. Lamy, L. Jorda, O. Groussin, J. R. Brucato, J. Carvano, A. Alvarez-Candal, D. Cruikshank, and M. Fulchignoni. Asteroids 2867 Steins and 21 Lutetia: surface composition from far infrared observations with the Spitzer space telescope. *Astronomy and Astrophysics*, 477(2):665–670, Jan. 2008.

[10] P. Beck, E. Quirico, D. Sevestre, G. Montes-Hernandez, A. Pommerol, and B. Schmitt. Goethite as an alternative origin of the 3.1 μm band on dark asteroids. *Astronomy and Astrophysics*, 526:A85, Feb. 2011.

[11] W. Benz and E. Asphaug. Catastrophic Disruptions Revisited. *Icarus*, 142(1):5–20, Nov. 1999.

[12] R. P. Binzel, A. Morbidelli, S. Merouane, F. E. DeMeo, M. Birlan, P. Vernazza, C. A. Thomas, A. S. Rivkin, S. J. Bus, and A. T. Tokunaga. Earth encounters as the origin of fresh surfaces on near-Earth asteroids. *Nature*, 463(7):331–334, Jan. 2010.

[13] R. P. Binzel, A. S. Rivkin, J. S. Stuart, A. W. Harris, S. J. Bus, and T. H. Burbine. Observed spectral properties of near-Earth objects: results for population distribution, source regions, and space weathering processes. *Icarus*, 170(2):259–294, Aug. 2004.

[14] D. Bodewits, M. S. Kelley, J. Y. Li, W. B. Landsman, S. Besse, and M. F. A'Hearn. Collisional Excavation of Asteroid (596) Scheila. *The Astrophysical Journal Letters*, 733(1):L3, May 2011.

[15] J. Borovicka, O. P. Popova, I. V. Nemtchinov, P. Spurny, and Z. Ceplecha. Bolides produced by impacts of large meteoroids into the Earth's atmosphere: comparison of theory with observations. I. Benesov bolide dynamics and fragmentation. *Astronomy and Astrophysics*, 334:713–728, June 1998.

[16] J. Borovička, P. Spurný, and P. Brown. Small Near-Earth Asteroids as a Source of Meteorites. In *Asteroids IV*, page 3307. arXiv.org, Feb. 2015.

[17] W. F. Bottke, M. Broz, D. P. O'Brien, A. Campo Bagatin, A. Morbidelli, and S. Marchi. The Collisional Evolution of the Main Asteroid Belt. In F. E. DeMeo and P. Michel, editors, *Asteroids IV*, pages 1–24. University of Arizona Press, May 2015.

[18] W. F. Bottke, D. D. Durda, D. Nesvorný, R. Jedicke, A. Morbidelli, D. Vokrouhlický, and H. Levison. The fossilized size distribution of the main asteroid belt. *Icarus*, 175(1):111–140, May 2005.

[19] W. F. Bottke, A. Morbidelli, R. Jedicke, J.-M. Petit, H. F. Levison, P. Michel, and T. S. Metcalfe. Debiased Orbital and Absolute Magnitude Distribution of the Near-Earth Objects. *Icarus*, 156(2):399–433, Apr. 2002.

[20] W. F. Bottke, D. Nesvorný, R. E. Grimm, A. Morbidelli, and D. P. O'Brien. Iron meteorites as remnants of planetesimals formed in the terrestrial planet region. *Nature*, 439(7):821–824, Feb. 2006.

[21] W. F. Bottke, D. Vokrouhlický, and D. Nesvorný. An asteroid breakup 160Myr ago as the probable source of the K/T impactor. *Nature*, 449(7):48–53, Sept. 2007.

[22] W. F. Bottke, D. Vokrouhlický, K. J. Walsh, M. Delbo, P. Michel, D. S. Lauretta, H. Campins, H. C. Connolly, D. J. Scheeres, and S. R. Chelsey. In search of the source of asteroid (101955) Bennu: Applications of the stochastic YORP model. *Icarus*, 247:191–217, Feb. 2015.

[23] W. F. J. Bottke, D. Vokrouhlický, D. P. Rubincam, and D. Nesvorný. The Yarkovsky and Yorp Effects: Implications for Asteroid Dynamics. *Annual Review of Earth and Planetary Sciences*, 34(1):157–191, May 2006.

[24] S. Breiter, P. Bartczak, M. Czekaj, B. Oczujda, and D. Vokrouhlický. The YORP effect on 25143 Itokawa. *Astronomy & Astrophysics*, 507(2):1073–1081, Nov. 2009.

[25] M. Brož and A. Morbidelli. The Eos family halo. *Icarus*, 223(2):844–849, Apr. 2013.

[26] M. Brož, A. Morbidelli, W. F. Bottke, J. Rozehnal, D. Vokrouhlický, and D. Nesvorný. Constraining the cometary flux through the asteroid belt during the late heavy bombardment. *Astronomy and Astrophysics*, 551:A117, Mar. 2013.

[27] R. Brunetto, M. J. Loeffler, D. Nesvorný, S. Sasaki, and G. Strazzulla. Asteroid Surface Alteration by Space Weathering Processes. In *Asteroids IV*, pages 1–21. Oct. 2015.

[28] T. H. Burbine, T. J. McCoy, A. Meibom, B. Gladman, and K. Keil. Meteoritic Parent Bodies: Their Number and Identification. *Asteroids III, W. F. Bottke Jr., A. Cellino, P. Paolicchi, and R. P. Binzel (eds), University of Arizona Press, Tucson.*, pages 653–667, 2002.

[29] H. Campins, J. de León, A. Morbidelli, J. Licandro, J. Gayon-Markt, M. Delbo, and P. Michel. The Origin of Asteroid 162173 (1999 JU3). *The Astronomical Journal*, 146(2):26, Aug. 2013.

[30] H. Campins, J. P. Emery, M. Kelley, Y. Fernández, J. Licandro, M. Delbo, A. Barucci, and E. Dotto. Spitzer observations of spacecraft target 162173 (1999 JU3). *Astronomy & Astrophysics*, 503(2):L17–L20, Aug. 2009.

[31] H. Campins, K. Hargrove, N. Pinilla-Alonso, E. S. Howell, M. S. Kelley, J. Licandro, T. Mothé-Diniz, Y. Fernández, and J. Ziffer. Water ice and organics on the surface of the asteroid 24 Themis. *Nature*, 464(7):1320–1321, Apr. 2010.

[32] H. Campins, J. Ziffer, J. Licandro, N. Pinilla-Alonso, Y. Fernández, J. d. León, T. Mothé-Diniz, and R. P. Binzel. Nuclear Spectra of Comet 162P/Siding Spring (2004 TU12). *The Astronomical Journal*, 132(3):1346–1353, Sept. 2006.

[33] D. Čapek and D. Vokrouhlický. Thermal stresses in small meteoroids. *Astronomy and Astrophysics*, 519:A75, Sept. 2010.

[34] M. T. Capria, F. Tosi, M. C. De Sanctis, F. Capaccioni, E. Ammannito, A. Frigeri, F. Zambon, S. Fonte, E. Palomba, D. Turrini, T. N. Titus, S. E. Schröder, M. Toplis, J. Y. Li, J. P. Combe, C. A. Raymond, and C. T. Russell. Vesta surface thermal properties map. *Geophysical Research Letters*, 41(5):1438–1443, Mar. 2014.

[35] B. Carry. Density of asteroids. *Planetary and Space Science*, 73(1):98–118, Dec. 2012.

[36] B. Carry, A. Matter, P. Scheirich, P. Pravec, L. Molnar, S. Mottola, A. Carbognani, E. Jehin, A. Marciniak, R. P. Binzel, F. E. DeMeo, M. Birlan, M. Delbo, E. Barbotin, R. Behrend, M. Bonnardeau, F. Colas, P. Farissier, M. Fauvaud, S. Fauvaud, C. Gillier, M. Gillon, S. Hellmich, R. Hirsch, A. Leroy, J. Manfroid, J. Montier, E. Morelle, F. Richard, K. Sobkowiak, J. Strajnic, and F. VACHIER. The small binary asteroid (939) Isberga. *Icarus*, 248:516–525, Mar. 2015.

[37] H. Clenet, M. Jutzi, J.-A. Barrat, E. I. Asphaug, W. Benz, and P. Gillet. A deep crust-mantle boundary in the asteroid 4 Vesta. *Nature*, 511(7):303–306, July 2014.

[38] G. J. Consolmagno, G. J. Golabek, D. Turrini, M. Jutzi, S. Sirono, V. Svetsov, and K. Tsiganis. Is Vesta an intact and pristine protoplanet? *Icarus*, 254:190–201, July 2015.

[39] J. de León, H. Campins, K. Tsiganis, A. Morbidelli, and J. Licandro. Origin of the near-Earth asteroid Phaethon and the Geminids meteor shower. *Astronomy and Astrophysics*, 513:A26, Apr. 2010.

[40] M. C. De Sanctis, E. Ammannito, M. T. Capria, F. Tosi, F. Capaccioni, F. Zambon, F. Carraro, S. Fonte, A. Frigeri, R. Jaumann, G. Magni, S. Marchi, T. B. McCord, L. A. McFadden, H. Y. McSween, D. W. Mittlefehldt, A. Nathues, E. Palomba, C. M. Pieters, C. A. Raymond, C. T. Russell, M. J. Toplis, and D. Turrini. Spectroscopic Characterization of Mineralogy and Its Diversity Across Vesta. *Science*, 336(6):697–700, May 2012.

[41] M. Delbo. The nature of near-Earth asteroids from the study of their thermal infrared emission. *PhD thesis*, pages 1–210, June 2004.

[42] M. Delbo, A. dell'Oro, A. W. Harris, S. Mottola, and M. Mueller. Thermal inertia of near-Earth asteroids and implications for the magnitude of the Yarkovsky effect. *Icarus*, 190(1):236–249, Sept. 2007.

[43] M. Delbo, J. Gayon-Markt, G. Busso, A. Brown, L. Galluccio, C. Ordenovic, P. Bendjoya, and P. Tanga. Asteroid spectroscopy with Gaia. *Planetary and Space Science*, 73(1):86–94, Dec. 2012.

[44] M. Delbo and A. W. Harris. Physical properties of near-Earth asteroids from thermal infrared observations and thermal modeling. *Meteoritics & Planetary Science*, 37(12):1929–1936, Dec. 2002.

[45] M. Delbo, A. W. Harris, R. P. Binzel, P. Pravec, and J. K. Davies. Keck observations of near-Earth asteroids in the thermal infrared. *Icarus*, 166(1):116–130, Nov. 2003.

[46] M. Delbo, G. Libourel, J. Wilkerson, N. Murdoch, P. Michel, K. T. Ramesh, C. Ganino, C. Verati, and S. Marchi. Thermal fatigue as the origin of regolith on small asteroids. *Nature*, 508(7):233–236, Apr. 2014.

[47] M. Delbo, S. Ligori, A. Matter, A. Cellino, and J. Berthier. First VLTI-MIDI Direct Determinations of Asteroid Sizes. *The Astrophysical Journal*, 694(2):1228–1236, Apr. 2009.

[48] M. Delbo and P. Michel. Temperature History and Dynamical Evolution of (101955) 1999 RQ 36: A Potential Target for Sample Return from a Primitive Asteroid. *The Astrophysical Journal Letters*, 728(2):L42, Feb. 2011.

[49] M. Delbo, M. Mueller, J. P. Emery, B. Rozitis, and M. T. Capria. Thermophysical modeling of asteroid surfaces. In *Asteroids IV*, pages 1–21. Oct. 2015.

[50] M. Delbo and P. Tanga. Thermal inertia of main belt asteroids smaller than 100 km from IRAS data. *Planetary and Space Science*, 57(2):259–265, Feb. 2009.

[51] F. E. DeMeo and B. Carry. Solar System evolution from compositional mapping of the asteroid belt. *Nature*, 505(7):629–634, Jan. 2014.

[52] D. D. Durda, W. F. Bottke, B. L. Enke, W. J. Merline, E. Asphaug, D. C. Richardson, and Z. M. Leinhardt. The formation of asteroid satellites in large impacts: results from numerical simulations. *Icarus*, 167(2):382–396, Feb. 2004.

[53] J. Durech. 433 Eros - comparison of lightcurve extrema from 1901-1931 with the present rotation state. *Astronomy and Astrophysics*, 431:381–383, Feb. 2005.

[54] J. Durech, B. Carry, M. Delbo, M. Kaasalainen, and M. Viikinkoski. Asteroid Models from Multiple Data Sources. In *Asteroids IV*. University of Arizona Press, Tucson, AZ, Jan. 2015.

[55] J. Durech, M. KAASALAINEN, B. D. Warner, M. Fauerbach, S. A. Marks, S. Fauvaud, M. Fauvaud, J. M. Vugnon, F. Pilcher, L. Bernasconi, and R. Behrend. Asteroid models from combined sparse and dense photometric data. *Astronomy and Astrophysics*, 493(1):291–297, Jan. 2009.

[56] M. J. Dykhuis and R. Greenberg. Collisional family structure within the Nysa-Polana complex. *Icarus*, 252:199–211, May 2015.

[57] A. Fujiwara, J. Kawaguchi, D. K. Yeomans, M. Abe, T. Mukai, T. Okada, J. Saito, H. Yano, M. Yoshikawa, D. J. Scheeres, O. Barnouin-Jha, A. F. Cheng, H. Demura, R. W. Gaskell, N. Hirata, H. Ikeda, T. Kominato, H. Miyamoto, A. M. Nakamura, R. Nakamura, S. Sasaki, and K. Uesugi. The Rubble-Pile Asteroid Itokawa as Observed by Hayabusa. *Science*, 312(5):1330–1334, June 2006.

[58] M. J. Gaffey and S. L. Gilbert. Asteroid 6 Hebe: The probable parent body of the H-Type ordinary chondrites and the IIE iron meteorites. *Meteoritics & Planetary Science*, 33(6):1281–1295, Nov. 1998.

[59] L. Galluccio, O. Michel, P. Bendjoya, and E. Slezak. Unsupervised Clustering on Astrophysics Data: Asteroids Reflectance Spectra Surveys and Hyperspectral Images. In *CLASSIFICATION AND DISCOVERY IN LARGE ASTRONOMICAL SURVEYS: Proceedings of the In-*

ternational Conference: "Classification and Discovery in Large Astronomical Surveys". AIP Conference Proceedings, pages 165–171. Hippolyte FIZEAU Laboratory, CNRS-University of Nice Sophia Antipolis; I3S Laboratoire, CNRS-University of Nice Sophia Antipolis 2000, route des Lucioles Les Algorithms-BP. 121-06903 Sophia Antipolis Cedex-France, AIP, Dec. 2008.

[60] J. Gayon-Markt, M. Delbo, A. Morbidelli, and S. Marchi. On the origin of the Almahata Sitta meteorite and 2008 TC3 asteroid. *Monthly Notices of the Royal Astronomical Society*, 424(1):508–518, July 2012.

[61] O. Golubov and Y. N. Krugly. Tangential Component of the YORP Effect. *The Astrophysical Journal Letters*, 752(1):L11, June 2012.

[62] R. Gomes, H. F. Levison, K. Tsiganis, and A. Morbidelli. Origin of the cataclysmic Late Heavy Bombardment period of the terrestrial planets. *Nature*, 435(7):466–469, May 2005.

[63] M. Gounelle. The asteroid–comet continuum: In search of lost primitivity. *Elements*, 2011.

[64] B. Gundlach and J. Blum. A new method to determine the grain size of planetary regolith. *Icarus*, 223(1):479–492, Mar. 2013.

[65] B. A. S. Gustafson. Geminid meteoroids traced to cometary activity on Phaethon. *Astronomy and Astrophysics*, 225:533–540, Nov. 1989.

[66] J. Hanuš, M. Brož, J. Durech, B. D. Warner, J. Brinsfield, R. Durkee, D. Higgins, R. A. Koff, J. Oey, F. Pilcher, R. Stephens, L. P. Strabla, Q. Ulisse, and R. Girelli. An anisotropic distribution of spin vectors in asteroid families. *Astronomy & Astrophysics*, 559:A134, Nov. 2013.

[67] J. Hanuš, M. Delbo, J. Durech, and V. Alí-Lagoa. Thermophysical modeling of asteroids from WISE thermal infrared data - Significance of the shape model and the pole orientation uncertainties. *Icarus*, 256:101–116, Aug. 2015.

[68] J. Hanuš, J. Durech, M. Brož, B. D. Warner, F. Pilcher, R. Stephens, J. Oey, L. Bernasconi, S. Casulli, R. Behrend, D. Polishook, T. Henych, M. Lehký, F. Yoshida, and T. Ito. A study of asteroid pole-latitude

distribution based on an extended set of shape models derived by the lightcurve inversion method. *Astronomy & Astrophysics*, 530:134, June 2011.

[69] A. Harris, M. Boslough, C. R. Chapman, L. Drube, and P. Michel. Asteroid Impacts and Modern Civilization: Can we Prevent a Catastrophe? In *Asteroids IV*. University of Arizona Press, Tucson, AZ, June 2015.

[70] A. W. Harris. A Thermal Model for Near-Earth Asteroids. *Icarus*, 131(2):291–301, Feb. 1998.

[71] A. W. Harris. The surface properties of small asteroids from thermal-infrared observations. *Asteroids, Comets, Meteors. Proceedings IAU Symposium No. 229, 2005 D. Lazzaro, S. Ferraz-Mello & J.A. Fernandez, eds*, 229:449–463, 2006.

[72] A. W. Harris and J. S. V. Lagerros. Asteroids in the Thermal Infrared. *Asteroids III, W. F. Bottke Jr., A. Cellino, P. Paolicchi, and R. P. Binzel (eds), University of Arizona Press, Tucson.*, pages 205–218, 2002.

[73] A. W. Harris, M. Mommert, J. L. Hora, M. Mueller, D. E. Trilling, B. Bhattacharya, W. F. Bottke, S. Chesley, M. Delbo, J. P. Emery, G. Fazio, A. Mainzer, B. Penprase, H. A. Smith, T. B. Spahr, J. A. Stansberry, and C. A. Thomas. ExploreNEOs. II. The Accuracy of the Warm Spitzer Near-Earth Object Survey. *The Astronomical Journal*, 141(3):75, Mar. 2011.

[74] P. Hartogh, D. C. Lis, D. Bockelée-Morvan, M. de Val-Borro, N. Biver, M. Küppers, M. Emprechtinger, E. A. Bergin, J. Crovisier, M. Rengel, R. Moreno, S. Szutowicz, and G. A. Blake. Ocean-like water in the Jupiter-family comet 103P/Hartley 2. *Nature*, 478(7):218–220, Oct. 2011.

[75] T. Hiroi, M. Abe, K. Kitazato, S. Abe, B. E. Clark, S. Sasaki, M. Ishiguro, and O. S. Barnouin-Jha. Developing space weathering on the asteroid 25143 Itokawa. *Nature*, 443(7):56–58, Sept. 2006.

[76] M. Horstmann and A. Bischoff. The Almahata Sitta polymict breccia and the late accretion of asteroid 2008 TC3. *Chemie der Erde - Geochemistry*, 74:149–183, June 2014.

[77] F. Hörz and M. Cintala. Impact experiments related to the evolution of planetary regoliths. *Meteoritics & Planetary Science*, 32(2):179–209, Mar. 1997.

[78] K. R. Housen and K. A. Holsapple. Impact cratering on porous asteroids. *Icarus*, 163(1):102–119, May 2003.

[79] K. R. Housen and K. A. Holsapple. Ejecta from impact craters. *Icarus*, 211(1):856–875, Jan. 2011.

[80] K. R. Housen, L. L. Wilkening, C. R. Chapman, and R. Greenberg. Asteroidal regoliths. *Icarus*, 39(3):317–351, Sept. 1979.

[81] H. H. Hsieh and D. Jewitt. A Population of Comets in the Main Asteroid Belt. *Science*, 312(5):561–563, Apr. 2006.

[82] T. R. Hunter, R. Kneissl, and A. Moullet. ALMA Observations of Asteroid 3 Juno at 60 Kilometer Resolution. *arXiv.org*, 2015.

[83] R. Jedicke, M. Granvik, M. Micheli, E. Rayan, T. Spahr, and D. K. Yeomans. Surveys, Follow-up & Population Statistics. In *Asteroids IV*, pages 1–22. University of Arizona Press, Tucson, AZ, Oct. 2015.

[84] P. Jenniskens, M. H. Shaddad, D. Numan, S. Elsir, A. M. Kudoda, M. E. Zolensky, L. Le, G. A. Robinson, J. M. Friedrich, D. Rumble, A. Steele, S. R. Chesley, A. Fitzsimmons, S. Duddy, H. H. Hsieh, G. Ramsay, P. G. Brown, W. N. Edwards, E. Tagliaferri, M. B. Boslough, R. E. Spalding, R. Dantowitz, M. Kozubal, P. Pravec, J. Borovicka, Z. Charvat, J. Vaubaillon, J. Kuiper, J. Albers, J. L. Bishop, R. L. Mancinelli, S. A. Sandford, S. N. Milam, M. Nuevo, and S. P. Worden. The impact and recovery of asteroid 2008 TC3. *Nature*, 458(7):485–488, Mar. 2009.

[85] D. Jewitt and J. Li. Activity in Geminid Parent (3200) Phaethon. *The Astronomical Journal*, 140(5):1519–1527, Nov. 2010.

[86] D. Jewitt, H. Weaver, J. Agarwal, M. Mutchler, and M. Drahus. A recent disruption of the main-belt asteroid P/2010A2. *Nature*, 467(7):817–819, Oct. 2010.

[87] D. Jewitt, H. Weaver, M. Mutchler, S. Larson, and J. Agarwal. Hubble Space Telescope Observations of Main-belt Comet (596) Scheila. *The Astrophysical Journal Letters*, 733(1):L4, May 2011.

[88] A. Johansen, E. Jaquet, J. N. Cuzzi, A. Morbidelli, and M. Gounelle. New Paradigms For Asteroid Formation. In *Asteroids IV*, pages 1–22. Oct. 2015.

[89] M. Jutzi, E. Asphaug, P. Gillet, J. A. Barrat, and W. Benz. The structure of the asteroid 4Vesta as revealed by models of planet-scale collisions. *Nature*, 494(7):207–210, Feb. 2013.

[90] M. Jutzi, P. Michel, W. Benz, and D. C. Richardson. Fragment properties at the catastrophic disruption threshold: The effect of the parent body's internal structure. *Icarus*, 207(1):54–65, May 2010.

[91] M. KAASALAINEN. Physical models of large number of asteroids from calibrated photometry sparse in time. *Astronomy and Astrophysics*, 422(2):L39–L42, July 2004.

[92] M. KAASALAINEN and J. Torppa. Optimization Methods for Asteroid Lightcurve Inversion. I. Shape Determination. *Icarus*, 153(1):24–36, Sept. 2001.

[93] M. KAASALAINEN, J. Torppa, and K. Muinonen. Optimization Methods for Asteroid Lightcurve Inversion. II. The Complete Inverse Problem. *Icarus*, 153(1):37–51, Sept. 2001.

[94] T. V. V. King, R. N. Clark, W. M. Calvin, D. M. Sherman, and R. H. Brown. Evidence for ammonium-bearing minerals on Ceres. *Science (ISSN 0036-8075)*, 255(5051):1551–1553, Mar. 1992.

[95] M. Küppers, L. O'Rourke, D. Bockelée-Morvan, V. Zakharov, S. Lee, P. von Allmen, B. Carry, D. Teyssier, A. Marston, T. Müller, J. Crovisier, M. A. Barucci, and R. Moreno. Localized sources of water vapour on the dwarf planet (1) Ceres. *Nature*, 505(7):525–527, Jan. 2014.

[96] J. S. V. Lagerros. Thermal physics of asteroids. I. Effects of shape, heat conduction and beaming. *Astronomy and Astrophysics*, 310:1011–1020, June 1996.

[97] J. S. V. Lagerros. Thermal physics of asteroids. III. Irregular shapes and albedo variegations. *Astronomy & Astrophysics*, 325:1226–1236, Sept. 1997.

[98] J. S. V. Lagerros. Thermal physics of asteroids. IV. Thermal infrared beaming. *Astronomy & Astrophysics*, 332:1123–1132, Apr. 1998.

[99] L. A. Lebofsky, M. A. Feierberg, A. T. Tokunaga, H. P. Larson, and J. R. Johnson. The 1.7- to 4.2-micron spectrum of asteroid 1 Ceres - Evidence for structural water in clay minerals. *Icarus*, 48(3):453–459, Dec. 1981.

[100] L. A. Lebofsky and G. H. Rieke. Thermal properties of 433 Eros. *Icarus*, 40(2):297–308, Nov. 1979.

[101] L. A. Lebofsky and J. R. Spencer. Radiometry and a thermal modeling of asteroids. In *Asteroids II*, pages 128–147. University of Arizona Press, Tucson, AZ, 1989.

[102] H. F. Levison, W. F. Bottke, M. Gounelle, A. Morbidelli, D. Nesvorný, and K. Tsiganis. Contamination of the asteroid belt by primordial trans-Neptunian objects. *Nature*, 460(7):364–366, July 2009.

[103] J. Licandro, H. Campins, M. Kelley, K. Hargrove, N. Pinilla-Alonso, D. Cruikshank, A. S. Rivkin, and J. Emery. (65) Cybele: detection of small silicate grains, water-ice, and organics. *Astronomy & Astrophysics*, 525:A34, Jan. 2011.

[104] J. Licandro, H. Campins, T. Mothé-Diniz, N. Pinilla-Alonso, and J. de León. The nature of comet-asteroid transition object (3200) Phaethon. *Astronomy and Astrophysics*, 461(2):751–757, Jan. 2007.

[105] B. Lopez, e. al, and C. Dominik. An Overview of the MATISSE Instrument — Science, Concept and Current Status. *The Messenger*, 157:5–12, 2014.

[106] S. C. Lowry, P. R. Weissman, S. R. Duddy, B. Rozitis, A. Fitzsimmons, S. F. Green, M. D. Hicks, C. Snodgrass, S. D. Wolters, S. R. Chesley, J. Pittichová, and P. van Oers. The internal structure of asteroid (25143) Itokawa as revealed by detection of YORP spin-up. *Astronomy & Astrophysics*, 562:A48, Feb. 2014.

[107] A. Luque, E. Ruiz-Agudo, and G. Cultrone. Direct observation of microcrack development in marble caused by thermal weathering. *Environmental Earth Sciences*, 62:1375–1386, 2011.

[108] C. Magri, G. J. Consolmagno, S. J. Ostro, L. A. M. Benner, and B. R. Beeney. Radar constraints on asteroid regolith compositions using 433 Eros as ground truth. *Meteoritics & Planetary Science*, 36(12):1697–1709, Dec. 2001.

[109] A. Mainzer, T. Grav, J. Bauer, J. Masiero, R. S. McMillan, R. M. Cutri, R. Walker, E. Wright, P. Eisenhardt, D. J. Tholen, T. Spahr, R. JEDICKE, L. Denneau, E. DeBaun, D. Elsbury, T. Gautier, S. Gomillion, E. Hand, W. Mo, J. Watkins, A. Wilkins, G. L. Bryngelson, A. Del Pino Molina, S. Desai, M. Gómez Camus, S. L. Hidalgo, I. Konstantopoulos, J. A. Larsen, C. Maleszewski, M. A. Malkan, J. C. Mauduit, B. L. Mullan, E. W. Olszewski, J. Pforr, A. Saro, J. V. Scotti, and L. H. Wasserman. NEOWISE Observations of Near-Earth Objects: Preliminary Results. *The Astrophysical Journal*, 743(2):156, Dec. 2011.

[110] A. Mainzer, T. Grav, J. Masiero, J. Bauer, R. S. McMillan, J. GIORGINI, T. Spahr, R. M. Cutri, D. J. Tholen, R. JEDICKE, R. Walker, E. Wright, and C. R. Nugent. Characterizing Subpopulations within the near-Earth Objects with NEOWISE: Preliminary Results. *The Astrophysical Journal*, 752(2):110, June 2012.

[111] A. Mainzer, F. Usui, and D. E. Trilling. Space-Based Thermal Infrared Studies of Asteroids. In *Asteroids IV*, pages 1–22. Mar. 2015.

[112] S. Marchi, M. Delbo, A. Morbidelli, P. Paolicchi, and M. Lazzarin. Heating of near-Earth objects and meteoroids due to close approaches to the Sun. *Monthly Notices of the Royal Astronomical Society*, 400(1):147–153, Nov. 2009.

[113] S. Marchi, S. Magrin, D. Nesvorný, P. Paolicchi, and M. Lazzarin. A spectral slope versus perihelion distance correlation for planet-crossing asteroids. *Monthly Notice of the Royal Astronomical Society*, 368(1):L39–L42, May 2006.

[114] S. Marchi, P. Paolicchi, M. Lazzarin, and S. Magrin. A General Spectral Slope-Exposure Relation for S-Type Main Belt and Near-Earth Asteroids. *The Astronomical Journal*, 131(2):1138–1141, Feb. 2006.

[115] J. R. Masiero, A. K. Mainzer, T. Grav, J. M. Bauer, R. M. Cutri, J. Dailey, P. R. M. Eisenhardt, R. S. McMillan, T. B. Spahr, M. F. Skrutskie, D. Tholen, R. G. Walker, E. L. Wright, E. DeBaun, D. Elsbury, T. I. Gautier, S. Gomillion, and A. Wilkins. Main Belt Asteroids with WISE/NEOWISE. I. Preliminary Albedos and Diameters. *The Astrophysical Journal*, 741(2):68, Nov. 2011.

[116] J. R. Masiero, A. K. Mainzer, T. Grav, J. M. Bauer, R. M. Cutri, C. Nugent, and M. S. Cabrera. Preliminary Analysis of WISE/NEOWISE 3-Band Cryogenic and Post-cryogenic Observations of Main Belt Asteroids. *The Astrophysical Journal Letters*, 759(1):L8, Nov. 2012.

[117] A. Matter, M. Delbo, B. Carry, and S. Ligori. Evidence of a metal-rich surface for the Asteroid (16) Psyche from interferometric observations in the thermal infrared. *Icarus*, 226(1):419–427, Sept. 2013.

[118] A. Matter, M. Delbo, S. Ligori, N. Crouzet, and P. Tanga. Determination of physical properties of the Asteroid (41) Daphne from interferometric observations in the thermal infrared. *Icarus*, 215(1):47–56, Sept. 2011.

[119] L. D. McFadden, M. C. Eppes, A. R. Gillespie, and B. Hallet. Physical weathering in arid landscapes due to diurnal variation in the direction of solar heating. *Geological Society of America Bulletin*, 117:161, 2005.

[120] P. Michel, W. Benz, P. Tanga, and D. C. Richardson. Collisions and Gravitational Reaccumulation: Forming Asteroid Families and Satellites. *Science*, 294(5):1696–1700, Nov. 2001.

[121] P. Michel and M. Delbo. Orbital and thermal evolutions of four potential targets for a sample return space mission to a primitive near-Earth asteroid. *Icarus*, 209(2):520–534, Oct. 2010.

[122] P. Michel and D. C. Richardson. Collision and gravitational reaccumulation: Possible formation mechanism of the asteroid Itokawa. *Astronomy and Astrophysics*, 554:L1, June 2013.

[123] A. Milani, A. Cellino, Z. Knežević, B. Novaković, F. Spoto, and P. Paolicchi. Asteroid families classification: Exploiting very large datasets. *Icarus*, 239:46–73, Sept. 2014.

[124] D. A. Minton and R. Malhotra. A record of planet migration in the main asteroid belt. *Nature*, 457(7):1109–1111, Feb. 2009.

[125] M. Mommert, J. L. Hora, A. W. Harris, W. T. Reach, J. P. Emery, C. A. Thomas, M. Mueller, D. P. Cruikshank, D. E. Trilling, M. Delbo, and H. A. Smith. The Discovery of Cometary Activity in Near-Earth Asteroid (3552) Don Quixote. *The Astrophysical Journal*, 781(1):25, Jan. 2014.

[126] A. Morbidelli, W. F. Bottke, D. Nesvorný, and H. F. Levison. Asteroids were born big. *Icarus*, 204(2):558–573, Dec. 2009.

[127] A. Morbidelli, R. Brasser, R. Gomes, H. F. Levison, and K. Tsiganis. Evidence from the Asteroid Belt for a Violent Past Evolution of Jupiter's Orbit. *The Astronomical Journal*, 140(5):1391–1401, Nov. 2010.

[128] A. Morbidelli, H. F. Levison, K. Tsiganis, and R. Gomes. Chaotic capture of Jupiter's Trojan asteroids in the early Solar System. *Nature*, 435(7):462–465, May 2005.

[129] A. Morbidelli and D. Vokrouhlický. The Yarkovsky-driven origin of near-Earth asteroids. *Icarus*, 163(1):120–134, May 2003.

[130] A. Morbidelli, K. J. Walsh, D. P. O'Brien, D. A. Minton, and W. F. Bottke. The Dynamical Evolution of the Asteroid Belt. In *Asteroids IV*, page 6204. University of Arizona Press, Tucson, AZ, Jan. 2015.

[131] D. Morrison. The diameter and thermal inertia of 433 Eros. *Icarus*, 28:125–132, May 1976.

[132] M. Mueller. *Surface Properties of Asteroids from Mid-Infrared Observations and Thermophysical Modeling*. PhD thesis, PhD thesis on arXiv.org, Nov. 2007.

[133] M. Mueller, M. Delbo, J. L. Hora, D. E. Trilling, B. Bhattacharya, W. F. Bottke, S. Chesley, J. P. Emery, G. Fazio, A. W. Harris, A. Mainzer,

M. Mommert, B. Penprase, H. A. Smith, T. B. Spahr, J. A. Stansberry, and C. A. Thomas. ExploreNEOs. III. Physical Characterization of 65 Potential Spacecraft Target Asteroids. *The Astronomical Journal*, 141(4):109, Apr. 2011.

[134] T. G. Müller and J. S. V. Lagerros. Asteroids as calibration standards in the thermal infrared for space observatories. *Astronomy & Astrophysics*, 381:324–339, Jan. 2002.

[135] N. Murdoch, P. sanchez, S. R. Schwartz, and H. Miyamoto. Asteroid Surface Geophysics. In *Asteroids IV*. University of Arizona Press, Tucson, AZ, Sept. 2015.

[136] T. Nakamura, T. Noguchi, M. Tanaka, M. E. Zolensky, M. Kimura, A. Tsuchiyama, A. Nakato, T. Ogami, H. Ishida, M. Uesugi, T. Yada, K. Shirai, A. Fujimura, R. Okazaki, S. A. Sandford, Y. Ishibashi, M. Abe, T. Okada, M. Ueno, T. Mukai, M. Yoshikawa, and J. Kawaguchi. Itokawa Dust Particles: A Direct Link Between S-Type Asteroids and Ordinary Chondrites. *Science*, 333(6):1113–1116, Aug. 2011.

[137] D. Nesvorný and W. F. Bottke. Detection of the Yarkovsky effect for main-belt asteroids. *Icarus*, 170(2):324–342, Aug. 2004.

[138] D. Nesvorný, D. Vokrouhlický, and A. Morbidelli. Capture of Trojans by Jumping Jupiter. *The Astrophysical Journal*, 768(1):45, May 2013.

[139] D. Nesvorný, D. Vokrouhlický, A. Morbidelli, and W. F. Bottke. Asteroidal source of L chondrite meteorites. *Icarus*, 200(2):698–701, Apr. 2009.

[140] C. P. Opeil, G. J. Consolmagno, and D. T. Britt. The thermal conductivity of meteorites: New measurements and analysis. *Icarus*, 208(1):449–454, July 2010.

[141] C. P. Opeil, G. J. Consolmagno, D. J. Safarik, and D. T. Britt. Stony meteorite thermal properties and their relationship with meteorite chemical and physical states. *Meteoritics & Planetary Science*, 47(3):319–329, Mar. 2012.

[142] S. J. Ostro, R. S. Hudson, M. C. Nolan, J.-L. Margot, D. J. Scheeres, D. B. Campbell, C. Magri, J. D. Giorgini, and D. K. Yeomans. Radar Observations of Asteroid 216 Kleopatra. *Science*, 288(5):836–839, May 2000.

[143] A. Parker, Ž. Ivezić, M. Jurić, R. Lupton, M. D. Sekora, and A. Kowalski. The size distributions of asteroid families in the SDSS Moving Object Catalog 4. *Icarus*, 198(1):138–155, Nov. 2008.

[144] C. M. Pieters, E. Ammannito, D. T. Blewett, B. W. Denevi, M. C. De Sanctis, M. J. Gaffey, L. Le Corre, J. Y. Li, S. Marchi, T. B. McCord, L. A. McFadden, D. W. Mittlefehldt, A. Nathues, E. Palmer, V. Reddy, C. A. Raymond, and C. T. Russell. Distinctive space weathering on Vesta from regolith mixing processes. *Nature*, 491(7):79–82, Nov. 2012.

[145] S. N. Raymond, T. Quinn, and J. I. Lunine. Making other earths: dynamical simulations of terrestrial planet formation and water delivery. *Icarus*, 168(1):1–17, Mar. 2004.

[146] S. N. Raymond, T. Quinn, and J. I. Lunine. High-resolution simulations of the final assembly of Earth-like planets I. Terrestrial accretion and dynamics. *Icarus*, 183(2):265–282, Aug. 2006.

[147] V. Reddy, J. A. Sanchez, W. F. Bottke, E. A. Cloutis, M. R. M. Izawa, D. P. O'Brien, P. Mann, M. Cuddy, L. Le Corre, M. J. Gaffey, and G. Fujihara. Chelyabinsk meteorite explains unusual spectral properties of Baptistina Asteroid Family. *Icarus*, 237:116–130, July 2014.

[148] A. S. Rivkin, E. Asphaug, and W. F. Bottke. The case of the missing Ceres family. *Icarus*, 243:429–439, Nov. 2014.

[149] A. S. Rivkin and J. P. Emery. Detection of ice and organics on an asteroidal surface. *Nature*, 464(7):1322–1323, Apr. 2010.

[150] M. S. Robinson, P. C. Thomas, J. Veverka, S. Murchie, and B. Carcich. The nature of ponded deposits on Eros. *Nature*, 413(6):396–400, Sept. 2001.

[151] B. Rozitis and S. F. Green. Directional characteristics of thermal-infrared beaming from atmosphereless planetary surfaces - a new thermophysical

model. *Monthly Notices of the Royal Astronomical Society*, 415(3):2042–2062, Aug. 2011.

[152] B. Rozitis and S. F. Green. The influence of rough surface thermal-infrared beaming on the Yarkovsky and YORP effects. *Monthly Notices of the Royal Astronomical Society*, 423(1):367–388, June 2012.

[153] B. Rozitis and S. F. Green. The influence of global self-heating on the Yarkovsky and YORP effects. *Monthly Notices of the Royal Astronomical Society*, 433(1):603–621, July 2013.

[154] B. Rozitis, E. MacLennan, and J. P. Emery. Cohesive forces prevent the rotational breakup of rubble-pile asteroid (29075) 1950 DA. *Nature*, 512(7):174–176, Aug. 2014.

[155] D. P. Rubincam. Radiative Spin-up and Spin-down of Small Asteroids. *Icarus*, 148(1):2–11, Nov. 2000.

[156] C. T. Russell, C. A. Raymond, A. Coradini, H. Y. McSween, M. T. Zuber, A. Nathues, M. C. De Sanctis, R. Jaumann, A. S. Konopliv, F. Preusker, S. W. Asmar, R. S. Park, R. Gaskell, H. U. Keller, S. Mottola, T. Roatsch, J. E. C. Scully, D. E. Smith, P. Tricarico, M. J. Toplis, U. R. Christensen, W. C. Feldman, D. J. Lawrence, T. J. McCoy, T. H. Prettyman, R. C. Reedy, M. E. Sykes, and T. N. Titus. Dawn at Vesta: Testing the Protoplanetary Paradigm. *Science*, 336(6):684–686, May 2012.

[157] N. Schorghofer. The Lifetime of Ice on Main Belt Asteroids. *The Astrophysical Journal*, 682(1):697–705, July 2008.

[158] M. K. Shepard, B. E. Clark, M. C. Nolan, E. S. Howell, C. Magri, J. D. Giorgini, L. A. M. Benner, S. J. Ostro, A. W. Harris, B. Warner, D. Pray, P. Pravec, M. Fauerbach, T. Bennett, A. Klotz, R. Behrend, H. Correia, J. Coloma, S. Casulli, and A. Rivkin. A radar survey of M- and X-class asteroids. *Icarus*, 195(1):184–205, May 2008.

[159] M. K. Shepard, B. E. Clark, M. Ockert-Bell, M. C. Nolan, E. S. Howell, C. Magri, J. D. Giorgini, L. A. M. Benner, S. J. Ostro, A. W. Harris, B. D. Warner, R. D. Stephens, and M. Mueller. A radar survey of M- and X-class asteroids II. Summary and synthesis. *Icarus*, 208(1):221–237, July 2010.

[160] C. Snodgrass, C. Tubiana, T. O. Team, J.-B. Vincent, H. Sierks, S. Hviid, R. Moissi, H. Boehnhardt, C. Barbieri, D. Koschny, P. Lamy, H. Rickman, R. Rodrigo, B. Carry, S. C. Lowry, R. J. M. Laird, P. R. Weissman, A. Fitzsimmons, S. Marchi, and O. Team. A collision in 2009 as the origin of the debris trail of asteroid P/2010A2. *Nature*, 467(7):814–816, Oct. 2010.

[161] J. R. Spencer. A rough-surface thermophysical model for airless planets. *Icarus*, 83(1):27–38, Jan. 1990.

[162] J. R. Spencer, L. A. Lebofsky, and M. V. Sykes. Systematic biases in radiometric diameter determinations. *Icarus*, 78(2):337–354, Apr. 1989.

[163] F. Spoto, A. Milani, and Z. Knežević. Asteroid family ages. *arXiv.org*, page 5461, Apr. 2015.

[164] P. Spurný. Recent fireballs photographed in central Europe. *Planetary and Space Science (ISSN 0032-0633)*, 42(2):157–162, Feb. 1994.

[165] T. S. Statler. Extreme sensitivity of the YORP effect to small-scale topography. *Icarus*, 202(2):502–513, Aug. 2009.

[166] J. S. Stuart and R. P. Binzel. Bias-corrected population, size distribution, and impact hazard for the near-Earth objects. *Icarus*, 170(2):295–311, Aug. 2004.

[167] R. J. Sullivan, P. C. Thomas, S. L. Murchie, and M. S. Robinson. Asteroid Geology from Galileo and NEAR Shoemaker Data. *Asteroids III, W. F. Bottke Jr., A. Cellino, P. Paolicchi, and R. P. Binzel (eds), University of Arizona Press, Tucson.*, pages 331–350, 2002.

[168] P. Tanga, B. Carry, F. Colas, M. Delbo, A. Matter, J. Hanuš, V. Alí-Lagoa, A. H. Andrei, M. Assafin, M. Audejean, R. Behrend, J. I. B. Camargo, A. Carbognani, M. Cedres Reyes, M. Conjat, N. Cornero, D. Coward, R. Crippa, E. de Ferra Fantin, M. Devogele, G. Dubos, E. Frappa, M. Gillon, H. Hamanowa, E. Jehin, A. Klotz, A. Kryszczyńska, J. Lecacheux, A. Leroy, J. Manfroid, F. Manzini, L. Maquet, E. Morelle, S. Mottola, M. Polińska, R. Roy, M. Todd, F. VACHIER, C. Vera Hernandez, and P. Wiggins. The non-convex shape of (234) Barbara, the

first Barbarian*. *Monthly Notices of the Royal Astronomical Society*, 448(4):3382–3390, Apr. 2015.

[169] E. F. Tedesco, P. V. Noah, M. Noah, and S. D. Price. The Supplemental IRAS Minor Planet Survey. *The Astronomical Journal*, 123(2):1056–1085, Feb. 2002.

[170] D. E. Trilling, M. Mueller, J. L. Hora, A. W. Harris, B. Bhattacharya, W. F. Bottke, S. Chesley, M. Delbo, J. P. Emery, G. Fazio, A. Mainzer, B. Penprase, H. A. Smith, T. B. Spahr, J. A. Stansberry, and C. A. Thomas. ExploreNEOs. I. Description and First Results from the Warm Spitzer Near-Earth Object Survey. *The Astronomical Journal*, 140(3):770–784, Sept. 2010.

[171] K. Tsiganis, R. Gomes, A. Morbidelli, and H. F. Levison. Origin of the orbital architecture of the giant planets of the Solar System. *Nature*, 435(7):459–461, May 2005.

[172] F. Usui, T. Kasuga, S. Hasegawa, M. Ishiguro, D. Kuroda, T. G. Müller, T. Ootsubo, and H. Matsuhara. Albedo Properties of Main Belt Asteroids Based on the All-Sky Survey of the Infrared Astronomical Satellite AKARI. *The Astrophysical Journal*, 762(1):56, Jan. 2013.

[173] P. Vernazza, R. P. Binzel, A. Rossi, M. Fulchignoni, and M. Birlan. Solar wind as the origin of rapid reddening of asteroid surfaces. *Nature*, 458(7):993–995, Apr. 2009.

[174] P. Vernazza, R. P. Binzel, C. A. Thomas, F. E. DeMeo, S. J. Bus, A. S. Rivkin, and A. T. Tokunaga. Compositional differences between meteorites and near-Earth asteroids. *Nature*, 454(7):858–860, Aug. 2008.

[175] P. Vernazza, M. Delbo, P. L. King, M. R. M. Izawa, J. Olofsson, P. Lamy, F. Cipriani, R. P. Binzel, F. Marchis, B. Merín, and A. Tamanai. High surface porosity as the origin of emissivity features in asteroid spectra. *Icarus*, 221(2):1162–1172, Nov. 2012.

[176] P. Vernazza, P. Lamy, O. Groussin, T. Hiroi, L. Jorda, P. L. King, M. R. M. Izawa, F. Marchis, M. Birlan, and R. Brunetto. Asteroid (21) Lutetia as a remnant of Earth's precursor planetesimals. *Icarus*, 216(2):650–659, Dec. 2011.

[177] J. Veverka, P. C. Thomas, M. Robinson, S. Murchie, C. Chapman, M. Bell, A. Harch, W. J. Merline, J. F. Bell, B. Bussey, B. Carcich, A. Cheng, B. Clark, D. Domingue, D. Dunham, R. Farquhar, M. J. Gaffey, E. Hawkins, N. Izenberg, J. Joseph, R. Kirk, H. Li, P. Lucey, M. Malin, L. McFadden, J. K. Miller, W. M. Owen, C. Peterson, L. Prockter, J. Warren, D. Wellnitz, B. G. Williams, and D. K. Yeomans. Imaging of Small-Scale Features on 433 Eros from NEAR: Evidence for a Complex Regolith. *Science*, 292(5):484–488, Apr. 2001.

[178] H. Viles, B. Ehlmann, C. F. Wilson, T. Cebula, M. Page, and M. Bourke. Simulating weathering of basalt on Mars and Earth by thermal cycling. *Geophysical Research Letters*, 37(1):18201, Sept. 2010.

[179] D. Vokrouhlický, W. F. Bottke, S. R. Chesley, D. J. Scheeres, and T. S. Statler. The Yarkovsky and YORP effects. In *Asteroids IV*. University of Arizona Press, Tucson, AZ, Sept. 2015.

[180] K. J. Walsh, M. Delbo, W. F. Bottke, D. Vokrouhlický, and D. S. Lauretta. Introducing the Eulalia and new Polana asteroid families: Reassessing primitive asteroid families in the inner Main Belt. *Icarus*, 225(1):283–297, July 2013.

[181] K. J. Walsh, A. Morbidelli, S. N. Raymond, D. P. O'Brien, and A. M. Mandell. A low mass for Mars from Jupiter's early gas-driven migration. *Nature*, 475(7):206–209, July 2011.

[182] K. J. Walsh, D. C. Richardson, and P. Michel. Rotational breakup as the origin of small binary asteroids. *Nature*, 454(7):188–191, July 2008.

[183] H. Yano, T. Kubota, H. Miyamoto, T. Okada, D. SCHEERES, Y. Takagi, K. Yoshida, M. Abe, S. Abe, O. Barnouin-Jha, A. Fujiwara, S. Hasegawa, T. Hashimoto, M. Ishiguro, M. Kato, J. Kawaguchi, T. Mukai, J. Saito, S. Sasaki, and M. Yoshikawa. Touchdown of the Hayabusa Spacecraft at the Muses Sea on Itokawa. *Science*, 312(5):1350–1353, June 2006.

[184] J. R. Zimbelman. The role of porosity in thermal inertia variations on basaltic lavas. *Icarus*, 68(2):366–369, Nov. 1986.

Aknowledgments

To be completed before final submission

Formal Acknowledgements

To be completed before final submission

Marco Delbo